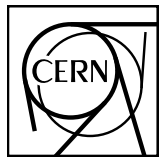


# EUROPEAN ORGANIZATION FOR NUCLEAR RESEARCH



March 26, 2018

## D-hadron correlations in p-Pb collisions at $\sqrt{s_{\text{NN}}} = 5.02 \text{ TeV}$

F. Colamaria, S. Kumar, M. Mazzilli

### Abstract

In this note, we present the analysis of azimuthal correlations of D mesons and primary charged  $\pi, K, p, e, \mu$  performed in the ALICE central barrel in p-Pb collisions at  $\sqrt{s_{\text{NN}}} = 5.02 \text{ TeV}$ , from 2016 data taking. The analysis is performed in an extended  $p_T$  range and with additional observables with respect to p-Pb 2013 data analysis. After a description of the analysis strategy, corrections and systematic uncertainties, the results obtained for prompt  $D^0$ ,  $D^{*+}$  and  $D^+$ mesons in different ranges of transverse momentum of the D meson and of the associated particles are presented. The results are then compared to Monte Carlo models and also with published 2013 p-Pb analysis results for the common  $p_T$  ranges. The first section of the note deals with the centrality-integrated analysis; the second is focused on the analysis as a function of the ZNA centrality.



**1** **Contents**

<b>2</b>	<b>1</b>	<b>Introduction and Motivation</b>	<b>3</b>
<b>3</b>	<b>2</b>	<b>Data/Monte Carlo samples and event selection</b>	<b>4</b>
<b>4</b>	<b>3</b>	<b>Analysis strategy</b>	<b>7</b>
5	3.1	Mass plots and cut optimization . . . . .	10
6	3.2	Code used for the analysis . . . . .	11
7	3.3	Further details on corrections . . . . .	11
8	3.3.1	Event Mixing . . . . .	11
9	3.3.2	Tracking and D-meson trigger efficiency . . . . .	19
10	3.3.3	Correction for bias on B to D decay topologies . . . . .	25
11	3.3.4	Secondary track contamination . . . . .	30
12	3.3.5	Beauty feed-down . . . . .	34
<b>13</b>	<b>4</b>	<b>Systematic uncertainties on <math>\Delta\phi</math> correlation distributions</b>	<b>38</b>
14	4.1	Uncertainty on S and B extraction . . . . .	38
15	4.2	Uncertainty on background correlation shape . . . . .	38
16	4.3	Uncertainty on D-meson cut stability . . . . .	42
17	4.4	Uncertainty on tracking efficiency evaluation . . . . .	42
18	4.5	Uncertainty on secondary particle contamination . . . . .	46
19	4.6	Uncertainty on feed-down subtraction . . . . .	47
20	4.7	Uncertainty on correction for the bias on B to D decay topologies . . . . .	51
21	4.8	Summary table . . . . .	52
<b>22</b>	<b>5</b>	<b>Results</b>	<b>53</b>
23	5.1	Comparing the three D meson correlation distributions . . . . .	53
24	5.2	Average of $D^0$ , $D^+$ and $D^{*+}$ results . . . . .	66
25	5.3	Fit observable $p_T$ trends and uncertainties . . . . .	69
26	5.3.1	Results for near-side yield and width, away-side yield and width, and baseline .	70
27	5.4	Comparison of 2016 p-Pb and 2013 p-Pb results . . . . .	86
28	5.5	Comparison of 2016 p-Pb and 2010 pp results . . . . .	86
29	5.6	Comparison of 2016 p-Pb and model expectations . . . . .	86
30	5.7	Planned results for SQM approvals . . . . .	86

31	<b>6 Analysis vs ZNA Centrality</b>	<b>97</b>
32	6.1 General information . . . . .	97
33	6.2 Analysis strategy . . . . .	97
34	6.2.1 Dataset and event selection . . . . .	97
35	6.2.2 Mass plots and D-meson selection . . . . .	98
36	6.2.3 Event mixing . . . . .	98
37	6.2.4 Tracking and trigger efficiency . . . . .	98
38	6.2.5 Correction for bias on B to D decay topologies . . . . .	109
39	6.2.6 Secondary track contamination . . . . .	109
40	6.2.7 Feed-down correction . . . . .	113
41	6.3 Systematic uncertainties . . . . .	113
42	6.3.1 S and B extraction . . . . .	123
43	6.3.2 Background correlation shape . . . . .	126
44	6.3.3 D-meson cut stability . . . . .	126
45	6.3.4 Tracking efficiency . . . . .	129
46	6.3.5 DCA cut stability . . . . .	133
47	6.3.6 Feed-down subtraction . . . . .	133
48	6.3.7 Correction for bias on B to D decay topologies . . . . .	133
49	6.3.8 Final table of systematics on correlation distributions . . . . .	133
50	6.3.9 Uncertainties on fit observables . . . . .	133
51	6.4 Results . . . . .	139
52	6.4.1 Single-meson azimuthal correlation distributions . . . . .	139
53	6.4.2 Average-D correlation distributions . . . . .	139
54	6.4.3 Observables from fit to correlation distributions . . . . .	152
55	6.4.4 Plots proposed for preliminaries . . . . .	162
56	<b>7 Bibliography</b>	<b>171</b>

## 57 1 Introduction and Motivation

58 The study of the azimuthal correlations of heavy-flavour particles and charged particles at the LHC  
 59 energies provides a way to characterize charm production and fragmentation processes in pp collisions.  
 60 The measurement also provide a way to probe our understanding of QCD in the perturbative regime,  
 61 accessible in a large kinematic range given the large mass of heavy quarks. Flavour conservation in  
 62 QCD implies that charm quarks are always produced as pairs of quarks and anti-quarks. The azimuthal  
 63 correlations obtained using a meson carrying a heavy quark as trigger particle with the other charged  
 64 particles in the same event give the possibility to study the underlying charm production mechanism in  
 65 detail. In particular, prompt charm quark-antiquark pair production is back to back in azimuth at first  
 66 order in leading-order perturbative-QCD (pQCD). If an hadron from the quark hadronization is taken as  
 67 trigger particle, a near-side (at  $\Delta\phi = 0$ ) and an away-side (at  $\Delta\phi = \pi$ ) peak would appear in the azimuthal  
 68 correlation distributions, coming from the fragmentation of the quark pair. Heavy quarks produced from  
 69 the splitting of a massless gluon can be rather collimated and may generate sprays of hadrons at small  
 70  $\Delta\phi$ . Finally, for hard-scattering topologies classified as “flavour-excitation”, a charm quark undergoes a  
 71 hard interaction from an initial splitting ( $g \rightarrow c\bar{c}$ ), leading to a big separation in rapidity of the hadrons  
 72 originating from the antiquark (quark) with respect to the trigger D meson and contribute to a rather flat  
 73 term to the  $\Delta\phi$ -correlation distribution.

74 Heavy-flavour correlation studies in more complex collision systems, like Pb-Pb, play a crucial role in  
 75 studying the modification of the fragmentation of charmed jets due to in-medium (or cold nuclear matter,  
 76 in case of p-Pb collisions) effects, in a similar way as it was done for di-hadron correlation studies in  
 77 heavy-ion collisions (see for example [5]). Furthermore, the recent observation of long range correlations  
 78 in p-Pb for light flavour hadrons ([3], [4]) and for heavy-flavour decay electrons (ALICE preliminary re-  
 79 sults) points to possible collective effects or effects originating from gluon saturation in the initial state.  
 80 More information could be extracted by the eventual observation of the same effect with D mesons.

81

82 In the following note, we first describe the analysis strategy for the p-Pb 2016 data sample in all its steps,  
 83 followed by the list of analysis corrections and the estimation of systematic uncertainties. Finally the  
 84 results of  $\Delta\phi$  correlations, and quantitative observable extracted to fits to those distributions, obtained for  
 85 prompt  $D^0$ ,  $D^+$  and  $D^{*+}$  in different ranges of transverse momentum for the D-meson (trigger particle)  
 86 and the associated particles are presented.

87 The extension of the momentum ranges (both for D mesons and associated particles) with respect to the  
 88 2013 p-Pb dataset, as well as the improved precision in the common ranges allow a more thorough inves-  
 89 tigation of the charm quark fragmentation properties (multiplicity of tracks as a function of momentum,  
 90 geometrical profile of charm jets,  $p_T$  distribution of the tracks inside the jet). This can also allow us to  
 91 put better constraints on the description of charm fragmentation and charm jet properties provided by  
 92 models. The possibility of spotting cold nuclear matter effects affecting the charm fragmentation in p-Pb  
 93 was severely limited, in the published paper, by the uncertainties on both pp and p-Pb samples. This will  
 94 no longer be the case with the new p-Pb data sample, as soon as a pp sample with equivalent precision  
 95 is collected (the pp reference run expected by the end of this year could be of help in this sense). In  
 96 addition, the new measurements can be used as solid and precise references in view of an analysis on  
 97 a Pb-Pb sample at the same energy (hopefully already in 2018 data taking, otherwise after the ALICE  
 98 upgrade).

## 99    2 Data/Monte Carlo samples and event selection

100 The data samples used for the analyses were the FAST and CENT\_woSDD samples from periods LHC16q  
 101 and LHC16t (AOD samples). The reason of choosing different types of data samples is explained later  
 102 on, in this section. It was verified, by looking at D-meson and associated charged track  $\eta$  and  $\varphi$  distribu-  
 103 tions, and at the mixed-event correlation distributions for each subsamples, that no visible differences is  
 104 present for the four periods, hence it was possible to perform the analysis directly on the merged samples  
 105 without any bias.

106 The Monte Carlo productions adopted for this study were:

- 107    1. LHC17d2a\_fast\_new, a HIJING production with enrichment of heavy quarks (charm and beauty)  
   108 and their decay products in each of the event, performed by PYTHIA6 with Perugia2011 tune,  
   109 and with forced hadronic decays of the charmed hadrons. This production was used for D-meson  
   110 efficiency evaluation, purity estimation and Monte Carlo closure test.
- 111    2. LHC17f2b\_cent\_woSDD and LHC17f2b\_fast, minimum-bias samples produced with DPMJET  
   112 generator, are used for the evaluation of the tracking efficiencies.

113 Table 1 shows the list of runs used for the analysis, for each of the data taking periods, and of the Monte  
 114 Carlo productions used to evaluate the corrections:

115 The trigger mask request for the event selection is kINT7. Only events with a reconstructed primary  
 116 vertex within 10 cm from the centre of the detector along the beam line are considered. This choice max-  
 117 imises the detector coverage of the selected events, considering the longitudinal size of the interaction  
 118 region, and the detector pseudorapidity acceptances. In the analysis, the center-of-mass reference frame  
 119 of the nucleon-nucleon collision is shifted in rapidity by  $y_{NN} = 0.465$  in the proton direction with re-  
 120 spect to the laboratory frame, due to the different per-nucleon energies of the proton and the lead beams.  
 121 Beam-gas events are removed by offline selections based on the timing information provided by the V0  
 122 and the Zero Degree Calorimeters, and the correlation between the number of hits and track segments in  
 123 the SPD detector. This is automatically performed in the Physic Selection, a positive outcome of which  
 124 is required during our event selection. The pile-up cuts for out-of-bunch pile-up protection are also in-  
 125 volved when calling the Physics Selection task. The minimum-bias trigger efficiency is 100% for events  
 126 with D mesons with  $p_T > 1 \text{ GeV}/c$ . For the analyzed data samples, the probability of pile-up from col-  
 127 lisions in the same bunch crossing is below 2% per triggered event (in most of the runs, well below 1%).  
 128 Events in which more than one primary interaction vertex is reconstructed with the SPD detector (with  
 129 minimum of 5 contributors, and a  $z$  distance greater than 0.8 cm) are rejected, which effectively removes  
 130 the impact of in-bunch pile-up events on the analysis. Out-of-bunch tracks are effectively rejected by the  
 131 Physics Selection pile-up cuts, and also by the request of at least one point in the SPD, which has a very  
 132 limited time acquisition window (300 ns). Indeed, though the default associated track selection requires  
 133 a minimum of 2 points in the ITS, as it will be shown later on full compatibility of the corrected results  
 134 with 2 and 3 minimum ITS clusters are obtained. For FAST and CENT\_woSDD samples, the latter case  
 135 indirectly forces the presence of a point in the SPD.

136 Since data collected during p-Pb 2016 data taking are distinguished into two categories - one including  
 137 SDD detector (CENT\_wSDD sample) and the second one without the SDD in the reconstruction, or  
 138 in the acquisition (CENT\_woSDD and FAST samples, respectively), a study of performance of the D-  
 139 hadron correlation analysis with respect to the data samples employed has been carried out for  $D^{*+}$  and  
 140  $D^+$  mesons (more sensitive to the presence of the SDD w.r.t. the  $D^0$ , due to their reconstruction from  
 141 three decay tracks).

142 For this reason, the D-hadron correlation distribution has been compared on LHC16q\_pass1\_CENT\_wSDD  
 143 and LHC16q\_pass1\_CENT\_woSDD and the relative statistical uncertainty has been estimated in order to

Type	Production	Run list	nEvents
Monte-Carlo	LHC17d2a_fast_new (c/b enriched), LHC17f2b_fast (MB), LHC17f2b_cent_woSDD (MB)	267166, 267165, 267164, 267163, 265525, 265521, 265501, 265500, 265499, 265435, 265427, 265426, 265425, 265424, 265422, 265421, 265420, 265419, 265388, 265387, 265385, 265384, 265383, 265381, 265378, 265377, 265344, 265343, 265342, 265339, 265338, 265336, 265335, 265334, 265332, 265309 = [36 runs]	50M
Data	LHC16q, pass1_CENT_woSDD	265525, 265521, 265501, 265500, 265499, 265435, 265427, 265426, 265425, 265424, 265422, 265421, 265420, 265419, 265388, 265387, 265385, 265384, 265383, 265381, 265378, 265377, 265344, 265343, 265342, 265339, 265338, 265336, 265335, 265334, 265332, 265309 = [32 runs]	261M total
	LHC16q, pass1_FAST	265525, 265521, 265501, 265500, 265499, 265435, 265427, 265426, 265425, 265424, 265422, 265421, 265420, 265419, 265388, 265387, 265385, 265384, 265383, 265381, 265378, 265377, 265344, 265343, 265342, 265339, 265338, 265336, 265335, 265334, 265332, 265309 = [32 runs]	260M
	LHC16t, pass1_CENT_woSDD	267166, 267165, 267164, 267163 = [4 runs]	40M
	LHC16t, pass1_FAST	267166, 267165, 267164, 267163 = [4 runs]	41M

**Table 1:** Data Set and Run list

understand if it was better to perform the analysis separately on the two data sample, applying in this case different corrections, or not. In particular, it was crucial for the correlation analysis involving the  $D^{*+}$  meson because the track reconstruction efficiency of the soft pion is  $\approx 10\%$  higher employing also the SDD information. Figure 1 shows the normalized azimuthal correlation distribution for low, mid and high  $p_T$  for  $D^{*+}$  meson. Blue points are referred to the woSDD sample while red points represents wSDD data. Figure 2 shows the relative statistical uncertainty extracted from the azimuthal correlation distributions for the  $D^{*+}$  in different kinematic ranges.

It can be observed that the data sample that includes the SDD information is characterized by  $\approx 10 - 15\%$  more statistics in each  $p_T$  ranges analyzed. This difference is related to the larger efficiency in track reconstruction with the wSDD sample - a larger number of tracks survives to the selection request of 3 points in the ITS, which is part of the selection requests applied on the previous D-h analysis.

As a result, the wSDD sample is also affected by a slightly lower relative statistical uncertainty (about 12-15%) due to several reasons: the larger tracking efficiency, the larger number of signal entries in the invariant mass distributions (again an effect of the larger tracking efficiency) and a slight increase of S/B, which reflects in a slight decrease of uncertainty from the sideband subtraction. It has also to be considered that, on the full sample including also the FAST cluster, the increase in performance would be further reduced. The overall statistical uncertainty difference resulting from the comparison is not

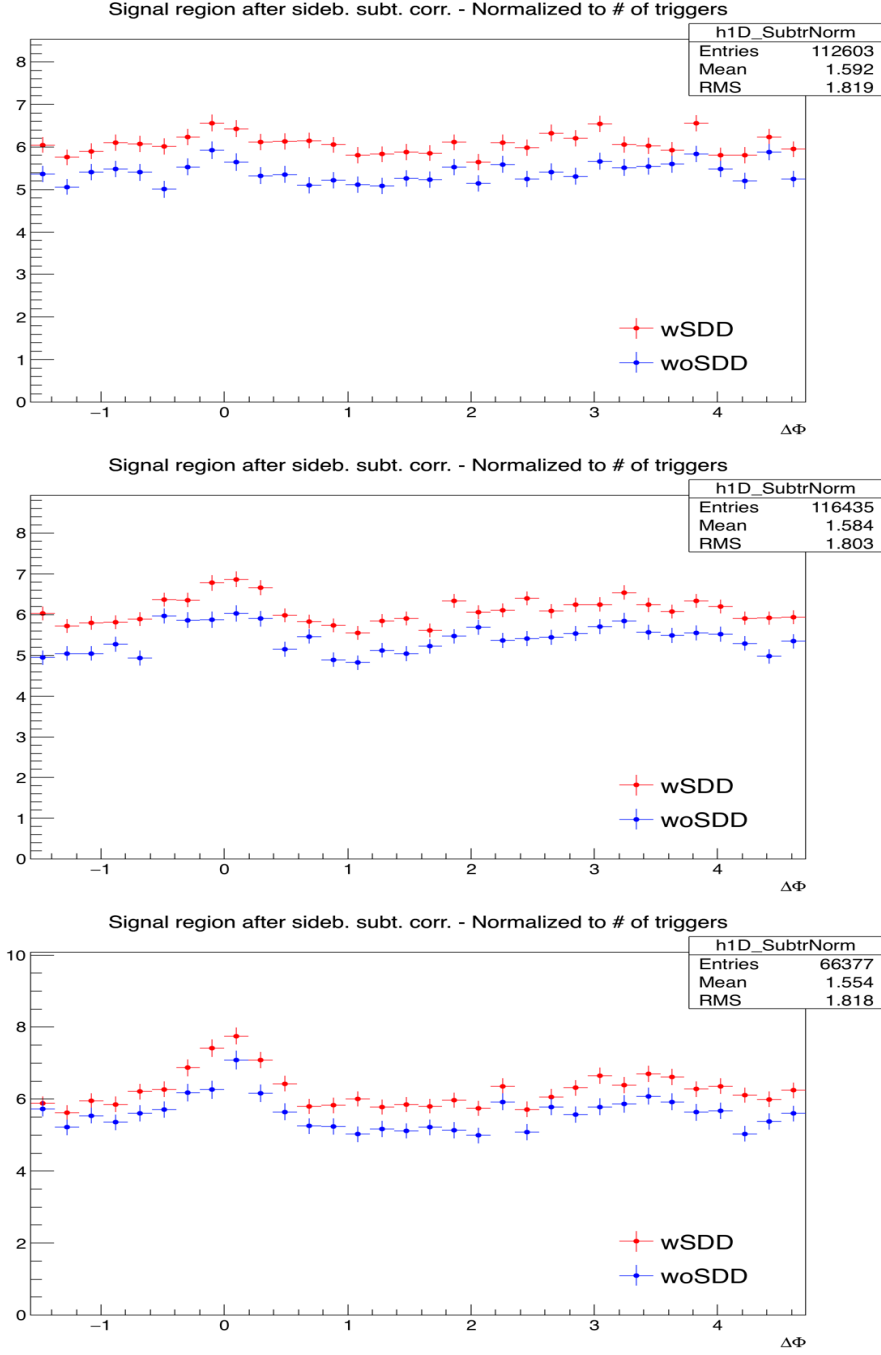


**Figure 1:** Normalized azimuthal correlation distribution of  $D^{*+}$  for low  $p_T$  ( $3 < p_T(D^{*+}) < 5 \text{ GeV}/c$ ) on the top panel, mid  $p_T$  ( $5 < p_T(D^{*+}) < 8 \text{ GeV}/c$ ) on the middle panel and high  $p_T$  ( $8 < p_T(D^{*+}) < 16 \text{ GeV}/c$ ) on the bottom panel with a  $p_T$  threshold for associated tracks of  $p_T(\text{assoc}) > 0.3 \text{ GeV}/c$ . Blue points are referred to the woSDD sample while red points represent wSDD data.

enough to justify the implementation of two different analysis and two subsequent different corrections either for  $D^{*+}$  and  $D^+$ .

In order to, to cope with the lower tracking efficiency w.r.t. 2013 data sample, after this study, it was decided to reduce the ITS request for the associated tracks from 3 (used on 2013 data) to 2 ITS clusters as default selection criterion.

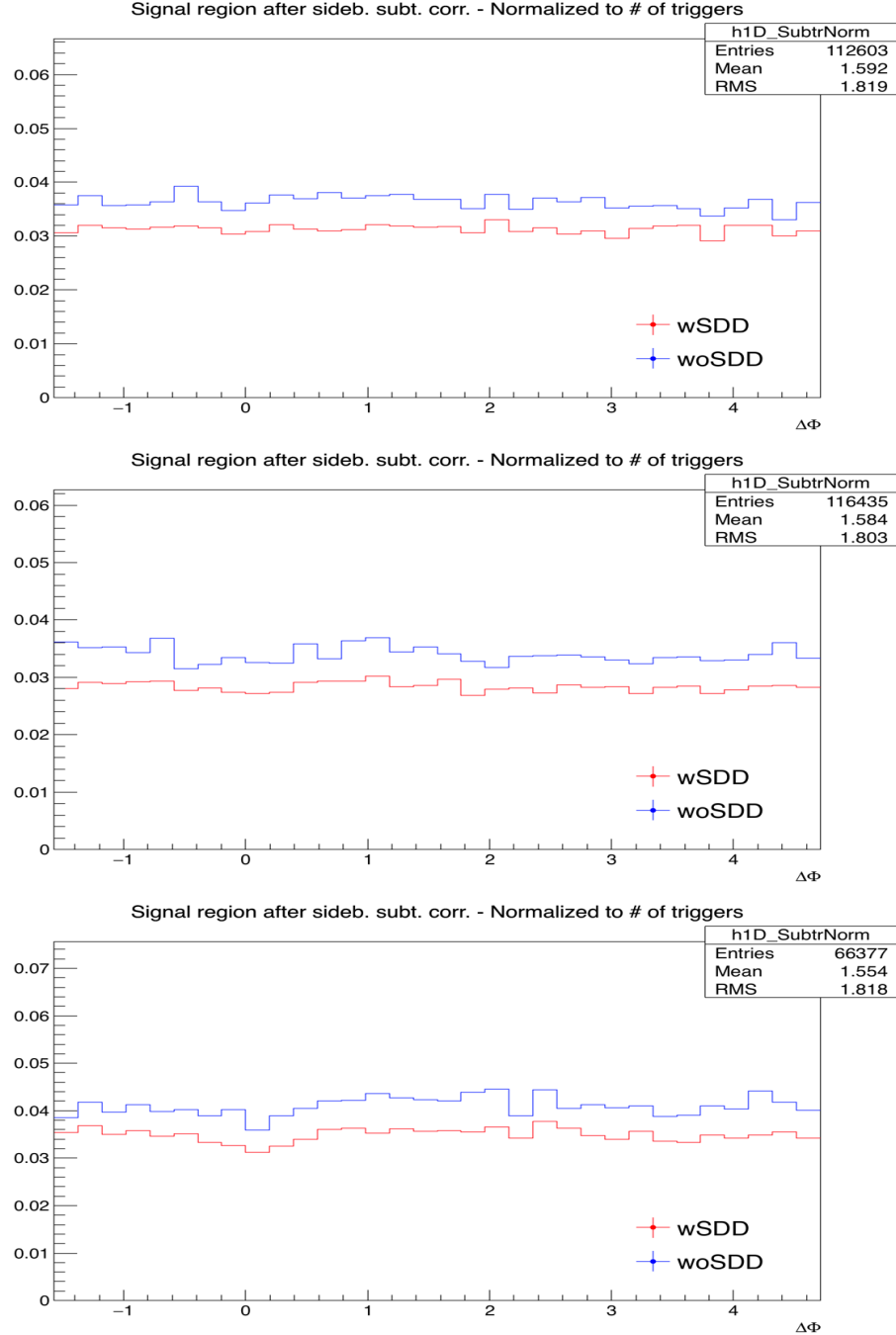


**Figure 2:** Statistical uncertainty extracted from the azimuthal correlation distribution of  $D^{*+}$  with associated charged particles. Top panel:  $3 < p_T(D^{*+}) < 5 \text{ GeV}/c$ . Mid panel:  $5 < p_T(D^{*+}) < 8 \text{ GeV}/c$ . Bottom panel:  $8 < p_T(D^{*+}) < 16 \text{ GeV}/c$ . Blue line is referred to the woSDD sample while the red line represents wSDD data.

### 166 3 Analysis strategy

167 The analysis follows the same strategy one used in 2013 p-Pb data sample (see published paper [2])  
 168 and analysis notes [7], [6]). Correlation pairs are formed by trigger particles (D mesons) reconstructed  
 169 and selected in the following  $p_T^{\text{trig}}$  ranges:  $3 < p_T^{\text{trig}} < 5 \text{ GeV}/c$ ,  $5 < p_T^{\text{trig}} < 8 \text{ GeV}/c$ ,  $8 < p_T^{\text{trig}} < 16$   
 170  $\text{GeV}/c$ ,  $16 < p_T^{\text{trig}} < 24 \text{ GeV}/c$ , and associated particles (charged tracks) for the following  $p_T^{\text{assoc}}$  re-  
 171 gions:  $p_T^{\text{assoc}} > 0.3 \text{ GeV}/c$ ,  $0.3 < p_T^{\text{assoc}} < 1 \text{ GeV}/c$ ,  $1 < p_T^{\text{assoc}} < 2 \text{ GeV}/c$ ,  $2 < p_T^{\text{assoc}} < 3 \text{ GeV}/c$ ,  
 172  $p_T^{\text{assoc}} > 3 \text{ GeV}/c$  (with the addition of  $p_T^{\text{assoc}} > 1 \text{ GeV}/c$  for comparison with p-Pb 2013 results). In this

analysis, the particle identification defines the trigger particle rather than a momentum cut and therefore the momentum range of the associated particles is not constrained by that of the trigger particle. Our definition of associated particle includes primary particles of the following species: pion, kaon, proton, electron, muon. The primary particle definition comprises particle coming from the primary vertex of interaction, including those coming from strong and electromagnetic decay of unstable particles, and particles deriving from the decay of hadrons with charm or beauty. We therefore include any charged  $\pi, K, p, e, \mu$  except those coming from weak decays of strange particles and particles produced in the interaction with the detector material. This definition corresponds to that used in the method AliAODM-CParticle::IsPyphysicalPrimary(). All associated particles surviving the selection cuts and not matching the adopted criterion are considered as a contamination whose contribution has to be corrected for.

183

184 The analysis is performed through the following steps:

- 185 1. **D meson selection and signal extraction.** For each single event, “trigger” particles are defined  
186 as the selected D meson candidates ( $D^0$ ,  $D^+$  and  $D^{*+}$ ) within a given  $p_T^{\text{trig}}$  range. The detection  
187 strategy for D mesons at central rapidity is the same performed for the analyses of the D-meson  
188 production at central rapidity [1], and also applied for the D-h analysis on 2010 pp and 2013 p-Pb  
189 samples [2]. It is based on the reconstruction of decay vertices displayed from the primary vertex  
190 by a few hundred  $\mu\text{m}$  and on the identification of the decay-particle species. The identification  
191 of the charged kaon and pion in the TPC and TOF detectors is also used, to further reduce the  
192 background at low  $p_T$ . An invariant-mass analysis is then used to extract the raw signal yield,  
193 using the same fit functions described in [2]. The D mesons are selected in the rapidity range  
194 varying from  $|y| < 0.5$  at low  $p_T$  to  $|y| < 0.8$  for  $p_T > 5 \text{ GeV}/c$ .
- 195 2. **Correlation of D candidates with associated tracks.** Particle pairs are formed by correlating each  
196 trigger particle with the charged primary particles passing the track selection (excluding those  
197 coming from the decay of the D-meson candidate) in a specified  $p_T^{\text{assoc}}$  interval (which can overlap  
198 with the  $p_T^{\text{trig}}$  range) and in the pseudo-rapidity range  $|\eta| < 0.8$ . For the  $D^0$  meson, also the low-  
199 momentum pion tracks from feed-down of  $D^{*+}$  mesons are removed via  $3\sigma$  invariant mass cut on  
200 the  $M(K\pi\pi) - M(K\pi)$  difference. This because these soft pion are not related to the charm quark  
201 fragmentation chain. For D meson candidates in the invariant mass signal region, defined by a  $\pm$   
202  $2\sigma$  interval around the D meson mass peak, the azimuthal angle difference  $\varphi^{\text{assoc}} - \varphi^{\text{trigg}} \equiv \Delta\varphi$  and  
203 the pseudorapidity difference  $\eta^{\text{assoc}} - \eta^{\text{trig}} \equiv \Delta\eta$  are evaluated and stored to build two-dimensional  
204 correlation distribution.
- 205 3. **Correction for limited acceptance and detector inhomogeneities with Event Mixing** The angular  
206 correlation distribution may be affected, even for uncorrelated pair of particles, by structures  
207 not due to physical effects, but originating from the limited detector acceptance, as well as from  
208 angular inhomogeneities in the trigger and track reconstruction efficiencies as a function of  $\Delta\varphi$   
209 and  $\Delta\eta$ . Effects of this kind are removed using the Event Mixing technique. In this technique, the  
210 analysis is executed on the same data sample of the standard one (called “same event” analysis,  
211 SE), but the trigger particles found in each event are correlated to charged particles reconstructed  
212 in different events (“Mixed Events” analysis, ME) with similar characteristic, in particular con-  
cerning the event multiplicity and z position of the primary vertex (see Section 3.3.1).

214

215 The differential yield of associated particles per trigger particle is obtained by

$$\frac{1}{N_{\text{trig}}} \frac{d^2 N^{\text{pair}}}{d\Delta\eta d\Delta\varphi} = B_{\text{ME}}(0,0) \times \frac{S(\Delta\eta, \Delta\varphi)}{B_{\text{ME}}(\Delta\eta, \Delta\varphi)}, \quad (1)$$

216 where  $N^{\text{pair}}$  is the total number of correlated D-hadron pairs. The functions  $S(\Delta\eta, \Delta\phi)$  and  $B_{ME}(\Delta\eta, \Delta\phi)$   
 217 are the signal and the mixed event background distributions, respectively. The later is normalized  
 218 to its value in  $(\Delta\eta, \Delta\phi) = (0, 0)$ , i.e.  $(B(0, 0))$ . Further details on the mixed-event correction are  
 219 provided in the next section.

220 **4. Subtraction of background correlation from signal distribution.** The invariant mass signal re-  
 221 gion also includes background D-meson candidates. Their contribution to the raw correlation  
 222 distribution is subtracted as follows. For each  $p_T$  bin, the mean and the sigma of the invariant mass  
 223 spectrum are extracted. For  $D^0$  and  $D^+$ , a “background” region is defined in the sidebands of the  
 224 mass distribution as the interval  $4 \text{ GeV}/c^2 < |m - m^{\text{pdg}}| < 8 \text{ GeV}/c^2$  (for the  $D^{*+}$  meson, only  
 225 the right sideband is used). The angular correlation distribution for background candidates in this  
 226 region is extracted and normalized with respect to the background in the signal region estimated  
 227 from the mass fit. This normalized background correlation distribution is then subtracted from  
 228 the raw signal one to obtain the signal correlation distribution. The normalization factor is the  
 229 ratio of the number of background candidates under the signal peak (obtained by integrating the  
 230 background of the fit function within the signal region) over the number of background candidates  
 231 in the sidebands (obtained via bin-counting in the sideband region). An example of the signal re-  
 232 gion, sideband and sideband-subtracted 1D correlation distributions (along  $\Delta\phi$ ) is shown in figure  
 233 3, together with the comparison of the three distributions after the normalization to the number of  
 234 triggers.

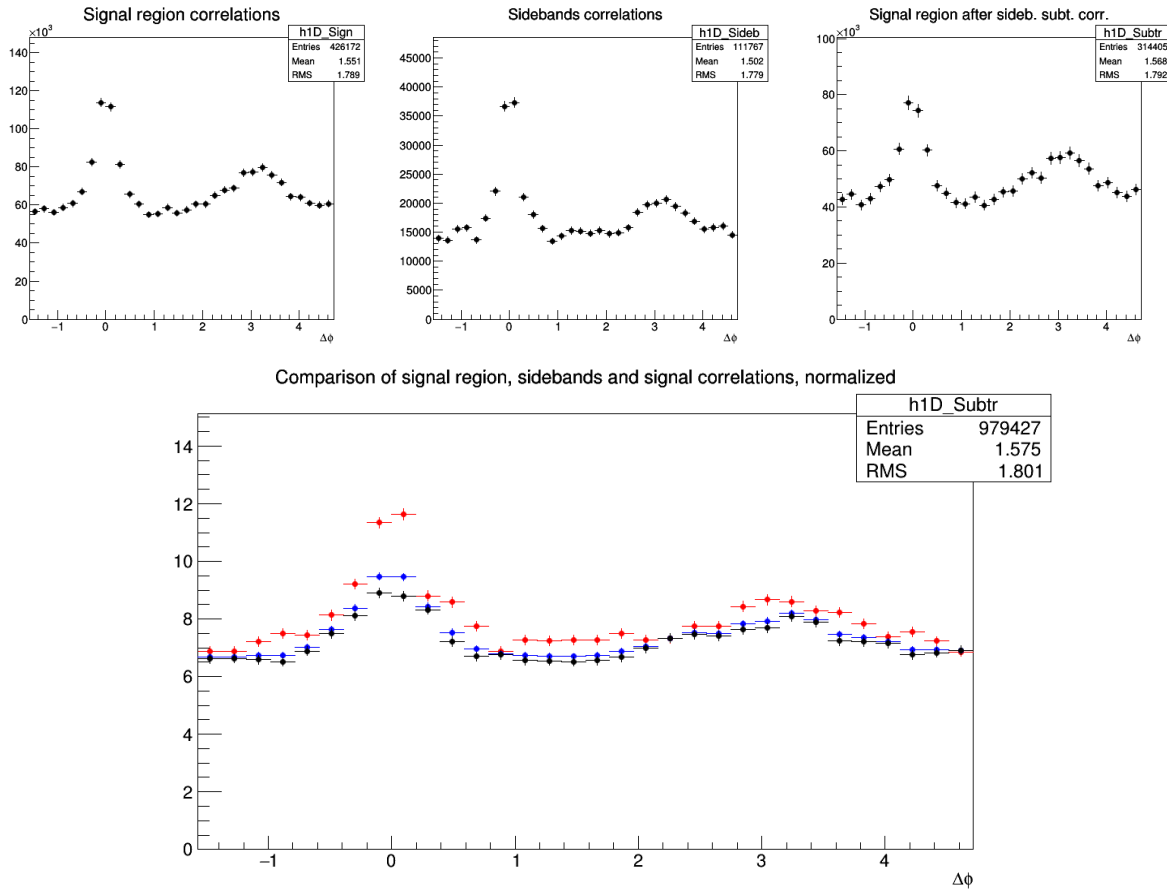


**Figure 3:** Top: Example of  $D^0$ -h signal region (left), sideband (middle), and signal minus sideband (right) correlation distributions. Bottom: signal region per-trigger normalized correlation distribution (blue), sideband region per-trigger normalized correlation distribution (red), background-subtracted per-trigger normalized correlation distribution (black).

- 235    5. **Correction for D meson efficiency and associated track efficiency.** After filling the signal and  
 236    background correlation distributions, it is necessary to take into account also for the correlations  
 237    with tracks, those are not reconstructed, or not passing the quality selection due to poor recon-  
 238    struction. In the same way, the loss of D-mesons which are not reconstructed, or do not pass the  
 239    selection, impacts the correlation distribution shape. Hence, each pair is weighted by the inverse  
 240    of the product of the associated track and D meson reconstruction efficiency,  $\epsilon_{trk}$  and  $\epsilon_{trig}$ . Further  
 241    details are provided later on in this section.
- 242    6. **Projection in  $\Delta\varphi$ .** The limited statistics available does not allow to study the two dimensional  
 243     $(\Delta\eta, \Delta\varphi)$  distribution, which is therefore projected to the  $\Delta\varphi$  axis by integrating on  $|\Delta\eta| < 1$ .  
 244    Despite, in principle, our maximum  $\Delta\eta$  acceptance is of  $|\Delta\eta| < 1.6$ , removing the large  $|\Delta\eta|$   
 245    regions allow us to reject angular regions with very low statistics, where fluctuations would be  
 246    amplified by a large mixed-event correction, and avoid the so-called wings effect.  
 247    As the difference in the azimuthal angle is periodic ( $\Delta\varphi = 0 = 2\pi$ ), the  $\Delta\varphi$ -range is limited to the  
 248    essential range of  $2\pi$ . The  $\Delta\varphi$ -limits are chosen to be  $[-\pi/2, 3\pi/2]$  in order to provide a good  
 249    visibility of the correlation pattern, which peaks around 0 and  $\pi$ .
- 250    7. **Correction for the contamination of secondary particles** The DCA to primary vertex cut, ap-  
 251    plied during the associated track selection, has the role of removing the secondary particles from  
 252    the associated track sample. Secondary particles are indeed produced either from long-lived  
 253    strange hadrons or from interaction of particles with the detector material. A residual contamina-  
 254    tion from secondary tracks is hence expected in the correlation distributions. This contamination  
 255    is estimated from Monte Carlo simulation based on Pythia as described more in detail in the next  
 256    section. The background-subtracted event-mixing corrected correlations are multiplied by a purity  
 257    factor to encounter this contribution.
- 258    8. **Correction for bias on B to D decay topologies** The presence of the topological cuts for the D-  
 259    meson selection indirectly induce a bias on the topology of the B to D decay topologies, favouring  
 260    cases with a small opening angle between the D-meson and the other tracks from the B decay.  
 261    This affects the feed-down component of the data correlation distributions. This effect is corrected  
 262    for with a procedure described in the subsection 3.3.3. Note that this correction is a novelty  
 263    with respect to the previous analyses, where only a quite conservative systematic uncertainty was  
 264    applied to take into account this effect.
- 265    9. **Correction for feed-down of D meson from b-hadron decay** The selection strategy employed  
 266    for the D meson candidates selection enhances the fraction of reconstructed D mesons coming  
 267    from the decay of a b-hadron. Typical values, with the cuts used for the D-meson selection, are of  
 268    the order of 10% or less. The correlation distribution of these secondary D mesons will be sensi-  
 269    tive to the properties of beauty jets and beauty hadron decay, which in general differ from those  
 270    relative to charm jets and hadrons. The procedure used to subtract this contribution is described in  
 271    the next paragraphs of this section.
- 272    10. **Study of correlation properties.** The properties of the azimuthal correlation distribution are quan-  
 273    tified by fitting the distribution with a function composed of two Gaussian functions, modelling  
 274    the near and the away side peaks, and a constant term describing the baseline. The mean of the  
 275    Gaussian are fixed at  $\Delta\varphi = 0$  and  $\Delta\varphi = \pi$ . To accomplish the  $2\pi$  periodicity of the  $\Delta\varphi$  variable, the  
 276    Gaussian functions are “duplicated” with mean at  $\Delta\varphi = 2\pi$  and  $\Delta\varphi = -\pi$ . The fitting procedure  
 277    is described in details in Section 5.

### 278    3.1 Mass plots and cut optimization

279    The invariant mass distributions of  $D^0$ ,  $D^{*+}$  and  $D^+$  in the various pt ranges are shown in Figure 4, 5  
 280    and 6 respectively. Note that the distributions are weighted by the D-meson selection and reconstruction

efficiency, to allow a correct normalization of the correlation distributions, which have also these weights.

For  $D^{*+}$ , the standard D2H p-Pb cuts (for the 2013 cross section analysis, [8]) were used. The same holds for the  $D^+$ , but with the addition of cuts on the normalized decay length in  $xy$  plane and of the normalized difference between measured and expected daughter track impact parameters (topomatic cut). A particular cut optimization was instead performed for the  $D^0$  meson. Twelve cut sets were tried, with the goal of increasing the S/B factor, in order to reduce fluctuations induced by the sideband subtraction (the limiting factor for the analysis performance). In Figure 7 the  $D^0$ -h correlation distributions are shown for the different cut sets, in exemplary kinematic regions (left column), together with the bin-by-bin relative statistical uncertainty on the data points (right column). The best cut set (option G) was defined from the standard cuts used for the p-Pb 2013 cross section analysis, with a tightened selection on the cosine of the pointing angle, and with the addition of a cut on the normalized decay length in  $xy$  plane and of a selection on the normalized difference between measured and expected daughter track impact parameters (topomatic cut).

### 3.2 Code used for the analysis

The code used for D meson-hadron correlation analysis is fully committed in AliPhysics. The analysis classes can be found in `$ALICE_ROOT/PWGHF/correlationHF/`. The D meson specific classes where the aforementioned steps are carried out are `AliAnalysisTaskDStarCorrelations`, `AliAnalysisTaskSEDOCorrelations` and `AliAnalysisTaskDplusCorrelations`. The classes which are common to the D meson specific analysis which includes the associated particle cuts and the correlation observables are `AliHFAssociatedTrackCuts`, `AliHFCorrelator`, `AliHFOfflineCorrelator`, `AliReducedParticle` and `AliDhCorrelationExtraction`. Several additional classes and macros in the same folder deal with the correction steps.

The final results presented here are extracted are the HFCJ pPb (n. 88) train runs 290-293 (for  $D^0$  and  $D^+$ ) and 286-289 (for  $D^{*+}$ ).

### 3.3 Further details on corrections

#### 3.3.1 Event Mixing

The event-mixing technique is used for correcting the raw correlation distribution for effects arising from the detector limited acceptance in rapidity and detector spatial inhomogeneities. The calculation of the Event Mixing correlation distribution is performed online. An event pool is created, where events preceding the one containing a D candidate are stored based on their properties (position of the vertex along the z axis and multiplicity). Each time a D meson candidate is found in an event, only the events contained in the same pool as the event under analysis is used to evaluate the correlations for the event mixing correction.

For  $D^0$  and  $D^+$ , an offline approach for the mixed-event correction has been developed. In this approach, D-meson triggers and associated tracks from every analyzed event are stored in dedicated TTree, together with the needed kinematic information to build correlation distributions, and with identifiers of the events to which they belong. In this way, it is possible to correlate each D meson with all the tracks belonging to the same pool over the full event sample, and not being limited to the same subjob as for the online analysis. This allows to increase the statistics of the mixed-event correlation distributions. It was verified that online and offline approaches are fully compatible within the statistical uncertainties.

The multiplicity and z vertex position bins for the pools used in the p-Pb analysis (for both approaches) are the following:

- Multiplicity bins:  $(0, 35); (35, 55); (55, +\infty)$

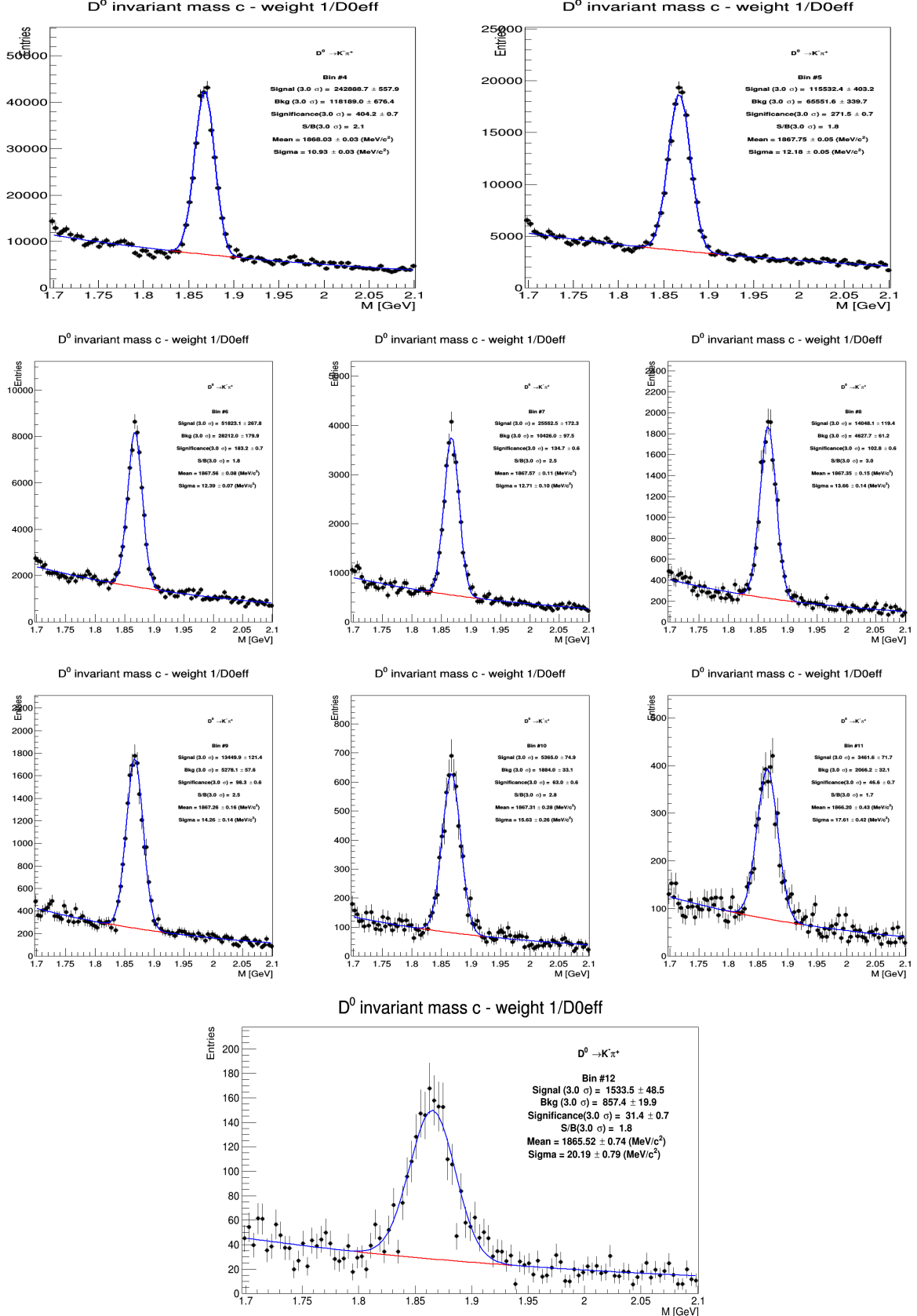


**Figure 4:** Invariant mass distributions of  $D^0$  corrected with efficiency in different  $p_T$  regions. Top:  $3 < p_T^D < 4$  GeV/c (left),  $4 < p_T^D < 5$  GeV/c (right), Mid 1:  $5 < p_T^D < 6$  GeV/c (left),  $6 < p_T^D < 7$  GeV/c (middle),  $7 < p_T^D < 8$  GeV/c (right); Mid2:  $8 < p_T^D < 10$  GeV/c,  $10 < p_T^D < 12$  GeV/c (middle),  $12 < p_T^D < 16$  GeV/c (right) and Bottom:  $16 < p_T^D < 24$  GeV/c.

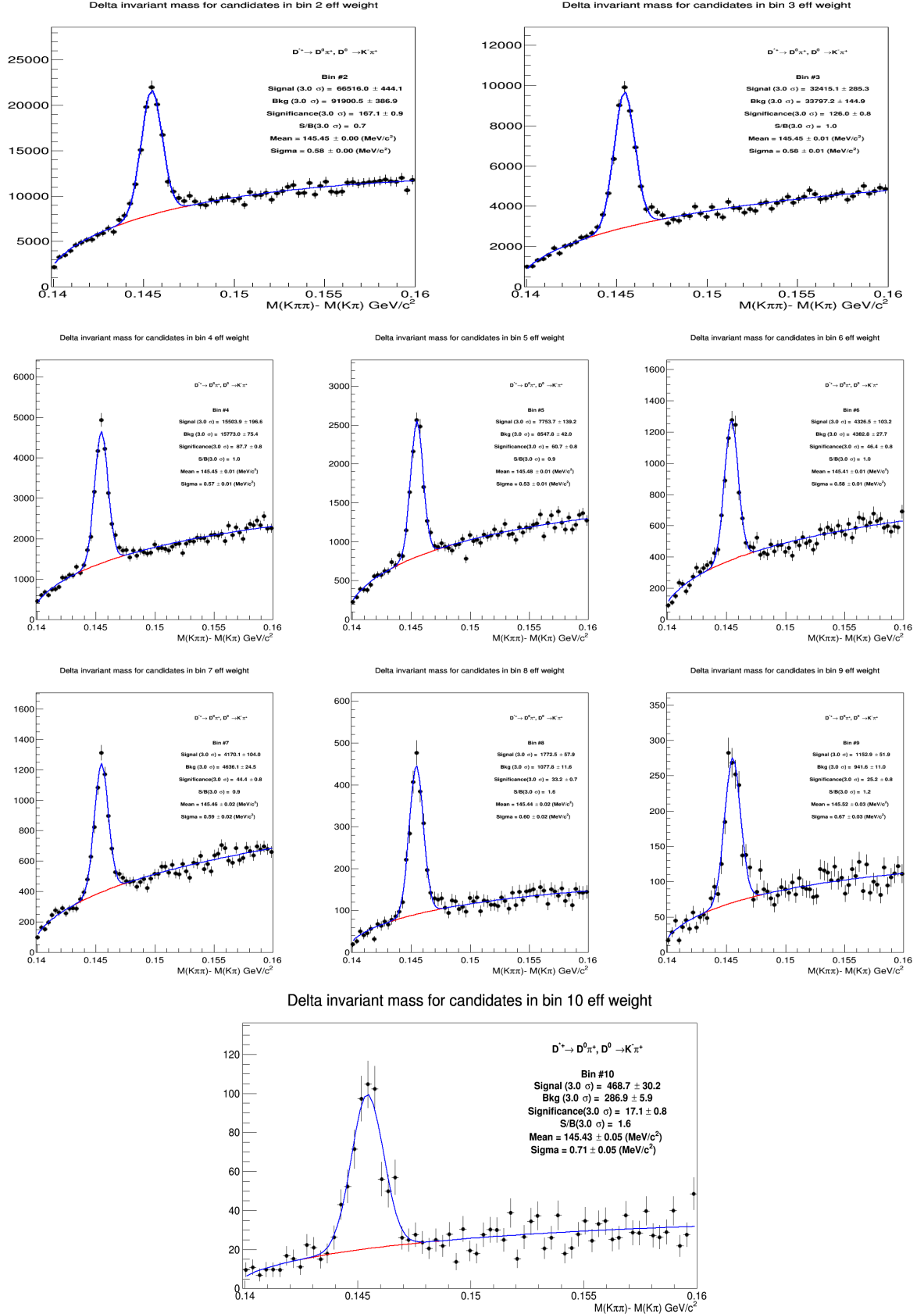


**Figure 5:** Invariant mass distributions of  $D^{*+}$  corrected with efficiency in different  $p_T$  regions. Top:  $3 < p_T^D < 4$  GeV/c (left),  $4 < p_T^D < 5$  GeV/c (right), Mid 1:  $5 < p_T^D < 6$  GeV/c (left),  $6 < p_T^D < 7$  GeV/c (middle),  $7 < p_T^D < 8$  GeV/c (right); Mid2:  $8 < p_T^D < 10$  GeV/c,  $10 < p_T^D < 12$  GeV/c (middle),  $12 < p_T^D < 16$  GeV/c (right) and Bottom:  $16 < p_T^D < 24$  GeV/c .

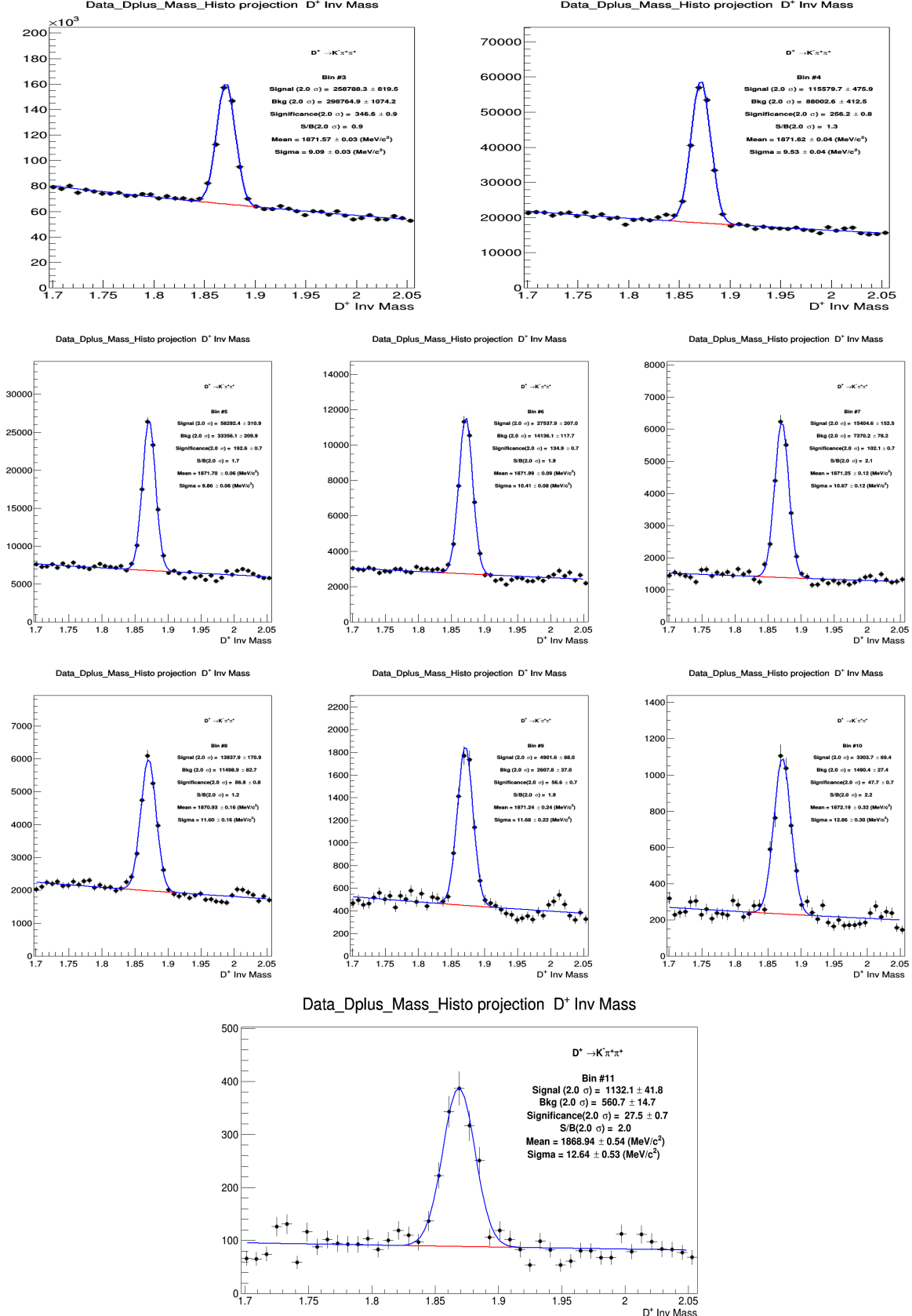


**Figure 6:** Invariant mass distribution of D<sup>+</sup> corrected with efficiency in different p<sub>T</sub> regions. Top: 3 < p<sub>T</sub><sup>D</sup> < 4 GeV/c (left), 4 < p<sub>T</sub><sup>D</sup> < 5 GeV/c (right), Mid 1: 5 < p<sub>T</sub><sup>D</sup> < 6 GeV/c (left), 6 < p<sub>T</sub><sup>D</sup> < 7 GeV/c (middle), 7 < p<sub>T</sub><sup>D</sup> < 8 GeV/c (right); Mid2: 8 < p<sub>T</sub><sup>D</sup> < 10 GeV/c, 10 < p<sub>T</sub><sup>D</sup> < 12 GeV/c (middle), 12 < p<sub>T</sub><sup>D</sup> < 16 GeV/c (right) and Bottom: 16 < p<sub>T</sub><sup>D</sup> < 24 GeV/c .

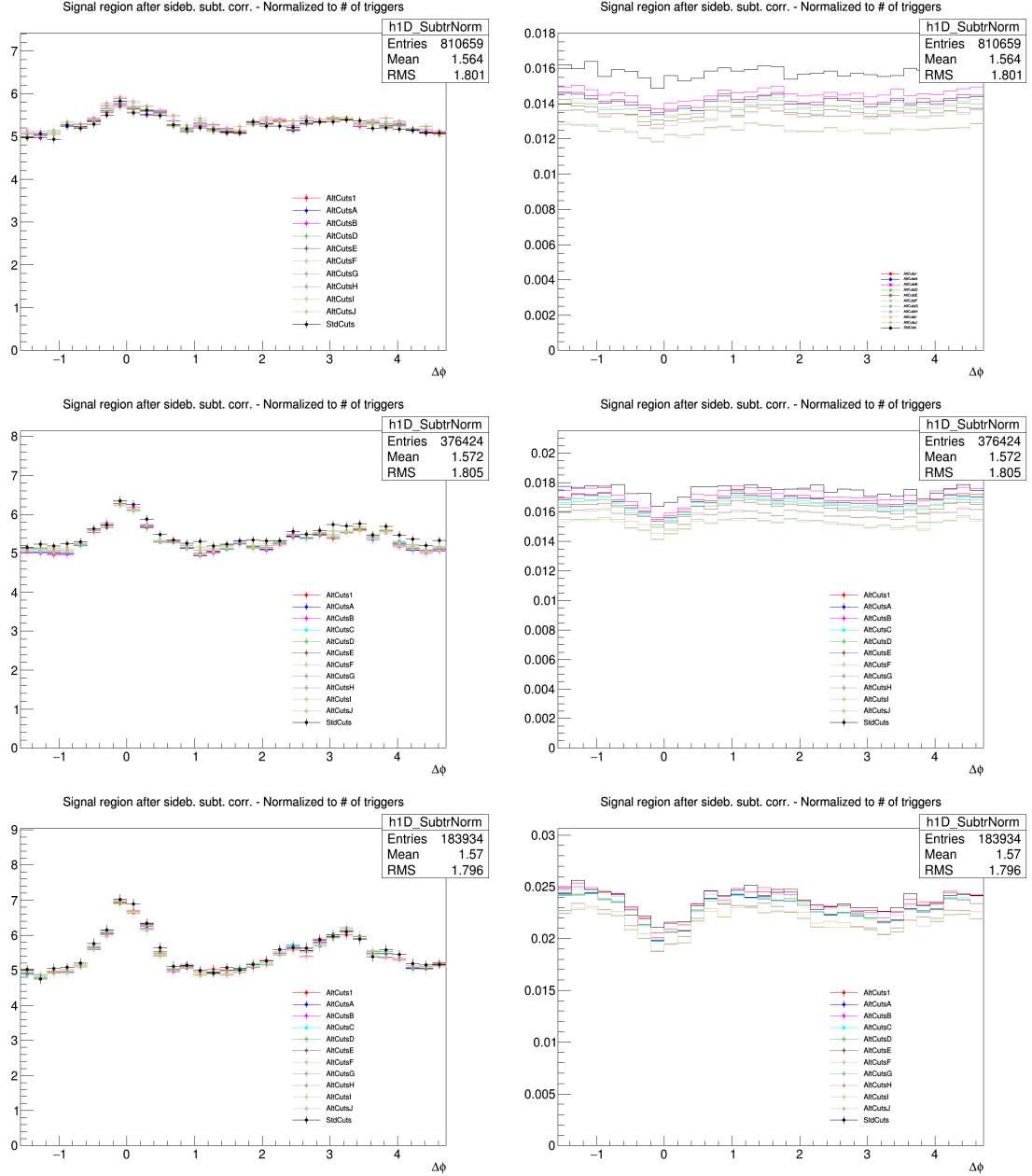


**Figure 7:**  $D^0$ - $h$  correlation distributions with different cut options (left) and point-by-point relative statistical uncertainty (right) for  $3 < p_T^D < 5 \text{ GeV}/c$  (top),  $5 < p_T^D < 8 \text{ GeV}/c$  (middle),  $8 < p_T^D < 16 \text{ GeV}/c$  (bottom), in all cases with associated track  $p_T > 0.3 \text{ GeV}/c$ .

324 – Vertex z (cm) = (-10, -1.5); (-1.5, 3.5); (3.5, 10)

325 In an ideal case, the mixed event distribution is expected to have a constant flat distribution as function  
 326 of  $\Delta\varphi$  and a triangular shaped distribution in  $\Delta\eta$  deriving from the limited  $\eta$  acceptance of the detector.  
 327 In case, instead of detector inefficient regions, or holes, in the same angular position for D meson and  
 328 associated tracks, these structures produce an excess of correlations at  $\Delta\varphi = 0$  in the  $\Delta\varphi$  distribution. The  
 329 obtained distribution is used as a weight in each correlation bin, i.e., the corrected correlation distribution  
 330 is calculated as follows:

$$\frac{dN^{corr}(\Delta\varphi\Delta\eta)}{d\Delta\varphi d\Delta\eta} = \frac{\frac{dN^{SE}(\Delta\varphi\Delta\eta)}{d\Delta\varphi d\Delta\eta}}{\frac{dN^{ME}(\Delta\varphi\Delta\eta)}{d\Delta\varphi d\Delta\eta}} \frac{dN^{ME}(0,0)}{d\Delta\varphi d\Delta\eta} \quad (2)$$

331 In Eq. 2, the last term stands for the average of the bins in the region  $-0.2 < \Delta\eta < 0.2$ ,  $-0.2 < \Delta\varphi < 0.2$   
 332 (multiple bins are used to minimize the effect of statistical fluctuations on the normalization of the mixed-  
 333 event plots). This kind of normalization, adopted in the analysis of hadron-hadron correlations, relies  
 334 on the fact that at  $(\Delta\eta, \Delta\varphi) = (0, 0)$  the trigger and associated particle experience the same detector  
 335 effects. In the D meson case this is true only on average and not at very low  $p_T$ , since D mesons are  
 336 reconstructed from particles that can go in different detector region. However,  $(\Delta\eta, \Delta\varphi) = (0, 0)$  is in  
 337 any case the region with maximum efficiency for the pairs (both correlated and uncorrelated). Thus the  
 338 same convention was adopted.

339 The mixed-event correlation distributions are built in both D meson signal and sideband regions. Both  
 340 are corrected with the relative distributions. An example of the mixed-event distributions, and of the  
 341 outcome of the mixed-event correction, is provided in Figures 8 and 9. The expected triangular shape  
 342 in  $\Delta\eta$ , for the mixed-event distributions, addresses the effect of the limited detector pseudo-rapidity  
 343 acceptance. Note that the mixed-event distribution is limited to the interval  $|\Delta\eta| < 1$ : the decision to  
 344 limit the mixed-event correction, and thus the whole analysis, to this range was taken in order to avoid  
 345 the so-called “wing effect”, i.e. the wing-like structures arising in the correlation distribution at large  $\Delta\eta$   
 346 due to the limited filling of the correlation bins in that region.

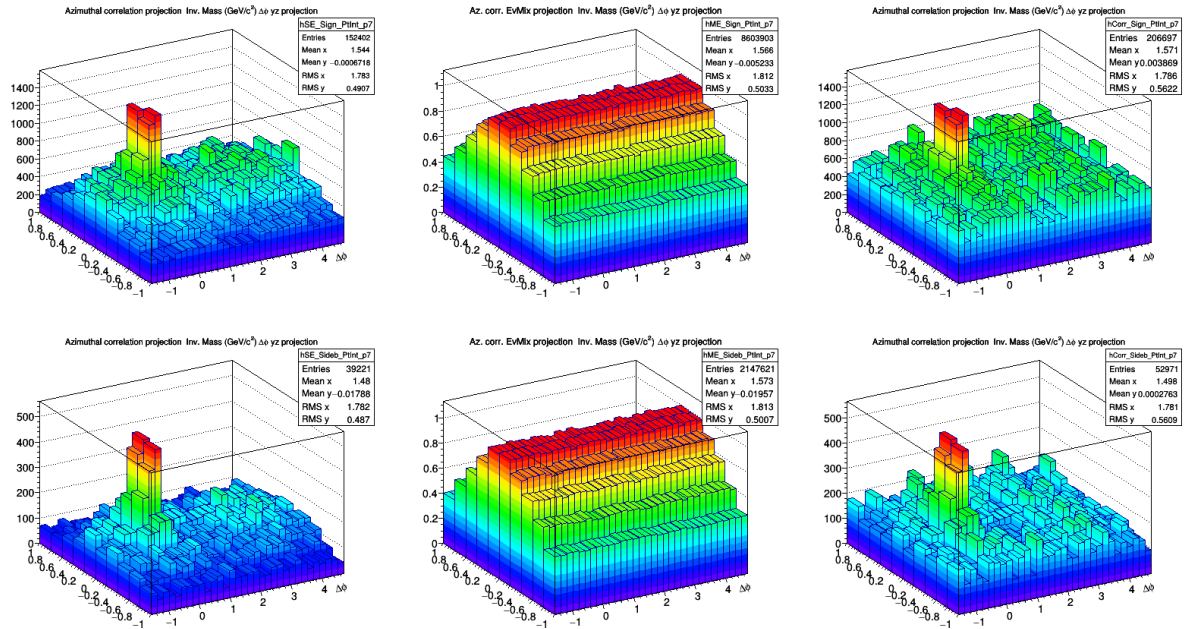


**Figure 8:**  $D^0$  meson ( $\Delta\phi, \Delta\eta$ ) correlation for in the signal region (top row) and sidebands (bottom row) from Single Event (left) and Mixed Event analysis (center) for high  $p_T$ :  $8 < p_T < 16 \text{ GeV}/c$  with associated  $p_T > 0.3 \text{ GeV}/c$ . The right column shows the SE/ME corrected distributions.

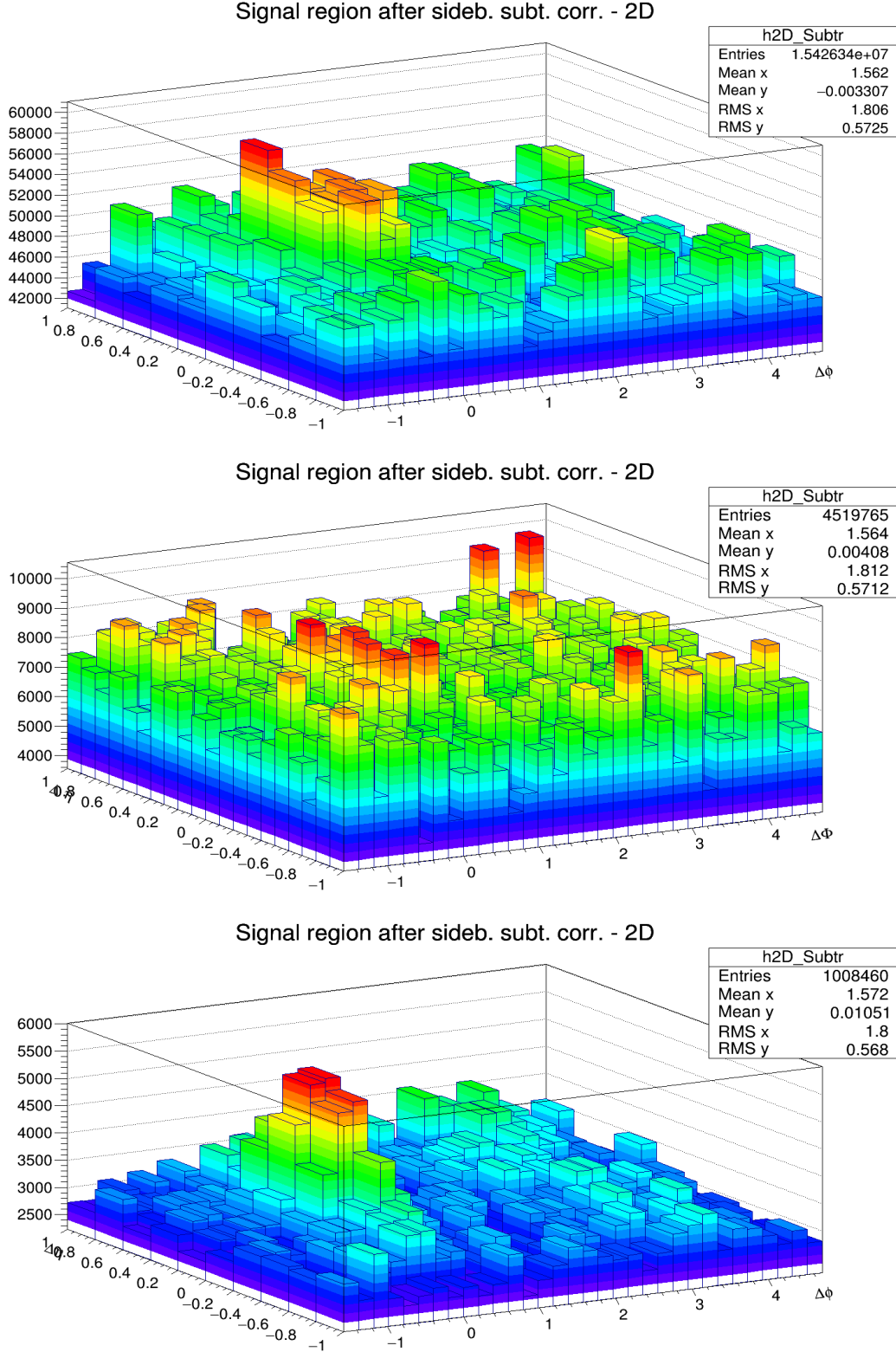


**Figure 9:** Top:  $(\Delta\phi, \Delta\eta)$  correlation distribution of  $D^0$ -h with  $3 < p_T < 5$  GeV/c and associated track kinematic range:  $0.3 < p_T < 1.0$  GeV/c Mid:  $(\Delta\phi, \Delta\eta)$  correlation distribution of  $D^{*+}$ -h with  $3 < p_T < 5$  GeV/c and associated track  $p_T$  Threshold:  $p_T > 0.3$  GeV/c Bottom:  $(\Delta\phi, \Delta\eta)$  correlation distribution of  $D^+$ -h with  $8 < p_T < 16$  GeV/c and associated track  $p_T$  threshold:  $p_T > 0.3$  GeV/c. All the plots are shown after the mixed-event correction and the sideband subtraction.

347 **3.3.2 Tracking and D-meson trigger efficiency**

348 **(i) Tracking efficiency** - The tracking efficiency was calculated by obtaining the ratio between the yield  
349 at the reconstructed level and generated level, for a defined “type” of particles (in our case non-identified  
350 particles) and it is estimated differentially in  $p_T$ ,  $\eta$ , and  $z_{vtx}$  of the charged particles.

351

352 Tracking efficiency maps were produced as TH3D histograms ( $p_T$ ,  $\eta$ ,  $z_{vtx}$ ) obtained from MC analysis  
353 on the minimum-bias samples LHC17f2b\_fast and LHC17f2b\_cent\_woSDD, considering only primary  
354 pions, kaons, protons, electrons and muons, and applying at reconstructed level the track selections  
355 (summarized in Table. 2). These efficiency maps were used in the analysis tasks to extract single track  
356 efficiencies; each correlation pairs found in the data analysis was inserted in correlation plots with a  
357 weight of **1/efficiency value**. As a cross-check, the tracking efficiency was evaluated, with the same  
358 criteria, also on the LHC17f2a\_fast and LHC17f2a\_cent\_woSDD samples, which were produced with  
359 EPOS-LHC generator instead of SPMJET. Compatibility within 1% between the efficiency values on the  
360 two samples was found. The 1D ( $p_T$  dependence) tracking efficiency, evaluated on f2b samples (blue)  
361 and on f2a samples (red) are shown in Fig. 10, as well as the ratio of f2b over f2a efficiencies.

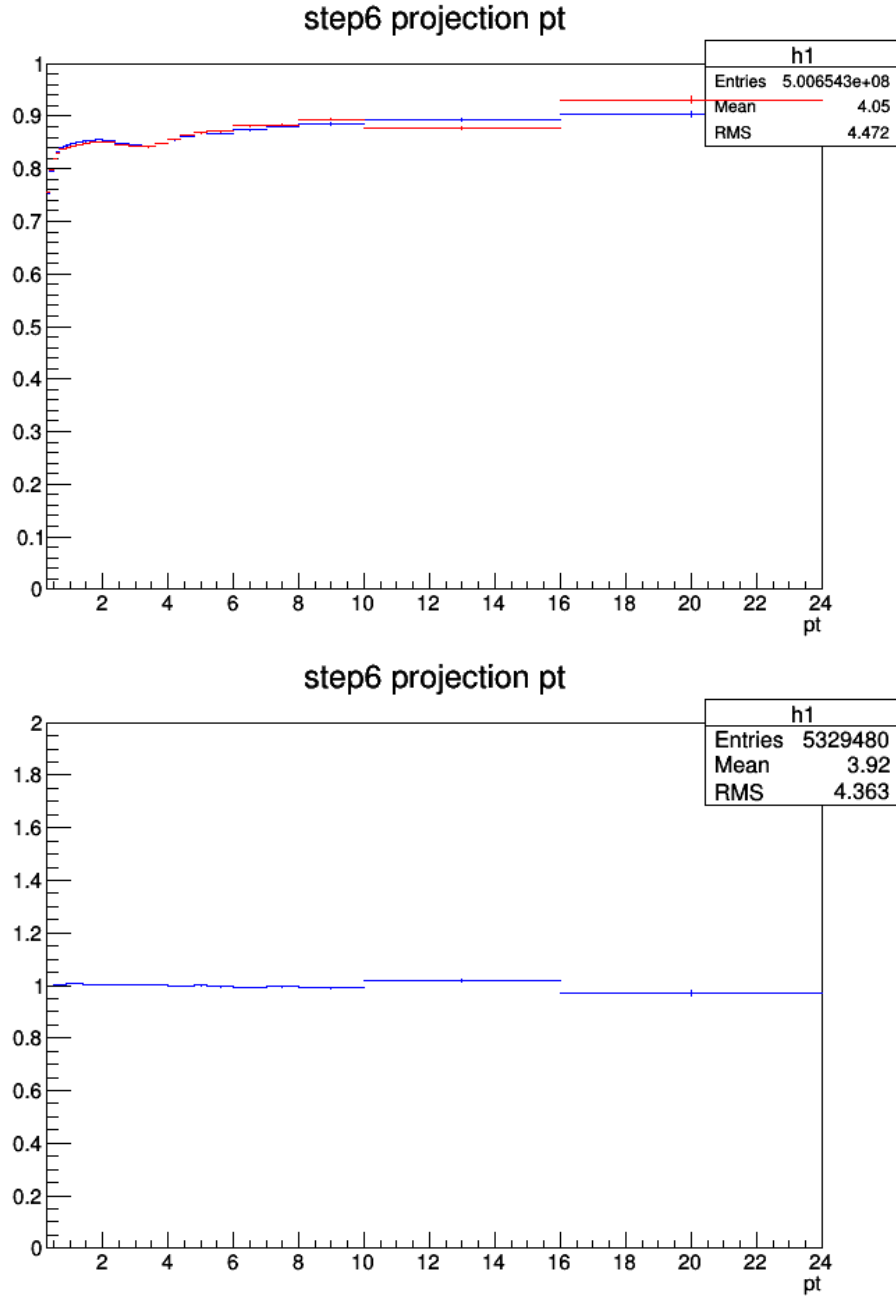


**Figure 10:** 1D (vs  $p_T$ ) tracking efficiency map for standard track selection, evaluated on f2b samples (blue) and f2a samples (red) on top panel, and their ratios on bottom panel.

- 362 Details of cuts at event level and particle/track selection at different steps are listed in Table 2 .  
 363
- 364 **(ii) D meson efficiency** - Due to limited statistics, the correlation analysis is performed in quite wide  $p_T$   
 365 bins and in each of them the reconstruction and selection efficiency of D mesons is not flat, in particular  
 366 in the lower  $p_T$  region. We correct for the  $p_T$  dependence of the trigger efficiency within each  $p_T$ -bin.
- 367 This correction is applied online, by using a map of D meson efficiency as a function of  $p_T$  and event  
 368 multiplicity (in terms of SPD tracklets in  $|\eta| < 1$ ) extracted from the enriched Monte Carlo sample  
 369 LHC17d2a\_fast\_new. The  $\eta$  dependence was neglected due to the statistics of the available Monte Carlo  
 370 sample, which rule out the possibility of performing a 3D study.

<b>MC Generated</b>	
Stages	Cuts
1. MC Part with Generated Cuts	<b>After Event Selection</b> Charge PDG Code Physical Primary <b>Kinematics Cuts</b> $-0.8 < \eta < 0.8$ $p_T > 0.3 \text{ (GeV}/c)$
2. MC Part with Kine Cuts	
<b>MC Reconstructed</b>	
4. Reco tracks	<b>After Event Selection</b> Physical Primary <b>Kinematics Cuts</b> $-0.8 < \eta < 0.8$ $p_T > 0.3 \text{ (GeV}/c)$
5. Reco tracks with Kine Cuts	<b>Quality Cuts</b> SetRequireSigmaToVertex(kFALSE) SetDCAToVertex2D(kFALSE) SetMinNCrossedRowsTPC(70) SetMinRatioCrossedRowsOverFindableClustersTPC(0.8) SetMinNClustersITS(2) SetMaxChi2PerClusterTPC(4) SetMaxDCAToVertexZ(1) SetMaxDCAToVertexXY(1) SetRequireTPCRefit(TRUE) SetRequireITSRefit(FALSE)
6. MC true with Quality Cuts	<b>Same as step 6</b>
7. Reco tracks with Quality Cuts	

**Table 2:** The list of event and particle/track selection cuts used in the estimation of single track efficiency

371 To properly count the number of trigger particles used to normalize the correlation distributions,  $N_{\text{trig}}$ ,  
 372 each D meson is weighted with the inverse of its efficiency in the invariant mass distribution. The main  
 373 role of the correction for the D meson efficiency is to account for the  $p_T$  dependence of the correlation  
 374 distribution within a given D meson  $p_T$  interval. Indeed, only the  $p_T$  shape of the D meson efficiency  
 375 within the correlation  $p_T^{\text{trig}}$  ranges is relevant while the average value in the  $p_T$  range is simplified due to  
 376 the normalization of the correlation distribution to the number of trigger particles.

377 Efficiency plots for  $D^0$ ,  $D^+$  and  $D^{*+}$  mesons are shown in Figs. 11 and 12.

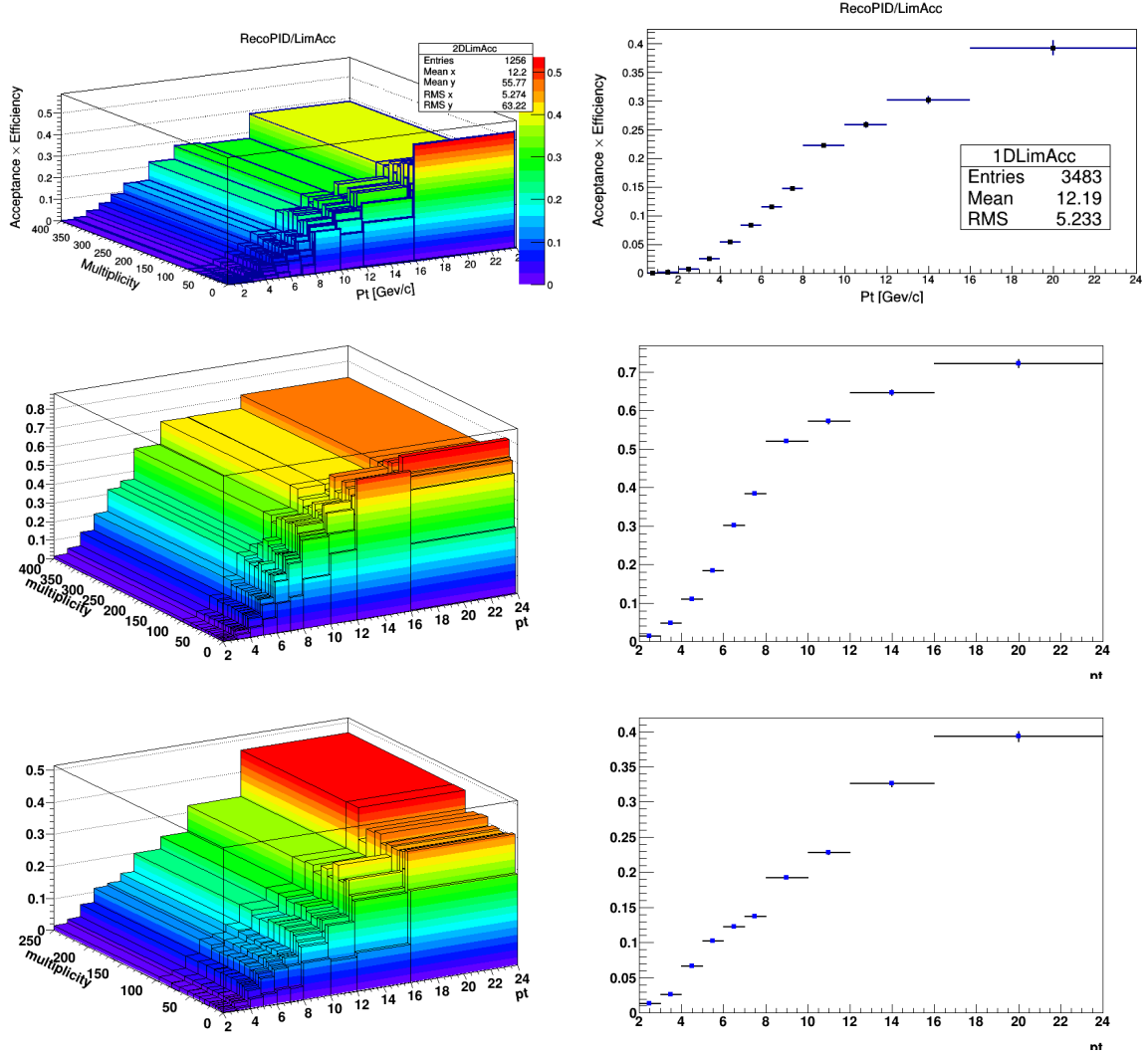


**Figure 11:** Top panel: ( $p_T$ , multiplicity) dependence (left) and  $p_T$  dependence (right) of prompt  $D^+$  meson efficiency. Mid panel: ( $p_T$ , multiplicity) dependence (left) and  $p_T$  dependence (right) of prompt  $D^{*+}$  meson efficiency. Bottom panel: ( $p_T$ , multiplicity) dependence (left) and  $p_T$  dependence (right) of prompt  $D^0$  meson efficiency.

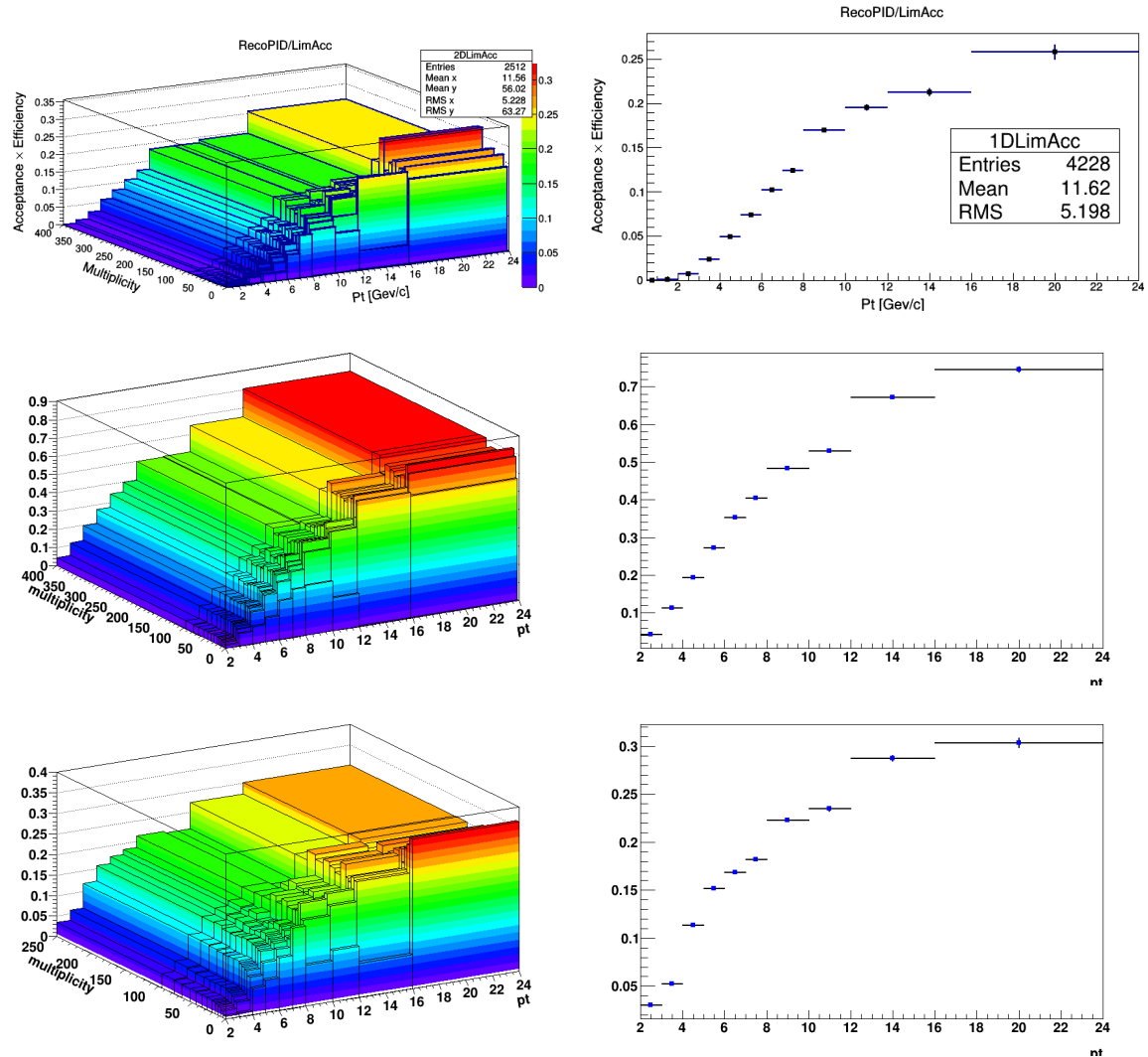


**Figure 12:** Top panel: ( $p_T$ , multiplicity) dependence (left) and  $p_T$  dependence (right) of feed-down  $D^+$  meson efficiency. Mid panel: ( $p_T$ , multiplicity) dependence (left) and  $p_T$  dependence (right) of feed-down  $D^{*+}$  meson efficiency. Bottom panel: ( $p_T$ , multiplicity) dependence (left) and  $p_T$  dependence (right) of feed-down  $D^0$  meson efficiency.

378 It was observed that multiplicity dependence of the efficiency does not bias the extraction of the signal  
 379 yield from the invariant mass distributions (which, as anticipated, are also weighted in the same manner).  
 380 In addition, the multiplicity dependence of the efficiencies (shown for the  $D^0$ , in integrated  $p_T$  range, in  
 381 Fig. 13) is rather flat in the range 20-80 tracklets, where about 90% of the reconstructed  $D$ -mesons are  
 found, which explains why it has a negligible effect on the correlation distributions on this data sample.

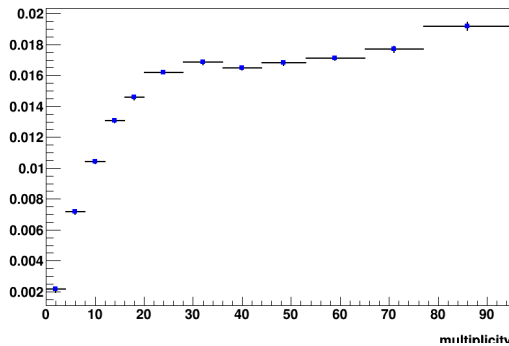


**Figure 13:** Prompt  $D^0$  meson efficiency as a function of multiplicity (SPD tracklet in  $|\eta| < 1$ .

383 **3.3.3 Correction for bias on  $B$  to  $D$  decay topologies**

384 To verify the consistency of the analysis chain and of the corrections applied to the correlation distribu-  
385 tions extracted from data, a Monte Carlo closure test was setup and tried on the  $D^0$ - $h$  analysis.

386 On the Monte Carlo enriched with charm and beauty quarks (LHC17d2a\_fast\_new), the correlation analy-  
387 sis was performed both at kinematic level and at reconstructed level. At kinematic level, only acceptance  
388 cuts were applied on the  $D$  mesons and the associated particles, using the Monte Carlo information for  
389 the identification of the  $D$  mesons and the hadrons in the event and rejecting the non-primary particles.  
390 At reconstructed level, the analysis was performed as if it were executed on data, applying the event se-  
391 lection, the acceptance cuts for  $D$  mesons and the associated particles, selecting the  $D$  meson candidates  
392 with filtering cuts on their daughters, topological cuts and PID selection, and then keeping only the true  
393  $D$  mesons by matching with the Monte Carlo truth; non-primary particles were rejected by means of  
394 the DCA selection. Event mixing correction was applied both at reconstructed and at kinematic level,  
395 where it takes into account just the effects of the acceptance cuts. In addition, at reconstructed level, the  
396 efficiency corrections for  $D$  mesons and associated tracks were also applied.

397 Examples of correlation plots at both steps are shown in Figures 14 and 15, separating the correlation  
398 contribution of associated tracks and  $D$  mesons from different origins, as described in the legend of the  
399 plots.

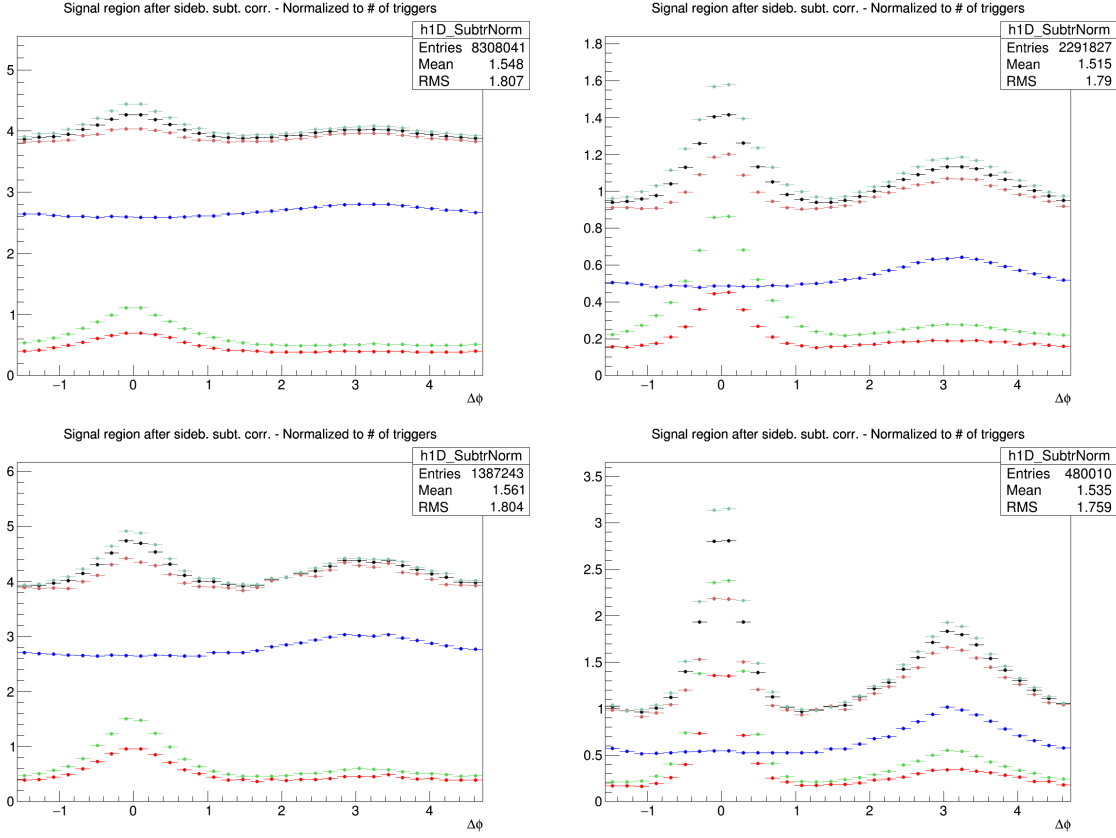


**Figure 14:**  $D^0$ -hadrons azimuthal correlation distribution obtained from Monte Carlo, at kinematic step. Black points: All  $D^0$ -all hadrons, normalized by all  $D^0$  triggers; light red points:  $D^0$  from c-hadrons from c, normalized by c- $D^0$  triggers; dark red points:  $D^0$  from c-all hadrons, normalized by c- $D^0$  triggers; light green points:  $D^0$  from b-hadrons from b, normalized by b- $D^0$  triggers; dark green points:  $D^0$  from b-all hadrons, normalized by b- $D^0$  triggers; blue points: All  $D^0$ -hadrons from light quarks, normalized by all  $D^0$  triggers. The panels show the ranges:  $3 < p_T(D) < 5 \text{ GeV}/c$ ,  $0.3 < p_T(\text{assoc}) < 1 \text{ GeV}/c$  (top-left);  $3 < p_T(D) < 5 \text{ GeV}/c$ ,  $p_T(\text{assoc}) > 1 \text{ GeV}/c$  (top-right);  $8 < p_T(D) < 16 \text{ GeV}/c$ ,  $0.3 < p_T(\text{assoc}) < 1 \text{ GeV}/c$  (bottom-left);  $8 < p_T(D) < 16 \text{ GeV}/c$ ,  $p_T(\text{assoc}) > 1 \text{ GeV}/c$  (bottom-right).

400 The consistency check was performed to verify whether, after having applied all the corrections to the  
 401 azimuthal correlation plots at reconstructed level, the results were compatible with the ones at kinematic  
 402 level. Hence, the ratios of fully corrected reconstructed plots over kinematic plots were evaluated in all  
 403 the  $D^0$   $p_T$  bins and for the various  $p_T$  thresholds for the associated tracks, separating the contributions for  
 404 the different origins of particles and triggers. The ratios, shown in Figure 16, denote a good compatibility  
 405 with 1, within the uncertainties, with the only exception being due to some structures in the near side  
 406 region for the beauty origin case. These structures were already found in the pp 2010 and p-Pb 2013  
 407 analysis, and it was verified that they are induced by our topological selection for the  $D$  mesons. Indeed,  
 408 in cases in which the  $D$  meson triggers come from B hadrons, applying the topological cuts (especially  
 409 the cosine of the pointing angle) tends to favour cases with a small angular opening between the products  
 410 of the B hadron decay (i.e. the  $D$  meson trigger itself and other particles), with respect to cases where  
 411 the B decay particles are less collinear.

412 In the Monte Carlo closure test, this situation is reflected in the correlation distributions at reconstructed  
 413 level, where the topological selection is applied, while it does not occur at kinematic level. Hence, in  
 414 the reconstructed/kinematic ratio, the distribution would show an excess for  $\Delta\phi = 0$  (due to the favoured  
 415 decays with small opening angle), which is then compensated by a depletion for larger values of  $\Delta\phi = 0$

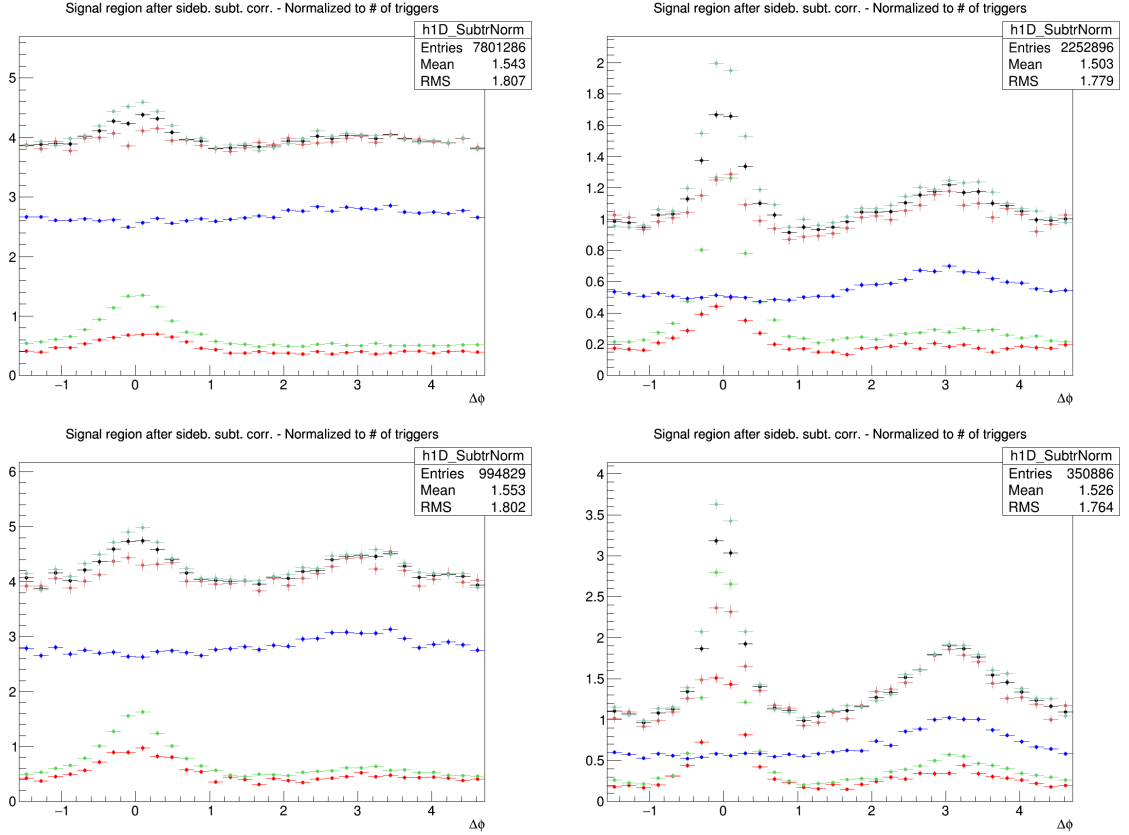


**Figure 15:**  $D^0$ -hadrons azimuthal correlation distribution obtained from Monte Carlo, at reconstructed step. Black points: All  $D^0$ -all hadrons, normalized by all  $D^0$  triggers; light red points:  $D^0$  from c-hadrons from c, normalized by c- $D^0$  triggers; dark red points:  $D^0$  from c-all hadrons, normalized by c- $D^0$  triggers; light green points:  $D^0$  from b-hadrons from b, normalized by b- $D^0$  triggers; dark green points:  $D^0$  from b-all hadrons, normalized by b- $D^0$  triggers; blue points: All  $D^0$ -hadrons from light quarks, normalized by all  $D^0$  triggers. The panels show the ranges:  $3 < p_T(D) < 5 \text{ GeV}/c$ ,  $0.3 < p_T(\text{assoc}) < 1 \text{ GeV}/c$  (top-left);  $3 < p_T(D) < 5 \text{ GeV}/c$ ,  $p_T(\text{assoc}) > 1 \text{ GeV}/c$  (top-right);  $8 < p_T(D) < 16 \text{ GeV}/c$ ,  $0.3 < p_T(\text{assoc}) < 1 \text{ GeV}/c$  (bottom-left);  $8 < p_T(D) < 16 \text{ GeV}/c$ ,  $p_T(\text{assoc}) > 1 \text{ GeV}/c$  (bottom-right).

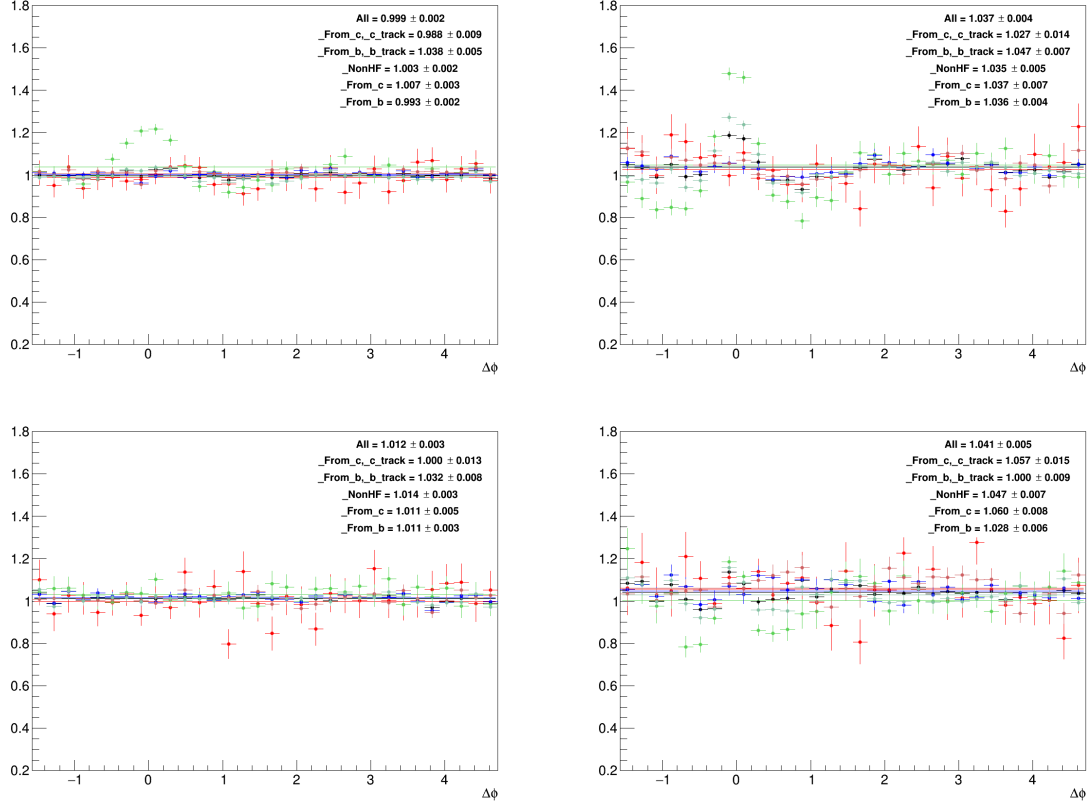


**Figure 16:** Ratios of fully corrected azimuthal correlation plots at reconstructed level over azimuthal correlation plots at kinematic level, in the two  $D^0$   $p_T$  bins, for the different associated  $p_T$  ranges. Black points: All  $D^0$ -all hadrons, normalized by all  $D^0$  triggers; light red points:  $D^0$  from c-hadrons from c, normalized by c- $D^0$  triggers; dark red points:  $D^0$  from c-all hadrons, normalized by c- $D^0$  triggers; light green points:  $D^0$  from b-hadrons from b, normalized by b- $D^0$  triggers; dark green points:  $D^0$  from b-all hadrons, normalized by b- $D^0$  triggers; blue points: All  $D^0$ -hadrons from light quarks, normalized by all  $D^0$  triggers. The panels show the ranges:  $3 < p_T(D) < 5 \text{ GeV}/c$ ,  $0.3 < p_T(\text{assoc}) < 1 \text{ GeV}/c$  (top-left);  $3 < p_T(D) < 5 \text{ GeV}/c$ ,  $p_T(\text{assoc}) > 1 \text{ GeV}/c$  (top-right);  $8 < p_T(D) < 16 \text{ GeV}/c$ ,  $0.3 < p_T(\text{assoc}) < 1 \text{ GeV}/c$  (bottom-left);  $8 < p_T(D) < 16 \text{ GeV}/c$ ,  $p_T(\text{assoc}) > 1 \text{ GeV}/c$  (bottom-right).

(corresponding to B decays with larger angles, which are disfavoured). These structures are prominent at low  $D^0 p_T$ , where the topological cuts are tighter, and tend to disappear at higher  $p_T$ , where the selections are released. They are also larger in the higher associated track  $p_T$  ranges, where the fraction of B-hadron decay tracks dominate the overall correlation distributions.

The data correlation distribution need to be corrected for this bias, and in particular for the enhancement of b-origin correlation pairs at the centre of the near side region, which would influence the near-side peak features. In order to do this, the amount of the b-origin excess is evaluated from the Reco/Kine ratio, by considering the b- $D^0$ -all tracks case (dark green points). The excess at Reco level (affecting data) is quantified as a  $\Delta\varphi$  modulation **modul** for the five points an each side of the  $\Delta\varphi = 0$  value (or, equivalently, on the first five points of the reflected distributions, which start from  $\Delta\varphi = 0$ ). This is done separately in each  $p_T$  range. Then, the correction is done by applying this modulation to the data correlation distributions, but taking into account that only the correlation entries from  $B \rightarrow D$  are affected, while the  $c \rightarrow D$  correlations need to be left unaltered. In particular, it has to be considered that:

- On data, the  $B \rightarrow D$  correlation pairs are only a fraction ( $1-f_{\text{prompt}}$ ) of the total.
- The amplitude of  $B \rightarrow D|_{\text{amplit}}$  correlation pattern is different (greater) than the amplitude of the  $c \rightarrow D|_{\text{amplit}}$  correlation pattern:

Thus, the following equation is applied to get the corrected  $C(\Delta\varphi)_{\text{corr}}$  data points starting from the raw ones,  $C(\Delta\varphi)_{\text{raw}}$ :

$$C(\Delta\varphi)_{\text{corr}} = C(\Delta\varphi)_{\text{raw}} \cdot \left[ \frac{c \rightarrow D|_{\text{amplit}}}{(B+c) \rightarrow D|_{\text{amplit}}} \cdot f_{\text{prompt}} + \frac{B \rightarrow D|_{\text{amplit}}}{(B+c) \rightarrow D|_{\text{amplit}}} \cdot (1 - f_{\text{prompt}}) \cdot \frac{1}{\mathbf{modul}} \right] \quad (3)$$

where  $(B+c) \rightarrow D|_{\text{amplit}} = c \rightarrow D|_{\text{amplit}} \cdot f_{\text{prompt}} + B \rightarrow D|_{\text{amplit}} \cdot (1 - f_{\text{prompt}})$ , and where the two amplitudes are evaluated from the Monte Carlo distributions of Figure 15 at reconstructed level (so, including the bias), and  $f_{\text{prompt}}$  with the procedure described in 3.3.5. Applying the **modul** factor to the beauty part of the data correlation distributions brings its value back to the generated level case, effectively removing the bias. The effect of the correction is a shift of the data points in the near-side region (in general, downward in the first and second points, the upward in the others). The maximum value of the shift is of about 5%, at the centre of the near-side peak, for the lowest D-meson  $p_T$  range ( $3 < p_T < 5 \text{ GeV}/c$ ) and the highest associated track  $p_T$  range ( $p_T > 3 \text{ GeV}/c$ ). The typical values are instead of a couple of percentage points. The correction is zero in the highest D-meson  $p_T$  range. To take into account for possible inaccuracies in the definition of the modulations, or in their rescaling, a systematic uncertainty is applied on the corrected data points, with value  $|C(\Delta\varphi)_{\text{corr}} - C(\Delta\varphi)_{\text{raw}}| / \sqrt{12}$ , on each side of the data points affected by the bias (symmetric uncertainty).

446 **3.3.4 Secondary track contamination**

447 The secondary tracks inside the associated track sample, due to interaction of primary track with the de-  
 448 tector material or to decays of strange hadrons, are mostly removed by the DCA cuts applied during the  
 449 cut selection phase ( $DCA(xy) < 1 \text{ cm}$ ,  $DCA(z) < 1 \text{ cm}$ ). Anyway, a small fraction of secondary tracks  
 450 survives this cut, and the data correlation distributions have to be corrected for this residual contami-  
 451 nation. The fraction of surviving secondary tracks is evaluated via a study on the LHC17d2a\_fast\_new  
 452 sample, by counting the number of tracks accepted by the selection whose corresponding generated-  
 453 level track doesn't satisfy the `IsPhysicalPrimary()` call, and dividing this number by the total number  
 454 of accepted tracks. The outcome of the check is reported in Figure 17. As it's visible, no more than  
 455 5% secondary tracks pass the selection. Moreover, the fraction of residual secondary tracks is flat along  
 456 the  $\Delta\varphi$  axis, as shown, for exemplary  $p_T$  regions, in Figure 18, where the inhomogeneities are always  
 457 below 1%. For this reason, it is possible to directly scale the data correlation distributions by their purity  
 458 fraction (i.e. 1 - secondary contamination). This is done with an associated  $p_T$  dependence, due to the  
 459 increase of the purity with the track  $p_T$ , while the purity fraction is taken flat versus the D-meson  $p_T$ .  
 460 The purity values that were chosen are the following:

- 461 –  $p_T(\text{assoc}) > 0.3 \text{ GeV}/c : 0.958$
- 462 –  $p_T(\text{assoc}) > 1 \text{ GeV}/c : 0.973$
- 463 –  $0.3 < p_T(\text{assoc}) < 1 \text{ GeV}/c : 0.953$
- 464 –  $1 < p_T(\text{assoc}) < 2 \text{ GeV}/c : 0.969$
- 465 –  $2 < p_T(\text{assoc}) < 3 \text{ GeV}/c : 0.982$
- 466 –  $p_T(\text{assoc}) > 3 \text{ GeV}/c : 0.990$

467 It was also verified with the same Monte Carlo study that applying the DCA selection rejects less than  
 468 0.2% primary tracks (tagged as false positives) from the associated track sample, again with a flat az-  
 469 imuthal distribution, inducing hence a fully negligible bias on the data correlation distributions. This is  
 470 shown in Figure 19. This was also verified for specific charm-origin and beauty-origin tracks, due to  
 471 their larger DCA with respect to primary tracks from light quarks. In this case, the fraction of rejected  
 472 charm and beauty tracks stays below 1% in all the kinematic ranges apart from the associated track  $p_T$   
 473 regions 0.3-1 and  $> 0.3 \text{ GeV}/c$ , where the rejection can be as high as 2%. In these kinematic ranges,  
 474 though, the data correlation distributions are dominated by non-heavy-flavour tracks, as it was verified  
 475 from the simulations, hence the overall bias is still contained below 1%, thus negligible.

476 These studies were performed on an enriched Monte Carlo sample, which could not fully reproduce  
 477 the relative abundancies of the species. Anyway, for events with a reconstructed D-meson, this bias is  
 478 expected to be minor, and only these events are used in the data analysis. In any case, the percentages  
 479 obtained from the study were found to be consistent within 1% with the outcome of the studies for the  
 480 p-Pb 2013 analysis, which reassures us on the full validity of these results.

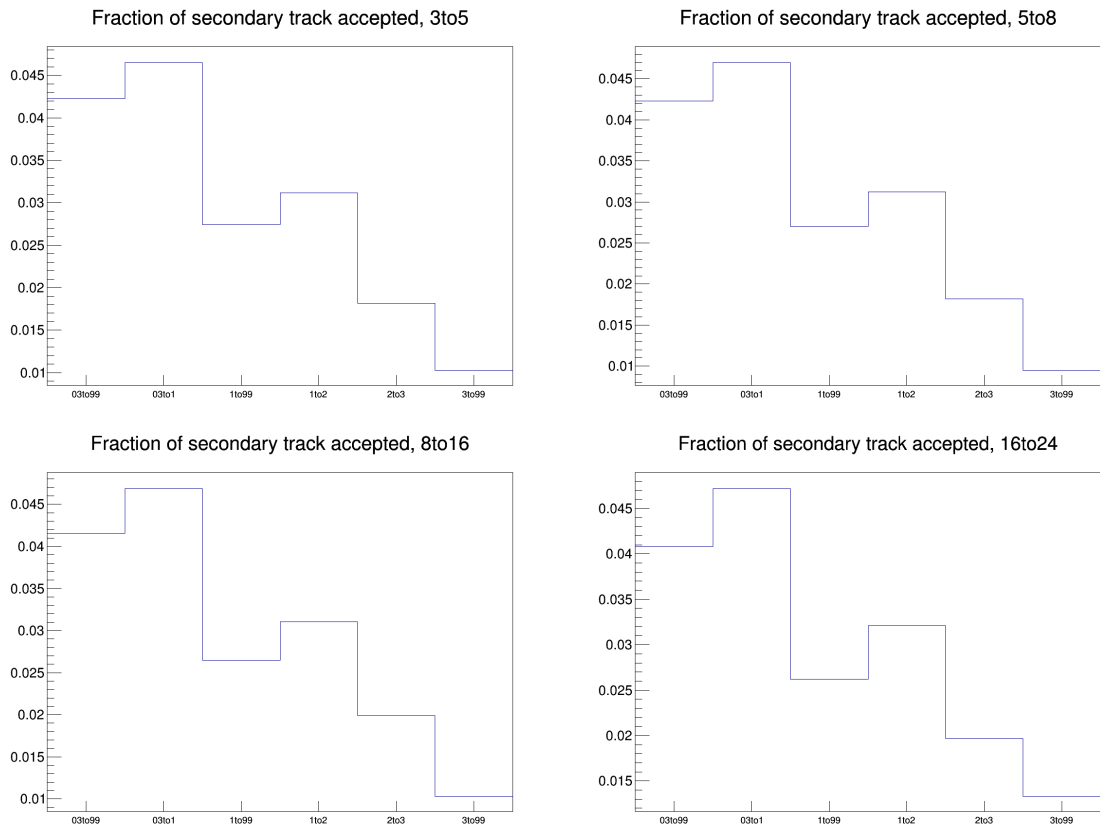


**Figure 17:** Fraction of secondary tracks over total amount of tracks which pass the DCA selection. The four panel show the fractions for the D-meson  $p_T$  ranges: 3-5, 5-8, 8-16, 16-24, respectively. Inside each panel, the associated track  $p_T$  ranges are shown on the  $x$ -axis.

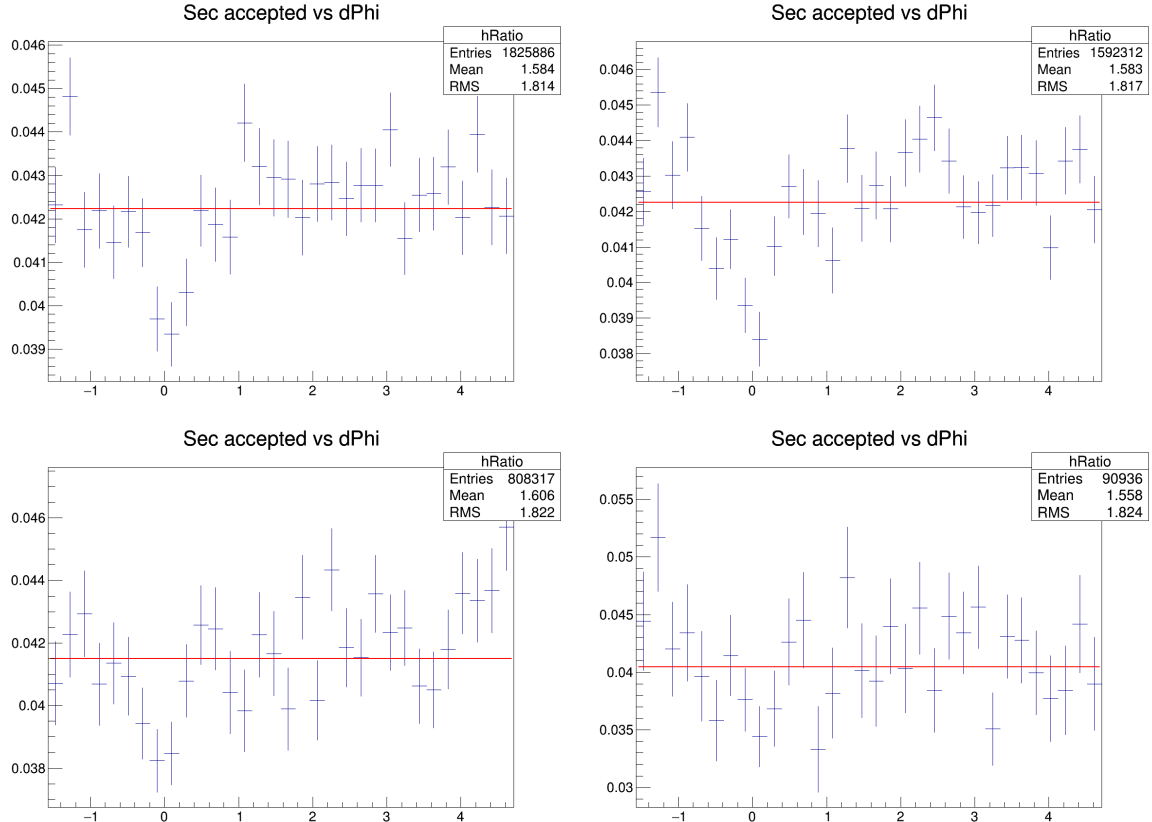


**Figure 18:**  $\Delta\phi$  dependence of the fraction of secondary tracks in the  $D^0$ - $h$  correlation distributions. The four panel show the fractions for the  $D$ -meson  $p_T$  ranges: 3-5, 5-8, 8-16, 16-24, respectively. The associated track  $p_T$  ranges are the integrated one, i.e.  $p_T > 0.3 \text{ GeV}/c$ .

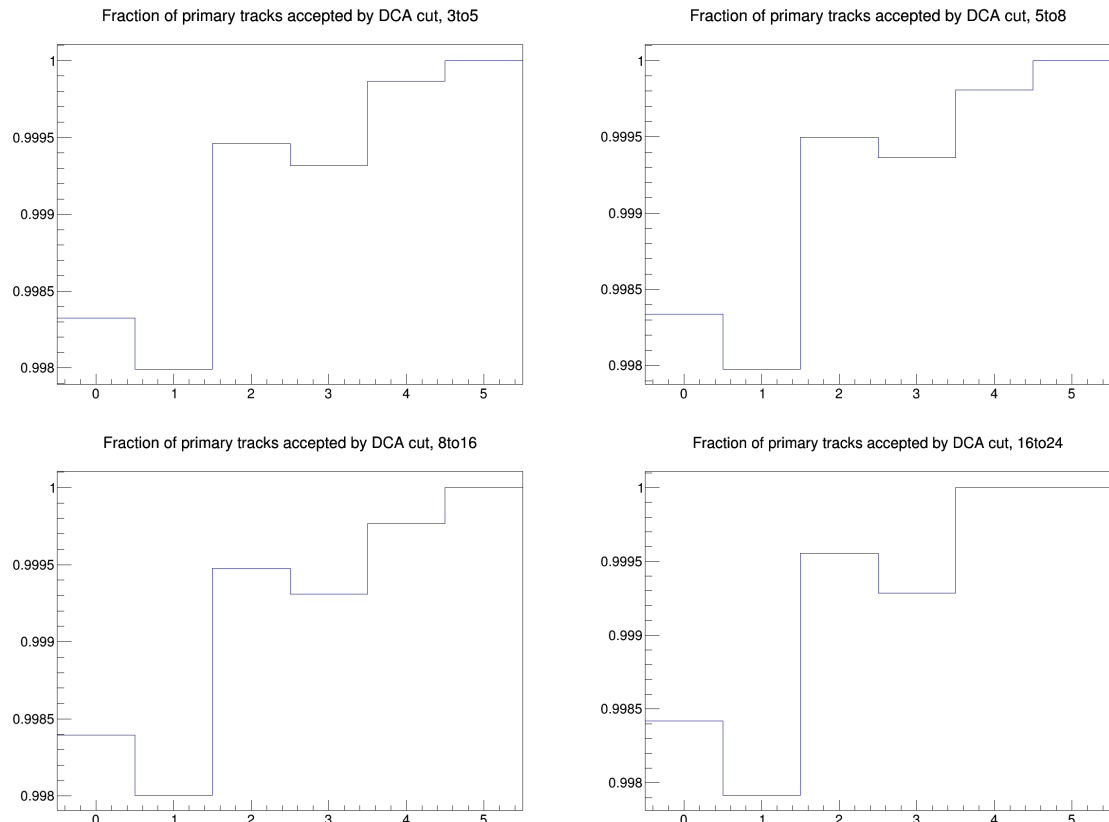


**Figure 19:** Fraction of primary tracks rejected by the DCA selection. The four panel show the fractions for the D-meson  $p_T$  ranges: 3-5, 5-8, 8-16, 16-24, respectively. Inside each panel, the associated track  $p_T$  ranges are shown on the  $x$ -axis.

481 **3.3.5 Beauty feed-down**

482 The contribution of correlations of D meson from b-hadron decay is subtracted from the data correlation  
 483 distributions as:

$$\tilde{C}_{\text{prompt D}}(\Delta\phi) = \frac{1}{f_{\text{prompt}}} \left( \tilde{C}_{\text{inclusive}}(\Delta\phi) - (1 - f_{\text{prompt}}) \tilde{C}_{\text{feed-down}}^{\text{MC templ}}(\Delta\phi) \right). \quad (4)$$

484 In the above equation,  $\tilde{C}_{\text{inclusive}}(\Delta\phi)$  and  $\tilde{C}_{\text{prompt D}}(\Delta\phi)$  are per-trigger azimuthal correlation distribu-  
 485 tions before and after feed-down contribution subtraction,  $f_{\text{prompt}}$  is the fraction of prompt D meson  
 486 and  $\tilde{C}_{\text{feed-down}}^{\text{MC templ}}$  is a template of the azimuthal correlation distribution for the feed-down component ob-  
 487 tained from home-made Monte Carlo simulation at generated level, using PYTHIA6 with Perugia2011  
 488 tune. In order to avoid biases related to the different event multiplicity in real and simulated events,  
 489 the correlation distribution was shifted to have its minimum coinciding with the baseline of the data  
 490 azimuthal-correlation distribution before feed-down subtraction.

491 The value of  $f_{\text{prompt}}$  (Figure 20), which depends on D-meson species and varies as a function of the  $p_T$ ,  
 492 is estimated on the basis of FONLL predictions for the production of feed-down D mesons at central  
 493 rapidity, in pp collisions at  $\sqrt{(s)} = 5$  TeV, and using the reconstruction efficiency of prompt and feed-  
 494 down D mesons, following the so-called  $N_b$  approach defined in [1]. Typical values are about 8-10%  
 495 for the  $D^0$ , about 4-7% for the  $D^+$  and about 5-8% for the  $D^{*+}$ . The procedure adopted is the same  
 496 as what done in the past analysis [7]: however, in p-Pb, in order to consider a possible non-zero  $v_2$ -  
 497 like modulation of the baseline, a range of  $0 < v_2 < 0.2$  values for tracks and for secondary D mesons  
 498 is considered for the systematic uncertainty evaluation (using an hypothesis of no modulation for both  
 499 cases for central values).

500 Examples of the PYTHIA templates used for the feed-down contribution subtraction are shown in Figures  
 501 21 (Figure 22 shows the same templates but for prompt D mesons).

502 The feed-down subtraction was performed after rescaling the data correlation distributions for the purity  
 503 fraction, and correcting them by the near-side modulation induced by the bias on the B decay topology.

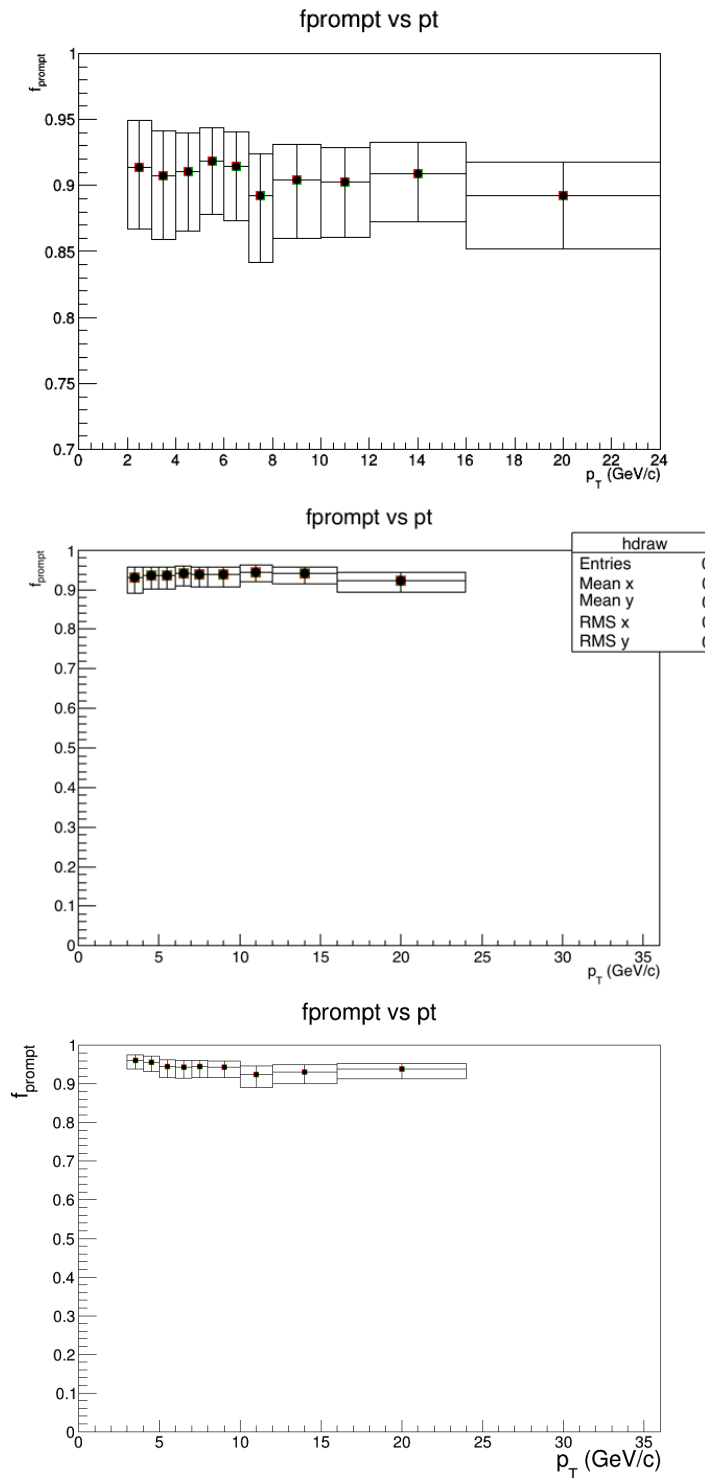


**Figure 20:**  $f_{\text{prompt}}$  as a function of the  $p_T$  for  $D^0$  (top),  $D^{*+}$  (mid) and  $D^+$  (bottom) estimated on the basis of FONLL predictions

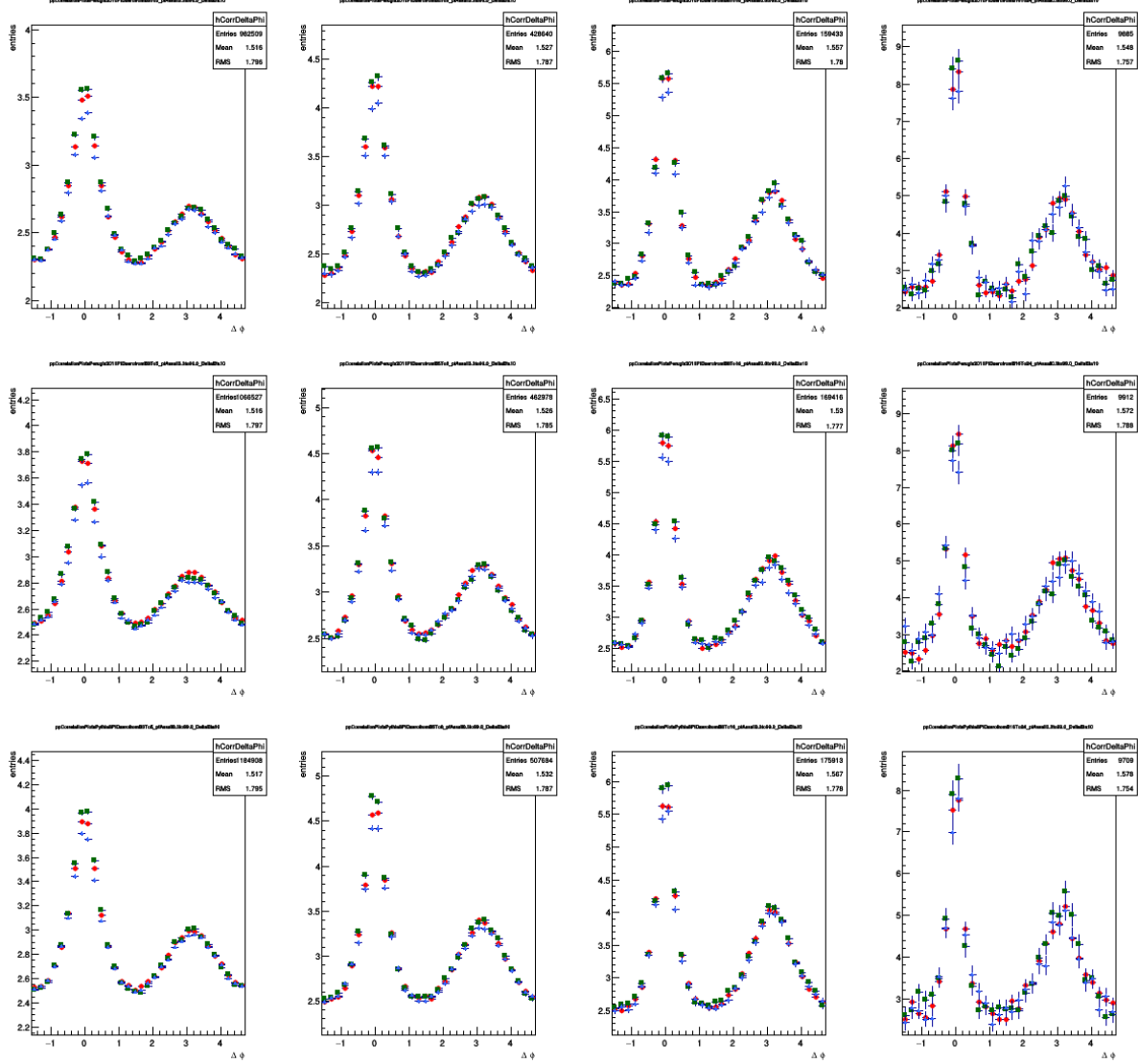


**Figure 21:** Azimuthal correlation distribution between D meson from b-hadron decay and charged particles obtained from Monte Carlo simulations based on Pythia-Perugia2010 tune (row1), Pythia-Perugia2011 tune (row2), Pythia8 tune 4C (row3) for associated track  $p_T > 0.3$  GeV/ $c$  and D-meson  $p_T$  ranges: 3-5, 5-8, 8-16, 16-24 GeV/ $c$ . D<sup>0</sup> in blue, D<sup>+</sup> in green, D<sup>\*+</sup> in red.

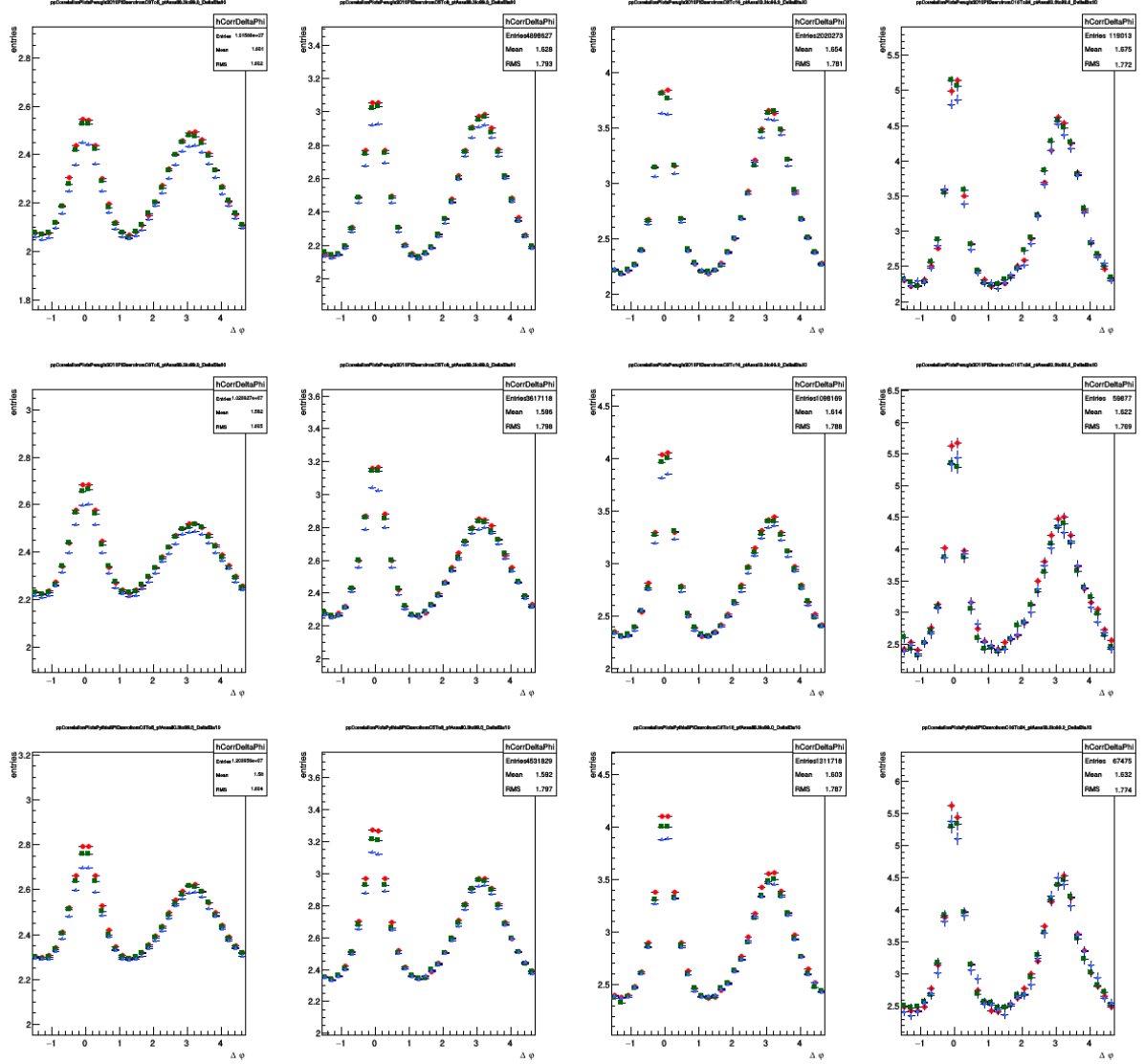


**Figure 22:** Azimuthal correlation distribution between prompt D meson and charged particles obtained from Monte Carlo simulations based on Pythia-Perugia2010 tune (row1), Pythia-Perugia2011 tune (row2), Pythia8 tune 4C (row3) for associated track  $p_T > 0.3$  GeV/ $c$  and D-meson  $p_T$  ranges: 3-5, 5-8, 8-16, 16-24 GeV/ $c$  .  $D^0$  in blue,  $D^+$  in green,  $D^{*+}$  in red.

## 504 4 Systematic uncertainties on $\Delta\phi$ correlation distributions

### 505 4.1 Uncertainty on S and B extraction

506 The systematic uncertainty for the D meson yield extraction was determined separately for the three  
 507 mesons. It was obtained by evaluating the value of the signal candidate from the invariant mass spectra  
 508 with the following differences with respect to the standard approach:

- 509 – Changing the background fit function, for  $D^0$  and  $D^+$  (tried with polynomials of 1st and 2nd order)  
 510 and for  $D^{*+}$  (tried with polynomials of 2nd order and a power function);
- 511 – Changing the range in which the signal is extracted from the Gaussian fit;
- 512 – Reducing the range of invariant mass axis in which the signal region is defined (and S and B are  
 513 extracted);
- 514 – Rebinning the invariant mass distributions before the fit for  $D^0$  and  $D^+$
- 515 – Extracting S and B via integral of the fit functions or B via bin counting and S via integral of the  
 516 Gaussian function.

517 Both the value of the yield and the sidebands correlations normalization factor are affected by changing  
 518 the yield extraction approach, while the rest of the procedure to extract the azimuthal correlation dis-  
 519 tribution is the same as in the standard analysis. The fully corrected azimuthal correlation plots were  
 520 evaluated, for each of these approaches, in all D meson  $p_T$  bins and for each value of associated tracks  
 521  $p_T$  threshold. The ratios of the correlation distributions obtained with the standard yield extraction pro-  
 522 cedure and by differentiating the approach were evaluated. From the average of these ratios, which  
 523 are found to be flat versus  $\Delta\phi$ , a systematic uncertainty can be extracted, which was taken of 1% for  
 524  $3 < p_T(D) < 16 \text{ GeV}/c$  and of 2% in  $16 < p_T(D) < 24 \text{ GeV}/c$ . No dependence versus the associated  
 525 track  $p_T$  was assumed, since from a physics point of view we don't expect a modification of the signal  
 526 and sideband values to have a dependence of this kind. Figures 23, show the ratios obtained by the  
 527 above mentioned procedure for exemplary  $p_T$  ranges, which anyway span over the full kinematic ranges  
 528 analyzed, for  $D^0$ -h correlations. Figures 24 and 25 show the same ratios for  $D^{*+}$ -h,  $D^+$ -h as well.

### 529 4.2 Uncertainty on background correlation shape

530 The systematic uncertainty for the subtraction of the background correlations includes the effects due to  
 531 a potentially biased description of the background correlation shape, which is evaluated from of the side-  
 532 bands correlations. In particular, the background correlation shape could present some hidden invariant  
 533 mass dependence. To estimate this uncertainty, the invariant mass range of the sidebands definitions was  
 534 varied with respect to the default values. For the  $D^0$  meson, the usual range of the sidebands is 4 to 8  $\sigma$   
 535 from the centre of the peak of the Gaussian fit and it was modified, for both sidebands to:

- 536 – inner half (4 to 6  $\sigma$  from the centre of the peak);
- 537 – outer half (6 to 8  $\sigma$  from the centre of the peak)
- 538 – extended to 4 to 10  $\sigma$  (in case this is possible without exceeding the fitting range of the mass plots)

539 Slightly different variations, but with the same reasoning, were considered for the  $D^+$  meson.

540 For the  $D^{*+}$  meson, the usual range of sideband in invariant mass spectra is 5 to 10  $\sigma$  (only on the right  
 541 side) from the centre of the peak of the Gaussian fit of the invariant mass spectra, and it was modified to:

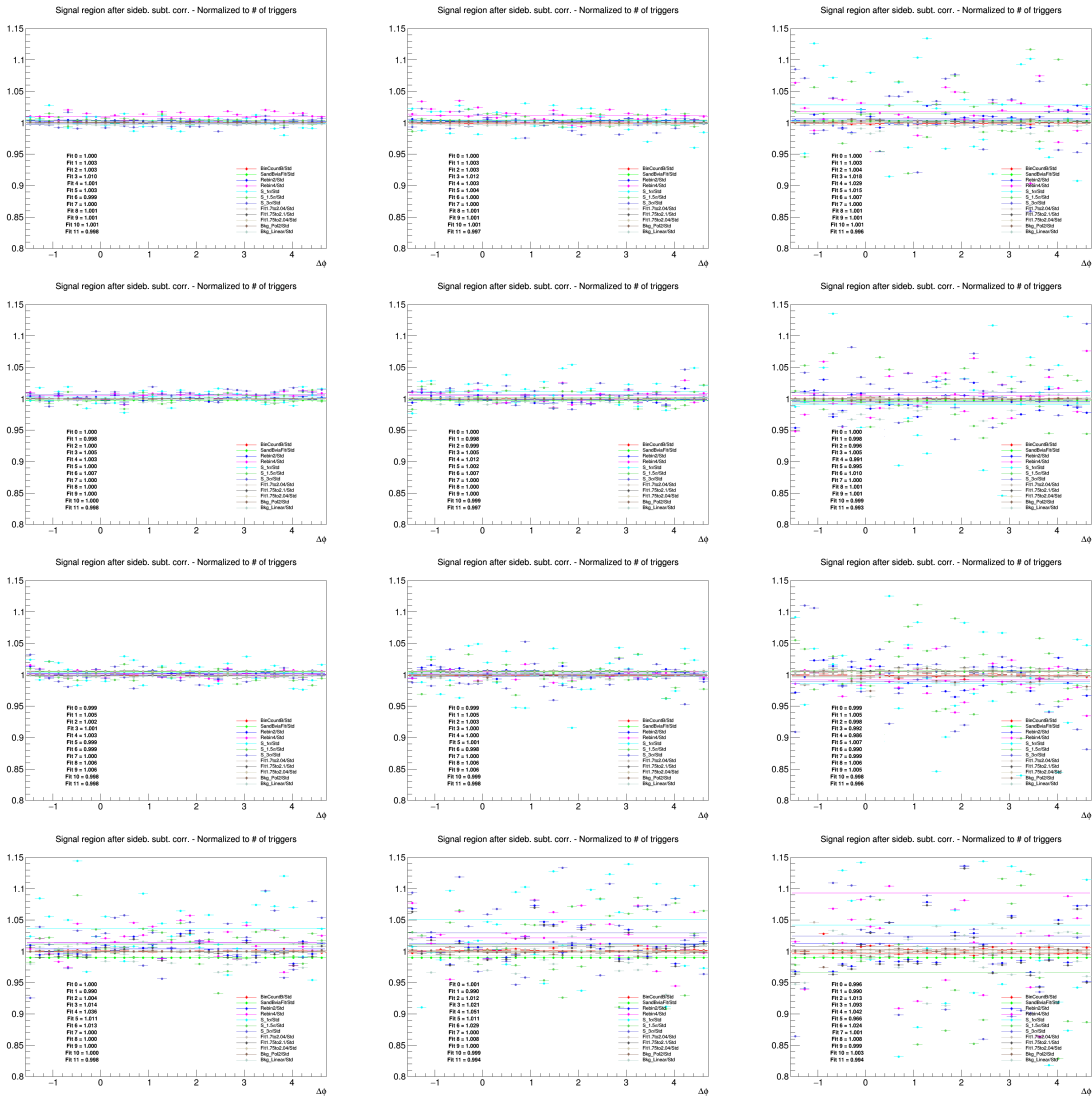


**Figure 23:** Ratios of  $D^0$ - $h$  correlation plots obtained changing S and B extraction procedure over those obtained with standard yield extraction procedure. Rows:  $p_T(D^0)$  3-5, 5-8, 8-16, 16-24  $\text{GeV}/c$ . In each row, the panels show the associated track  $p_T$  ranges 0.3-1, 1-2,  $>3 \text{ GeV}/c$ , respectively.

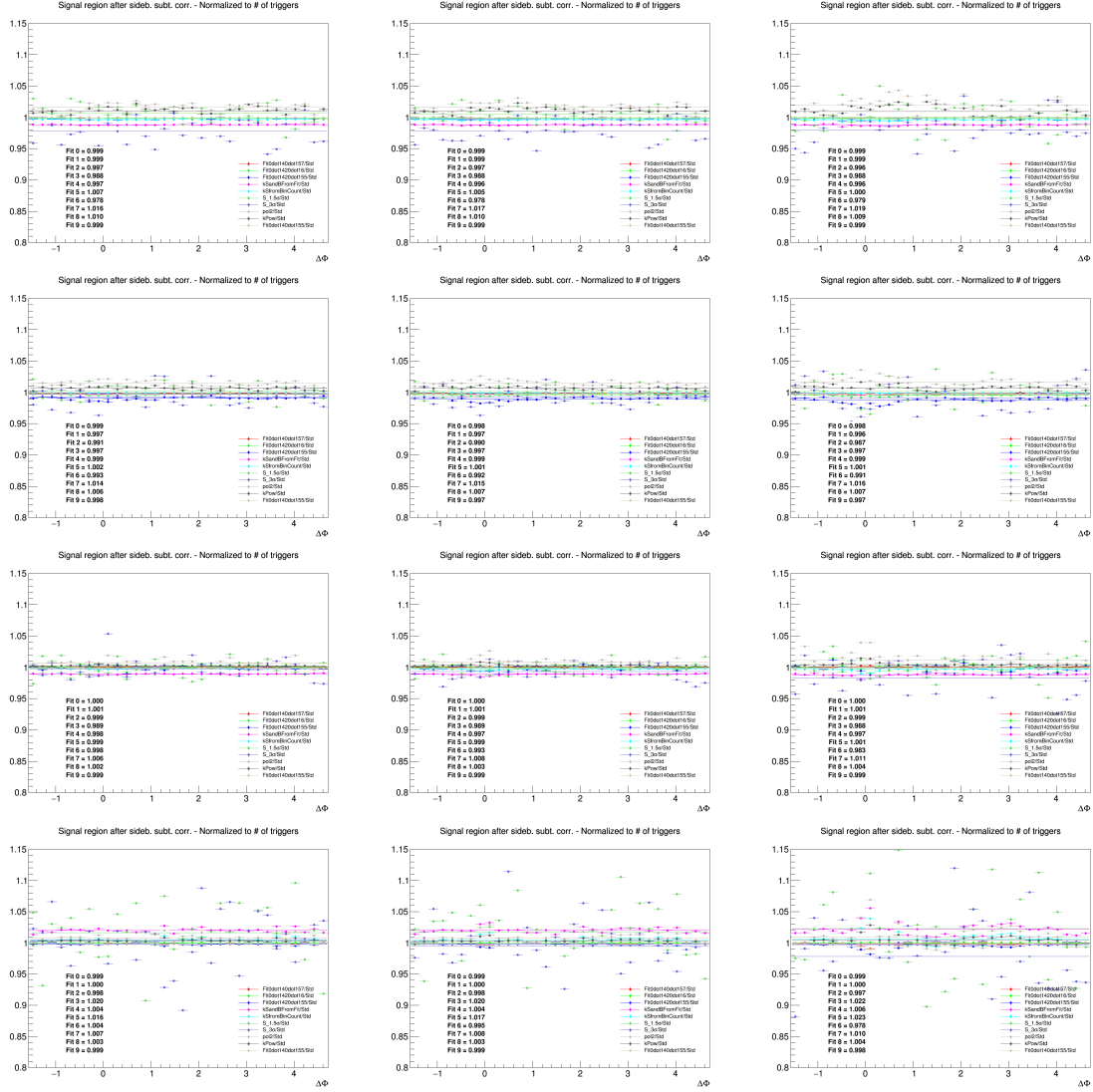


**Figure 24:** Ratios of  $D^*+ - h$  correlation plots obtained changing S and B extraction procedure over those obtained with standard yield extraction procedure. Rows:  $p_T(D^*)$  3-5, 5-8, 8-16, 16-24  $\text{GeV}/c$ . In each row, the panels show the associated track  $p_T$  ranges  $>0.3 \text{ GeV}/c$ ,  $0.3-1 \text{ GeV}/c$  and  $>1 \text{ GeV}/c$ , respectively.

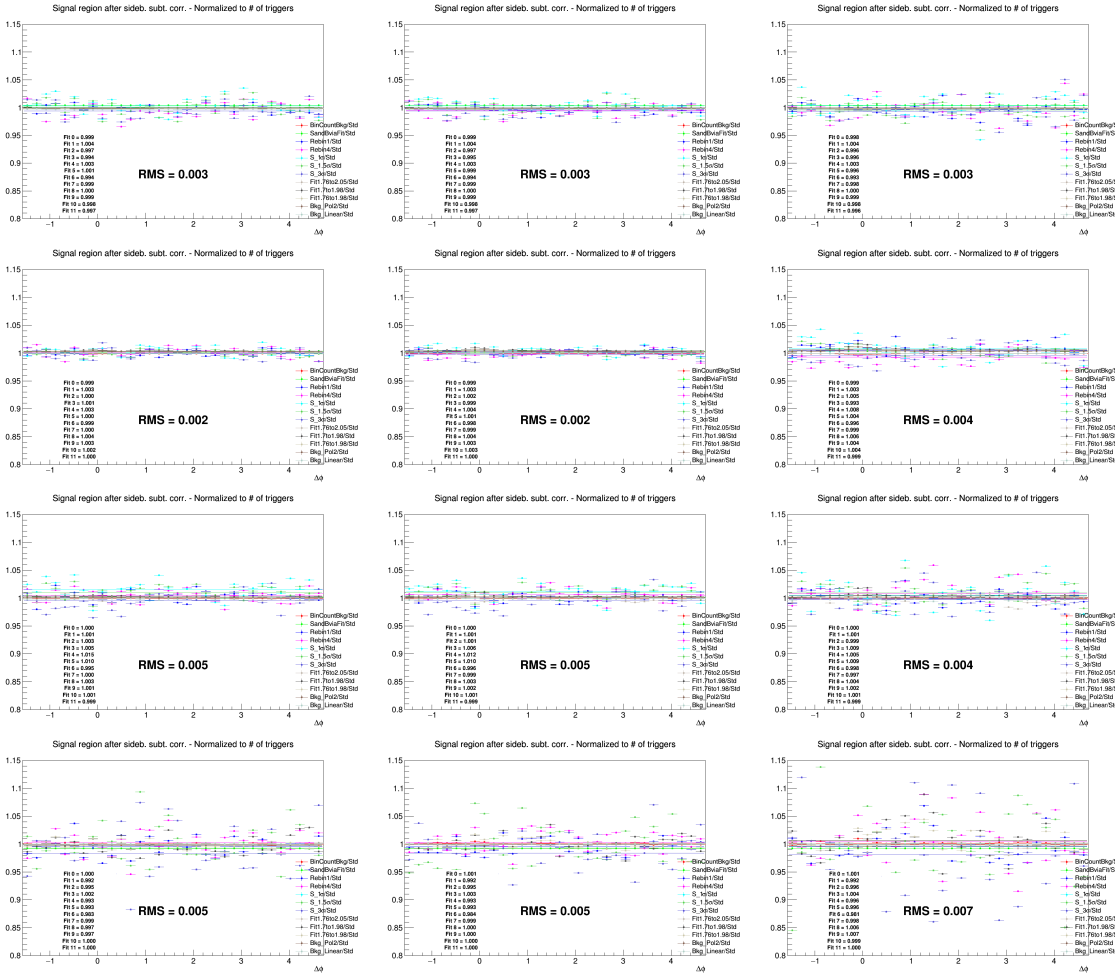


**Figure 25:** Ratios of D<sup>+</sup>-h correlation plots obtained changing S and B extraction procedure over those obtained with standard yield extraction procedure. Rows:  $p_T(D^+)$  3-5, 5-8, 8-16, 16-24 GeV/c. In each row, the panels show the associated track  $p_T$  ranges 0.3-1 GeV/c, >0.3 GeV/c, and >1 GeV/c, respectively.

- inner half (5 to 8  $\sigma$  from the centre of the peak);
- outer half (8 to 13  $\sigma$  from the centre of the peak);
- extended to 5 to 13  $\sigma$  from the centre of the peak;
- extended to 6 to 16  $\sigma$  from the centre of the peak.

The rest of the procedure for the azimuthal correlations distribution was unchanged, and the ratios of the fully corrected azimuthal correlation plots obtained with the standard sidebands range and the correlation plots extracted with different sidebands definitions, were evaluated for each D-meson  $p_T$  bin and associated tracks  $p_T$  threshold. Results of this check are shown in Figures 26, 27 and 28 for  $D^0$ ,  $D^{*+}$ ,  $D^+$  respectively, for exemplary  $p_T$  ranges, spanning over the full kinematic regions analysis. From the values of the ratios extracted from the checks, which do not show any azimuthal dependence a systematic uncertainty for the background subtraction can be evaluated. Also no dependence versus the associated track  $p_T$  was assumed also in this case. The uncertainty was hence taken of 1% for all the mesons in  $3 < p_T(D) < 16 \text{ GeV}/c$  and of 2%, 2.5% and 4% (for  $D^+$ ,  $D^0$ ,  $D^{*+}$  respectively) in  $16 < p_T(D) < 24 \text{ GeV}/c$ .

### 4.3 Uncertainty on D-meson cut stability

To study the systematics due to the topological selections on the D meson, the cut variation approach was used. For each D-meson, alternate sets of released and tightened selection cuts were applied to extract the correlation distribution, varying in particular the cosine of the pointing angle, the maximum DCA among the daughter tracks and the product of the daughter track impact parameters. For each set of cuts new 2D ( $p_T$  vs multiplicity), D meson efficiency map was computed. In Figures 29, 30, 31 (for  $D^0$ ,  $D^{*+}$  and  $D^+$ , respectively) the ratio of the different 1D efficiencies with the alternate cuts with respect to the default cut selection is chosen, to highlight how the different selections effectively varied the efficiency values, especially at low  $p_T$ , where cuts are more effective.

Figure 32, 33, 34 show the ratio of the correlation distributions with alternate cut sets over those with the standard approach, for exemplary  $p_T$  ranges covering the full kinematic region of interest for the analyses. The ratios are reasonably flat in  $\Delta\phi$ , hence a flat systematic was evaluated as systematic uncertainty from D-meson the cut variations. For the  $D^0$ , the uncertainty was considered of 2% for all the  $p_T$  ranges of trigger and tracks analyzed. For the  $D^{*+}$ , the uncertainty was considered of 1.5% for  $3 < p_T(D) < 8 \text{ GeV}/c$  and of 1% for  $8 < p_T(D) < 24 \text{ GeV}/c$ . For the  $D^+$ , the uncertainty was considered of 1% for  $3 < p_T(D) < 16 \text{ GeV}/c$  and of 2% for  $16 < p_T(D) < 24 \text{ GeV}/c$ .

### 4.4 Uncertainty on tracking efficiency evaluation

The systematic uncertainty for the tracking efficiency includes the effects related to the set of filtering cuts defined for the associated tracks selection (mainly requests on the quality of reconstructed tracks for the TPC and ITS detectors). This uncertainty was determined by repeating the full analysis using different selections for the cuts on the associated tracks with respect to the usual selection (TPC only tracks with at least 2 points in the ITS). The alternative selections were: pure TPConly selection, meaning TPC tracks with no requests on the number of hits in the ITS, and TPC+ITS selection, which requires filterbit 4 with, in addition, at least 3 points in the ITS, ITS refit and a hit in at least an SPD layer. The ratios of the azimuthal correlation distributions with different sets of tracks selection over distributions with standard selection were evaluated, and are shown in Figures 35 and 36 for  $D^0$ -h correlations. Their values were used to determine a systematic uncertainty, which as the previous ones could be assigned flat in  $\Delta\phi$ , and which was estimated of 3% in all the ranges of  $p_T$  analyzed.

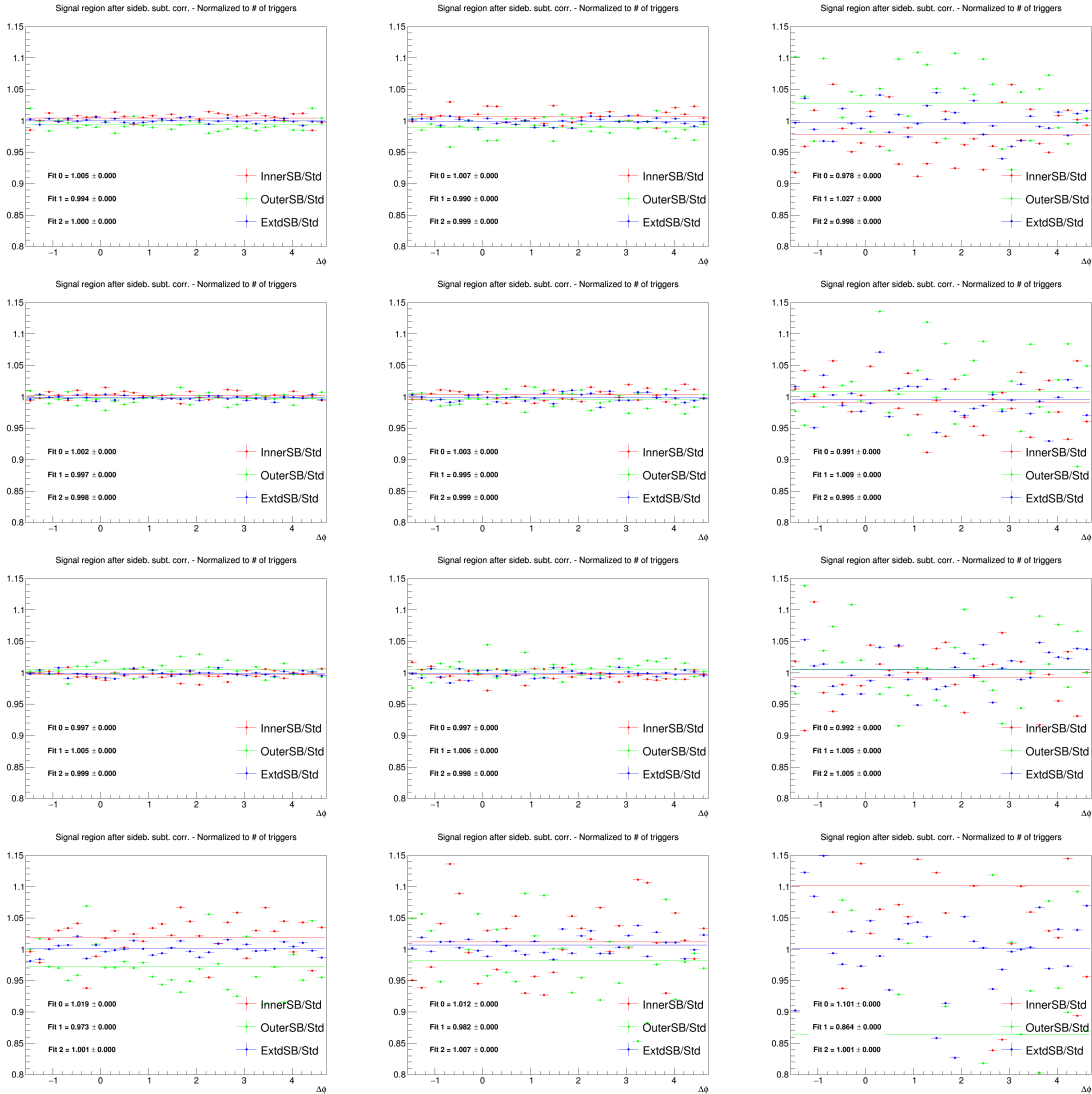


**Figure 26:** Ratios of D<sup>0</sup>-h correlation plots obtained by changing the sideband ranges over those obtained with standard sideband ranges. Rows: p<sub>T</sub>(D<sup>0</sup>) 3-5, 5-8, 8-16, 16-24 GeV/c. In each row, the panels show the associated track p<sub>T</sub> ranges 0.3-1, 1-2, >3 GeV/c, respectively.

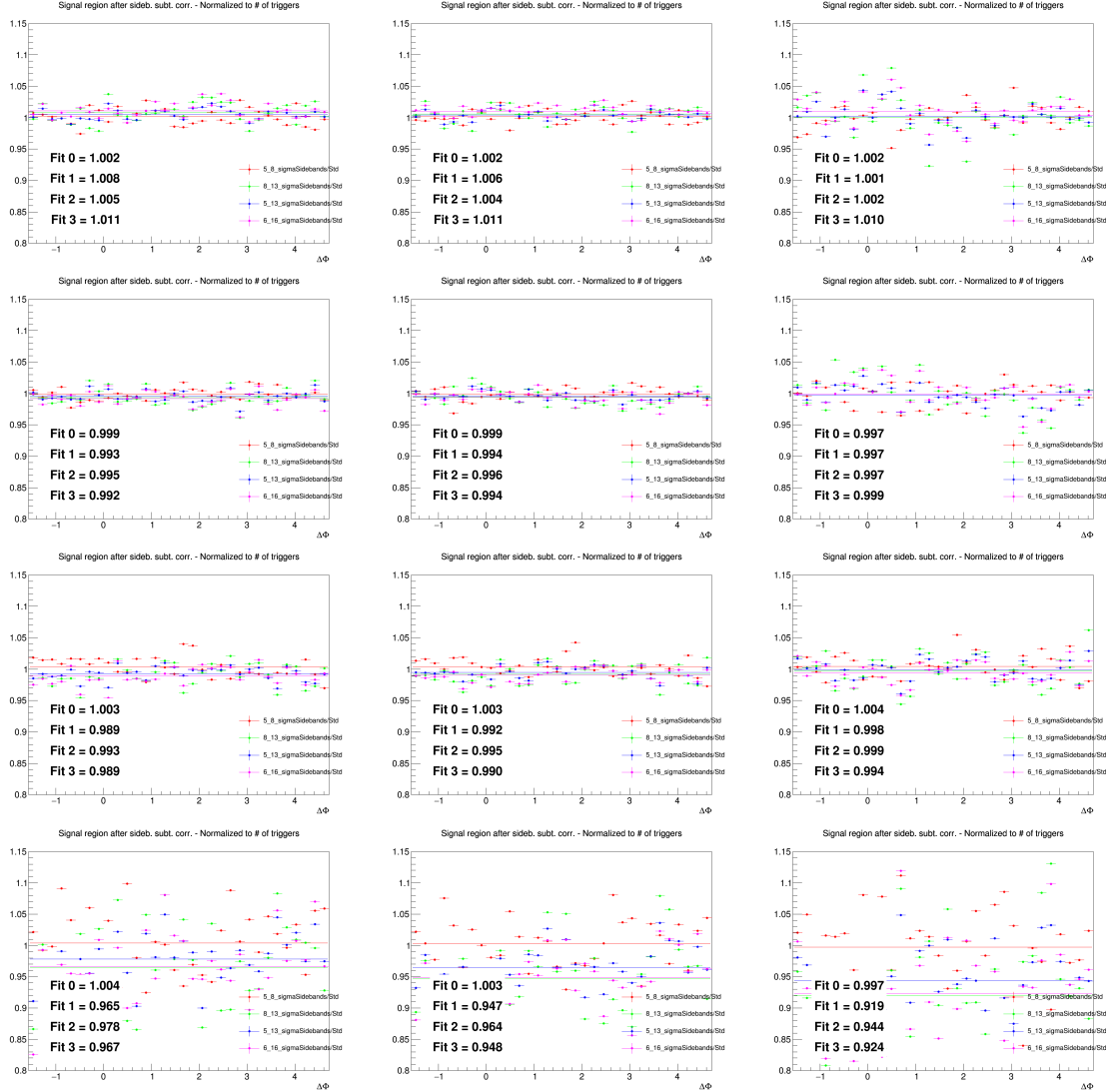


**Figure 27:** Ratios of  $D^*-h$  correlation plots obtained by changing the sideband ranges over those obtained with standard sideband ranges. Rows:  $p_T(D^*)$  3-5, 5-8, 8-16, 16-24 GeV/ $c$ . In each row, the panels show the associated track  $p_T$  ranges 0.3-1,  $>0.3$  GeV/ $c$  and  $>1$  GeV/ $c$ , respectively.

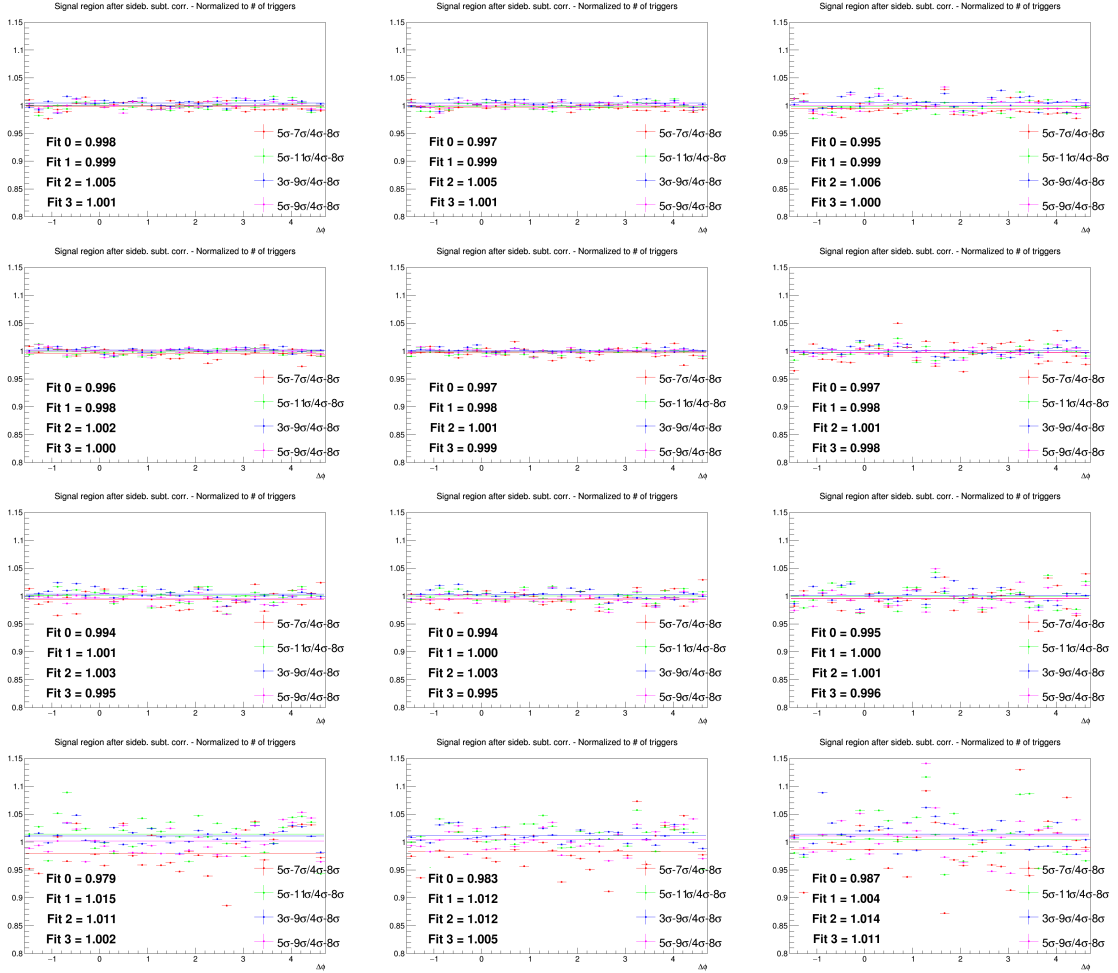


**Figure 28:** Ratios of  $D^+ - h$  correlation plots obtained by changing the sideband ranges over those obtained with standard sideband ranges. Rows:  $p_T(D^+)$  3-5, 5-8, 8-16, 16-24 GeV/ $c$ . In each row, the panels show the associated track  $p_T$  ranges 0.3-1,  $>0.3$  GeV/ $c$  and  $>1$  GeV/ $c$ , respectively.

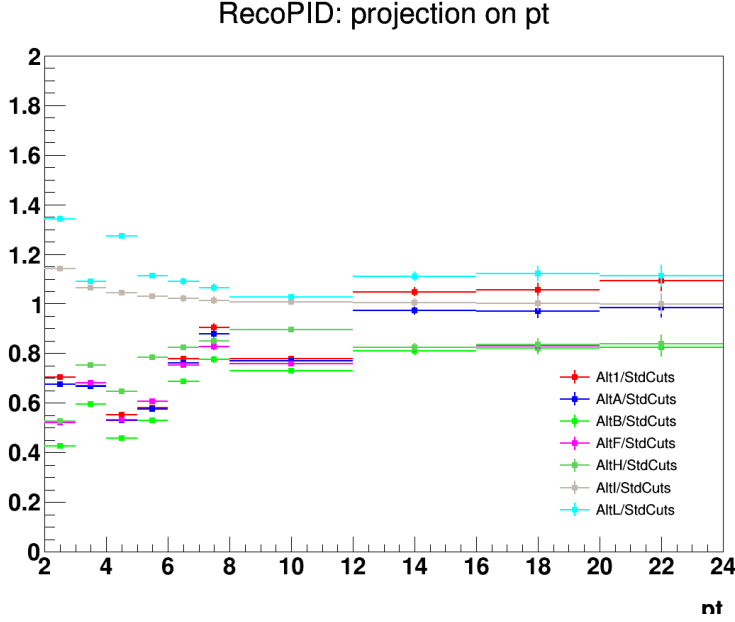


**Figure 29:** Ratio of  $D^0$  efficiencies with alternate cut variations w.r.t. the standard cut used for the analysis.

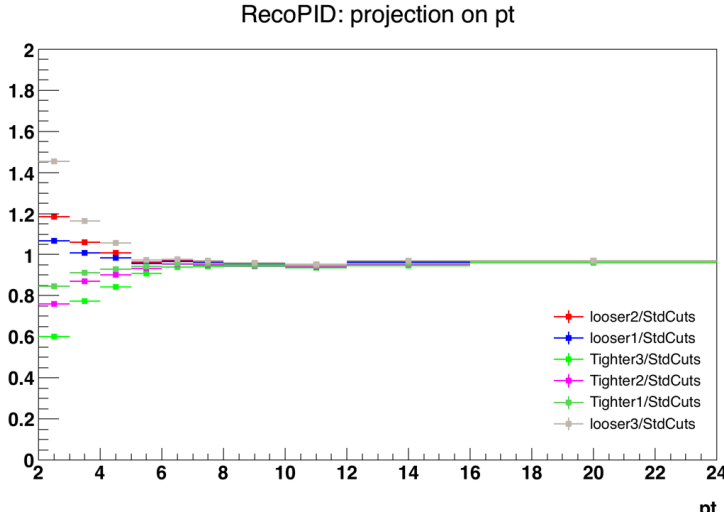


**Figure 30:** Ratio of  $D^{*+}$  efficiencies with alternate cut variations w.r.t. the standard cut used for the analysis.

#### 584 4.5 Uncertainty on secondary particle contamination

585 Secondary particles, i.e. particles coming from strange hadrons decays or particles produced in interactions with the material, are expected to be tagged and removed by means of a distance of closest approach (DCA) from primary vertex cut. The uncertainty arising from the residual contamination of 586 secondary tracks can be estimated from a Monte Carlo study, at reconstructed level. The number of 587 primary/secondary tracks which are accepted/rejected from the DCA cut was determined for different 588 values of the DCA selection, and the correlation distributions for the various cases were evaluated. The 589 variations were done in the  $xy$  direction, where the DCA resolution is better, and the following cases 590 were tried (in addition to the default 1 cm cut): 0.1 cm, 0.25 cm, 0.5 cm, filtering DCA cut (i.e. 2.4 cm). 591

592 Figure 37 shows the amount of secondary tracks which are accepted by the DCA cut, over the total 593 number of tracks (primary and secondary) accepted by the selection, for the various DCA selections that 594 were tried. This is shown for the exemplary case of  $5 < p_T < 8 \text{ GeV}/c$  (there's no  $p_T(D)$  dependence) and 595 as a function of the associated track  $p_T$  ranges. Hence, this quantity represents the residual contamination 596

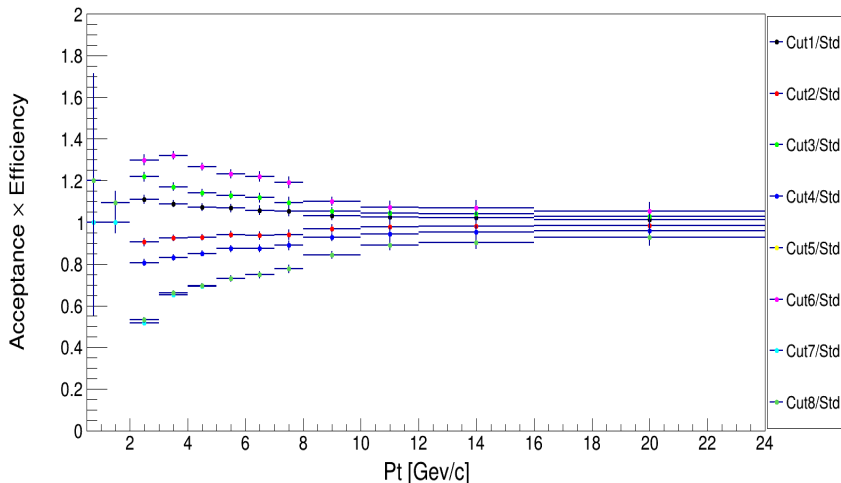


**Figure 31:** Ratio of  $D^+$  efficiencies with alternate cut variations w.r.t. the standard cut used for the analysis.

of secondary tracks in our reconstructed track sample. From these values, the corresponding primary track purities (1-contamination) were extracted, in each of the momentum ranges. It was also verified that, for all the cut selections, the  $\Delta\phi$  distributions of the residual contaminations were flat within 1%.

As a second step of the procedure to verify the DCA cut stability, the  $D^0$ -h data analysis was performed with all the different DCA selection (each time with the proper tracking efficiency map). After having extracted the correlation distributions, these were rescaled for the corresponding purities and compared with the purity-corrected correlation distributions obtained with the standard DCA selection. The ratios of the alternate selections over the standard selection, after the purity correction of both, are shown in Figures 38 and 39.

The ratios show a flat trend along the  $\Delta\phi$  axis and, in general, a discrepancy from the value of 1 of no more than 3% (the worst case being the 0.3-1 GeV/c range for the associated track). Hence, a flat and symmetric 3% systematical uncertainty on the evaluation of the secondary contamination was assigned on the base of this check in 0.3-1 GeV/c, reduced to 2.5% in  $> 0.3$  GeV/c and to 1.5% for the other ranges. This amount also covers possible biases in the estimation of the purity (the  $\Delta\phi$  distribution of the residual contamination is always contained inside 1%, as previously said).

## 4.6 Uncertainty on feed-down subtraction

As described in the 3.3.5 section, the feed-down subtraction from the data distributions is performed by means of simulation templates of  $B \rightarrow D$ -h correlation distributions from PYTHIA6 generator, with Perugia2011 tune, and considering the central value of  $f_{\text{prompt}}$  to extract the feed-down D-meson contribution. In order to evaluate a systematic uncertainty on this procedure, the feed-down subtraction procedure was repeated considering, together with PYTHIA6+Perugia2011 templates, also PYTHIA6+Perugia2010 and PYTHIA8 simulations. In each case, not only the central value of the measured  $f_{\text{prompt}}$  was considered to rescale the distributions, but also the maximum and minimum values of its total uncertainty.

Then, the envelope of nine the different cases obtained by varying the templates and the  $f_{\text{prompt}}$  assumption was considered, and a value of the systematics defined as the envelope spread divided by  $\sqrt{3}$  was taken as systematic uncertainty. This uncertainty was assumed uncorrelated among the different  $\Delta\phi$  points.

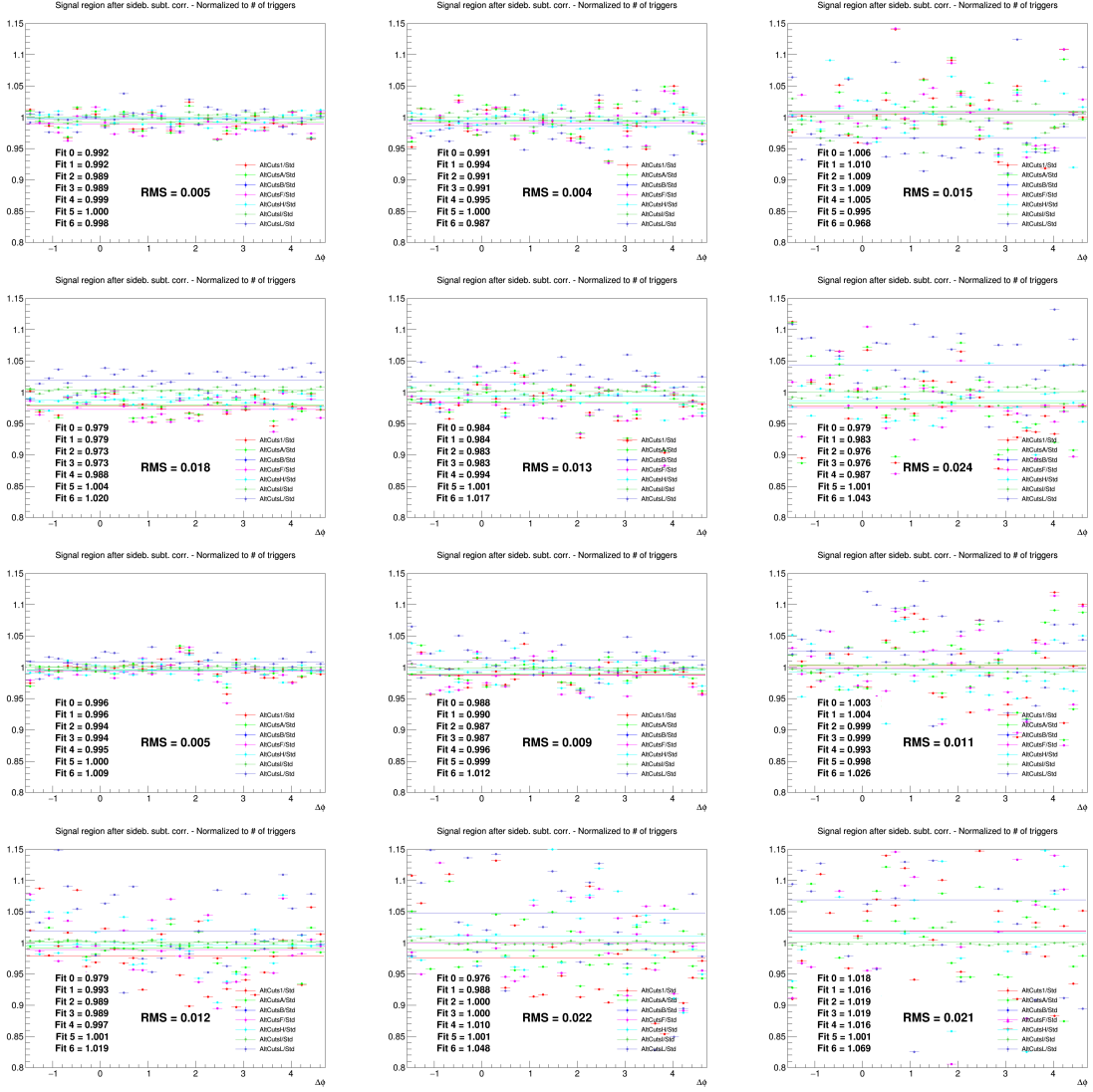


**Figure 32:** Ratios of  $D^0$ - $h$  correlation plots obtained with alternate D-meson cut sets over those obtained with standard selection. Rows:  $p_T(D^0)$  3-5, 5-8, 8-16, 16-24 GeV/ $c$ . In each row, the panels show the associated track  $p_T$  ranges 0.3-1, 1-2, 2-3 GeV/ $c$ , respectively.

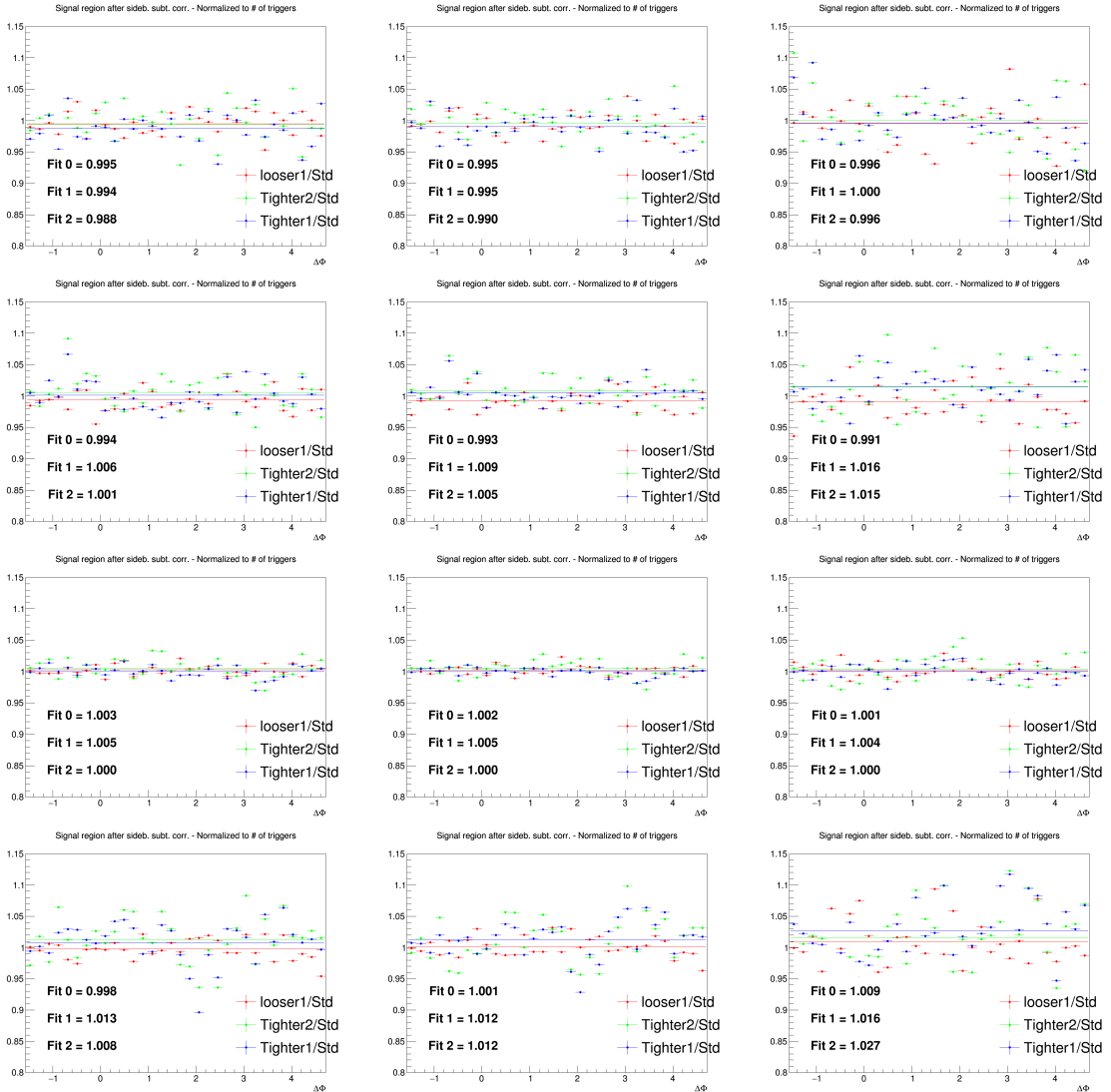


**Figure 33:** Ratios of  $D^{*+} - h$  correlation plots obtained with alternate D-meson cut sets over those obtained with standard selection. Rows:  $p_T(D^{*+})$  3-5, 5-8, 8-16, 16-24  $\text{GeV}/c$ . In each row, the panels show the associated track  $p_T$  ranges 0.3-1,  $>0.3 \text{ GeV}/c$ ,  $>1 \text{ GeV}/c$ , respectively.

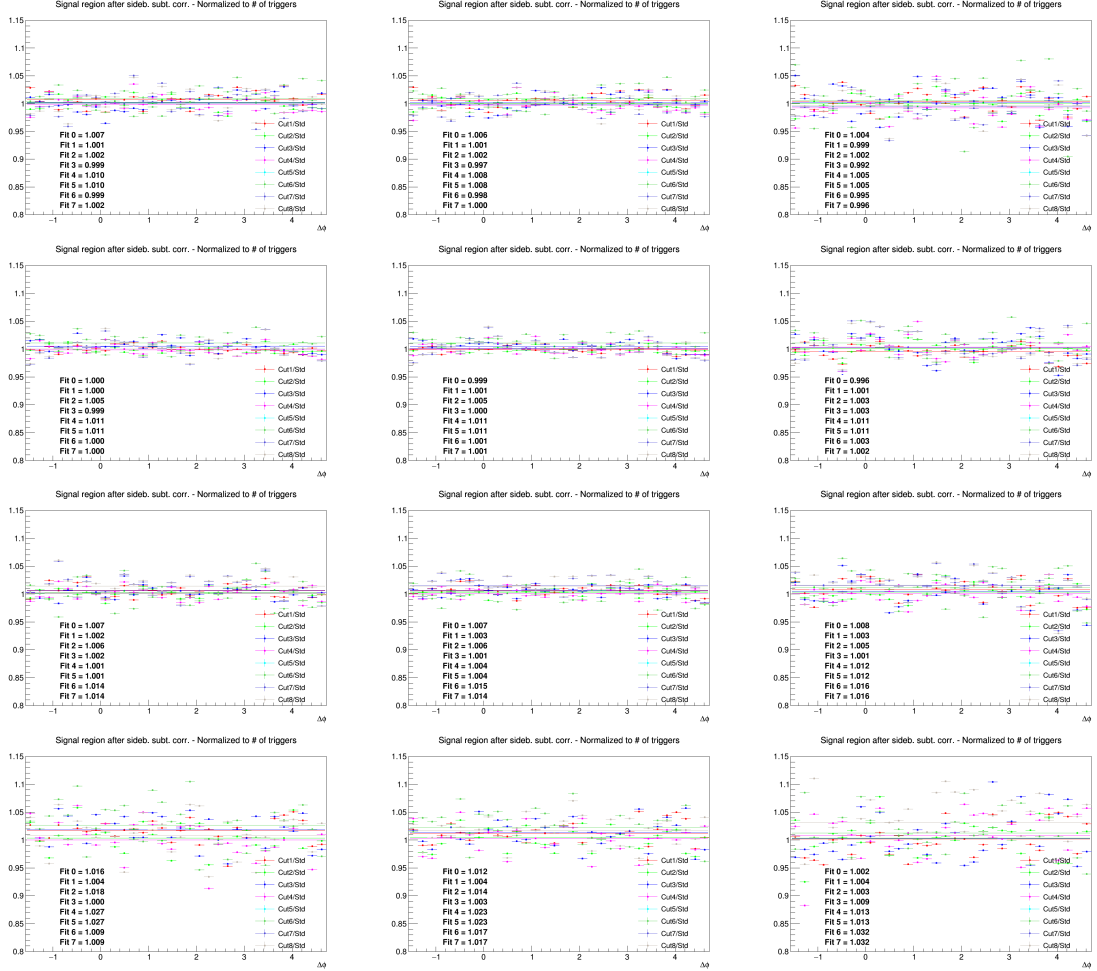


**Figure 34:** Ratios of D<sup>+</sup> - h correlation plots obtained with alternate D-meson cut sets over those obtained with standard selection. Rows:  $p_T(D^+)$  3-5, 5-8, 8-16, 16-24 GeV/c. In each row, the panels show the associated track  $p_T$  ranges 0.3-1, >0.3 GeV/c, >1 GeV/c, respectively.



**Figure 35:** Ratios of  $D^0$ -h correlation plots obtained with different associated tracks filtering selections. First 6 plots:  $p_T(D)$  3-5 GeV/ $c$ , next 6 plots:  $p_T(D)$  5-8 GeV/ $c$ . Each bunch of 6 plots has  $p_T(\text{assoc})$  of  $>0.3$ , 0.3-1,  $>1$ , 1-2, 2-3,  $<3$  GeV/ $c$ , respectively.

## 624 4.7 Uncertainty on correction for the bias on $B$ to $D$ decay topologies

625 The evaluation of this systematic uncertainty was already explained in Section 3.3.3. For each of the  
 626 five data points close to the center of the near-side peak, which are affected by the bias, a bilateral and  
 627 symmetric uncertainty of amplitude  $|C(\Delta\phi)_{\text{corr}} - C(\Delta\phi)_{\text{raw}}|/\sqrt{12}$  was assigned.

628 This because the uncorrected data points are expected to be the extreme (with the current D-meson  
 629 selection, the bias is always upwards at the centre of the peak, and always upwards on its sides). We  
 630 then assume that, if the correction is properly evaluated, the corrected data points are at the centre of the  
 631 possible spread of the true unbiased results. In this case, the span of the possible true results (in case  
 632 of underestimation/overestimation of the bias) goes from the uncorrected data points to its symmetric  
 633 value, with respect to the corrected data point, on the other direction. If this distribution is uniform,  
 634 and constrained by these two values, the  $1\sigma$  confidence region for the position of the is in a bilateral  
 635  $|C(\Delta\phi)_{\text{corr}} - C(\Delta\phi)_{\text{raw}}|/\sqrt{12}$  window, centered on the  $C(\Delta\phi)_{\text{corr}}$  points.



**Figure 36:** Ratios of  $D^0$ - $h$  correlation plots obtained with different associated tracks filtering selections. First 6 plots:  $p_T(D) 8-16 \text{ GeV}/c$ , next 6 plots:  $p_T(D) 16-24 \text{ GeV}/c$ . Each bunch of 6 plots has  $p_T(\text{assoc})$  of  $>0.3$ ,  $0.3-1$ ,  $>1$ ,  $1-2$ ,  $<3 \text{ GeV}/c$ , respectively.

636 This source of uncertainty was assumed uncorrelated among the  $\Delta\phi$  points.

#### 637 4.8 Summary table

638 A summary of the  $\Delta\phi$ -correlated uncertainties affecting the correlation distributions is show in Figure  
639 40. They are the S and B extraction uncertainty, the background shape uncertainty, the cut variation  
640 uncertainty, the tracking efficiency uncertainty and the secondary particle contamination uncertainty.

641 The overall amount of  $\Delta\phi$ -correlated uncertainties is about 5-6% (depending on the  $p_T$  bin) for the single  
642 D-meson cases; when evaluating the averages of the distributions (see next section), this uncertainty  
643 shrinks to 4-5%. This uncertainty is a global scale factor of the distributions, and is quoted as a label in  
644 the plots.

645 The systematics uncertainties from feed-down subtraction and  $B \rightarrow D$  decay topology bias, instead are  
646  $\Delta\phi$  dependent, and are hence reported as uncorrelated boxes in the plots. They do not amount to more  
647 than 4%, in every bin of all the kinematic ranges studied.

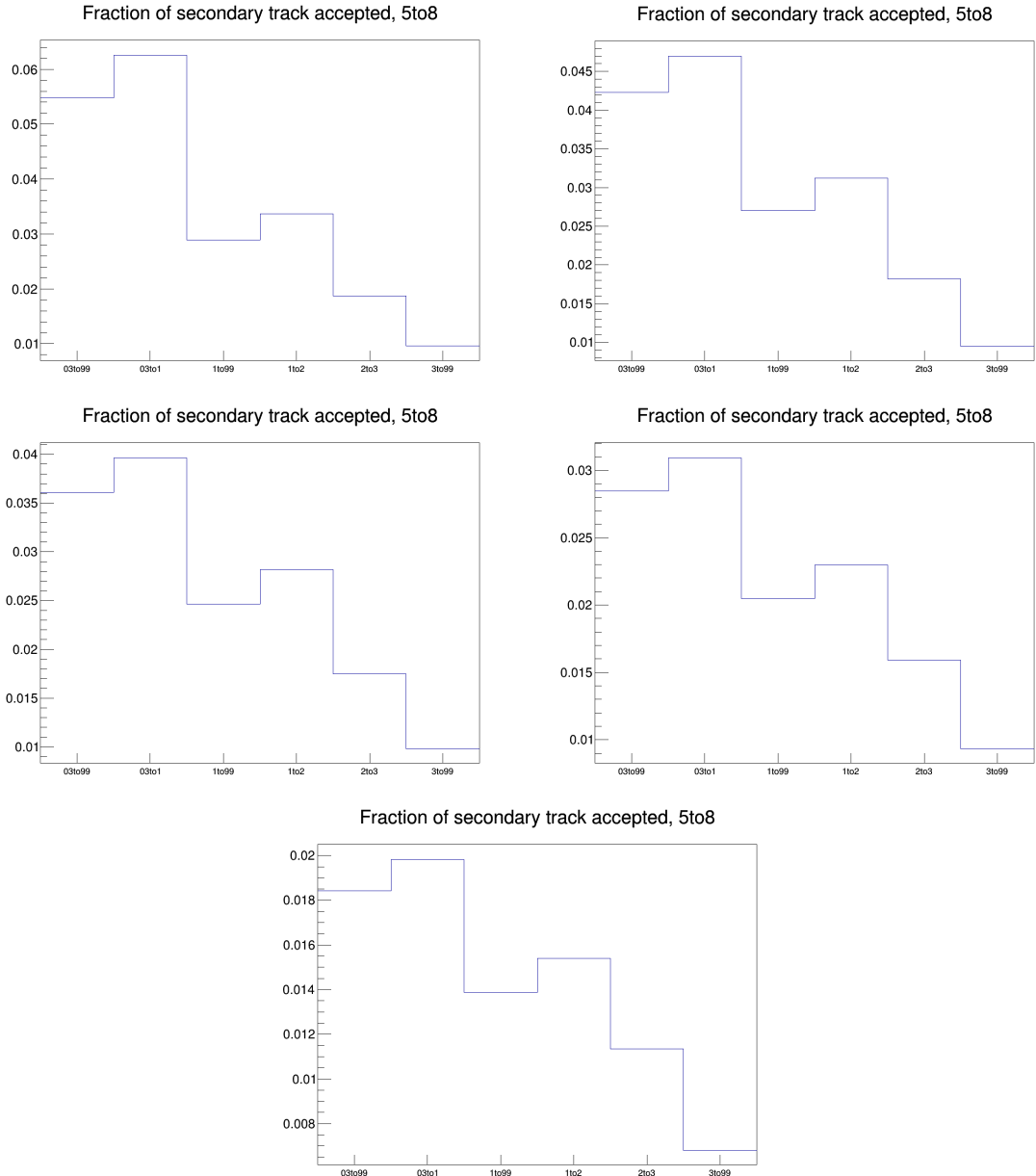


**Figure 37:** Secondary track contamination as a function of the associated track  $p_T$ , for the various DCA selections tried. The plots are ordered from the loosest to the tightest selection, i.e.:  $\text{DCA}(xy) < 2.4 \text{ cm}$ ,  $< 1 \text{ cm}$ ,  $< 0.5 \text{ cm}$ ,  $< 0.25 \text{ cm}$ ,  $< 0.1 \text{ cm}$ .

## 648 5 Results

### 649 5.1 Comparing the three D meson correlation distributions

650 To check the compatibility of three D meson analyses, Figure 41 shows the corrected azimuthal corre-  
 651 lation distributions (except for the feed-down subtraction and the secondary contamination removal) for  
 652  $D^0\text{-}h$ ,  $D^{*+}\text{-}h$  and  $D^+\text{-}h$ , in each column, on the data sample used in the analysis. Results are shown for  
 653  $3 < D p_T < 5 \text{ GeV}/c$ ,  $5 < D p_T < 8 \text{ GeV}/c$ ,  $8 < D p_T < 16 \text{ GeV}/c$  and  $16 < D p_T < 24 \text{ GeV}/c$  with  
 654 associated tracks  $p_T > 0.3$ ,  $p_T > 1$ ,  $0.3 < p_T < 1 \text{ GeV}/c$ ,  $1 < p_T < 2 \text{ GeV}/c$ ,  $2 < p_T < 3 \text{ GeV}/c$  and  
 655  $p_T > 3 \text{ GeV}/c$ .

656 Figures 42, 43, 44, 45 show the superimposed correlation distributions from the single-meson analyses

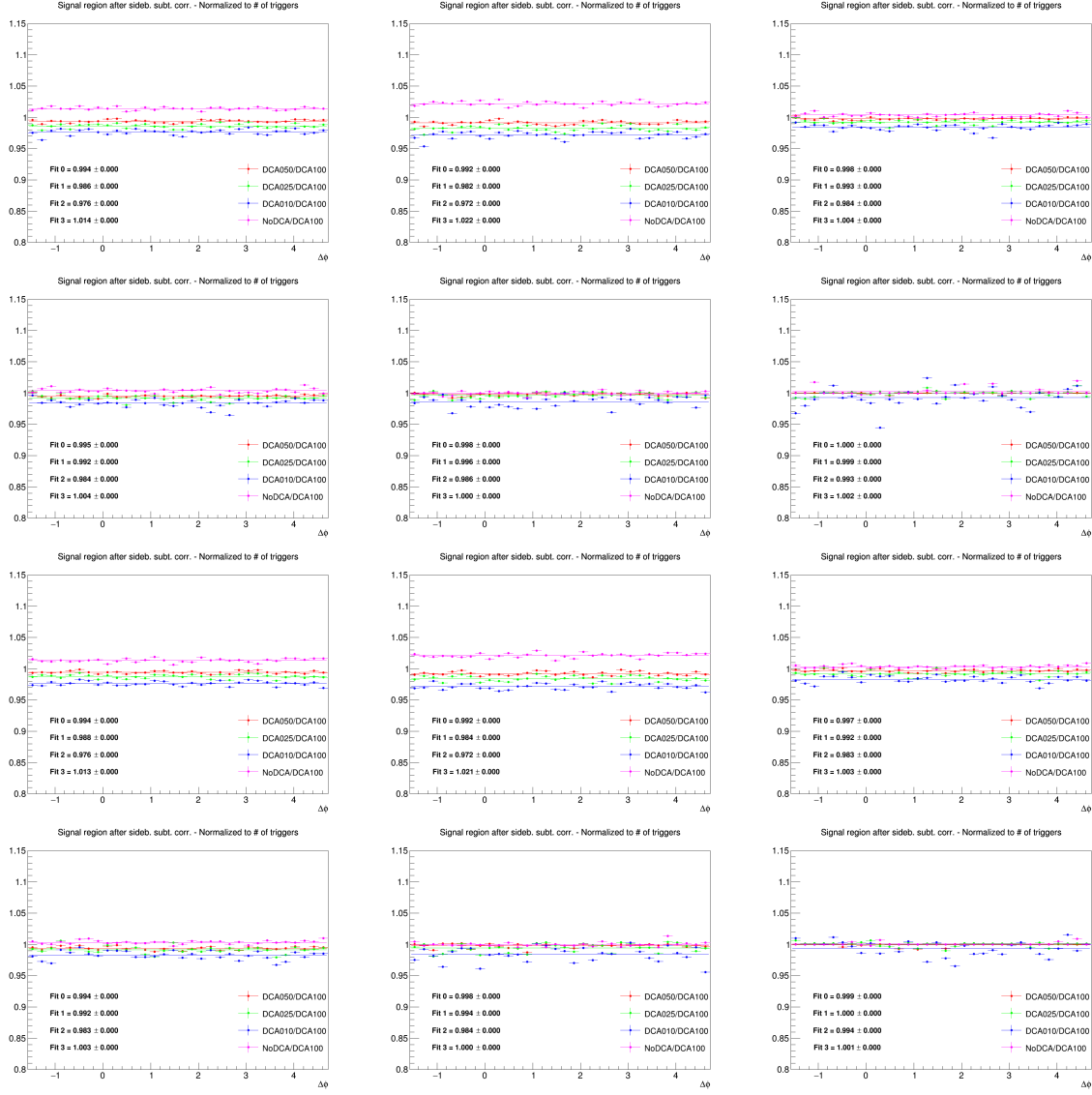


**Figure 38:** Ratios of correlation plots (with  $D^0$  as trigger meson) obtained with different associated DCA selections, after purity correction. First 6 plots:  $p_T(D)$  3-5 GeV/ $c$ , next 6 plots:  $p_T(D)$  5-8 GeV/ $c$ . Each bunch of 6 plots has  $p_T(\text{assoc})$  of >0.3, 0.3-1, >1, 1-2, 2-3, <3 GeV/ $c$ , respectively.

657 (same plots as previous figure) for better visualize the agreement among the different D-meson species  
 658 results.

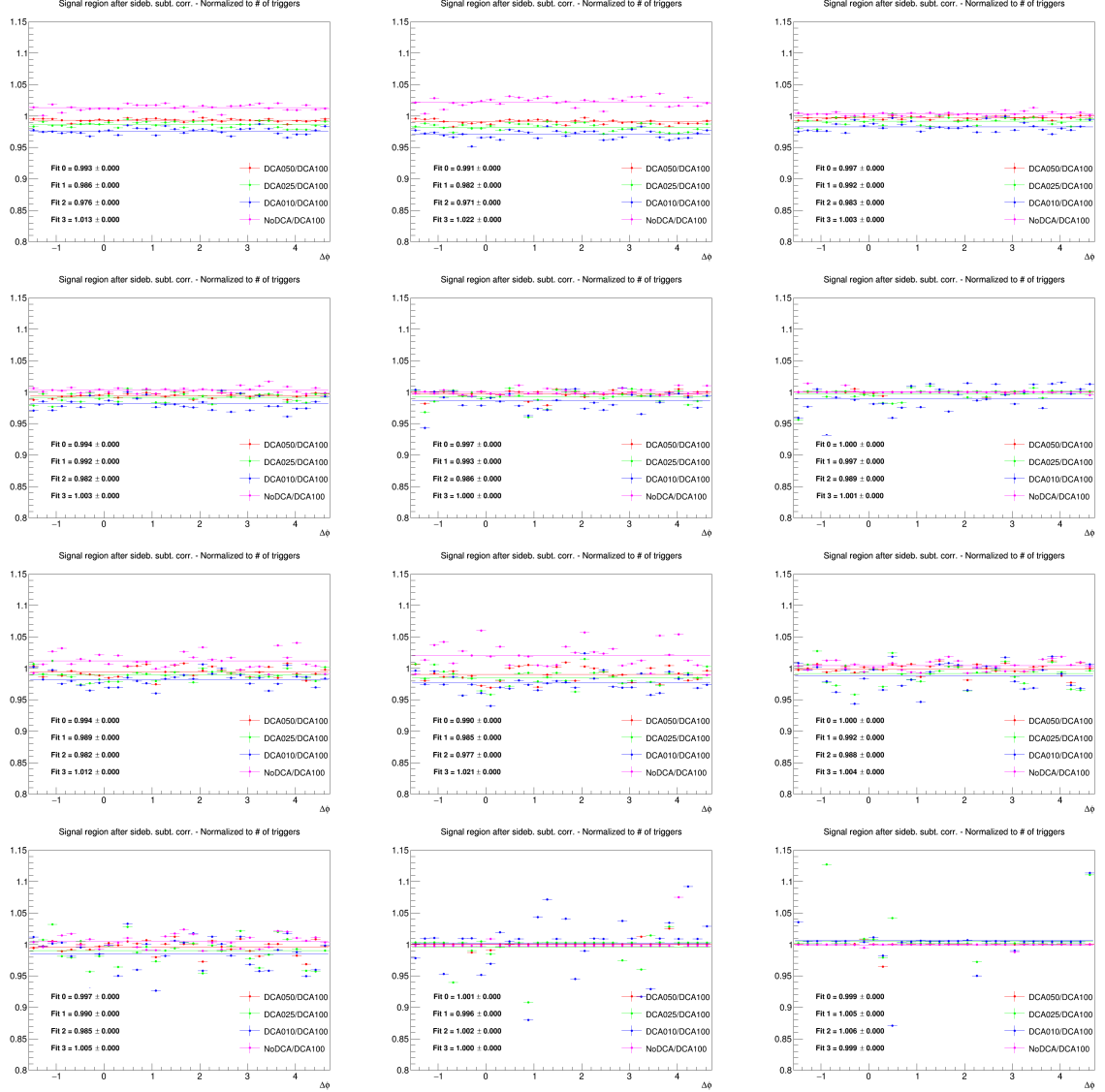


**Figure 39:** Ratios of correlation plots (with  $D^0$  as trigger meson) obtained with different associated DCA selections, after purity correction. First 6 plots:  $p_T(D) 8\text{-}16 \text{ GeV}/c$ , next 6 plots:  $p_T(D) 16\text{-}24 \text{ GeV}/c$ . Each bunch of 6 plots has  $p_T(\text{assoc})$  of  $>0.3$ ,  $0.3\text{-}1$ ,  $>1$ ,  $1\text{-}2$ ,  $2\text{-}3$ ,  $<3 \text{ GeV}/c$ , respectively.

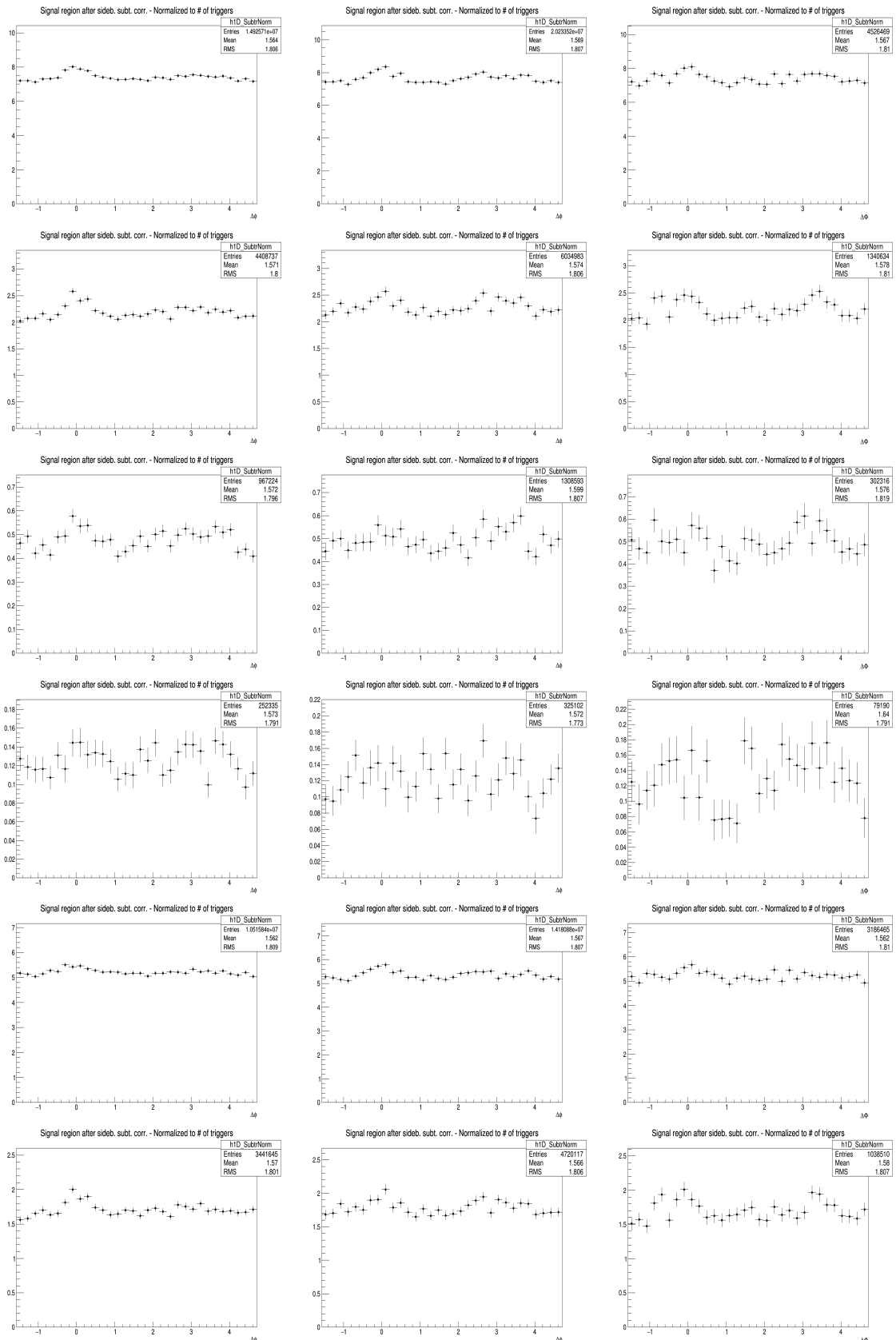
pPb Sample	$D^0$				$D^*$				$D^+$			
$D p_T$ Range (GeV/c)	3-5	5-8	8-16	16-24	3-5	5-8	8-16	16-24	3-5	5-8	8-16	16-24
<b>S and B Extraction</b>	1%	1%	1%	2%	1%	1%	1%	2%	1%	1%	1%	2%
<b>Background Correlation Shape</b>	1%	1%	1%	2.5%	1%	1%	1%	4%	1%	1%	1%	2%
<b>D meson Cut Variation</b>	2%	2%	2%	2%	1.5%	1.5%	1%	1%	1%	1%	1%	2%

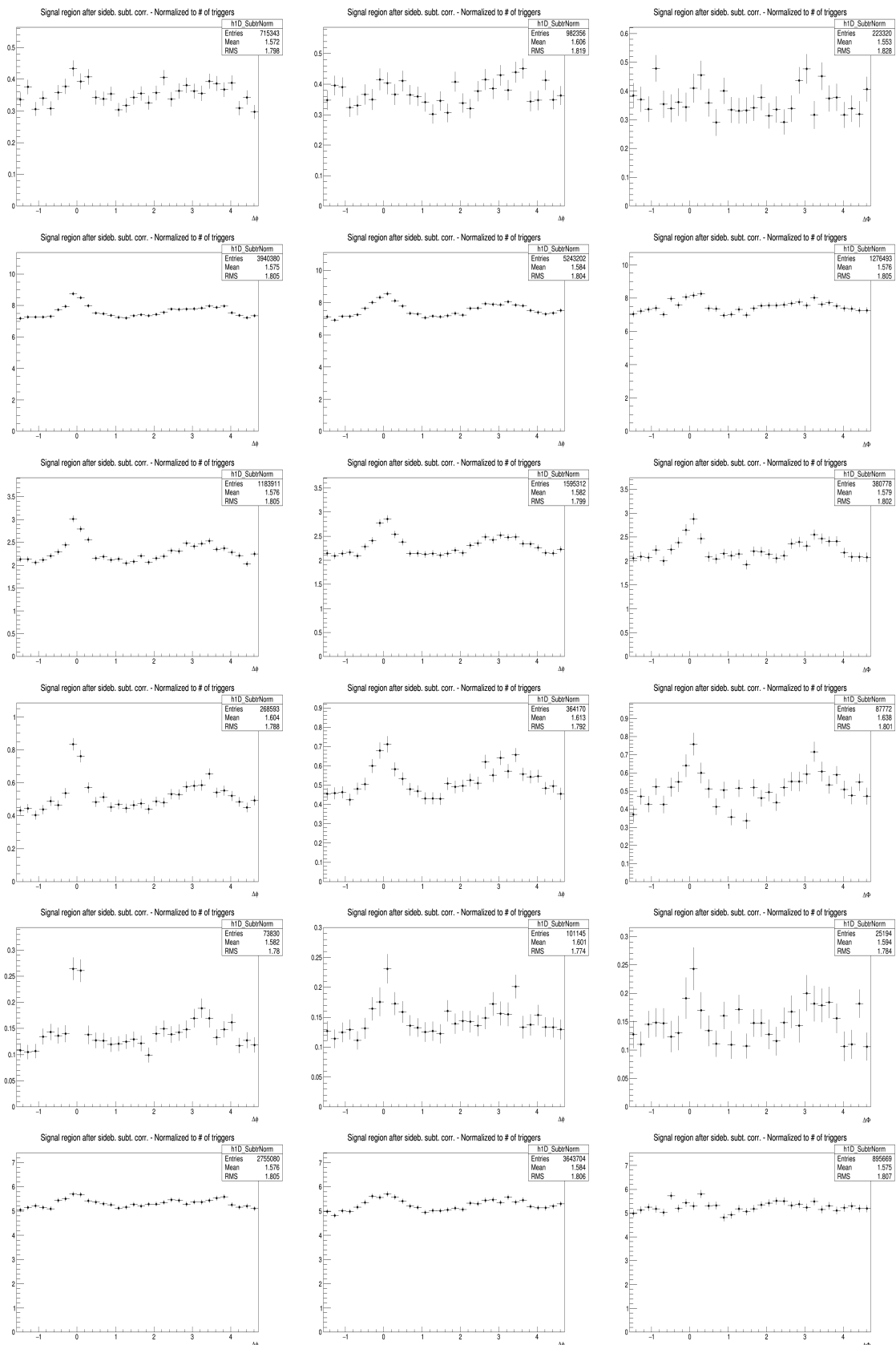
pPb Sample	$D^0, D^*$ and $D^+$ (common for all the $p_T(D)$ ranges)						
Assoc ( $p_T$ ) Ranges (GeV/c)	> 0.3	> 1.0	> 2.0	> 3.0	0.3-1.0	1.0-2.0	2.0-3.0
<b>Track Efficiency</b>	3.5%	3.5%	3.5%	3.5%	3.5%	3.5%	3.5%
<b>Purity</b>	2.5%	1.5%	1.5%	1.5%	3%	1.5%	1.5%

**Figure 40:** Summary of the  $\Delta\phi$ -correlated uncertainties associated to the correlation distributions, for three D-mesons, in the different kinematic ranges of D meson and hadrons.

## 5.1 Comparing the three D meson correlation distributions

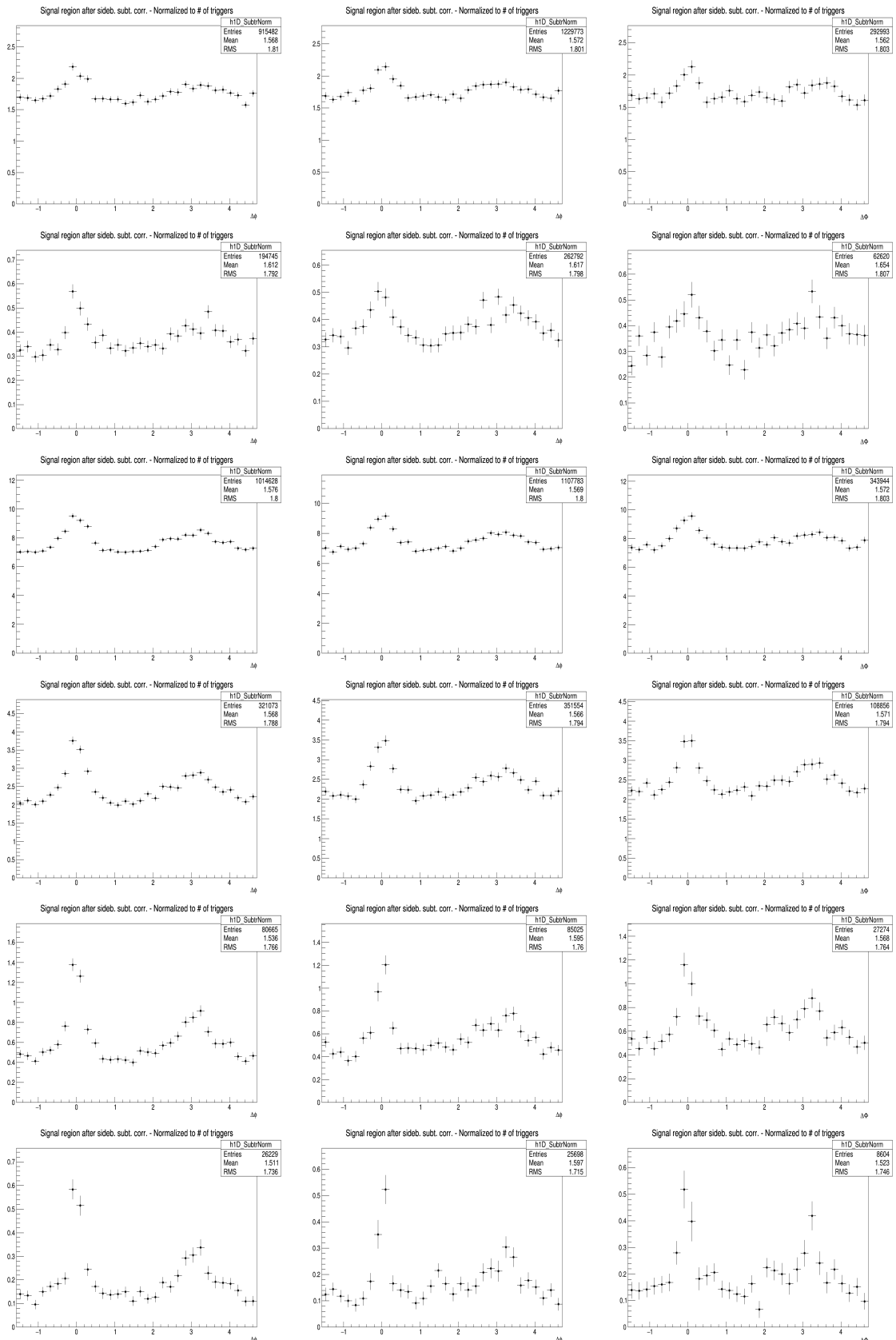
57

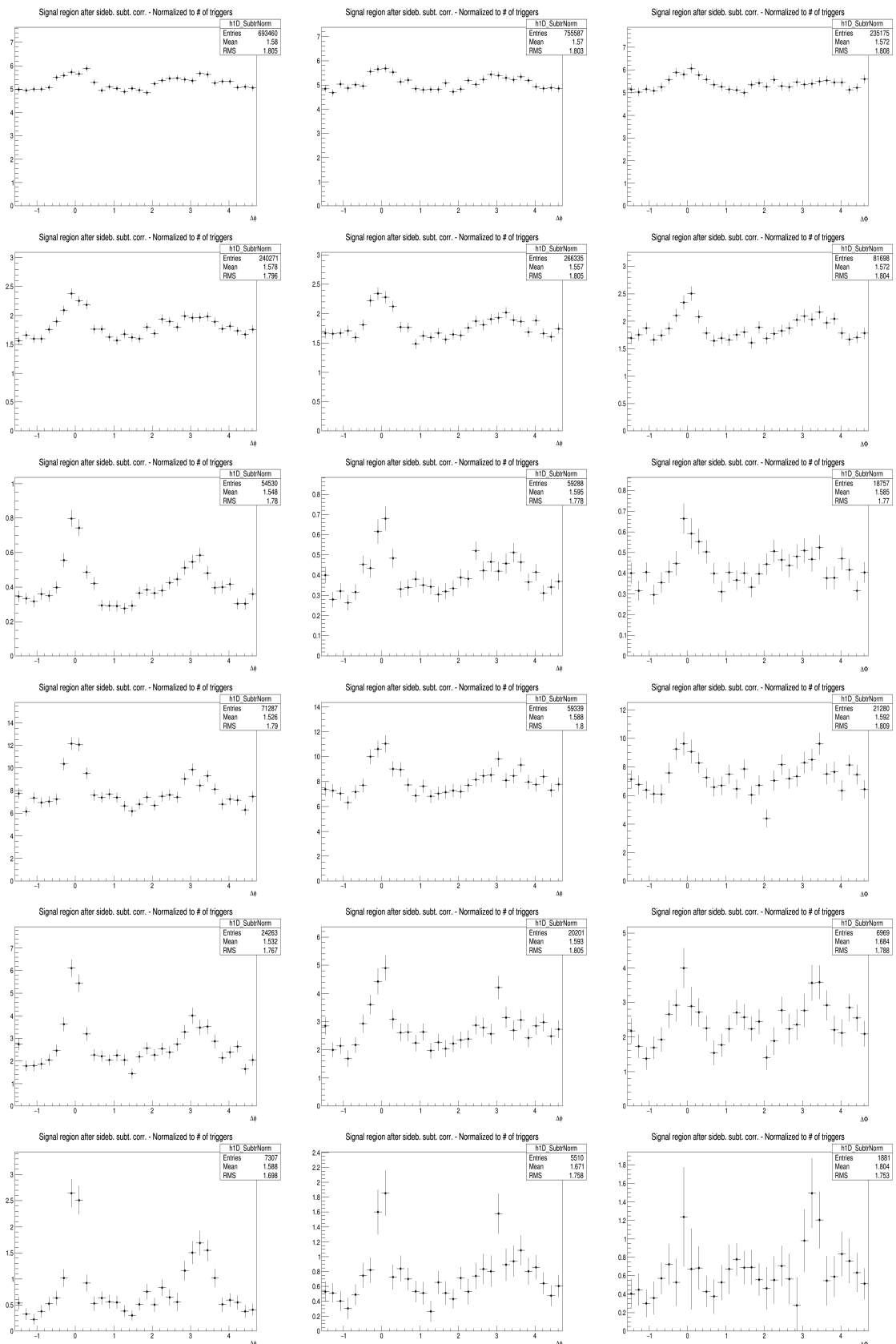




## 5.1 Comparing the three D meson correlation distributions

59





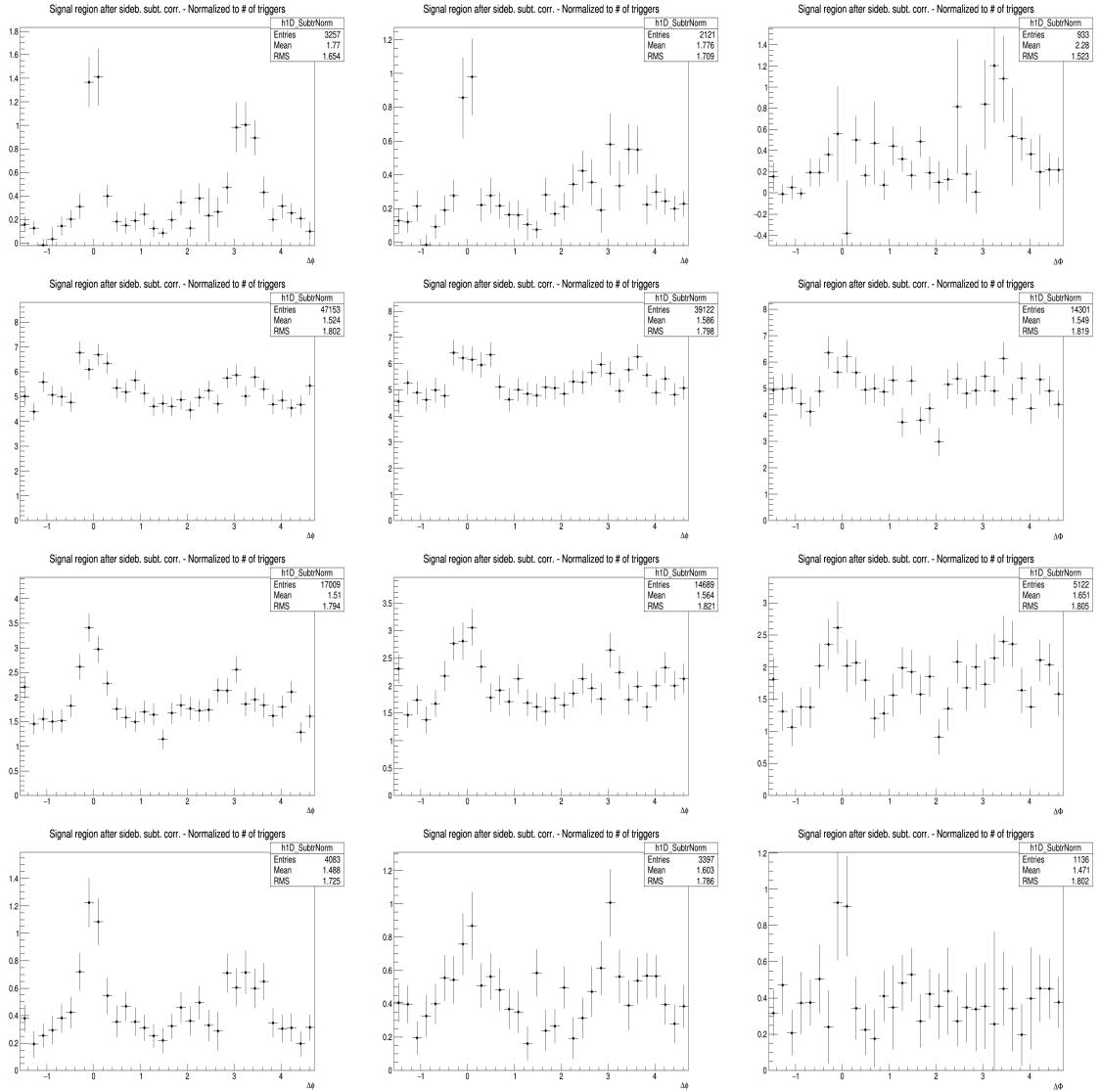


**Figure 41:** Corrected distribution of D-hadrons azimuthal correlations for the three species (apart from feed-down and purity), from analysis on the data sample, for the analyzed D-meson (**Column-Left:**  $D^0$ , **Column-Middle:**  $D^+$  and **Column-Right:**  $D^{*+}$ ) and different associated tracks  $p_T$  ranges (**Row 1-7:**  $3 < D_{pT} < 5 \text{ GeV}/c$ ,  $p_T$  (Assoc)  $> 0.3, > 1.0, > 2.0, > 3.0, 0.3-1.0, 1.0-2.0$  and  $2.0-3.0 \text{ GeV}/c$  respectively), (**Row 8-14:**  $5 < D_{pT} < 8 \text{ GeV}/c$ ,  $p_T$  (Assoc)  $> 0.3, > 1.0, > 2.0, > 3.0, 0.3-1.0, 1.0-2.0$  and  $2.0-3.0 \text{ GeV}/c$  respectively), (**Row 15-21:**  $8 < D_{pT} < 16 \text{ GeV}/c$ ,  $p_T$  (Assoc)  $> 0.3, > 1.0, > 2.0, > 3.0, 0.3-1.0, 1.0-2.0$  and  $2.0-3.0 \text{ GeV}/c$  respectively) and (**Row 22-28:**  $16 < D_{pT} < 24 \text{ GeV}/c$ ,  $p_T$  (Assoc)  $> 0.3, > 1.0, > 2.0, > 3.0, 0.3-1.0, 1.0-2.0$  and  $2.0-3.0 \text{ GeV}/c$  respectively)

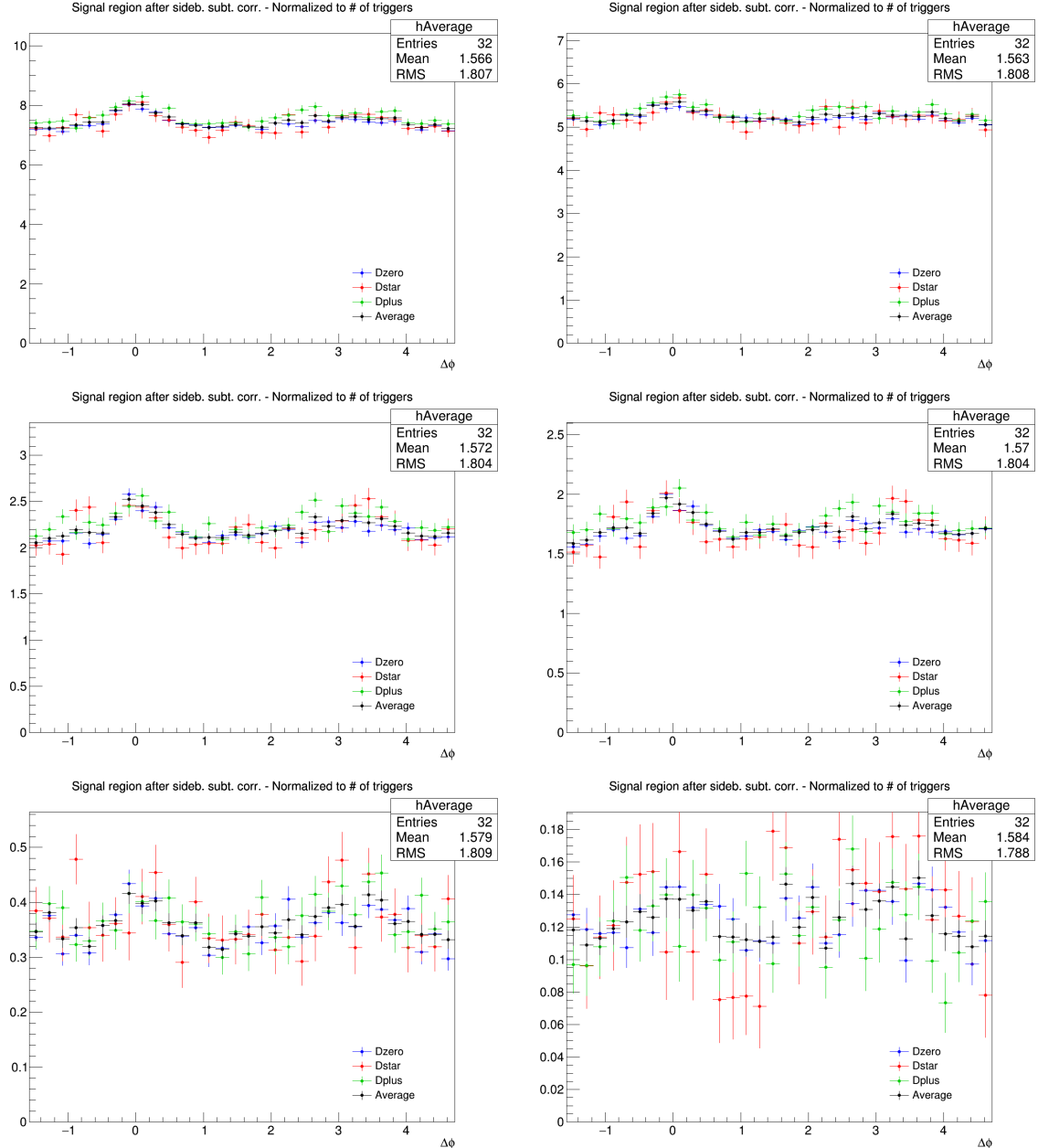


**Figure 42:** Superimposition of the corrected distribution of D-hadrons azimuthal correlations for the three species (apart from feed-down and purity), from analysis on the data sample, for the analyzed D-meson and different associated track  $p_T$  ranges, and D-meson  $p_T$  ranges (3-5 GeV/c on this page). **Panels from 1 to 6 of each page:**  $p_T$  (Assoc) > 0.3, 0.3-1.0, >1.0, 1.0-2.0, 2.0-3.0 and >3.0 GeV/c

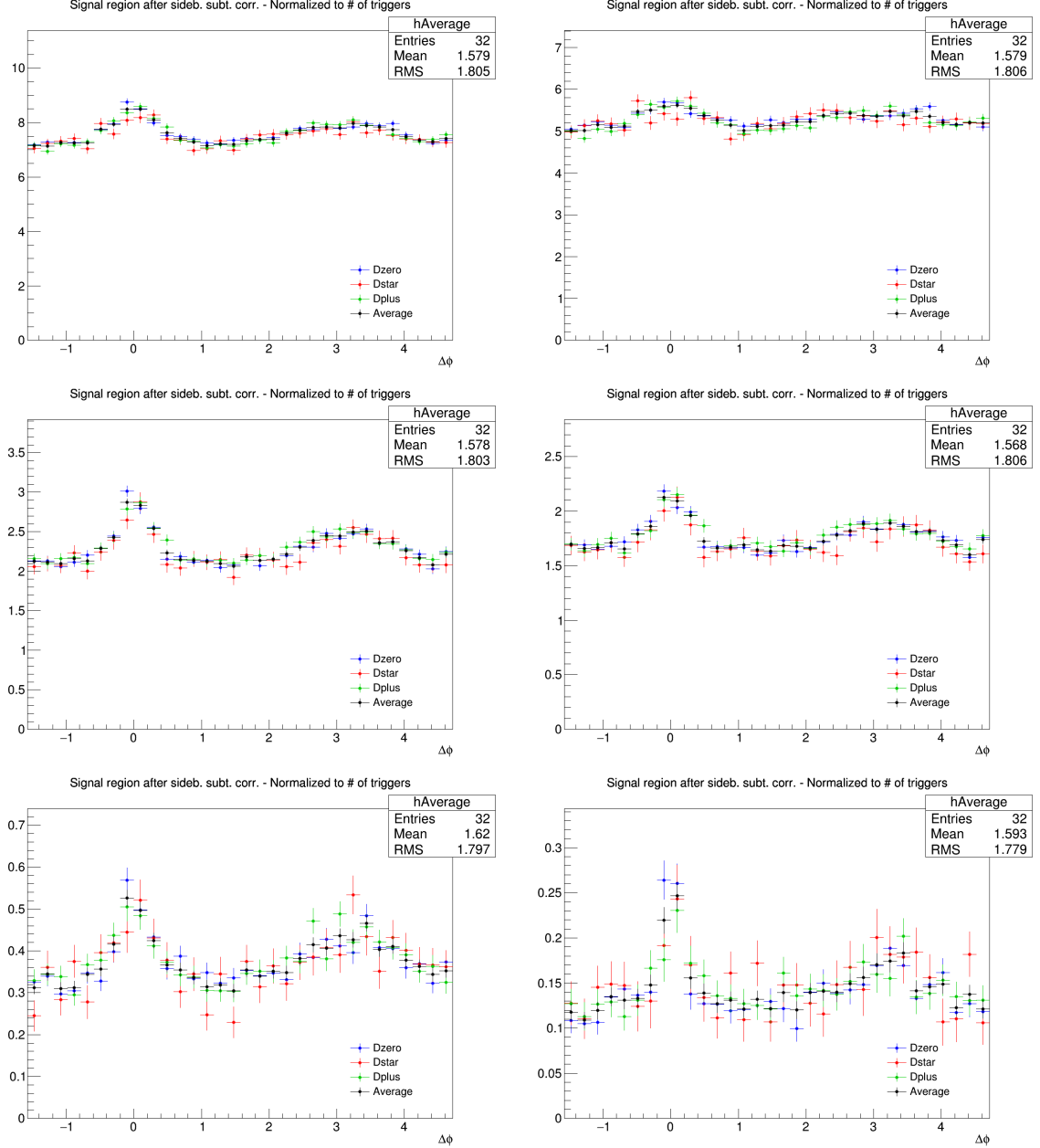


**Figure 43:** Superimposition of the corrected distribution of D-hadrons azimuthal correlations for the three species (apart from feed-down and purity), from analysis on the data sample, for the analyzed D-meson and different associated track  $p_T$  ranges, and D-meson  $p_T$  ranges (5-8 GeV/c on this page). **Panels from 1 to 6 of each page:**  $p_T(\text{Assoc}) > 0.3, 0.3-1.0, >1.0, 1.0-2.0, 2.0-3.0$  and  $>3.0 \text{ GeV}/c$

659 An agreement of the distributions from the three mesons within the uncertainties is found in all the  
660 kinematic ranges.

661 Despite being evaluated in the full  $2\pi$  range, the range of final results was then reduced to  $[0, \pi]$  radians,  
662 reflecting the points outside that range over the value of 0. This allowed to reduce the impact of statistical  
663 fluctuations on the data points (supposing equal statistics for a pair of symmetric bins, after the reflection  
664 the relative statistical uncertainty for the resulting bin is reduced by a factor  $1/\sqrt{2}$ ).

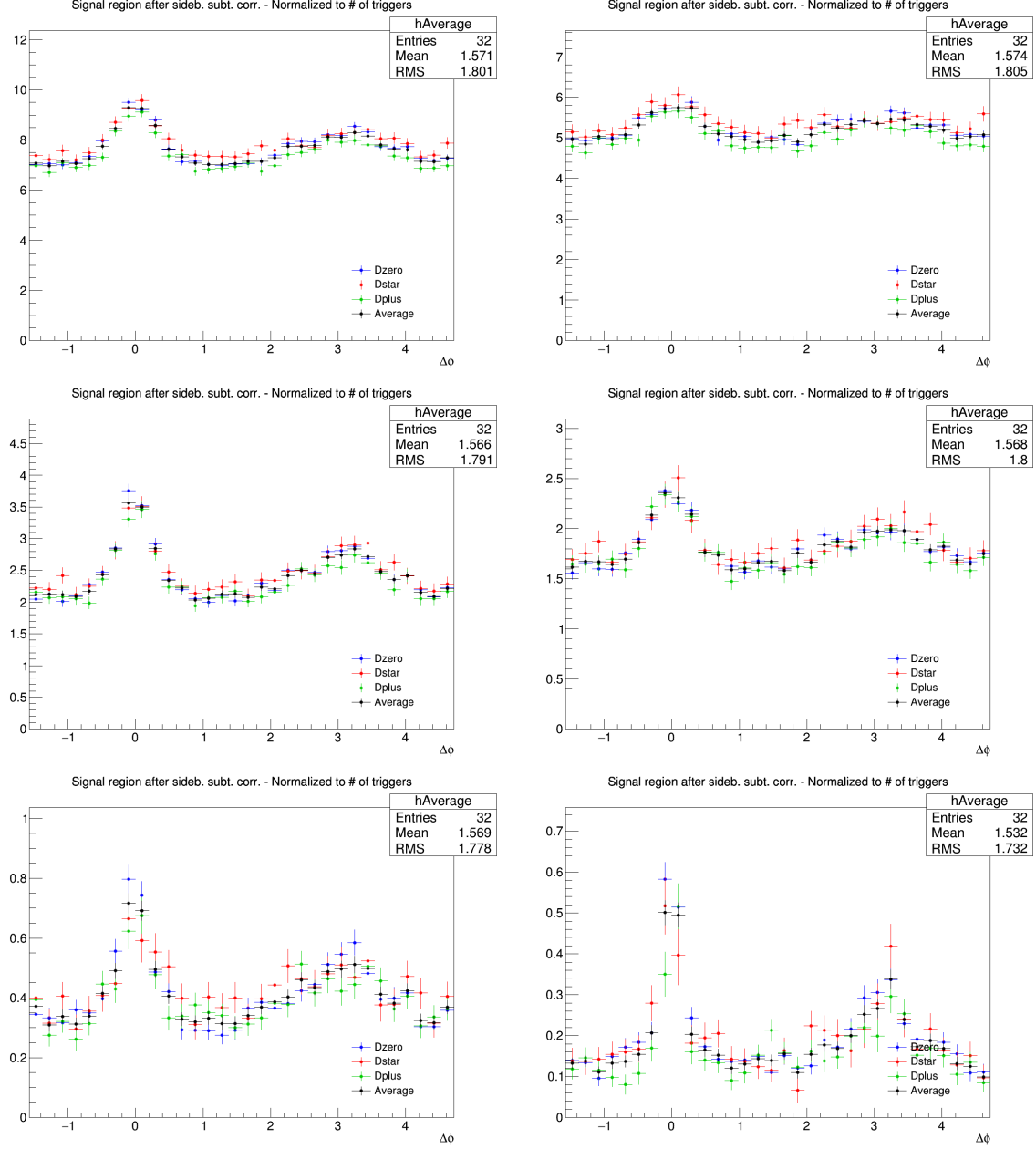


**Figure 44:** Superimposition of the corrected distribution of D-hadrons azimuthal correlations for the three species (apart from feed-down and purity), from analysis on the data sample, for the analyzed D-meson and different associated track  $p_T$  ranges, and D-meson  $p_T$  ranges (8-16 GeV/c on this page). **Panels from 1 to 6 of each page:**  $p_T$  (Assoc) > 0.3, 0.3-1.0, >1.0, 1.0-2.0, 2.0-3.0 and >3.0 GeV/c

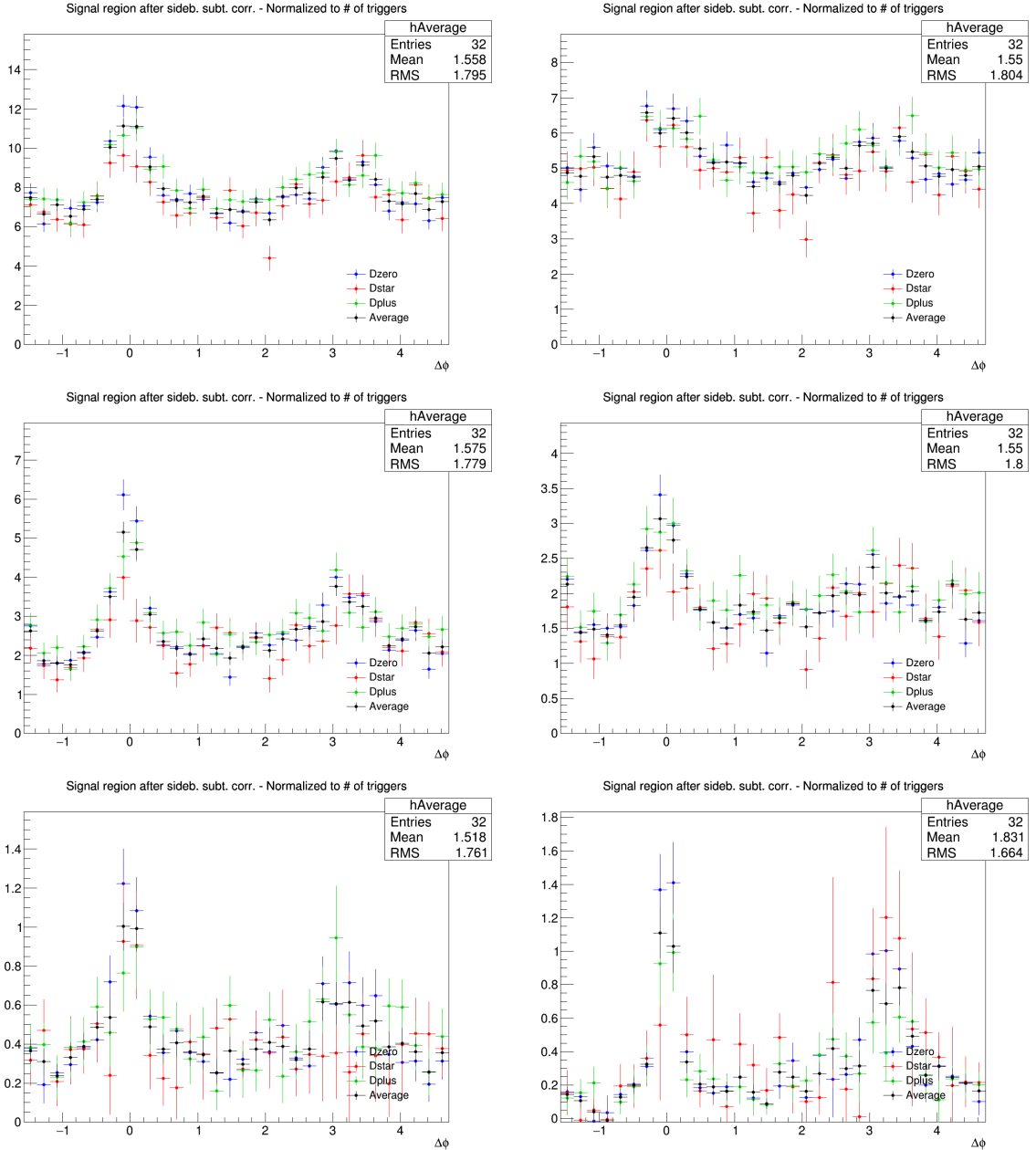


**Figure 45:** Superimposition of the corrected distribution of D-hadrons azimuthal correlations for the three species (apart from feed-down and purity), from analysis on the data sample, for the analyzed D-meson and different associated track  $p_T$  ranges, and D-meson  $p_T$  ranges (16-24 GeV/c on this page). **Panels from 1 to 6 of each page:**  $p_T(\text{Assoc}) > 0.3, 0.3-1.0, >1.0, 1.0-2.0, 2.0-3.0$  and  $>3.0 \text{ GeV}/c$

665 **5.2 Average of D<sup>0</sup>, D<sup>+</sup> and D<sup>\*+</sup> results**

666 Given the compatibility within the uncertainties among the D<sup>0</sup>, D<sup>+</sup> and D<sup>\*+</sup> azimuthal correlations, and  
 667 since no large differences are visible in the correlation distributions observed in Monte Carlo simulations  
 668 based on Pythia with Perugia0, 2010 and 2011 tunes<sup>1</sup>, it was possible to perform a weighted average  
 669 (eq. 5) of the azimuthal correlation distributions of D<sup>0</sup>, D<sup>+</sup> and D<sup>\*+</sup>, in order to reduce the overall  
 670 uncertainties. Although some correlation between the mesons could be present (about the 30% of the  
 671 D<sup>0</sup>, and also part of the D<sup>+</sup>, come from D<sup>\*+</sup> decays), the three selected D-meson samples can be treated  
 672 as uncorrelated. The sum of the statistical uncertainties; the systematics uncertainty on S and B extraction  
 673 and on background shape, are added in quadrature and the inverse of this sum was used as weight,  $w_i$ .

$$\left\langle \frac{1}{N_D} \frac{dN_{\text{assoc}}}{dp_T} \right\rangle_{D\text{mesons}} = \frac{\sum_{i=\text{meson}} w_i \frac{1}{N_D} \frac{dN_i^{\text{assoc}}}{d\Delta\phi}}{\sum_{i=\text{meson}} w_i}, w_i = \frac{1}{\sigma_{i,\text{stat}}^2 + \sigma_{i,\text{uncorr.syst}}^2} \quad (5)$$

674 The statistical uncertainty and the uncertainties on S and B extraction and on background shape (those  
 675 used for the weights) on the average were then recalculated using the following formula:

$$\sigma^2 = \frac{1}{n_D} \frac{\sum_{i=\text{meson}} w_i \sigma_i^2}{\sum_{i=\text{meson}} w_i} \quad (6)$$

676 where  $n_D$  is the number of mesons considered in the average. It can be observed that for  $\sigma_i^2 = 1/w_i$  the  
 677 formula coincides with the standard one giving the uncertainty on a weighted average. The contribution  
 678 to the average systematic uncertainty for those uncertainty sources not included in the weight definition,  
 679 was evaluated via error propagation on the formula of the weighted average (5), resulting in equation  
 680 (7) and (8) for sources considered uncorrelated and correlated among the mesons. In particular, the  
 681 uncertainties on the associated track reconstruction efficiency, on the contamination from secondary, on  
 682 the feed-down subtraction, and that resulting from the Monte Carlo closure test were considered fully  
 683 correlated among the mesons, while those deriving from the yield extraction (included in the weight  
 684 definition) and on the D meson reconstruction and selection efficiency were treated as uncorrelated.

$$\sigma^2 = \frac{\sum_{i=\text{meson}} w_i^2 \sigma_i^2}{(\sum_{i=\text{meson}} w_i)^2} \quad (7)$$

$$\sigma = \frac{\sum_{i=\text{meson}} w_i \sigma_i}{\sum_{i=\text{meson}} w_i} \quad (8)$$

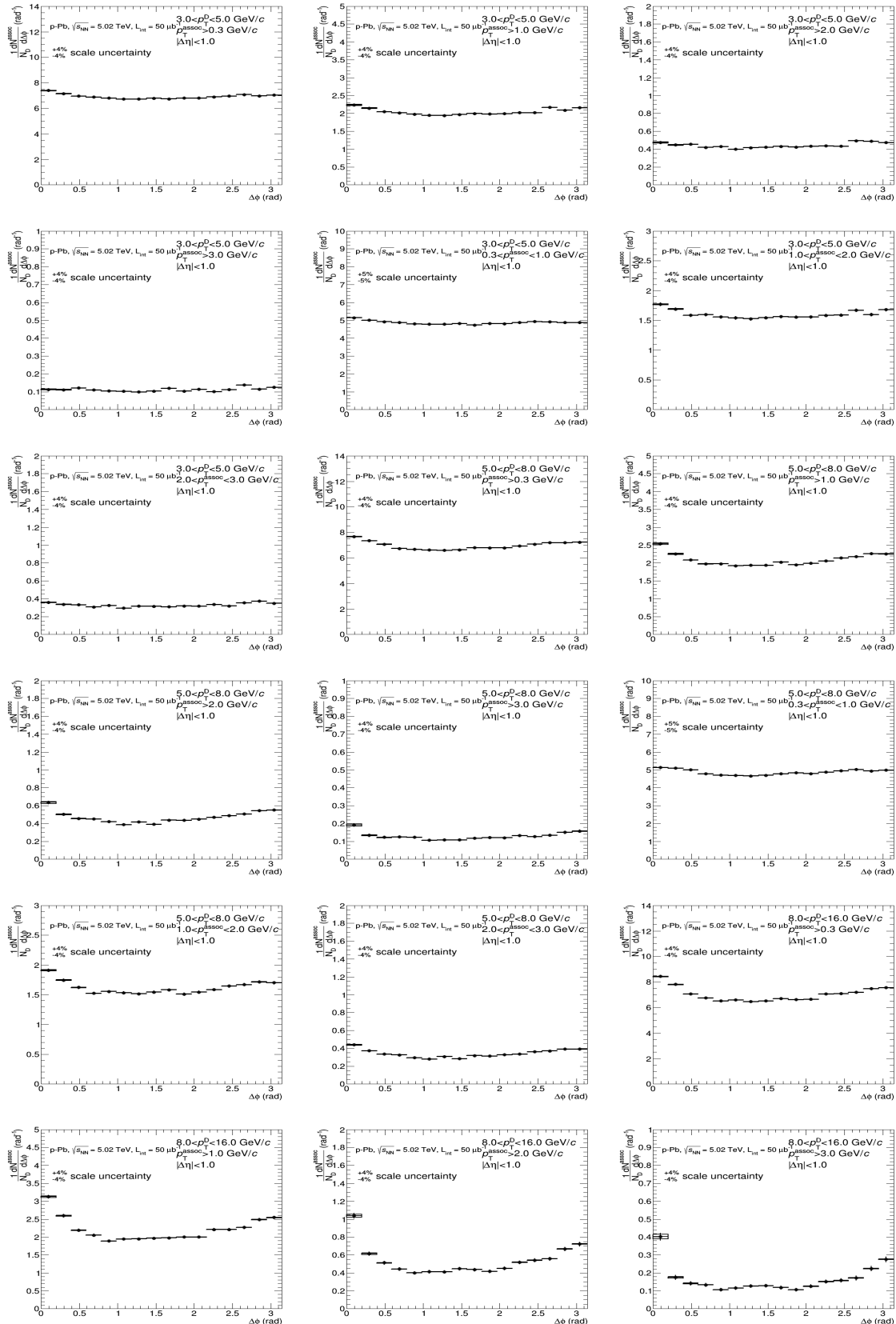
685 Figure 46 shows the averages of the azimuthal correlation distributions of D<sup>0</sup>, D<sup>+</sup> and D<sup>\*+</sup> and charged  
 686 particles with  $p_T > 0.3$  GeV/c,  $0.3 < p_T < 1$  GeV/c,  $p_T > 1$  GeV/c,  $1 < p_T < 2$  GeV/c,  $2 < p_T <$   
 687  $3$  GeV/c,  $p_T < 3$  GeV/c in the D meson  $p_T$  ranges  $3 < p_T < 5$  GeV/c,  $5 < p_T < 8$  GeV/c,  $8 < p_T <$   
 688  $16$  GeV/c and  $16 < p_T < 24$  GeV/c. As expected, a rising trend of the height of the near-side peak  
 689 with increasing D-meson  $p_T$  is observed, together with a decrease of the baseline level with increasing  
 690  $p_T$  of the associated tracks. To further increase the statistical precision on the averaged correlation  
 691 distributions, given the symmetry around 0 on the azimuthal axis, the distributions were reflected and  
 692 shown in the range  $[0, \pi]$ . This reduces the statistical uncertainty on the points by, approximately, a factor  
 693 of  $1/\sqrt{2}$ .

---

<sup>1</sup>A slight near side hierarchy is present among the three meson results, with D<sup>\*+</sup> meson having a lower peak amplitude than D<sup>0</sup> and D<sup>+</sup>. It was verified that this is induced by the presence of D<sup>0</sup> and D<sup>+</sup> mesons coming from D<sup>\*+</sup>, the latter having on average a larger  $p_T$  and coming, hence, on average, from a larger  $p_T$  quark parton, which fragments in slightly more tracks in the near-side.

## 5.2 Average of $D^0$ , $D^+$ and $D^{*+}$ results

67



694 The usage of weighted average requires, as an underlying assumption, identical results expected for  
695 different species (or, at least, compatible within the uncertainties). Anyway, it was also verified that the  
696 usage of the arithmetic average instead of the weighted average increases the uncertainties on the points,

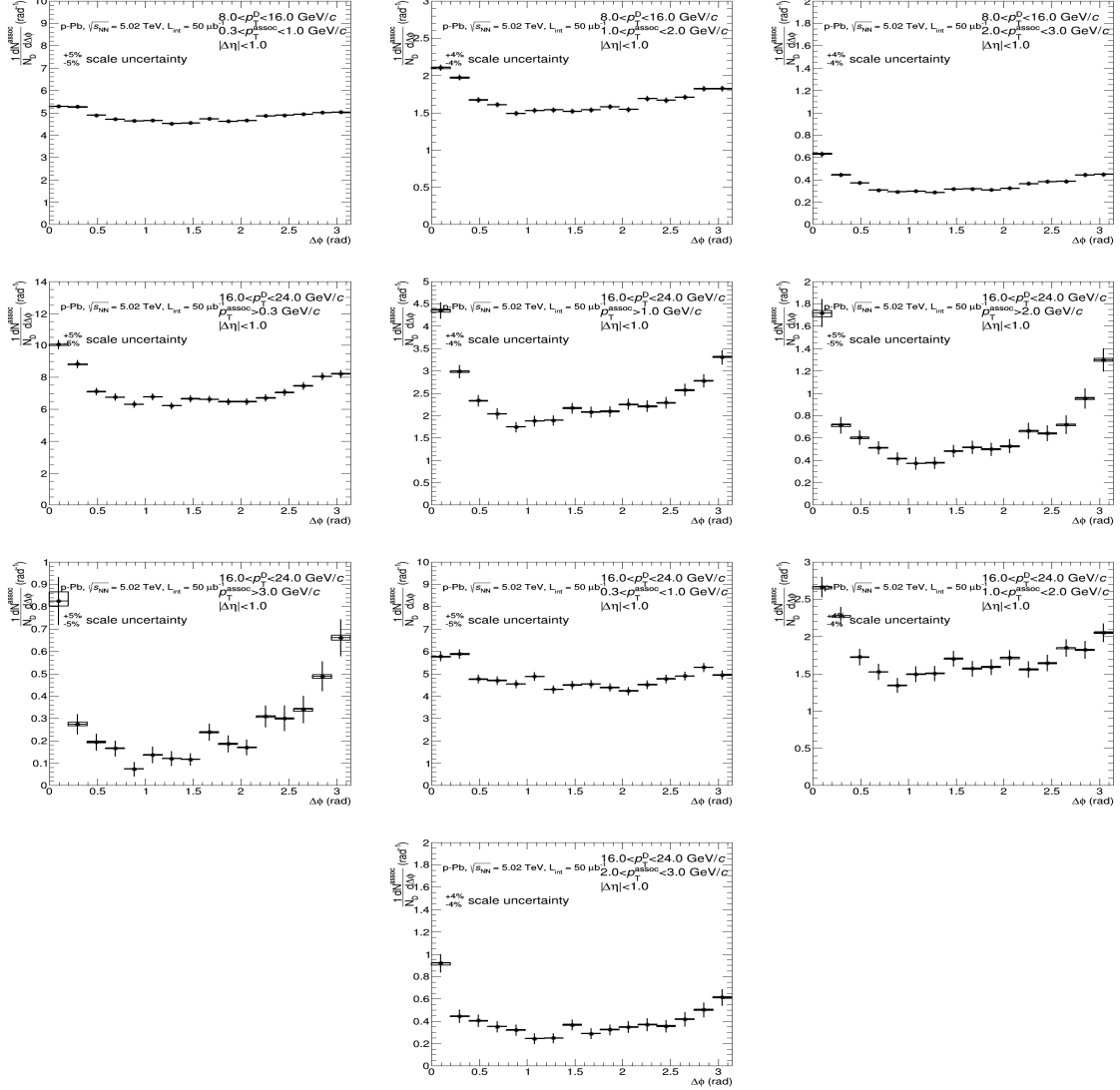


**Figure 46:** Average of  $D^0$ ,  $D^+$  and  $D^{*+}$  azimuthal correlation distributions, in the  $D$  meson  $p_T$  ranges  $3 < p_T < 5 \text{ GeV}/c$ ,  $5 < p_T < 8 \text{ GeV}/c$ ,  $8 < p_T < 16 \text{ GeV}/c$  and  $16 < p_T < 24 \text{ GeV}/c$ , with associated tracks with  $p_T > 0.3 \text{ GeV}/c$ ,  $p_T > 1 \text{ GeV}/c$  and  $0.3 < p_T < 1 \text{ GeV}/c$ .

697 but produces a negligible shift of their central values.

### 698 5.3 Fit observable $p_T$ trends and uncertainties

699 In order to extract quantitative and physical information from the data correlation patterns, the averaged  
700 D-h correlation distributions are fitted with two Gaussian functions (with means fixed at  $\Delta\varphi=0$  and  $\Delta\varphi=\pi$   
701 values), plus a constant term (baseline). A periodicity condition is also applied to the fit function to obtain  
702 the same value at the bounds of  $2\pi$  range. The expression of the fit function is reported below (equation  
703 9):

$$f(\Delta\varphi) = c + \frac{Y_{NS}}{\sqrt{2\pi}\sigma_{NS}} e^{-\frac{(\Delta\varphi-\mu_{NS})^2}{2\sigma_{NS}^2}} + \frac{Y_{AS}}{\sqrt{2\pi}\sigma_{AS}} e^{-\frac{(\Delta\varphi-\mu_{AS})^2}{2\sigma_{AS}^2}} \quad (9)$$

704 where baseline is calculated as the weighted average of the points lying in the so-called "transverse  
705 region", i.e. the interval  $\frac{\pi}{4} < |\Delta\varphi| < \frac{\pi}{2}$ .

706 An example of the results from the fit is shown in Figure 47

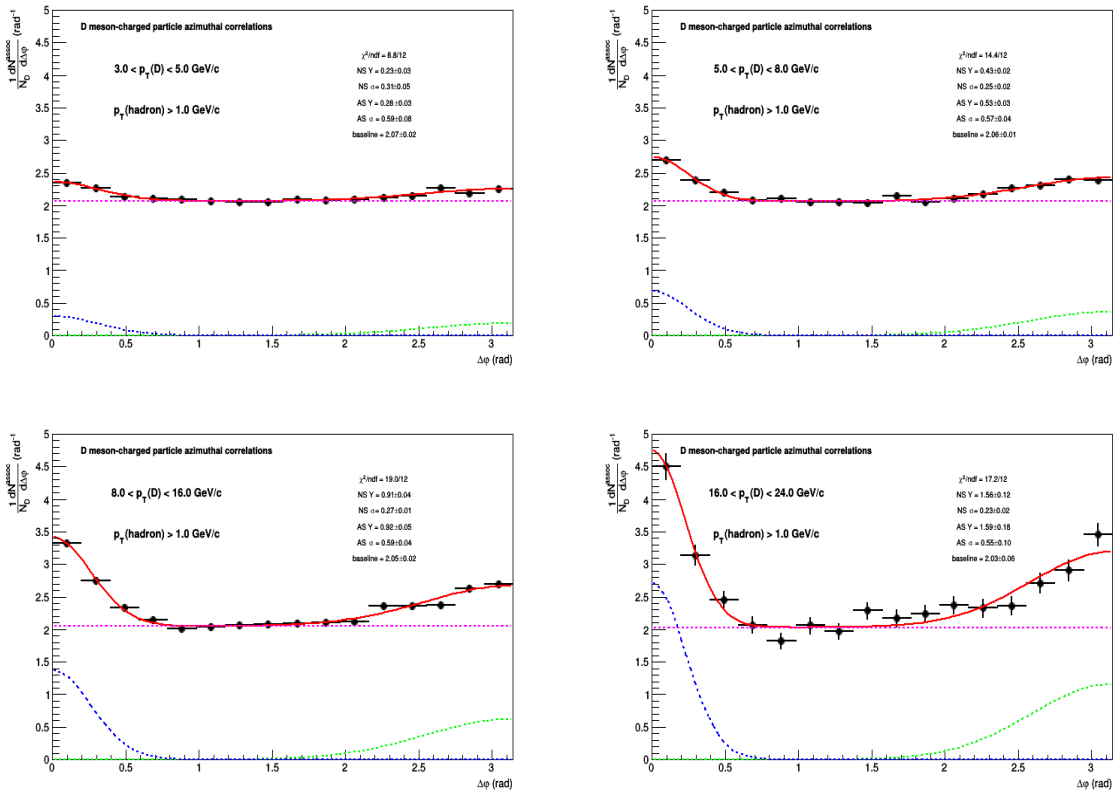


Figure 47: Example of fit to azimuthal correlation distributions and baseline estimation.

707 From the fit outcome, it is possible to retrieve the near-side and away-side yield and widths (integral  
708 and sigma of the Gaussian functions, respectively), as well as the baseline height of the correlation  
709 distribution. The near-side observables give information on the multiplicity and angular spread of the  
710 tracks from the fragmentation of the charm jet which gave birth to the D-meson trigger. At first order,  
711 instead, the away-side observables are related to the hadronization of the charm parton produced in the  
712 opposite direction (though the presence of NLO processes for charm production breaks the full validity  
713 of this assumption). The baseline value is a rough indicator of the underlying event multiplicity, though

714 below the baseline level also charm and beauty-related pairs are contained (especially in cases of NLO  
 715 production for the heavy quarks).

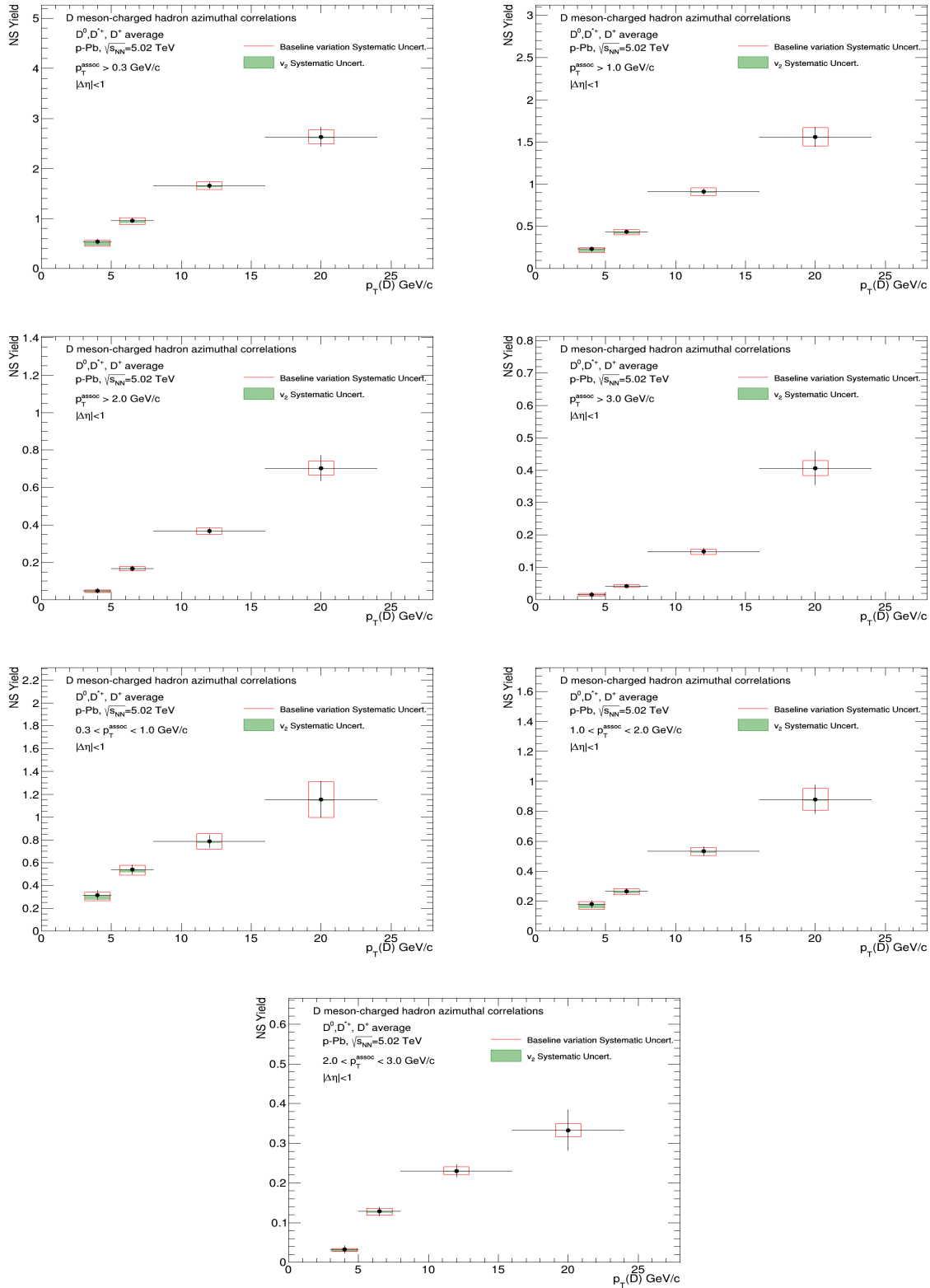
716 The evaluation of the systematic uncertainties on the observables obtained from the fits is performed as  
 717 follows:

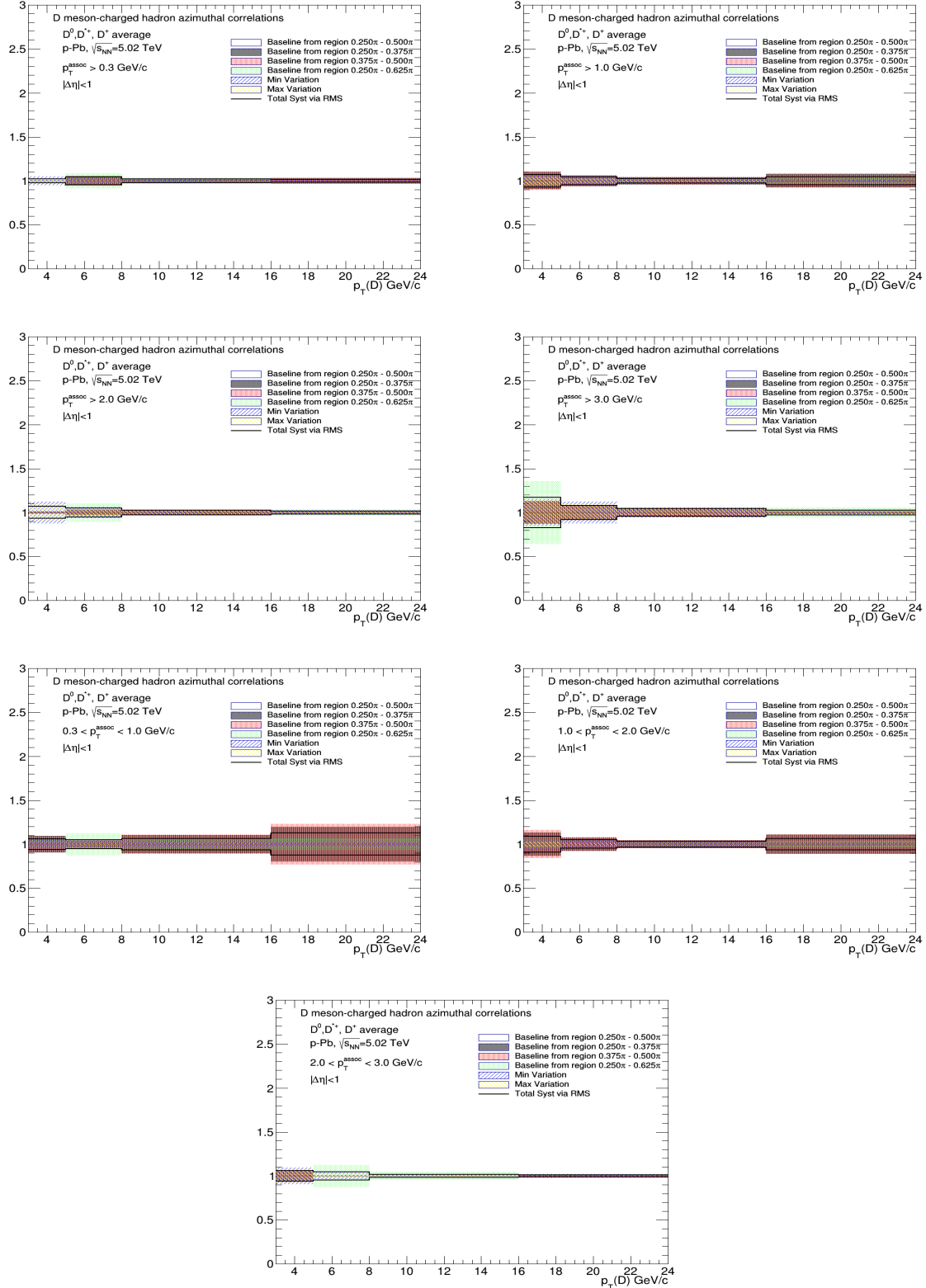
- 718 – The fits are repeated by changing the range of the transverse region in which the baseline is evalu-  
 ated. Alternate definitions of  $\frac{\pi}{4} < |\Delta\phi| < \frac{3\pi}{8}$ ,  $\frac{3\pi}{8} < |\Delta\phi| < \frac{\pi}{2}$  and  $\frac{\pi}{4} < |\Delta\phi| < \frac{5\pi}{8}$  are considered.
- 720 – In addition,  $\Delta\phi$  correlation points are shifted to the upper and lower bounds of their uncorrelated  
 721 systematic boxes, and refitted.
- 722 – The fits are also repeated by moving the baseline value from its default value (i.e. with the default  
 723 transverse region) on top and on bottom of its statistic uncertainty. This helps to account, though  
 724 in a systematic uncertainty, for the statistical uncertainty on the baseline position (since in the fit  
 725 the baseline is constrained, and its error is not propagated to the other observables).
- 726 – The envelope between (i) the RMS of the relative variations of the parameters between the fit  
 727 outcomes defined in the first two points, and (ii) the relative variations of the parameters from the  
 728 fit outcomes defined in the third point, is considered as systematic uncertainty for the near-side  
 729 and away-side widths.
- 730 – For the estimation of the baseline and of the near-side and away-side yields, instead, the previous  
 731 value is added in quadrature with the  $\Delta\phi$ -correlated systematics in the correlation distributions,  
 732 since these values are affected by a change in the global normalization of the distributions.
- 733 – In addition, for all the fit observables, an additional fit variation is performed assuming, instead  
 734 of a flat baseline, a  $v_{2\Delta}$ -like modulation, with the following  $v_2$  values for the associated tracks  
 735 (assuming  $v_{2\Delta} = v_2(h) \cdot v_2(D)$ ): 0.04 (0.3-1 GeV/c), 0.06 ( $>0.3$  GeV/c), 0.08 (1-2 GeV/c), 0.09 ( $>1$   
 736 GeV/c, 2-3 GeV/c), 0.1 ( $>3$  GeV/c), on the basis of ATLAS preliminary results for heavy-flavour  
 737 muons at 8 TeV; for the D-meson triggers the following  $v_2$  values were instead assumed: 0.05 (3-5  
 738 GeV/c), 0.03 (5-8 GeV/c), 0.02 (8-24 GeV/c), on the basis of previous ALICE measurements in  
 739 p-Pb collisions at 5 TeV [3]. The difference of the fit observables with respect to the standard fits  
 740 is taken as uncertainty. Due to its peculiarity, this systematic uncertainty is summed in quadrature  
 741 with the others to obtain the total uncertainty, but is also shown separately in the figures.

$$\sigma^{syst} = \sqrt{(Max(\Delta par^{ped.mode}, \Delta par^{\Delta\phi point}))^2 + (\sigma_{Syst}^{corr})^2} \quad (10)$$

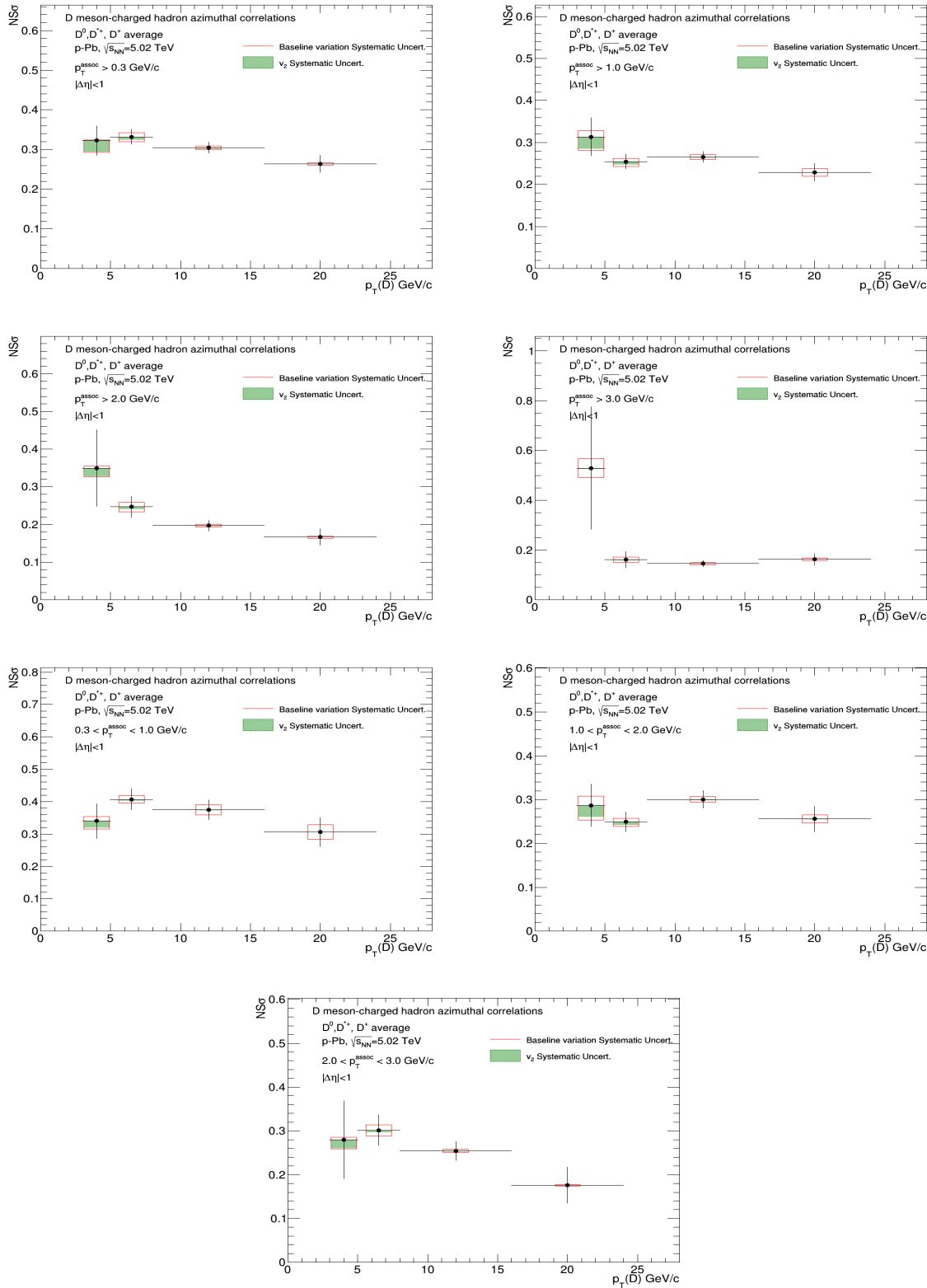
### 742 5.3.1 Results for near-side yield and width, away-side yield and width, and baseline

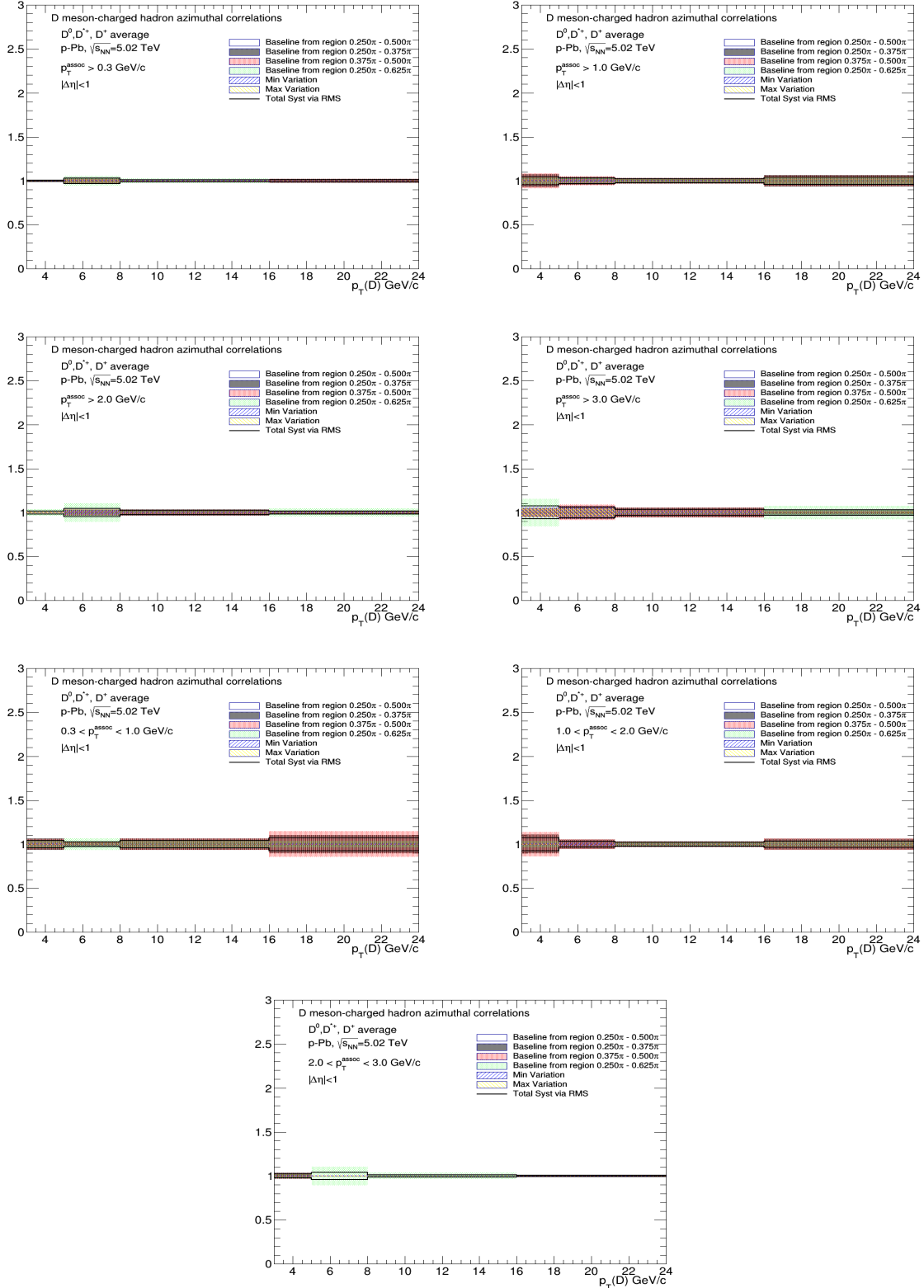
743 Figures 48, 49, 50, 51 and 52 show the near-side associated yield, width (the sigma of the Gaussian part  
 744 of the fit functions), away-side associated yield, width and the height of the baseline, for the average  
 745 correlation distributions, in the kinematic ranges studied in the analysis, together with their statistical  
 746 and systematic uncertainties. For each kinematic range, the correspondent plot showing the systematic  
 747 uncertainty of the considered observable from the variation of the fit procedure is reported as well (which  
 748 is the full systematic uncertainty for the widths). Figures 53, 54, 55, 56 and 57 show the full systematic  
 749 uncertainties for near side yield and width, away side yield and width, and baseline, with the breakdown  
 750 of fit variation,  $v_{2\Delta}$  and  $\Delta\phi$  correlated systematic uncertainties.



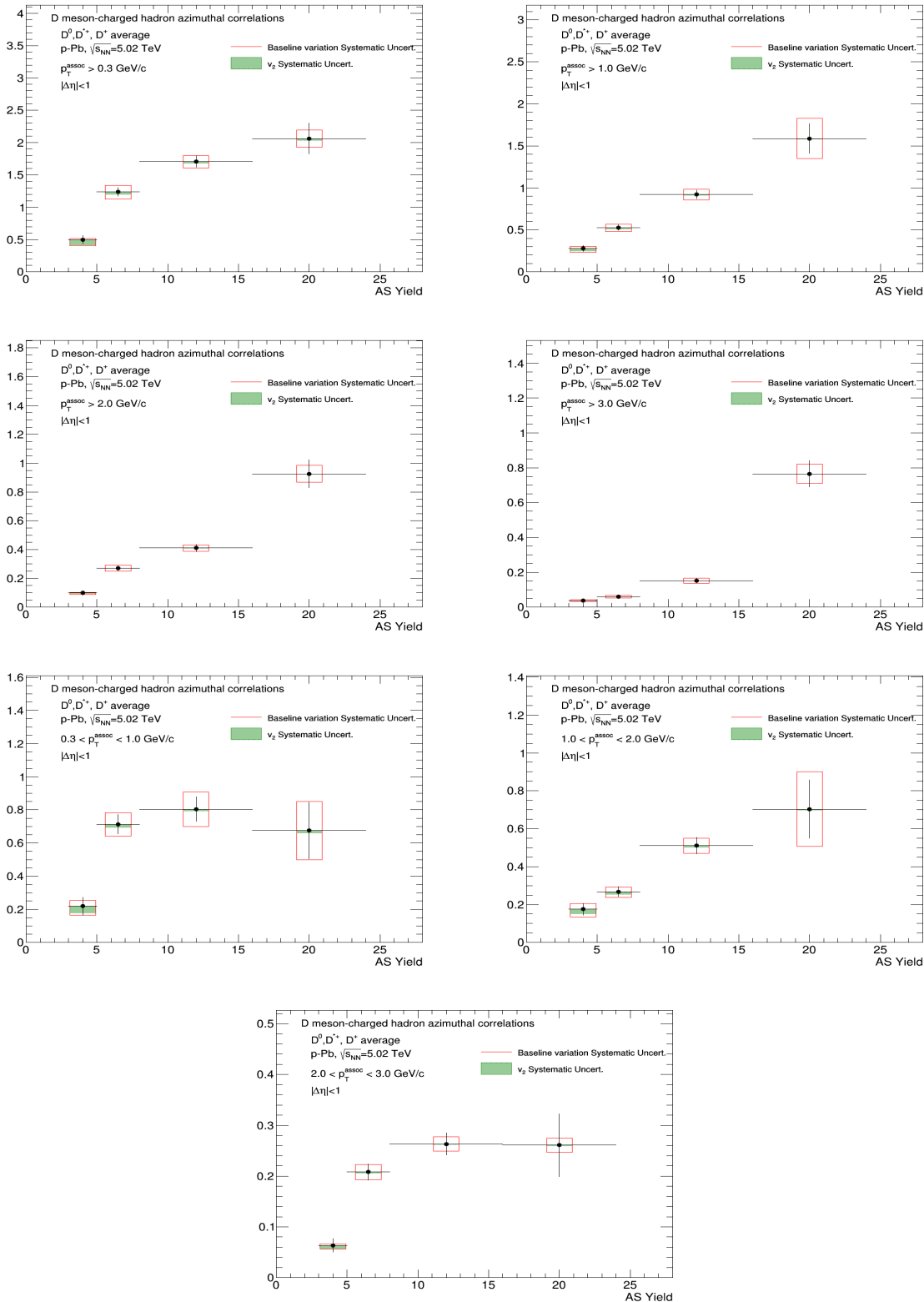


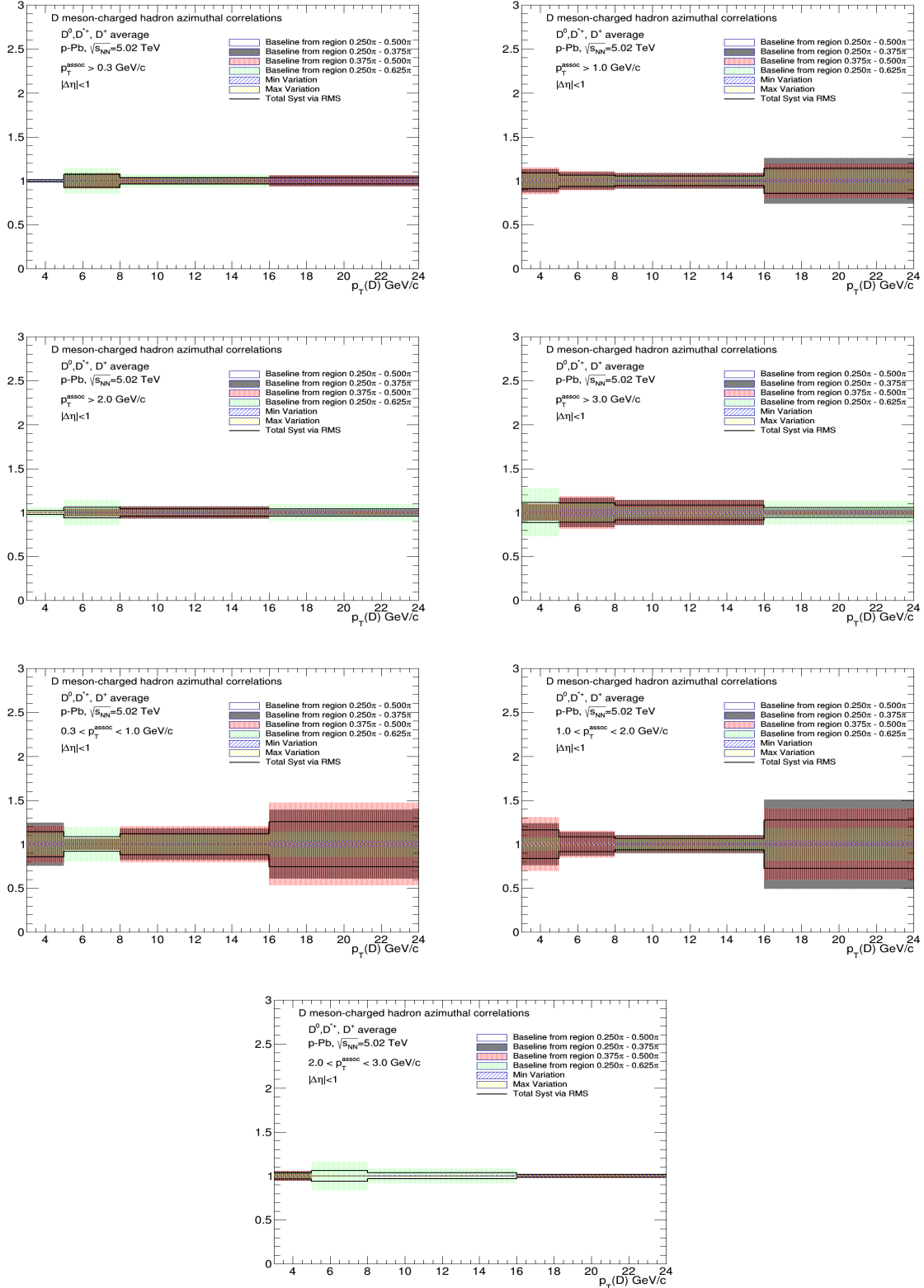
**Figure 48:** Top panels: near side yield  $p_T(D)$  trend for the D-meson average, extracted from fit to the azimuthal correlation distributions, for all the analyzed kinematic ranges of associated track  $p_T$ . Bottom panels: for each kinematic region the systematic uncertainties coming from the variation of the fit procedure are shown.



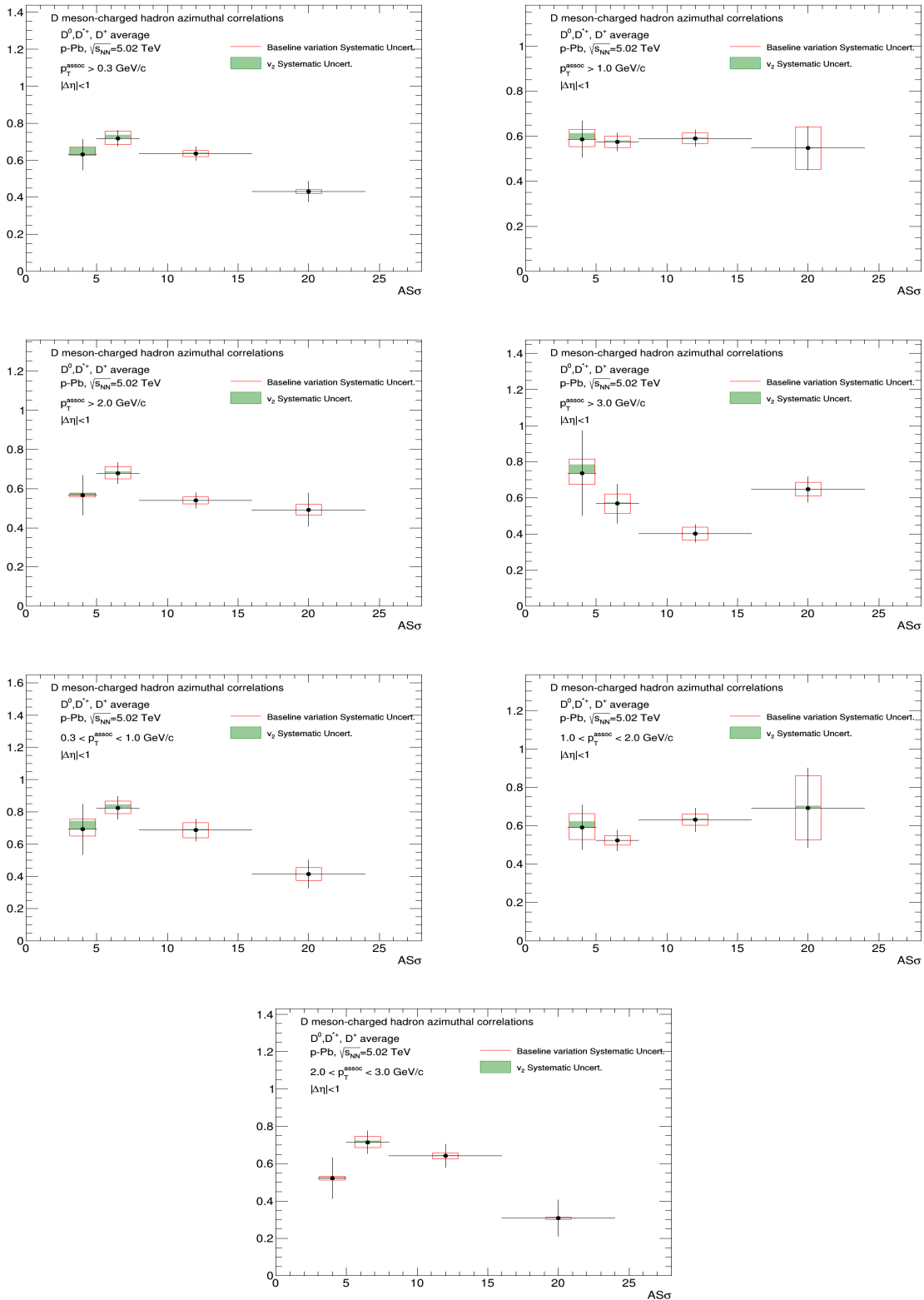


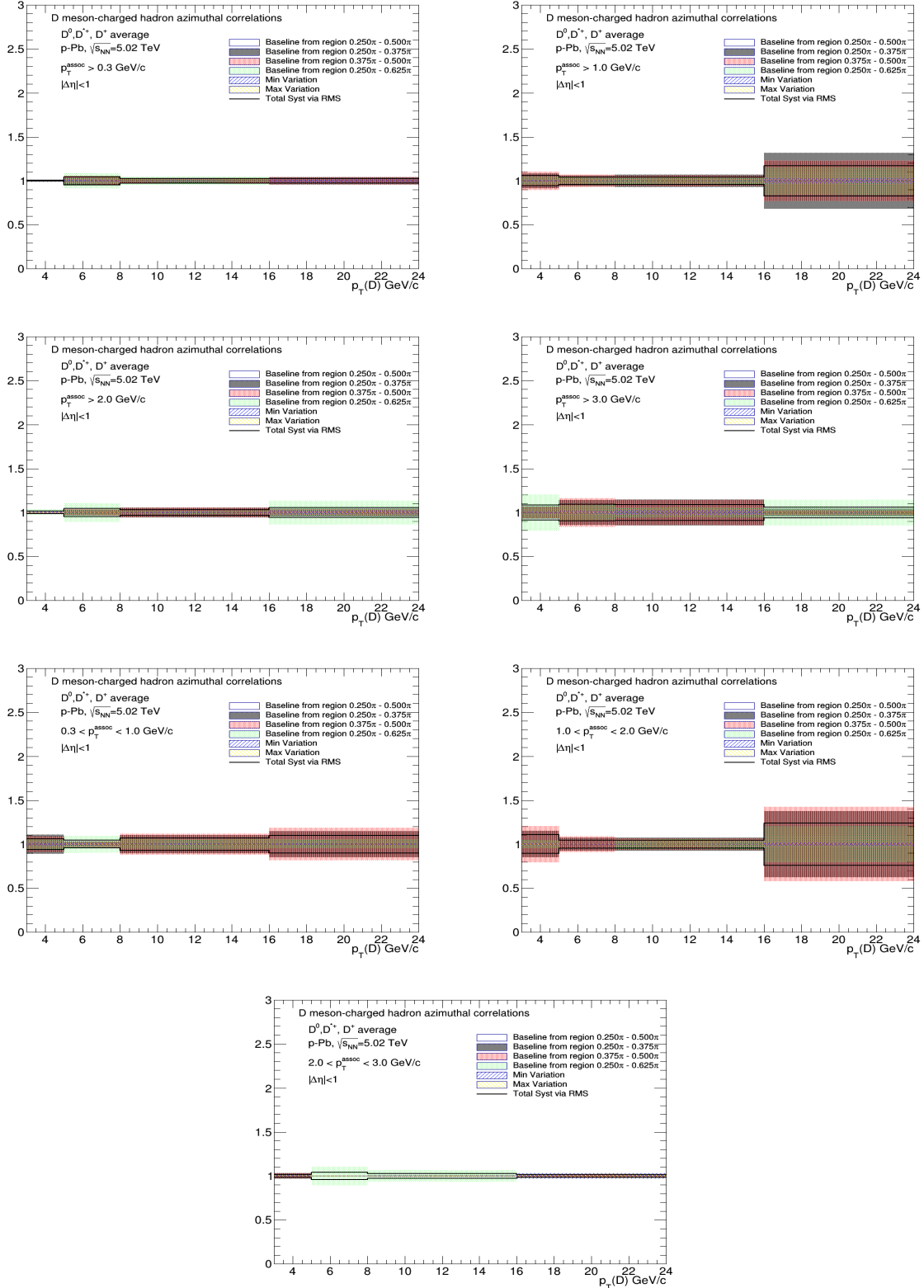
**Figure 49:** Top panels: near side width  $p_T(D)$  trend for the D-meson average, extracted from fit to the azimuthal correlation distributions, for all the analyzed kinematic ranges of associated track  $p_T$ . Bottom panels: for each kinematic region the systematic uncertainties coming from the variation of the fit procedure are shown.



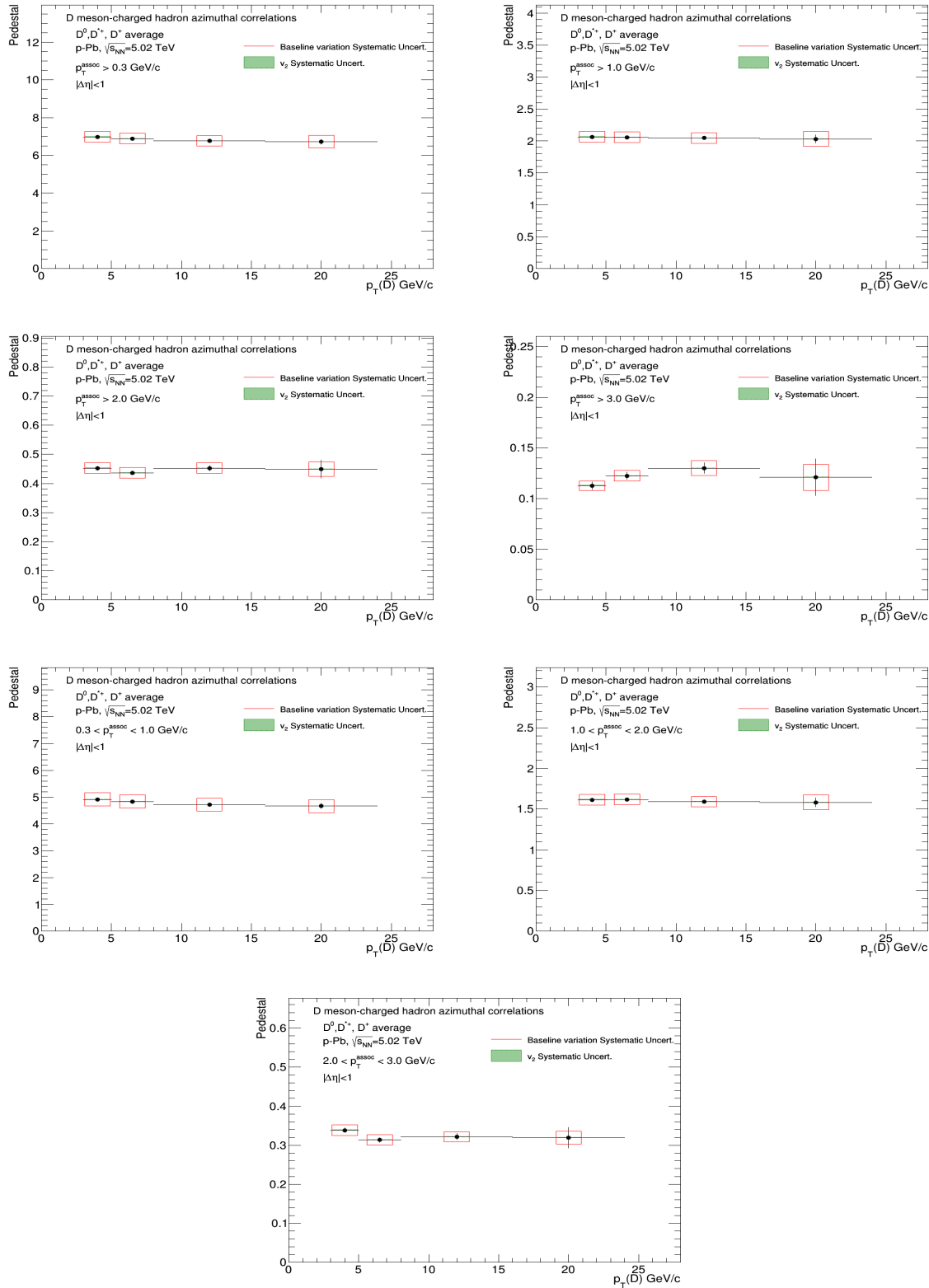


**Figure 50:** Top panels: away side yield  $p_T(D)$  trend for the D-meson average, extracted from fit to the azimuthal correlation distributions, for all the analyzed kinematic ranges of associated track  $p_T$ . Bottom panels: for each kinematic region the systematic uncertainties coming from the variation of the fit procedure are shown.





**Figure 51:** Top panels: away side width  $p_T(D)$  trend for the D-meson average, extracted from fit to the azimuthal correlation distributions, for all the analyzed kinematic ranges of associated track  $p_T$ . Bottom panels: for each kinematic region the systematic uncertainties coming from the variation of the fit procedure are shown.



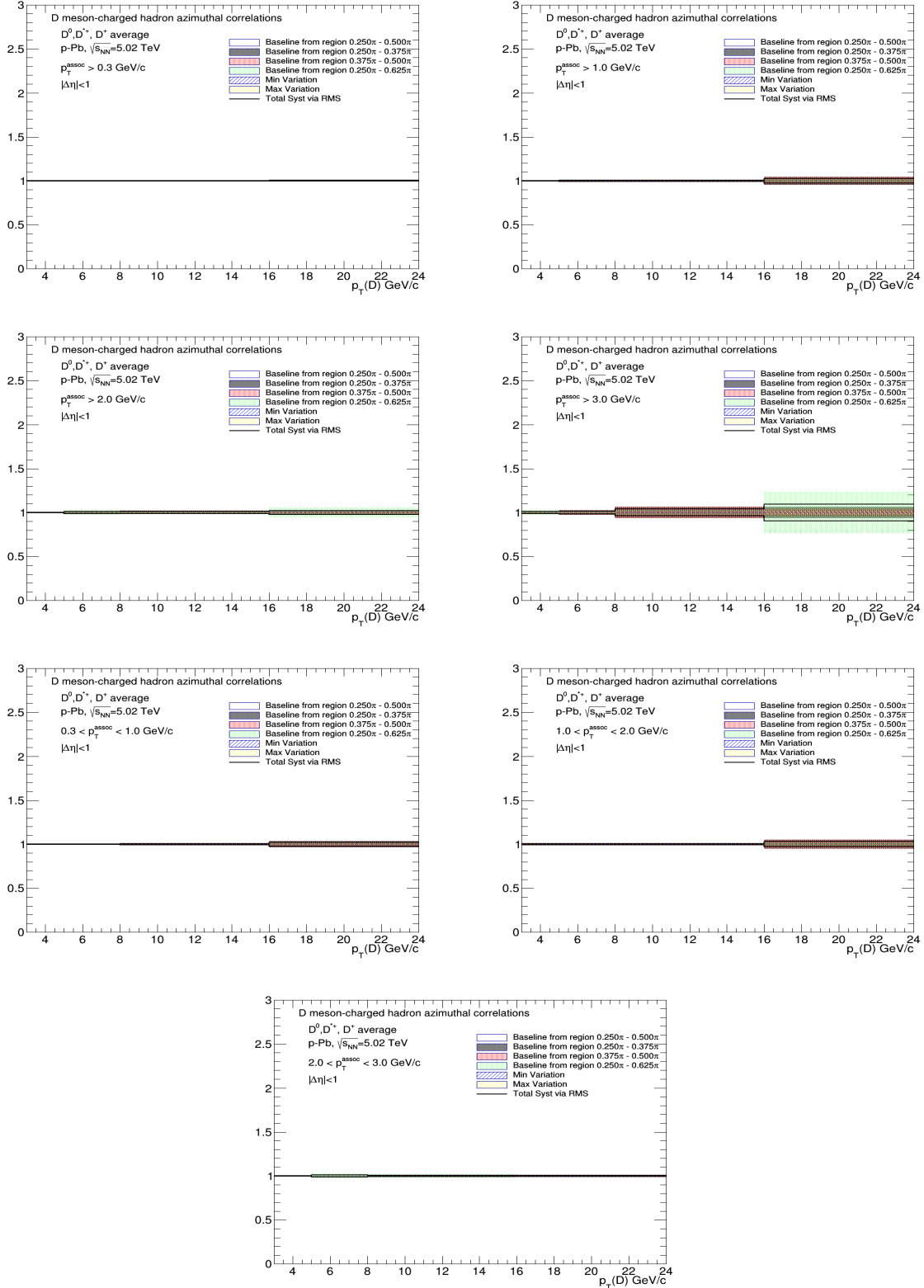


**Figure 52:** Top panels: baseline height trend for the D-meson average, extracted from fit to the azimuthal correlation distributions, for all the analyzed kinematic ranges of associated track  $p_T$ . Bottom panels: for each kinematic region the systematic uncertainties coming from the variation of the fit procedure are shown.

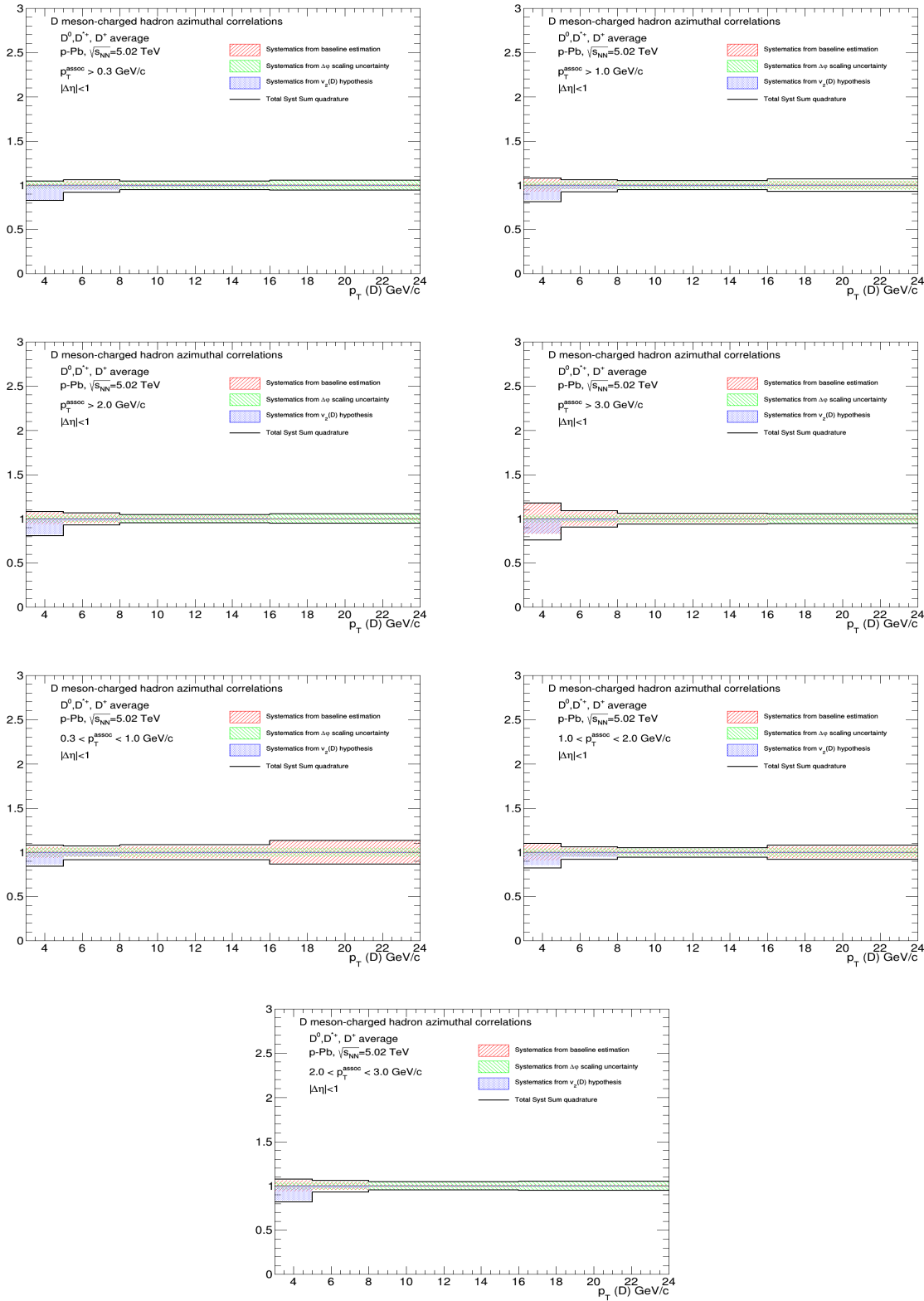


**Figure 53:** Total systematic uncertainty, and its components, for near-side yields in the different kinematic ranges analyzed

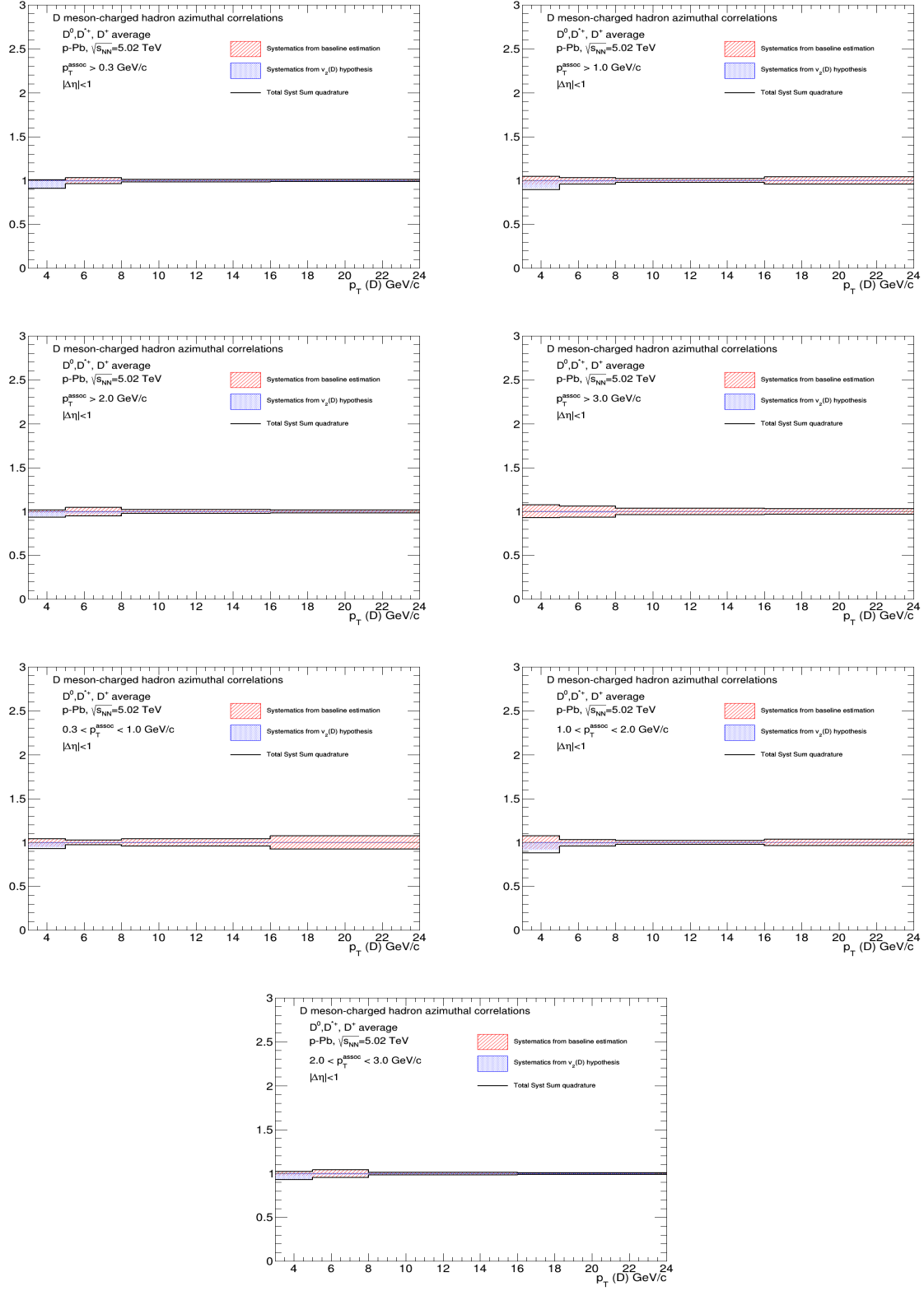


**Figure 54:** Total systematic uncertainty, and its components, for near-side sigma in the different kinematic ranges analyzed

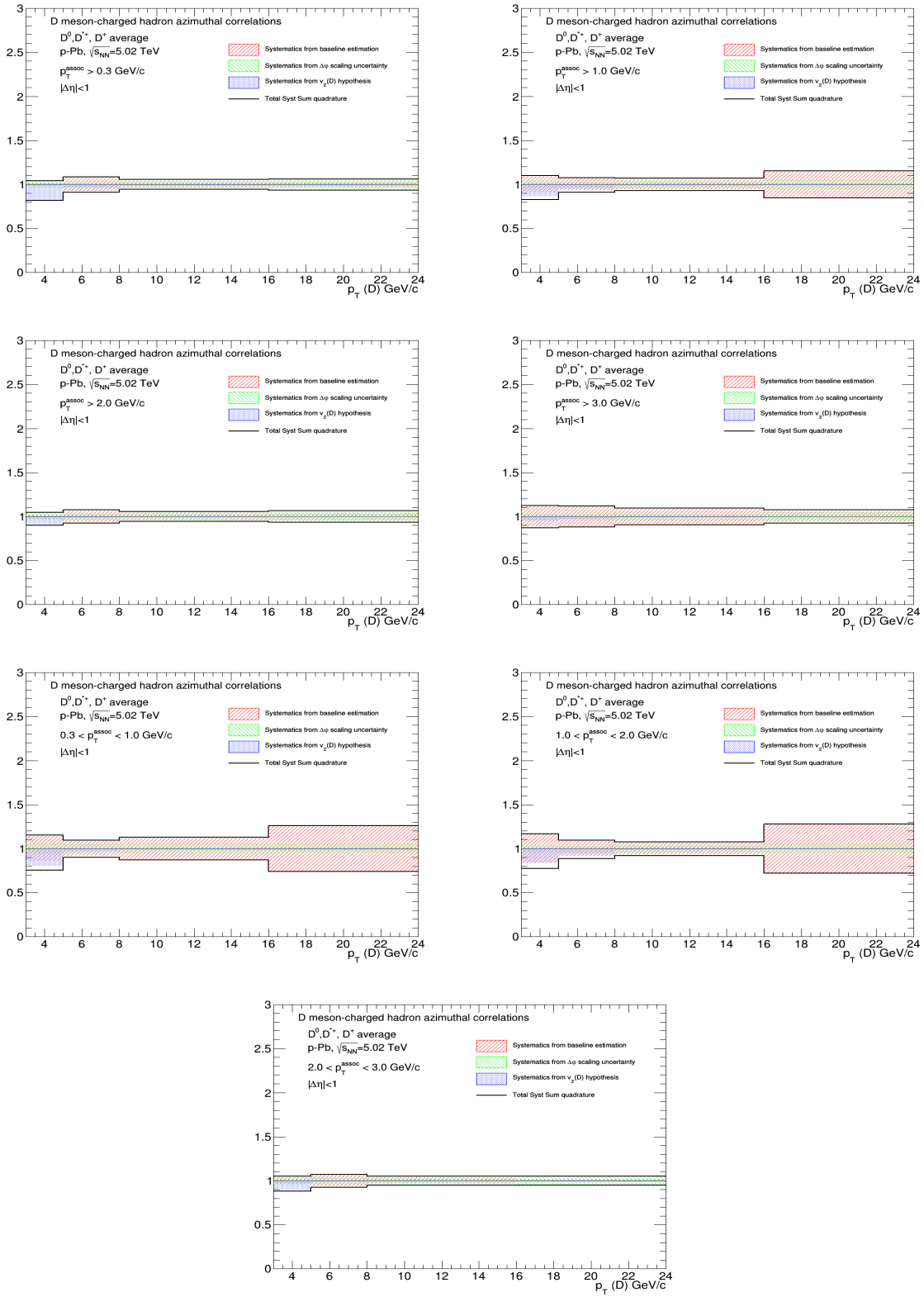


**Figure 55:** Total systematic uncertainty, and its components, for away-side yields in the different kinematic ranges analyzed

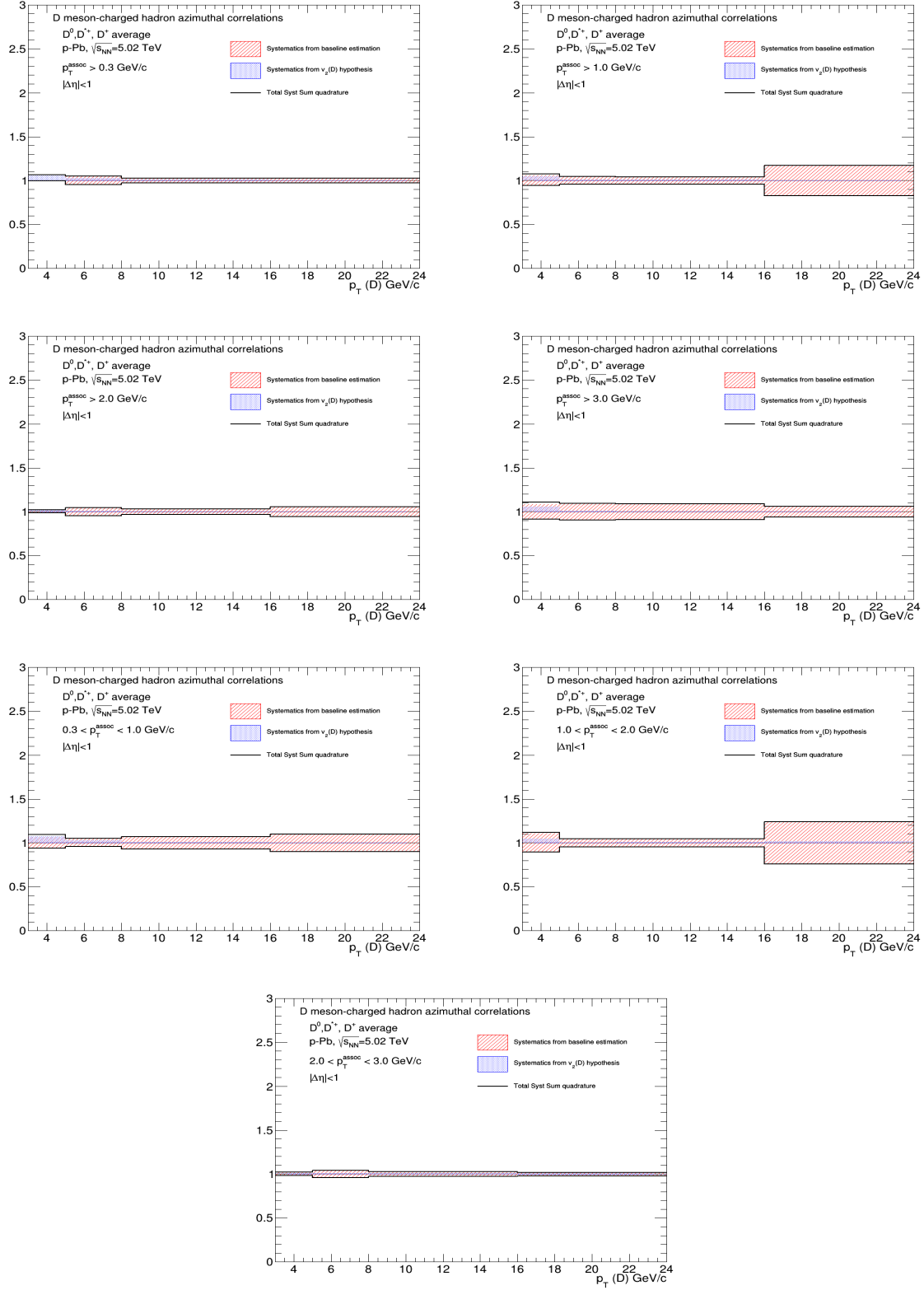


**Figure 56:** Total systematic uncertainty, and its components, for away-side sigma in the different kinematic ranges analyzed

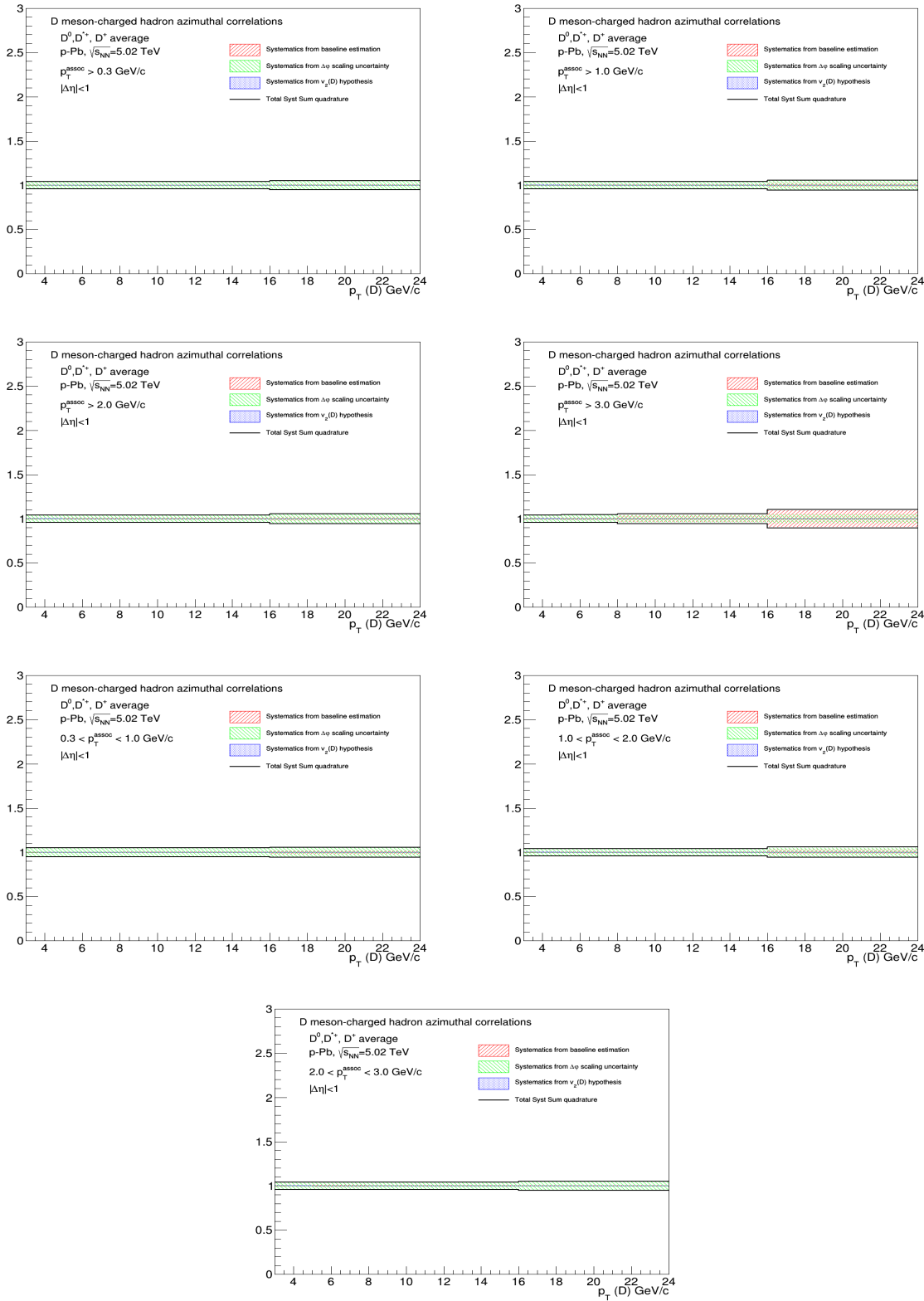


**Figure 57:** Total systematic uncertainty, and its components, for baseline heights in the different kinematic ranges analyzed.

#### 751 5.4 Comparison of 2016 p-Pb and 2013 p-Pb results

752 In Figure 58, the average correlation distributions from the published analysis in p-Pb 2013 sample  
 753 (black points) and the new p-Pb 2016 sample (red points), both at 5 TeV, are compared. As it's evident,  
 754 the statistical and systematic uncertainties are largely reduced in the new data sample. The feature of  
 755 the correlation distributions are the same in both systems, and an overall compatibility of the shapes is  
 756 observed.

757 Figure 59 shows the same comparison for the fit observables. Also in this case the uncertainties are  
 758 largely reduced for the 2016 analysis. The near-side widths are on top of each other; for the near-side  
 759 yields a slight decrease of the 2016 results is observed in some  $p_T$  ranges with respect to 2013 results,  
 760 though within the uncertainty, which were very large for the 2013 sample. The pedestal values are also  
 761 fully compatible within the two samples. The sensitivity to away-side observables was very poor for  
 762 2013 results, hence a comparison with 2016 data is difficult, anyway, within the large uncertainties, also  
 763 the away-side observables are compatible between the two datasets.

#### 764 5.5 Comparison of 2016 p-Pb and 2010 pp results

765 Figure 60 shows the comparison of the average D-h correlation distributions in pp 2010 data sample at  
 766  $\sqrt{s} = 7$  TeV (published in [2]) and in the new p-Pb 2016 sample at  $\sqrt{s_{NN}} = 5.02$  TeV. The results are  
 767 shown after the subtraction of the baseline. The precision of the new p-Pb results is much better than that  
 768 of pp results; the correlation distributions show very similar features in the two collision systems.

769 In Figure 61 the comparison is performed for the near-side peak observables, again in the common  
 770 kinematic ranges, where the same consideration about the uncertainties holds. The similarity of the  
 771 correlation distributions is reflected also in the near-side yield and width values, which do not seem to  
 772 differ within the uncertainties, pointing to the absence of strong effects from cold-nuclear matter effects  
 773 on the correlation distributions.

774 It has to be said that, on the base of a study performed with Pythia6-Perugia2011 simulations, a scaling  
 775 factor of about 0.93 is expected when passing from a center-of-mass energy of  $\sqrt{s} = 7$  TeV to  $\sqrt{s} = 5$   
 776 TeV, difficult to be appreciated with the current uncertainties, especially the pp ones.

#### 777 5.6 Comparison of 2016 p-Pb and model expectations

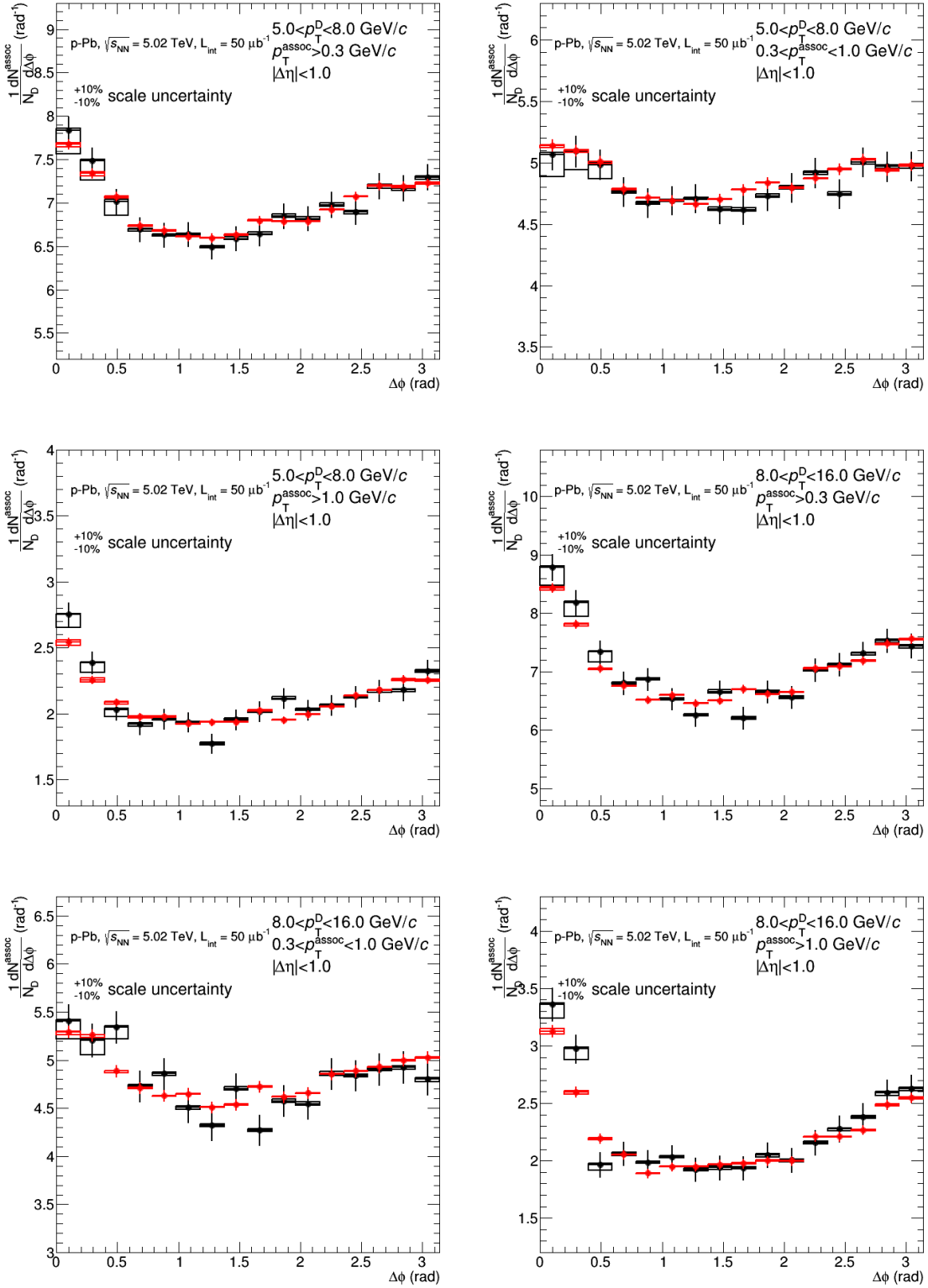
778 A comparison of the average D-h correlation distributions on the new p-Pb data samples with expec-  
 779 tations from Monte Carlo simulations (currently Pythia6-Perugia2011, Pythia6-Perugia2010, Pythia6-  
 780 Perugia0, PYTHIA8; POWHEG+PYTHIA and EPOS 3 will be added if they come in time) is shown in  
 781 Figure 62, after the baseline subtraction (which differs strongly between data and simulations, due to he  
 782 very different underlying event). The simulations, though being for pp, include the boost of the center-  
 783 of-mass along the beam axis present in p-Pb collisions and nuclear PDF. The shape of the correlation  
 784 distributions is well reproduced by all the models, together with their  $p_T$  trend and with the evolution of  
 785 the correlation peaks.

786 Figures 63 and 64 show the same comparison for the fit observables (peak yields and widths for near-side  
 787 and away-side, respectively), for all the addressed  $p_T$  ranges.

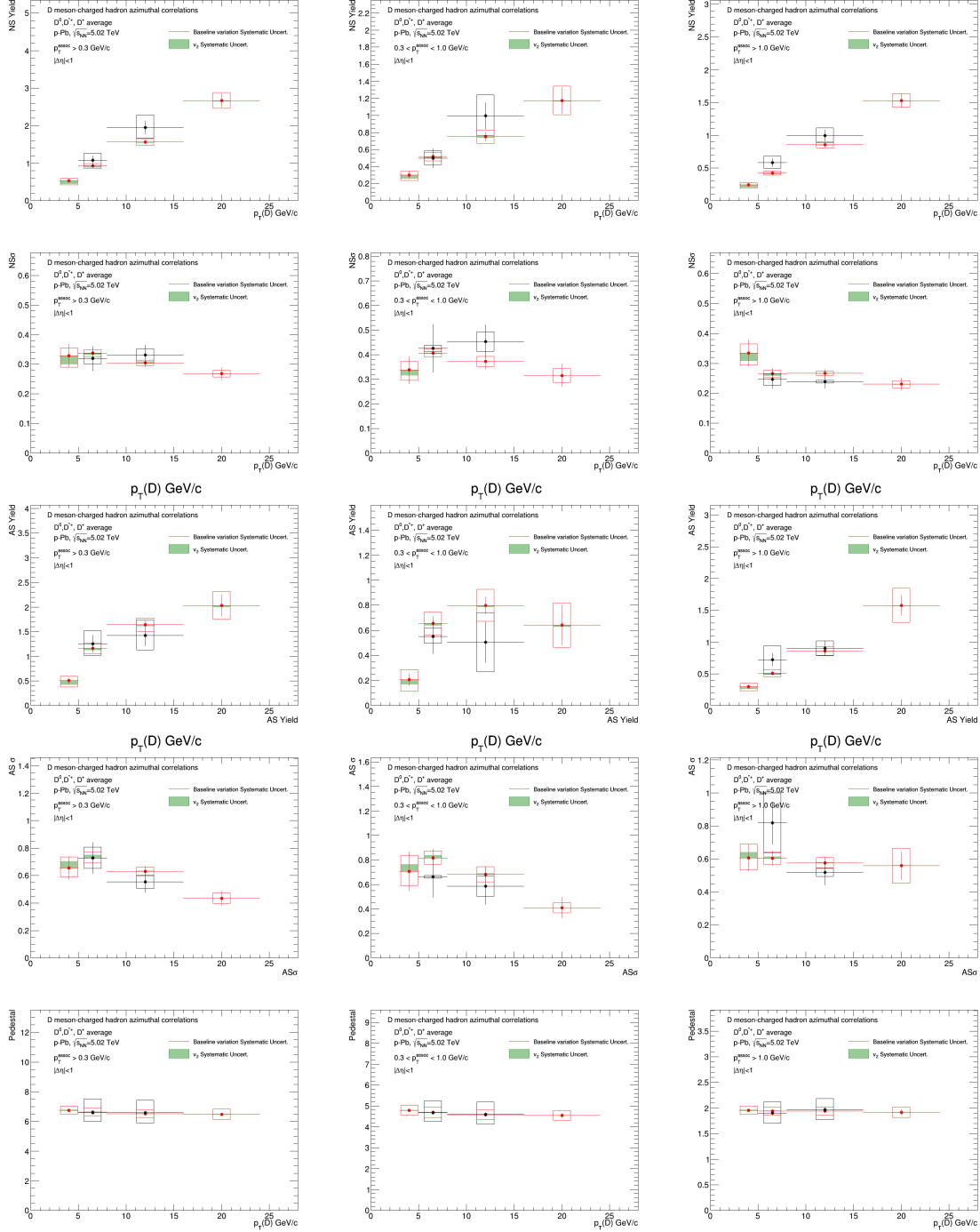
#### 788 5.7 Planned results for SQM approvals

789 We are planning to approve the following results, all shown in the previous figures (the final graphical  
 790 style of the plots is still to be finalized):

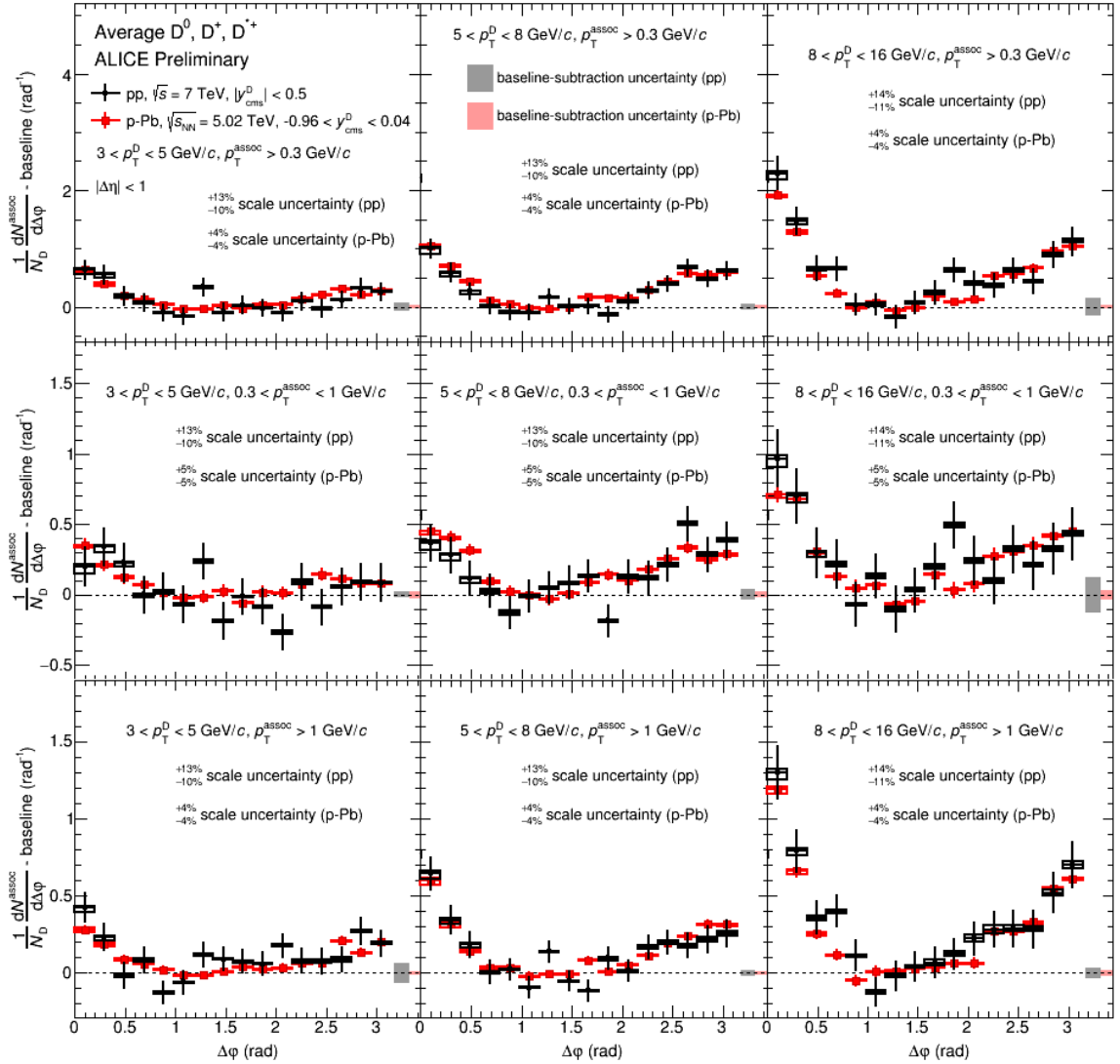
- 791 – Average D-h correlation distributions, in exemplary pT range
- 792 – Fit of D-h correlation distributions, in exemplary pT range



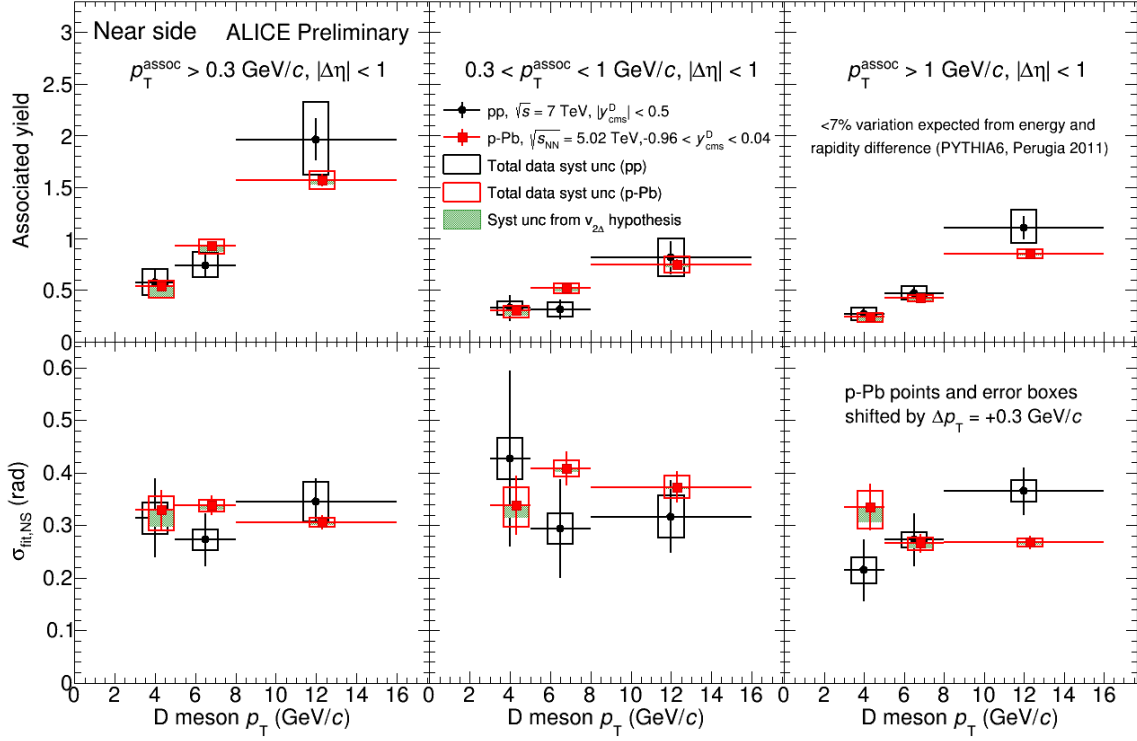
**Figure 58:** Comparison of 2016 (red) and 2013 (black) results for azimuthal correlation distributions, for the common  $p_T$  ranges.



**Figure 59:** Comparison of the average D-h azimuthal correlation properties between 2016 p-Pb (red) and 2013 p-Pb (black) data analysis, for the common  $p_T$  ranges of D meson and associated particles.

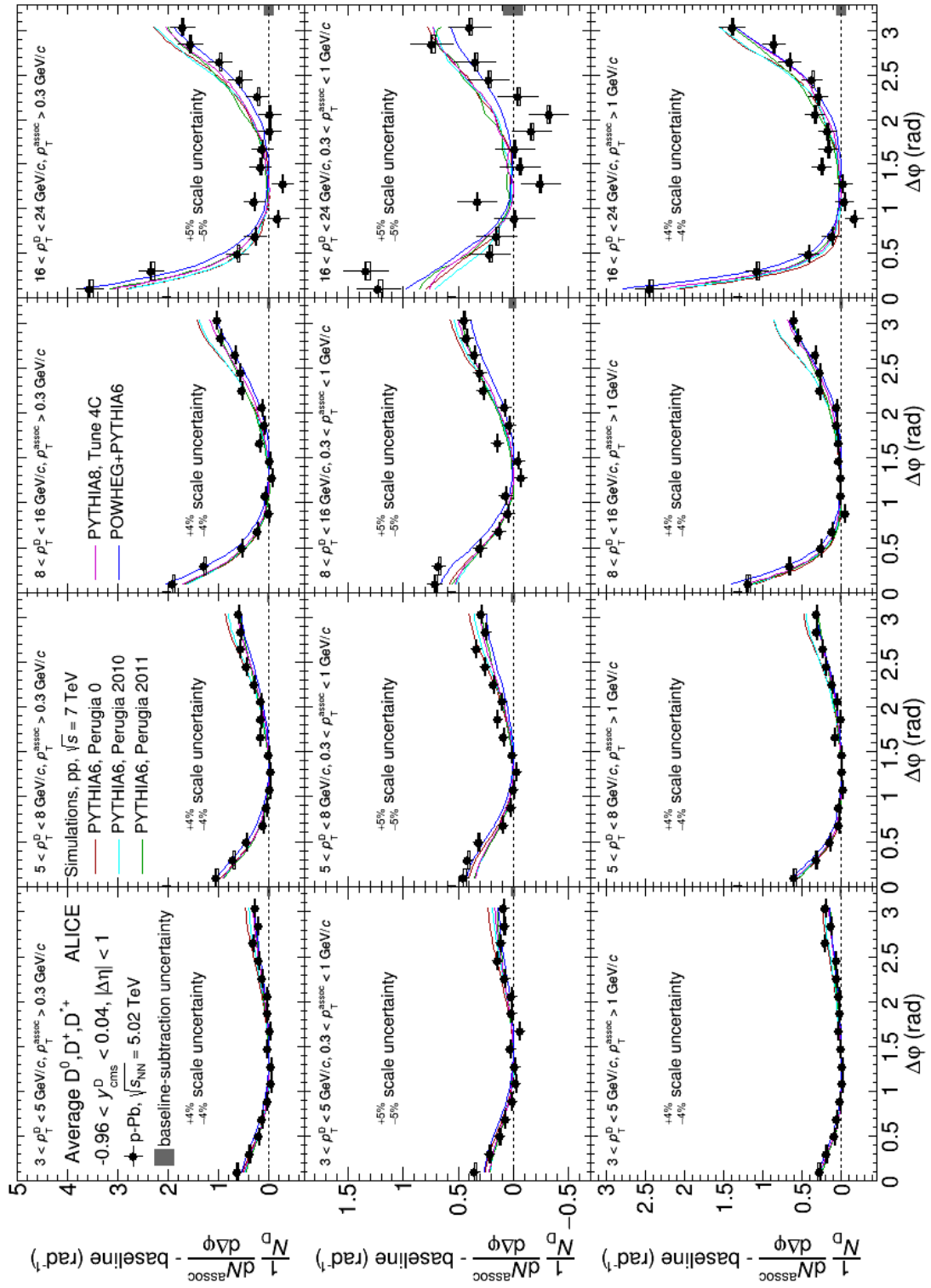


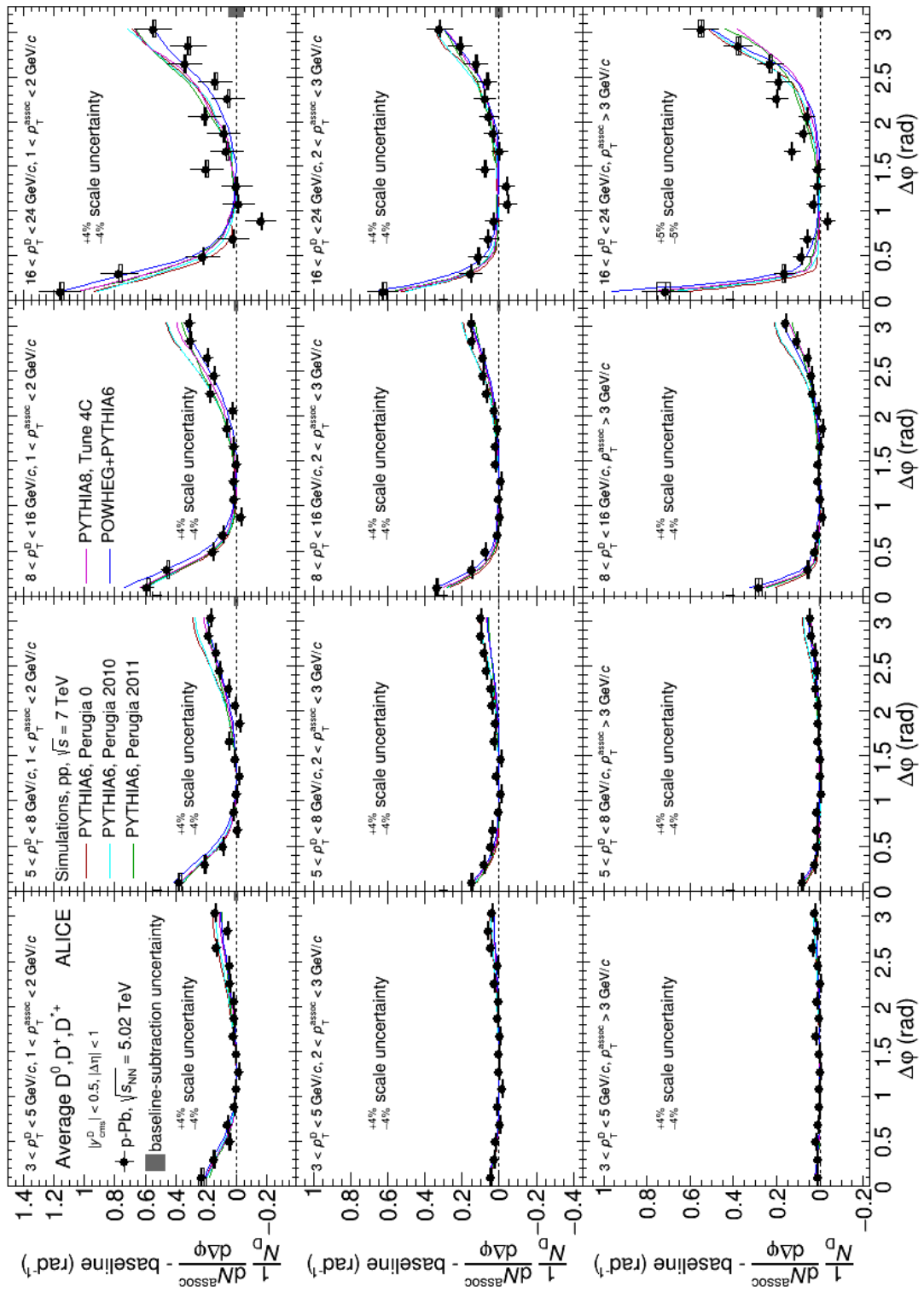
**Figure 60:** Comparison of pp 2010 (black) and p-Pb 2016 (red) average D-h azimuthal correlation distributions, for the common  $p_T$  ranges.



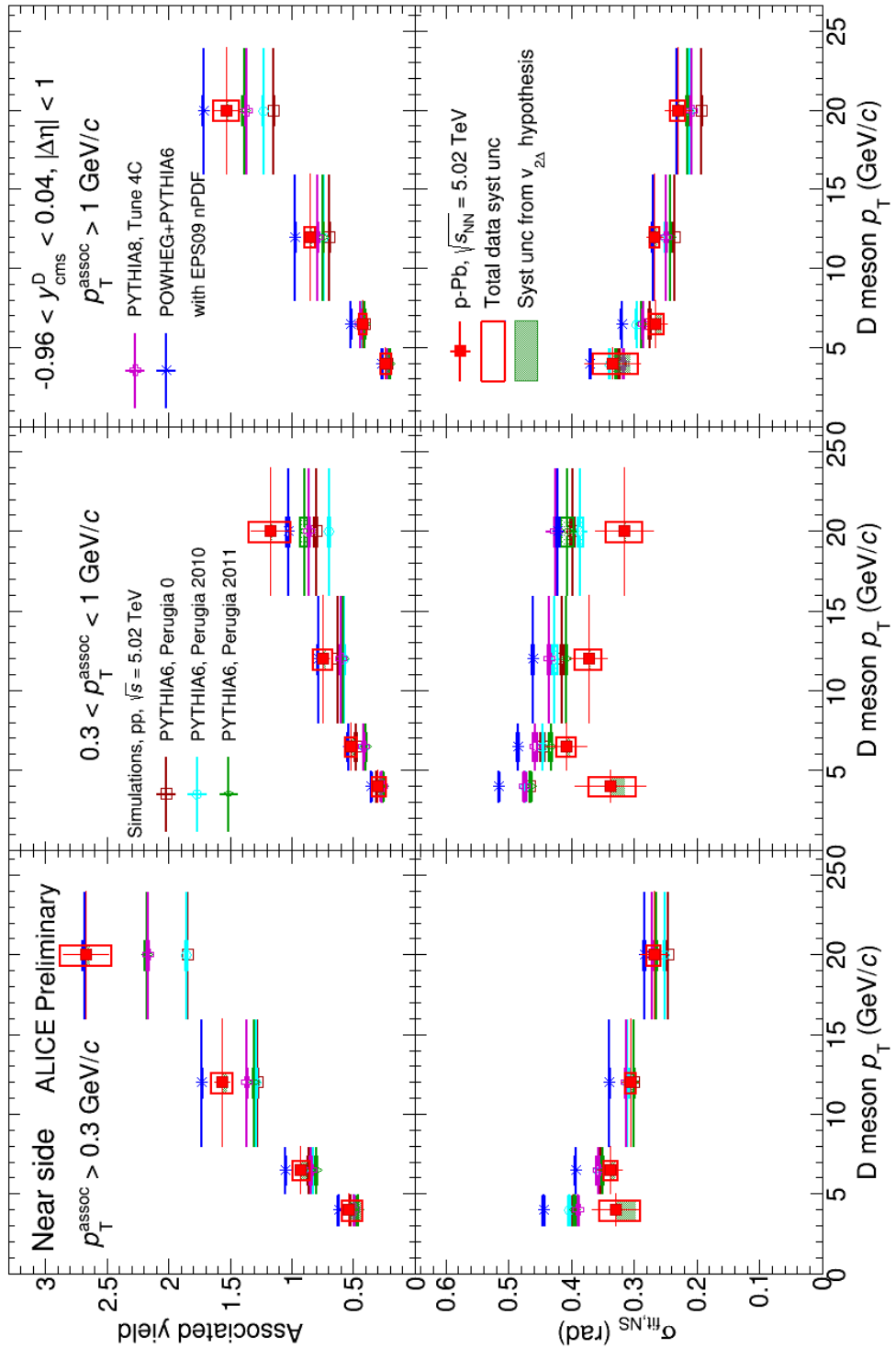
**Figure 61:** Comparison of pp 2010 (black) and p-Pb 2016 (red) near-side peak yields, for the common  $p_T$  ranges.

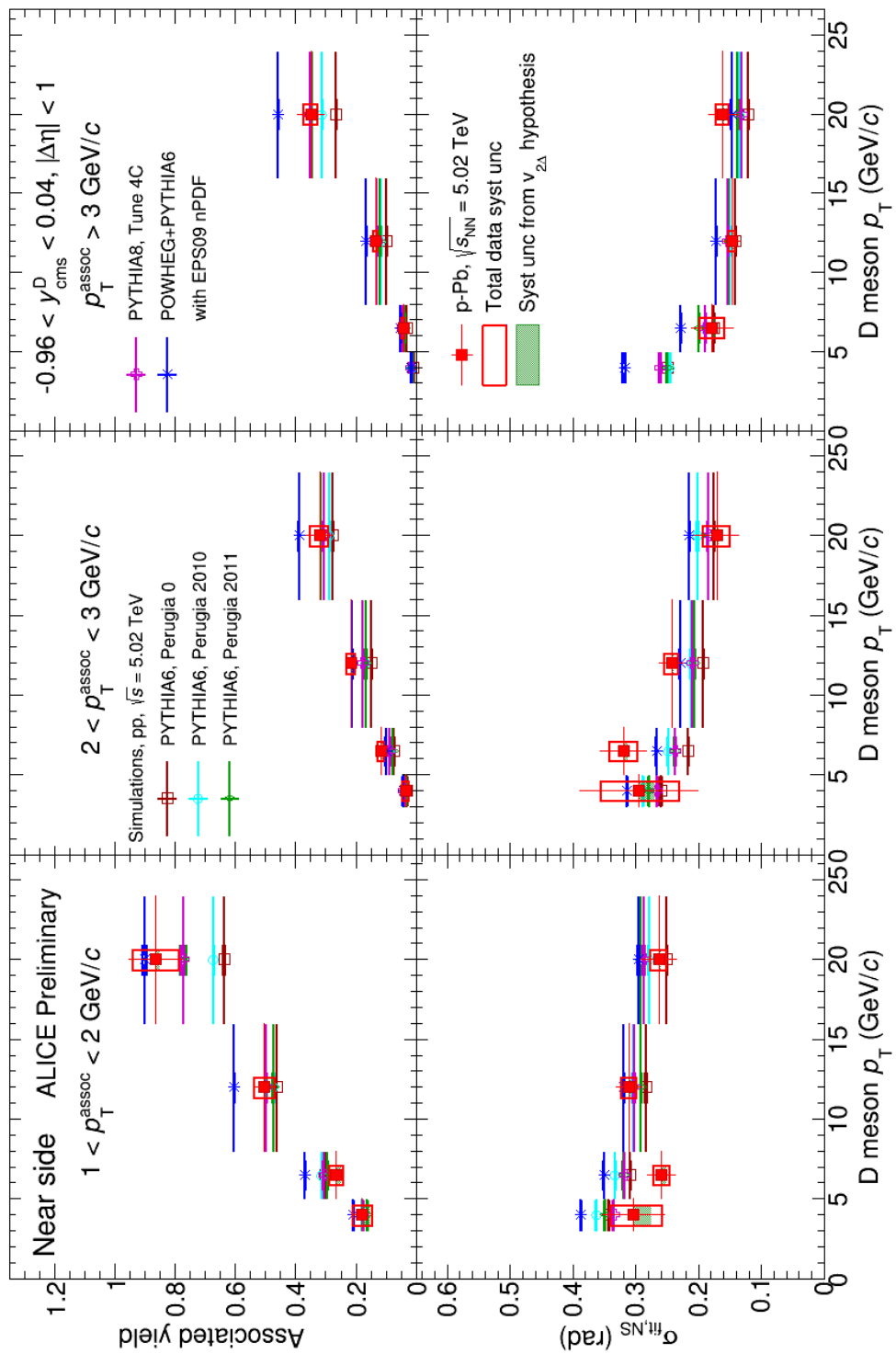
- 793 –  $p_T(D)$ ,  $p_T(\text{assoc})$  trend of NS yield, NS width, AS yield, AS sigma
- 794 – Comparison of correlation distributions with expectations from models (PYTHIA6, PYTHIA8, if  
795 in time POWHEG, EPOS)
- 796 – Comparison of fit observables with expectations from models (PYTHIA6, PYTHIA8, if in time  
797 POWHEG, EPOS)
- 798 – Comparison of correlation distributions with pp 2010 results
- 799 – Comparison of fit observables with pp 2010 results



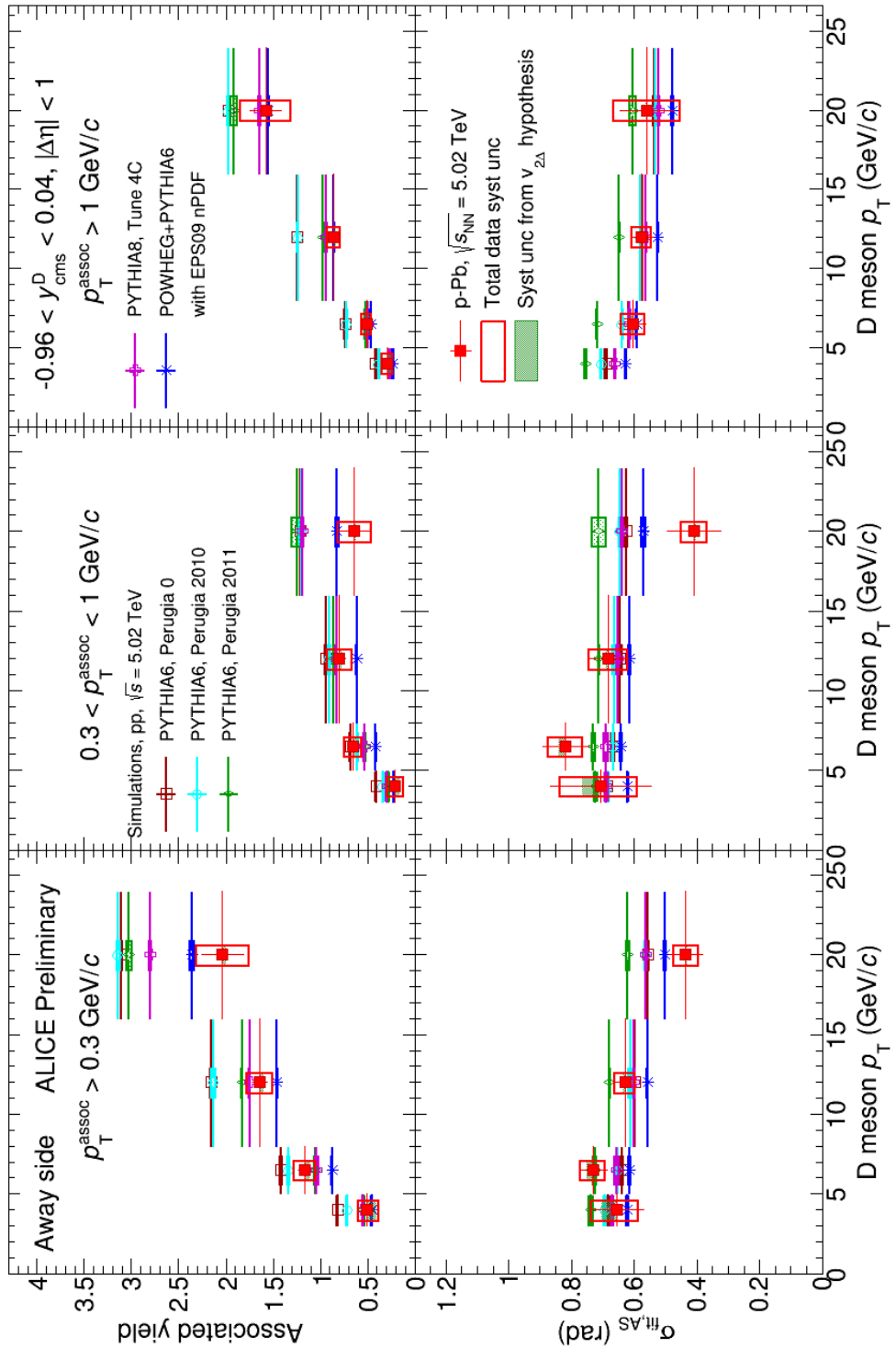


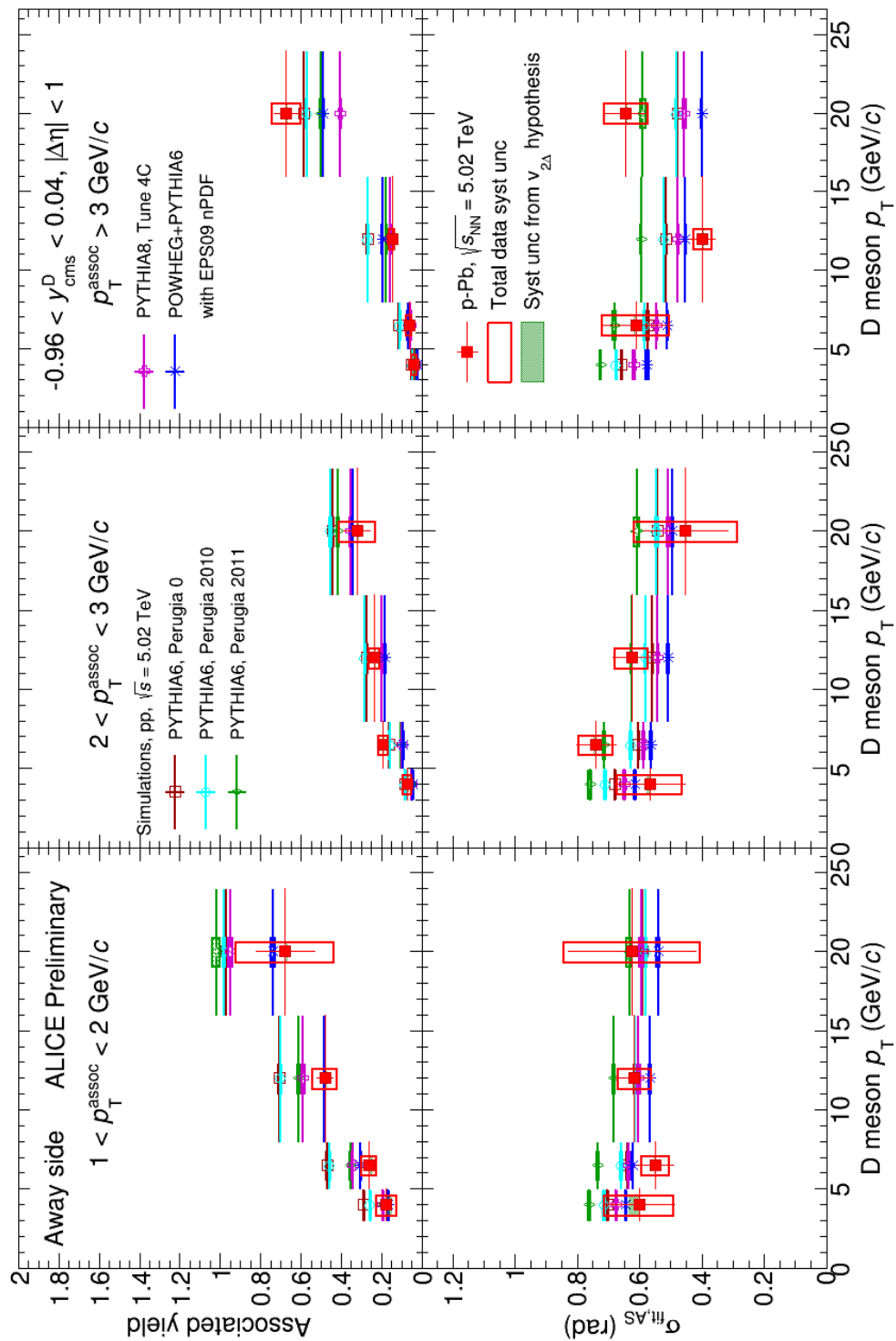
**Figure 62:** Comparison of p-Pb 2016 average D-h correlation distributions and model expectations, for all the studied kinematic ranges.





**Figure 63:** Comparison of near-side peak yields and widths from p-Pb 2016 results and model expectations, for all the studied kinematic ranges.





800 **6 Analysis vs ZNA Centrality**

801 **6.1 General information**

802 In the following section of the note, the D-h correlation analysis as a function of the ZNA centrality (in 0-  
 803 20%, 20-60%, 60-100% classes) is presented, and the results, aiming to be approved as preliminaries for  
 804 the QM2018 approval session, are presented. The goal of the analysis is to investigate possible modifica-  
 805 tions of the correlation peak features (in terms of associated yield and width) among the various centrality  
 806 classes, which could point toward a different fragmentation and hadronization of the charm quark at dif-  
 807 ferent collision centralities. The possibility of studying the D-meson v2 by subtracting low-multiplicity  
 808 from high-multiplicity events (with V0A estimator) was also checked, but the available statistics resulted  
 809 to be too low for such a study. Therefore, this latter study will not be shown here. The analysis proce-  
 810 dure, corrections applied and systematic uncertainty evaluation for the D-h correlation analysis versus  
 811 centrality are very similar on what was done for the centrality-integrated. For this reason, the descrip-  
 812 tion of the analyses will not be repeated (we will refer to paragraphs of the previous section), but only  
 813 the differences and the peculiarity related with the centrality slicing will be addressed. All the relevant  
 814 figures related to procedure, corrections, systematics and results will anyway be shown in the following.

815 **6.2 Analysis strategy**

816 The analysis strategy follows the same steps described in Section 3. Due to the lower statistics available,  
 817 due to the centrality slicing, the transverse momentum ranges of associated tracks are reduced to the  
 818 following three:  $p_T^{\text{assoc}} > 0.3 \text{ GeV}/c$ ,  $0.3 < p_T^{\text{assoc}} < 1 \text{ GeV}/c$ ,  $p_T^{\text{assoc}} > 0.3 \text{ GeV}/c$ . No variations are  
 819 instead done for the four D-meson  $p_T$  ranges:  $3 < p_T^{\text{trig}} < 5 \text{ GeV}/c$ ,  $5 < p_T^{\text{trig}} < 8 \text{ GeV}/c$ ,  $8 < p_T^{\text{trig}} < 16$   
 820  $\text{GeV}/c$ ,  $16 < p_T^{\text{trig}} < 24 \text{ GeV}/c$  (the last bin already suffers by statistics issues).

821 **6.2.1 Dataset and event selection**

822 The data samples and Monte Carlo productions exploited for the analysis are the same as those for the  
 823 cent-integrated studies, i.e. LHC16q+LHC16t (FAST and CENT\_wo\_SDD samples, granting a better  
 824 uniformity along  $\varphi$  and  $\eta$ ) for data and LHC17d2a\_fast\_new (HF enriched) and LHC17f2b\_cent\_woSDD\_fast  
 825 (minimum-bias) for Monte Carlo. The list of runs studied in the analysis is also the same as that showed  
 826 in Table 1. In addition to the previous event selection, described in Section 2, there is an additional  
 827 requirements for the centrality slicing: the ZNA estimator is employed to slice the data sample in three  
 828 complementary centrality classes (0-20%, 20-60%, 60-100%). The chosen slicing grants substantial dif-  
 829 ferences, in terms of average centrality, between the first and the third class, and also allows to fairly  
 830 equalize the number of D-mesons in each class (since the second and third classes are wider, but also  
 831 have a lower  $N_{\text{coll}}$  value w.r.t. the first).

832 The number of analyzed events for the three is approximately:

- 833 – 123M for 0-20% centrality
- 834 – 247M for 20-60% centrality
- 835 – 246M for 60-100% centrality

836 The possibility of using the V0A estimator was also studied - and fully-corrected results for V0A esti-  
 837 mator are also available - but the final choice of the centrality estimator fell on the ZNA. Indeed, this  
 838 estimator is more directly related to the collision geometry than the V0A, which is instead more pointed  
 839 toward a tagging of the event multiplicity.

840 **6.2.2 Mass plots and D-meson selection**

841 The topological selection is largely based on the cut values used for the cent-integrated analysis. For the  
 842  $D^0$ , a specific cut optimization in each centrality class was performed, but tightening/loosening the cut  
 843 values and checking the performance in terms of statistical uncertainties on the background-subtracted  
 844 azimuthal correlation distributions. Some small gain (about 5% to 10% depending on the kinematic  
 845 range) were obtained by:

- 846 – tightening the cosine of pointing angle for the 0-20% centrality
- 847 – slightly loosening the cosine of pointing angle and slightly tightening the normalized  $L_{xy}$  for  
 848 20-60% centrality
- 849 – loosening the cosine of pointing angle for the 60-100% centrality

850 A similar optimization was also tried for the  $D^+$  and  $D^{*+}$  mesons, but no gains were obtained, hence the  
 851 cent-integrated selection was applied.

852 Some of the mass plots for the three D mesons and in the three centrality classes are shown from Fig. 65  
 853 to Fig. 73. NOTE: in the following mass plots,  $D^0$  and  $D^{*+}$  entries are weighted by the inverse of the  
 854 D-meson reconstruction and selection efficiency, while  $D^+$  entries don't.

855 As from the standard procedure (described in details in Section 3), bidimensional ( $\Delta\eta, \Delta\varphi$ ) correlation  
 856 distributions are built for D-meson candidates found in the signal region and in the sidebands, and the  
 857 sidebands correlations, after a proper normalization, are subtracted from the signal region correlations to  
 858 remove the contribution from the correlations from D-meson combinatorial background under the peak.  
 859 The definition of the signal region and sideband does not change with respect to the centrality-integrated  
 860 analysis.

861 **6.2.3 Event mixing**

862 The correction for limited acceptance of the detector, and its local inefficiencies, follows exactly the  
 863 same procedure enounced in subsection 3.3.1. The only small difference deals with the definition of the  
 864 multiplicity ranges of the 9 mixed events pools. Since the three centrality classes contain event with  
 865 different SPD tracklet multiplicity distributions, a modification of these ranges was required to balance  
 866 the number of events entering in each mixed event pool, as follows:

- 867 – 0,55,80,500 for 0-20% centrality
- 868 – 0,35,55,500 for 20-60% centrality
- 869 – 0,20,30,500 for 60-100% centrality

870 **6.2.4 Tracking and trigger efficiency**

871 **(i) Tracking efficiency**

872 The associated track efficiency is based on an online weighting of the D-meson and associated track  
 873 correlation pairs, by means of a three-dimensional efficiency map, as described in details in subsection  
 874 3.3.2 (i). The same efficiency. This choice was based on the fact that no variations on the associated track  
 875 cuts was performed between the two analyses, so the efficiency is not varied, and that there is a negligi-  
 876 ble dependence of the tracking efficiency on the event centrality/multiplicity. The latter assumption was  
 877 checked by evaluating tracking efficiency maps for each centrality slice, i.e. running the tracking effi-  
 878 ciency task on a sample of Monte Carlo reproducing the same event multiplicity distributions (in terms  
 879 of SPD tracklets) observed on data for each slice.

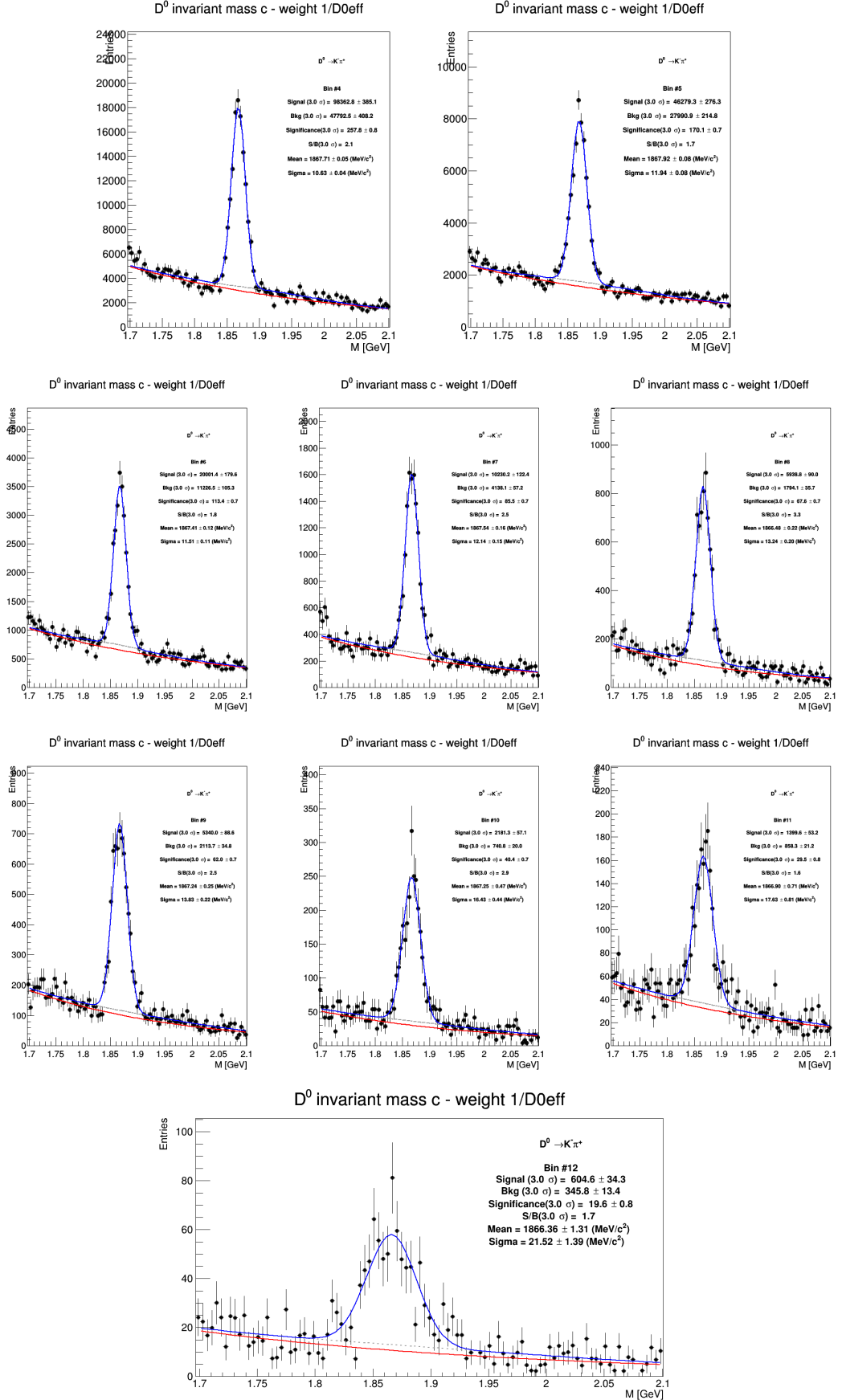


**Figure 65:** Invariant mass distributions of  $D^0$  corrected with efficiency in different  $p_T$  regions for 0-20% centrality class. Top:  $3 < p_T^D < 4$  GeV/c (left),  $4 < p_T^D < 5$  GeV/c right), Mid 1:  $5 < p_T^D < 6$  GeV/c (left),  $6 < p_T^D < 7$  GeV/c (middle),  $7 < p_T^D < 8$  GeV/c (right); Mid2:  $8 < p_T^D < 10$  GeV/c,  $10 < p_T^D < 12$  GeV/c (middle),  $12 < p_T^D < 16$  GeV/c (right) and Bottom:  $16 < p_T^D < 24$  GeV/c.

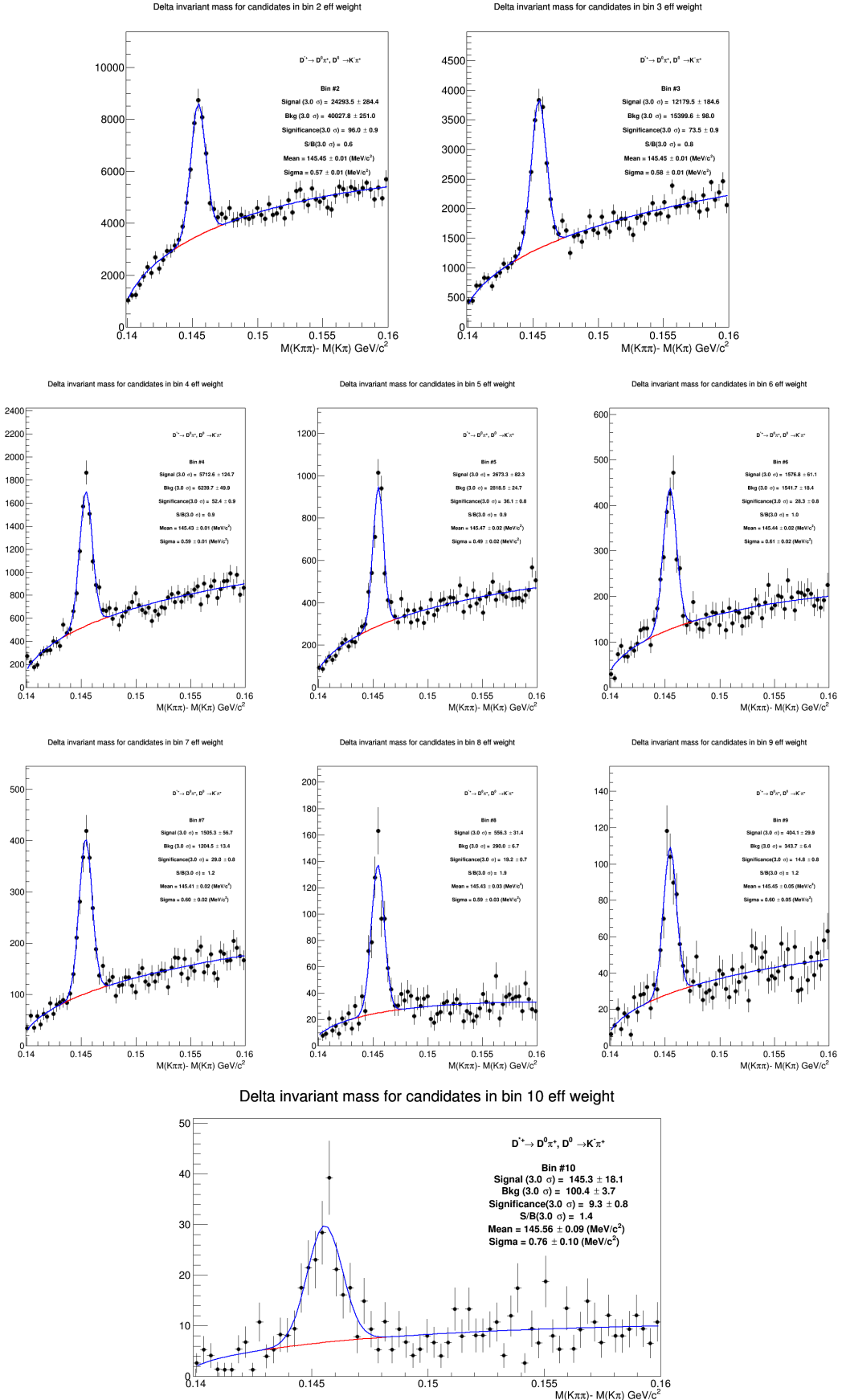


**Figure 66:** Invariant mass distributions of  $D^{*+}$  corrected with efficiency in different  $p_T$  regions for 0-20% centrality class. Top:  $3 < p_T^D < 4$  GeV/ $c$  (left),  $4 < p_T^D < 5$  GeV/ $c$  (right), Mid 1:  $5 < p_T^D < 6$  GeV/ $c$  (left),  $6 < p_T^D < 7$  GeV/ $c$  (middle),  $7 < p_T^D < 8$  GeV/ $c$  (right); Mid2:  $8 < p_T^D < 10$  GeV/ $c$ ,  $10 < p_T^D < 12$  GeV/ $c$  (middle),  $12 < p_T^D < 16$  GeV/ $c$  (right) and Bottom:  $16 < p_T^D < 24$  GeV/ $c$ .

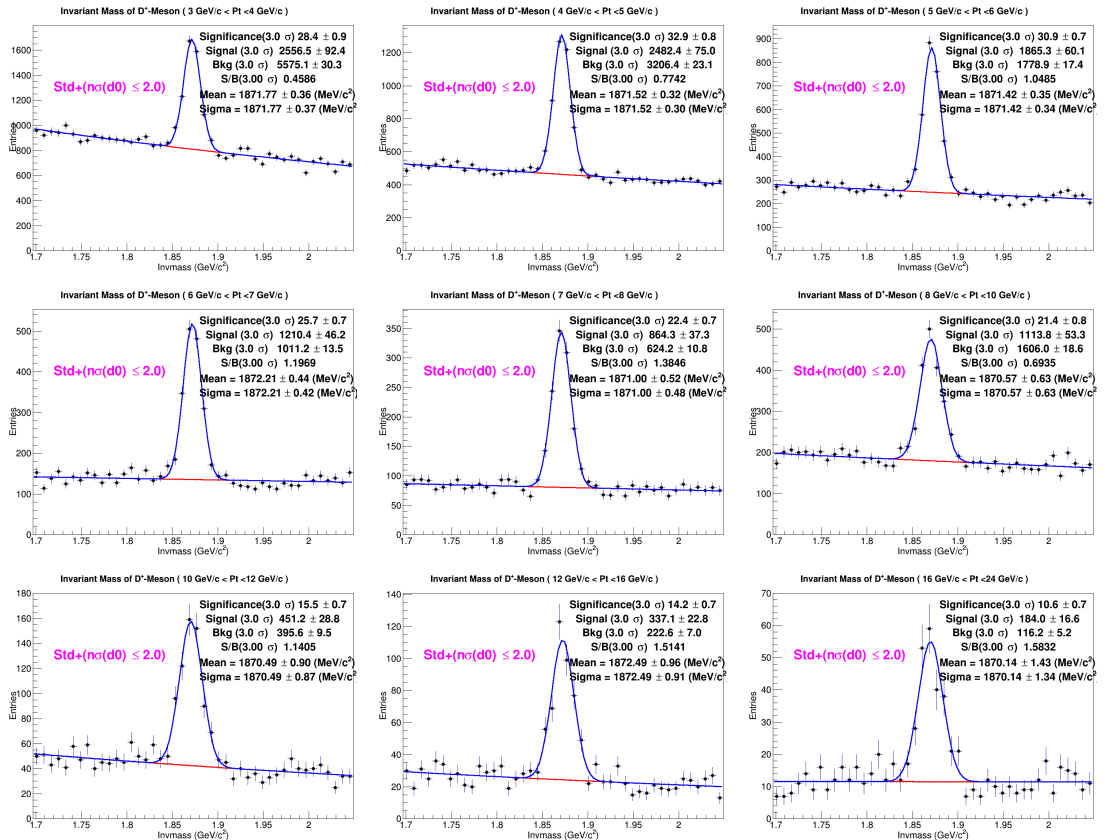


**Figure 67:** Invariant mass distributions of  $D^+$  corrected with efficiency in different  $p_T$  regions for 0-20% centrality class. From top-left to bottom-right:  $3 < p_T^D < 4 \text{ GeV}/c$  (left),  $4 < p_T^D < 5 \text{ GeV}/c$ ,  $5 < p_T^D < 6 \text{ GeV}/c$  (left),  $6 < p_T^D < 7 \text{ GeV}/c$ ,  $7 < p_T^D < 8 \text{ GeV}/c$ ,  $8 < p_T^D < 10 \text{ GeV}/c$ ,  $10 < p_T^D < 12 \text{ GeV}/c$ ,  $12 < p_T^D < 16 \text{ GeV}/c$ ,  $16 < p_T^D < 24 \text{ GeV}/c$ .

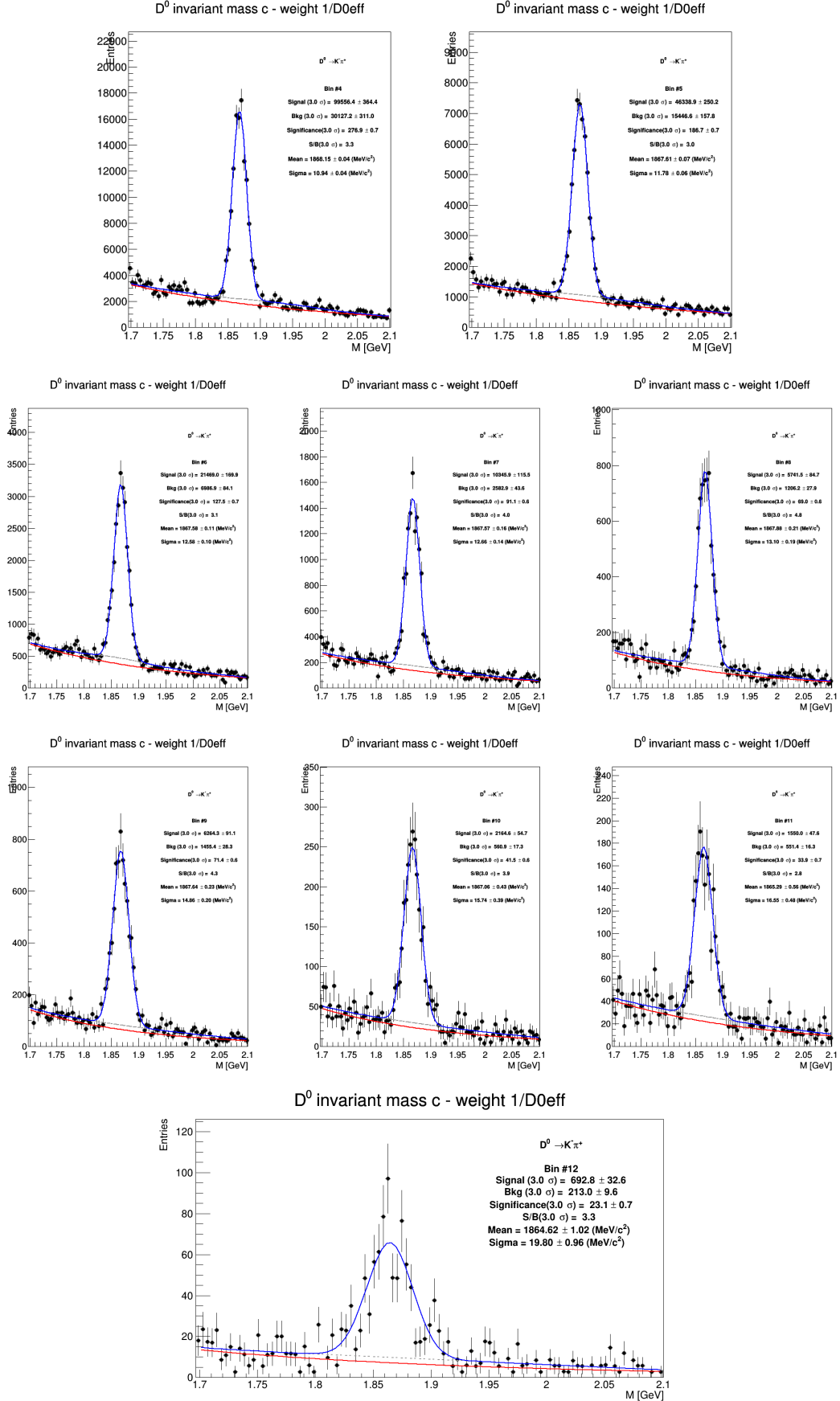


**Figure 68:** Invariant mass distributions of  $D^0$  corrected with efficiency in different  $p_T$  regions for 20-60% centrality class. Top:  $3 < p_T^D < 4 \text{ GeV}/c$  (left),  $4 < p_T^D < 5 \text{ GeV}/c$  right), Mid 1:  $5 < p_T^D < 6 \text{ GeV}/c$  (left),  $6 < p_T^D < 7 \text{ GeV}/c$  (middle),  $7 < p_T^D < 8 \text{ GeV}/c$  (right); Mid2:  $8 < p_T^D < 10 \text{ GeV}/c$ ,  $10 < p_T^D < 12 \text{ GeV}/c$  (middle),  $12 < p_T^D < 16 \text{ GeV}/c$  (right) and Bottom:  $16 < p_T^D < 24 \text{ GeV}/c$ .

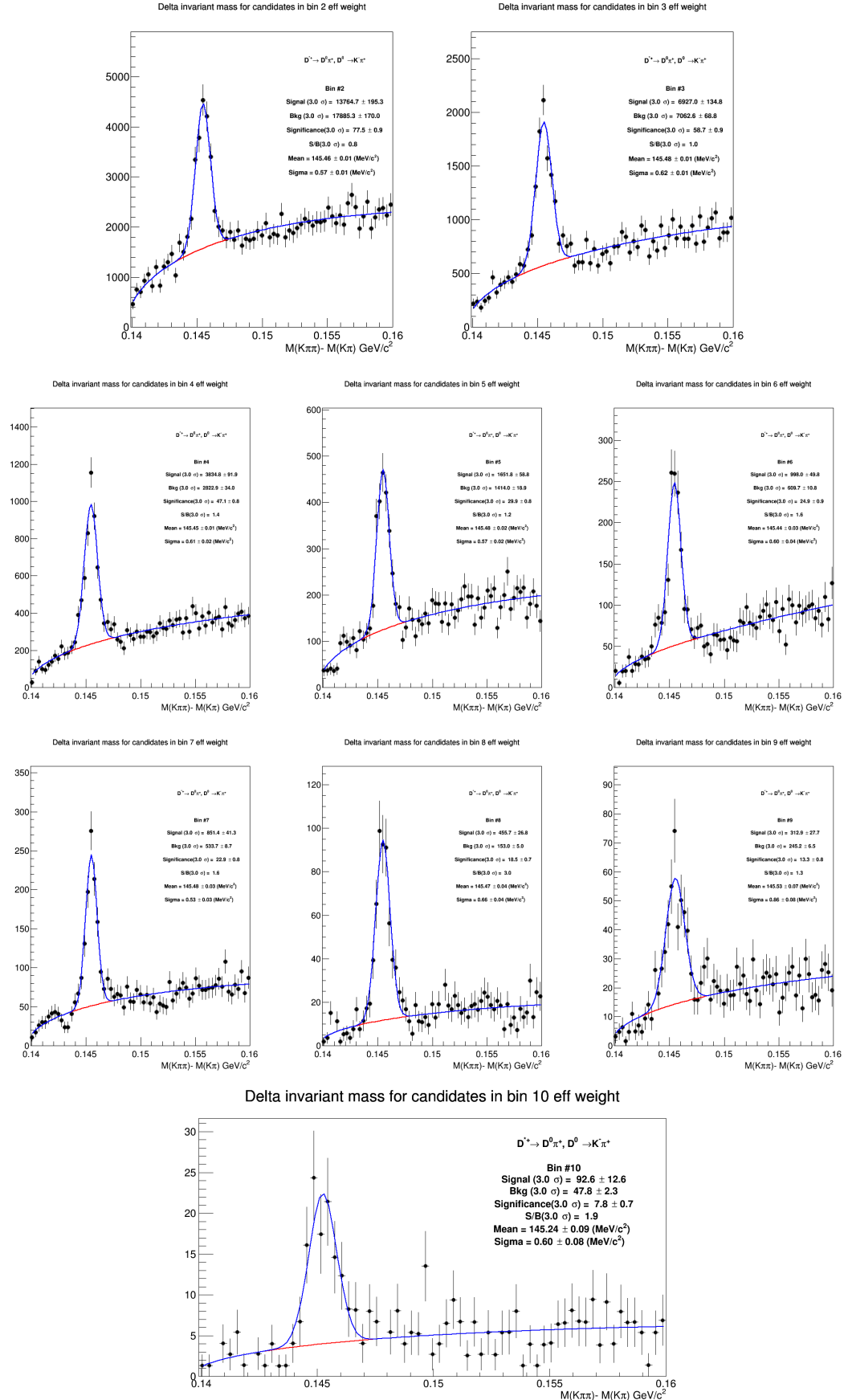


**Figure 69:** Invariant mass distributions of  $D^{*+}$  corrected with efficiency in different  $p_T$  regions for 20-60% centrality class. Top:  $3 < p_T^D < 4$  GeV/ $c$  (left),  $4 < p_T^D < 5$  GeV/ $c$  right), Mid 1:  $5 < p_T^D < 6$  GeV/ $c$  (left),  $6 < p_T^D < 7$  GeV/ $c$  (middle),  $7 < p_T^D < 8$  GeV/ $c$  (right); Mid2:  $8 < p_T^D < 10$  GeV/ $c$ ,  $10 < p_T^D < 12$  GeV/ $c$  (middle),  $12 < p_T^D < 16$  GeV/ $c$  (right) and Bottom:  $16 < p_T^D < 24$  GeV/ $c$ .

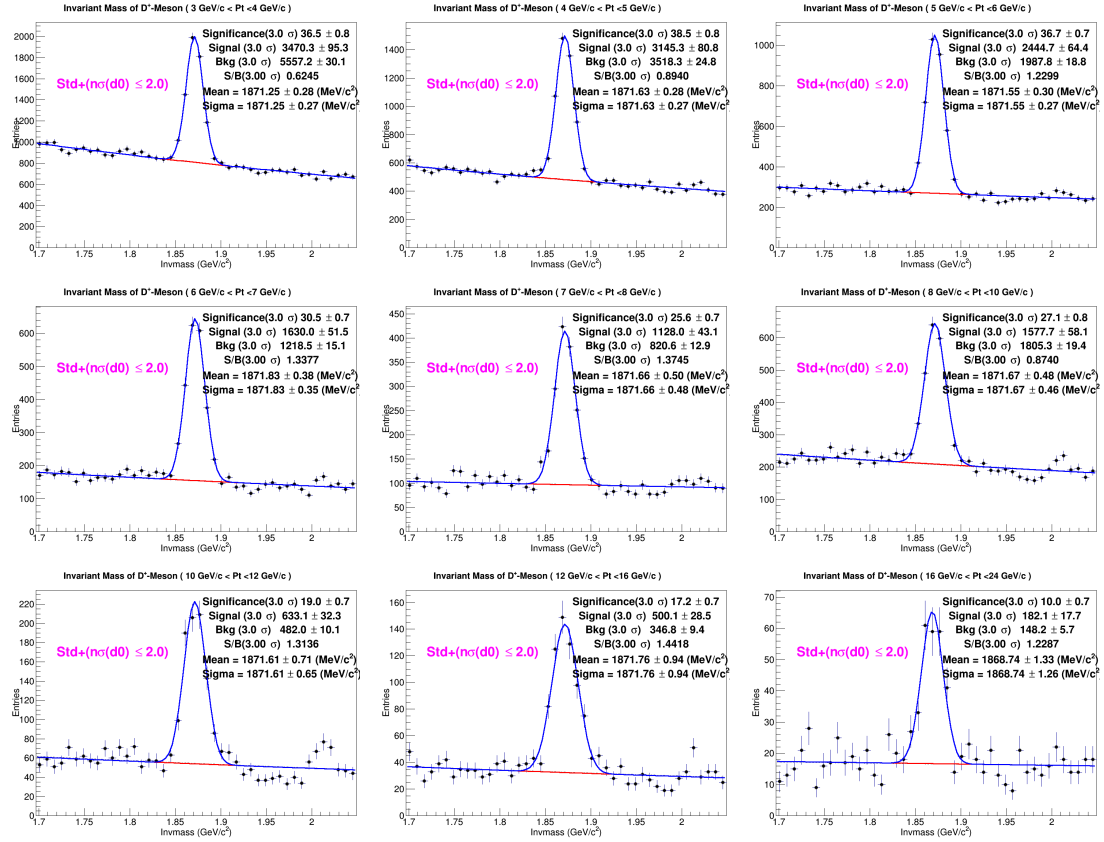


**Figure 70:** Invariant mass distributions of  $D^+$  corrected with efficiency in different  $p_T$  regions for 20-60% centrality class. From top-left to bottom-right:  $3 < p_T^D < 4 \text{ GeV}/c$  (left),  $4 < p_T^D < 5 \text{ GeV}/c$ ,  $5 < p_T^D < 6 \text{ GeV}/c$  (left),  $6 < p_T^D < 7 \text{ GeV}/c$ ,  $7 < p_T^D < 8 \text{ GeV}/c$ ,  $8 < p_T^D < 10 \text{ GeV}/c$ ,  $10 < p_T^D < 12 \text{ GeV}/c$ ,  $12 < p_T^D < 16 \text{ GeV}/c$ ,  $16 < p_T^D < 24 \text{ GeV}/c$ .

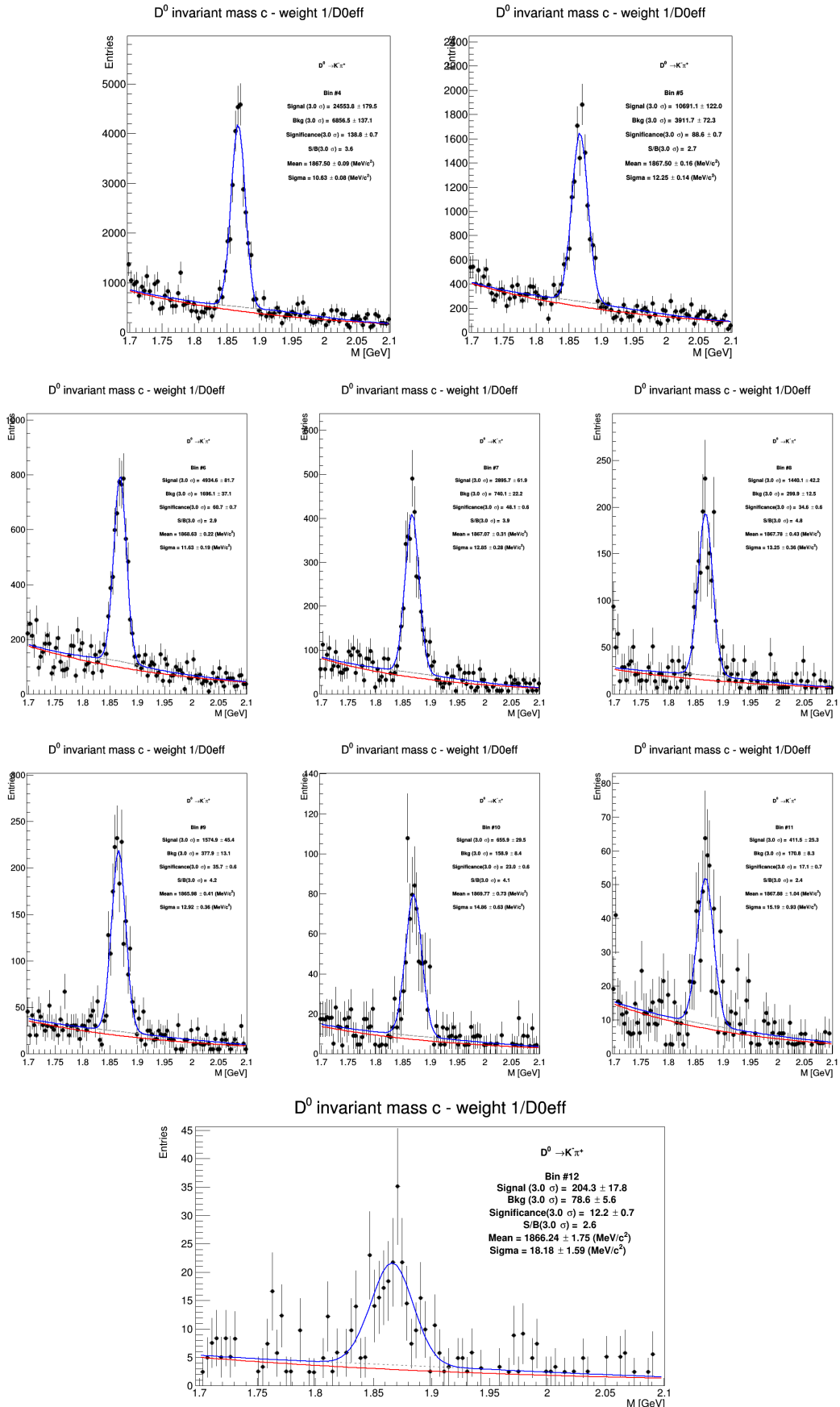


**Figure 71:** Invariant mass distributions of  $D^0$  corrected with efficiency in different  $p_T$  regions for 60-100% centrality class. Top:  $3 < p_T^D < 4 \text{ GeV}/c$  (left),  $4 < p_T^D < 5 \text{ GeV}/c$  right), Mid 1:  $5 < p_T^D < 6 \text{ GeV}/c$  (left),  $6 < p_T^D < 7 \text{ GeV}/c$  (middle),  $7 < p_T^D < 8 \text{ GeV}/c$  (right); Mid2:  $8 < p_T^D < 10 \text{ GeV}/c$ ,  $10 < p_T^D < 12 \text{ GeV}/c$  (middle),  $12 < p_T^D < 16 \text{ GeV}/c$  (right) and Bottom:  $16 < p_T^D < 24 \text{ GeV}/c$ .

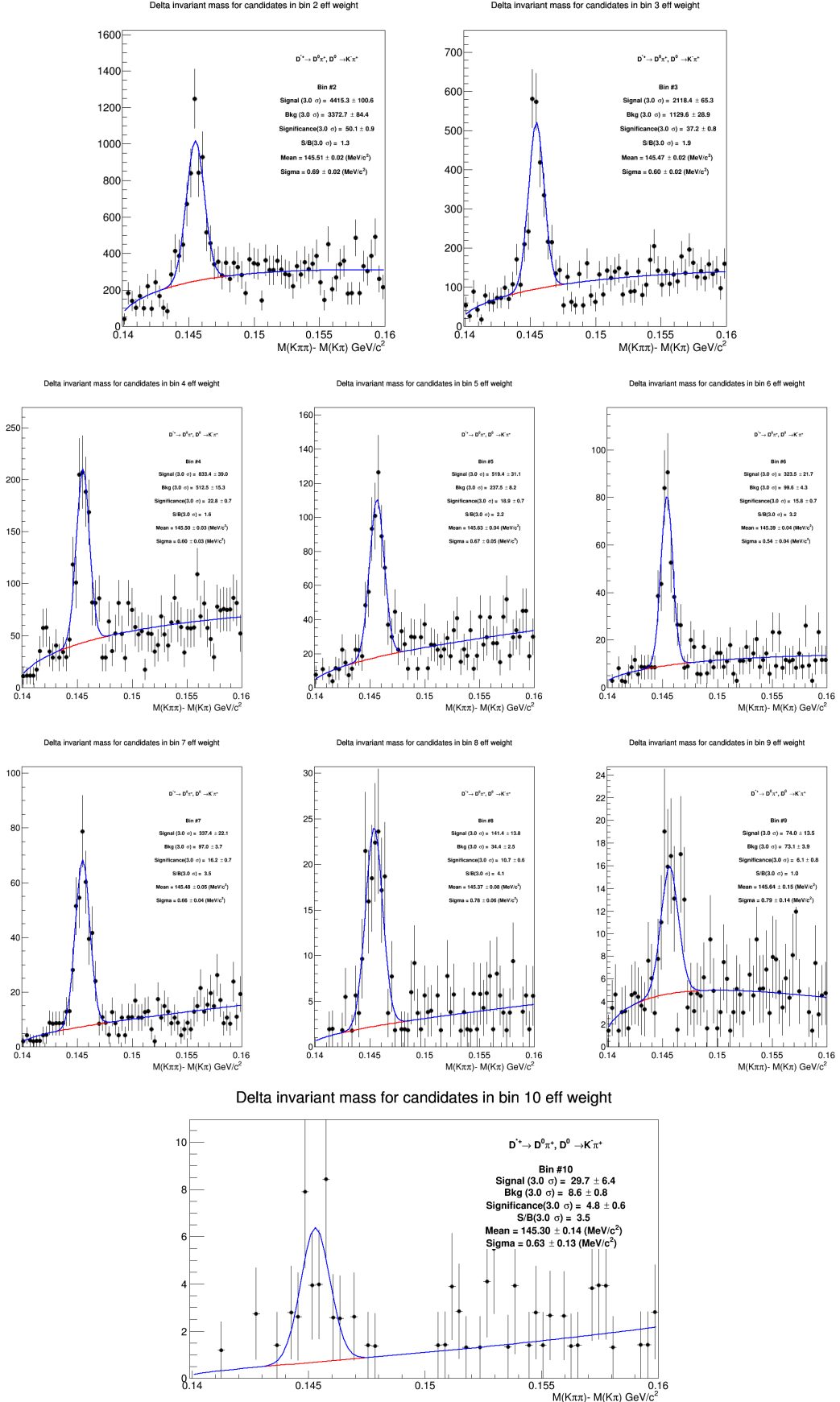


**Figure 72:** Invariant mass distributions of  $D^{*+}$  corrected with efficiency in different  $p_T$  regions for 60-100% centrality class. Top:  $3 < p_T^D < 4$  GeV/c (left),  $4 < p_T^D < 5$  GeV/c (right), Mid 1:  $5 < p_T^D < 6$  GeV/c (left),  $6 < p_T^D < 7$  GeV/c (middle),  $7 < p_T^D < 8$  GeV/c (right); Mid2:  $8 < p_T^D < 10$  GeV/c,  $10 < p_T^D < 12$  GeV/c (middle),  $12 < p_T^D < 16$  GeV/c (right) and Bottom:  $16 < p_T^D < 24$  GeV/c .

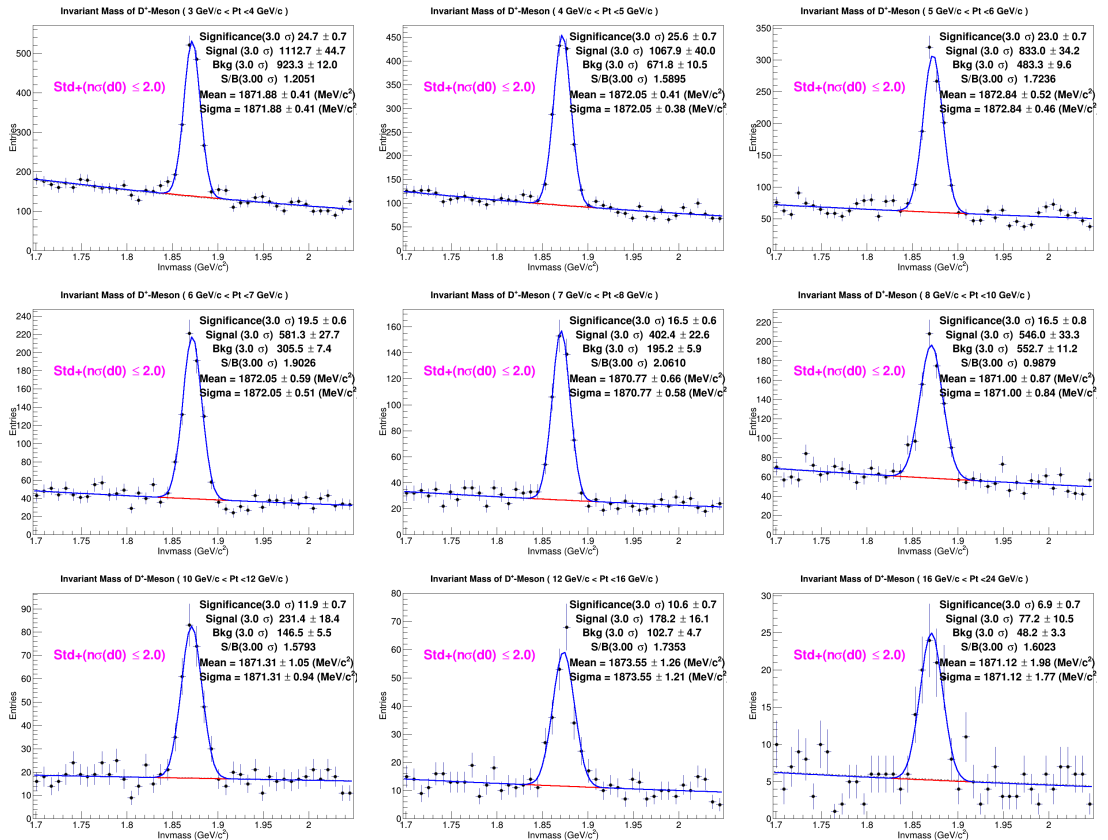


**Figure 73:** Invariant mass distributions of  $D^+$  corrected with efficiency in different  $p_T$  regions for 60-100% centrality class. From top-left to bottom-right:  $3 < p_T^D < 4 \text{ GeV}/c$  (left),  $4 < p_T^D < 5 \text{ GeV}/c$ ,  $5 < p_T^D < 6 \text{ GeV}/c$  (left),  $6 < p_T^D < 7 \text{ GeV}/c$ ,  $7 < p_T^D < 8 \text{ GeV}/c$ ,  $8 < p_T^D < 10 \text{ GeV}/c$ ,  $10 < p_T^D < 12 \text{ GeV}/c$ ,  $12 < p_T^D < 16 \text{ GeV}/c$ ,  $16 < p_T^D < 24 \text{ GeV}/c$ .

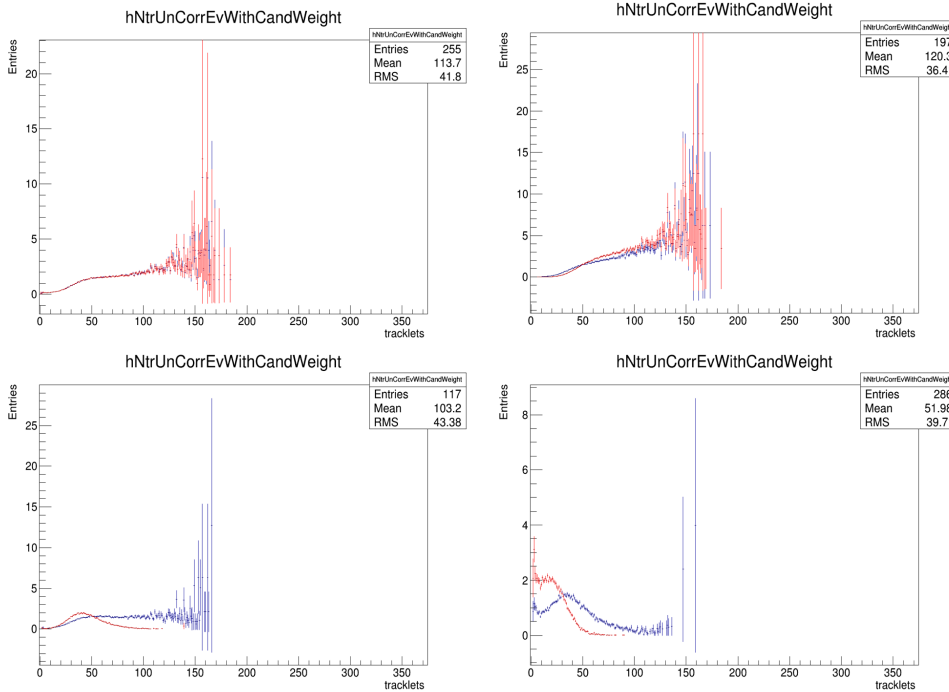


**Figure 74:** Event weights applied to Monte Carlo sample, to mimic the multiplicity distribution for centralities: 0-100% (cent-integrated), 0-20%, 20-60%, 60-100%. Blue points are for ZNA, red points for V0A estimator.

880 The event weights applied to the Monte Carlo events to mimick each centrality slice (as well as those  
 881 to reproduce the same multiplicity also for the centrality-integrated sample) are shown in Fig. 74. They  
 882 are presented for both ZNA and V0A estimator. As it is evident, the V0A tends to favour more high-  
 883 multiplicity events for the 0-20% centrality class, and low-multiplicity events for the 60-100%; the ZNA  
 884 estimator instead equalizes more the event multiplicity distribution in the three centrality slices.

885 After comparing the tracking efficiency maps evaluated applying the event weights on the monte Carlo  
 886 events, with those obtained running on the unweighted Monte Carlo sample, differences of the order of  
 887 few per mille were found, confirming the possibility of using the same tracking efficiency map for the  
 888 various centrality slices. As an example, the ratio of  $p_T$ -projection of the tracking efficiency maps when  
 889 0-20% weights are applied and where no weights are applied on the events is shown in Fig. 75, and it  
 890 results to be fully compatible with 1.

### 891 (ii) Trigger efficiency

892 Differently from the track efficiency, the D-meson reconstruction and selection efficiency can have a  
 893 dependence on the event multiplicity that has to be taken into account. This mainly depends on the lower  
 894 efficiency on the reconstruction of the primary vertex (included in the overall D-meson reconstruction  
 895 efficiency) for very low multiplicity events. Indeed, as it can be seen in Fig. 76, the efficiency is rather  
 896 flat above 20-30 tracklets, and starts to drop below that SPD tracklet multiplicity.

897 To consider this dependence, separate trigger efficiency maps were built for each centrality slice, by  
 898 running the trigger efficiency task on the reweighted Monte Carlo enriched sample (using the same event  
 899 weights described above). In Figs. 77, 78, 79, the trigger efficiency maps, and their projection onto the  
 900  $p_T$  axis, are shown for the three D mesons in each centrality class considered.

901 Then, the trigger efficiency correction follows the same procedure, based on an online-weighting of the  
 902 correlation pairs, described in subsection 3.3.2 (ii).

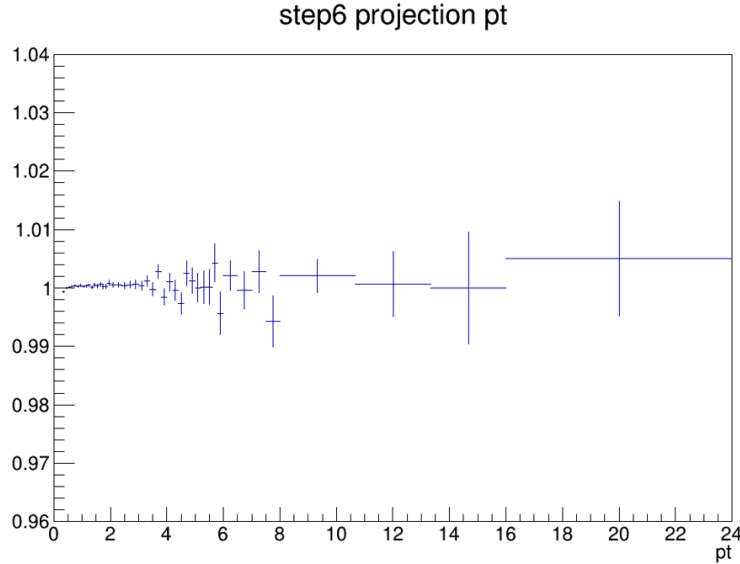


**Figure 75:** Ratio of 1D track efficiency map vs  $p_T$  with and without event weights (example for 0-20%) applied on the Monte Carlo sample.

### 903 6.2.5 Correction for bias on $B$ to $D$ decay topologies

904 As described in detail in subsection 3.3.3, performing a Monte Carlo closure test allows to spot a bias on  
 905 the correlation distributions, due to the presence of structures in the near-side region for  $B \rightarrow D$ -h correlations,  
 906 induced by the topological selection on the  $D$ . After the projection of the correlation distributions  
 907 on  $\Delta\phi$ , a correction has thus to be applied on the azimuthal correlation distributions. The procedure for  
 908 the evaluation of the correction to apply on data is repeated for each centrality class. The outcome of the  
 909 MC closure test, i.e. the Reco/Kine ratios, is shown for each centrality class in Fig. 80, 81, 82 (using the  
 910  $D^0$  meson as trigger).

911 As (slightly) visible from the plots, the  $B \rightarrow D$  structures are larger in 0-20% rather than in 60-100% if  
 912 only the associated tracks coming from beauty are considered (light-green point). Anyway, the situation  
 913 is reversed when considering all the associated tracks, i.e. also the uncorrelated pairs (dark-green points)  
 914 - which is the case to be considered to evaluate the correction. This is understandable, due to the lower  
 915 presence of uncorrelated pairs in 60-100%, which enhances the peak/baseline ratio w.r.t. 0-20%. This  
 916 also reflects in a (slightly) larger correction for 60-100% centrality class rather than for 20-60% and  
 917 0-20%. Anyway, the overall correction applied on data (following Equation 3) is always lower than 3%,  
 918 even for the worst case, being the lowest  $D$ -meson  $p_T$  bin ( $3 < p_T < 5$  GeV/c) and the highest associated  
 919 track  $p_T$  bin ( $p_T > 1$  GeV/c). Furthermore, the difference of the correction values among the different  
 920 centrality classes is never larger than 1.5%.

### 921 6.2.6 Secondary track contamination

922 The strategy for the purity correction and the Monte Carlo study for its quantitative evaluation are  
 923 similar to that described in subsection 3.3.4. A major improvement was introduced for the centrality-  
 924 dependent analysis: the correction for removing the secondary tracks passing the associated track selec-  
 925 tion is not anymore performed as a global scale factor of the correlation distributions (i.e. flat in  $\Delta\phi$ ),  
 926 but is now performed differentially along the azimuthal axis (i.e. applied bin-per-bin on the azimuthal  
 927 correlation distributions). This choice was done because, from the Monte Carlo analysis, the contamina-  
 928 tion of secondary particles in the selected track sample (or, in a complementary view, the purity) is not  
 929 completely flat in  $\Delta\phi$ , but shows some structures, in particular in the near-side region. Some examples  
 930 are shown in Fig. 83 (blue histogram), where the fraction of primary track vs  $\Delta\phi$  is shown for exemplary

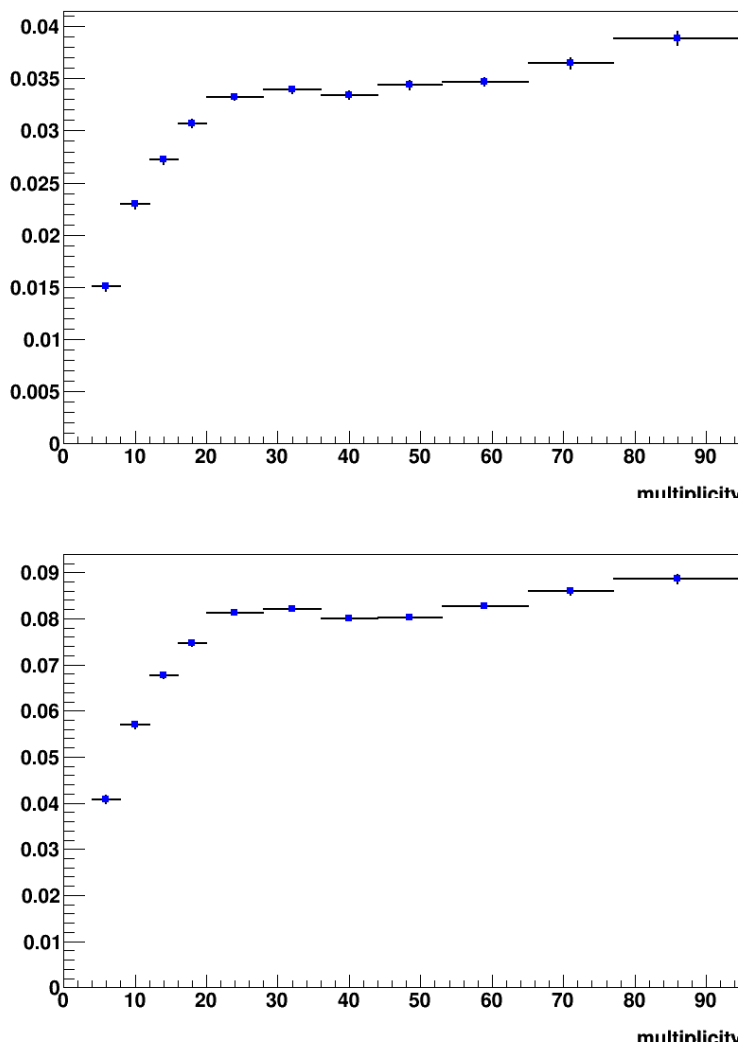


**Figure 76:** Multiplicity dependence of prompt (top) and non-prompt (bottom)  $D^*$  meson efficiency in 0-20% centrality class.

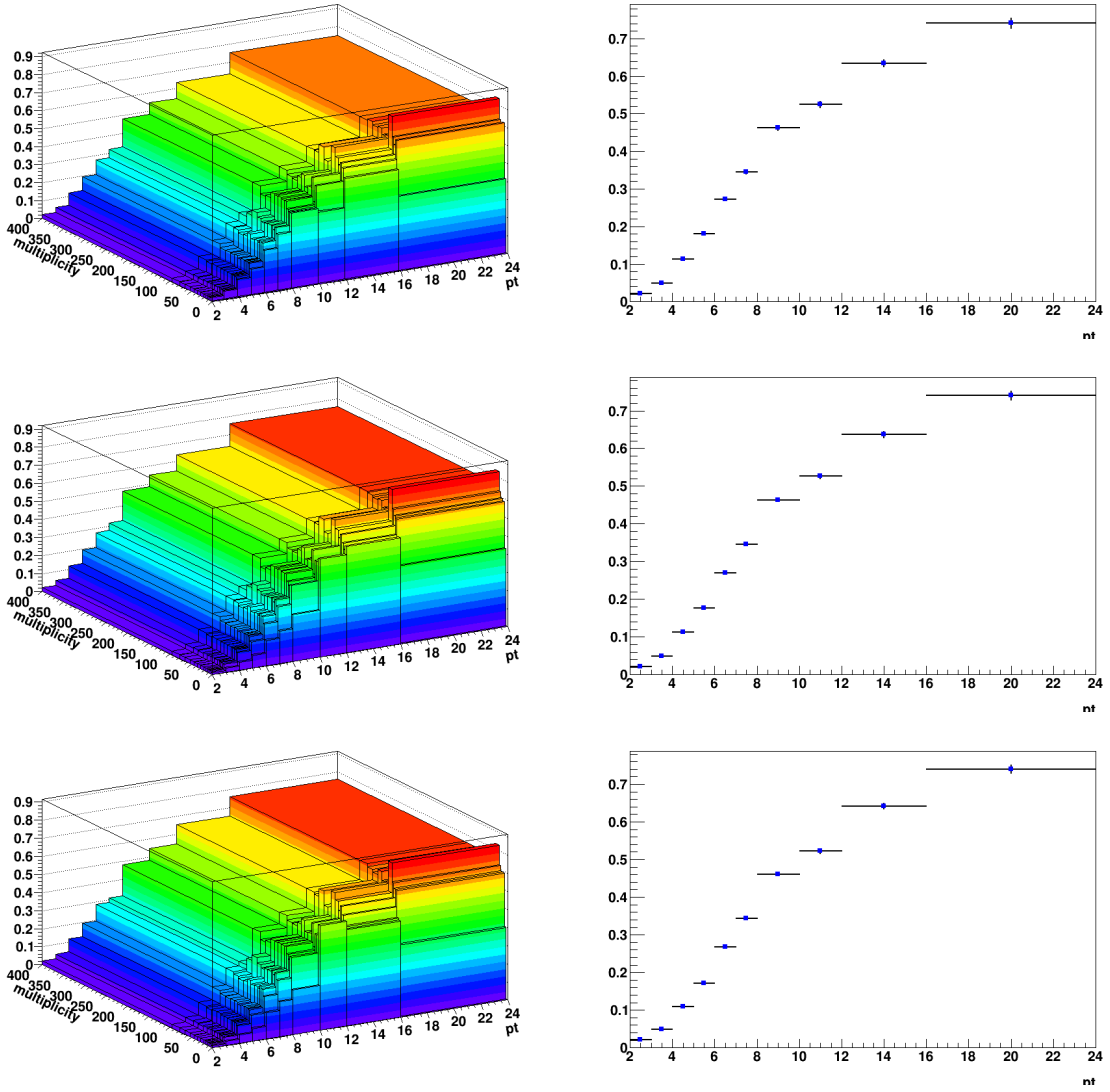


**Figure 77:** Top panel: ( $p_T$ , multiplicity) dependence (left) and  $p_T$  dependence (right) of prompt  $D^{*+}$  meson efficiency in 0-20%. Mid panel: ( $p_T$ , multiplicity) dependence (left) and  $p_T$  dependence (right) of prompt  $D^{*+}$  meson efficiency in 20-60%. Bottom panel: ( $p_T$ , multiplicity) dependence (left) and  $p_T$  dependence (right) of prompt  $D^{*+}$  meson efficiency in 60-100%.

931 kinematic regions.

932 Though these structures are small (about 1%), they could be amplified after the subtraction of the base-  
933 line, when going to the yield evaluation. For this reason, the  $\Delta\phi$ -differential correction was chosen  
934 implemented. In particular, three approaches were tried, by multiplying the data correlation distribution  
935 by:

- 936 – the MC primary/inclusive histogram (blue histogram in Fig. 83)  
937 – a polynomial fit applied to the MC primary/inclusive histogram (red curve in Fig. 83)  
938 – a moving average, considering 3 points, of the MC primary/inclusive histogram (blue histogram in  
939 Fig. 83)

940 Each approach has pros and cons, since directly using the primary/inclusive histogram gives a correction

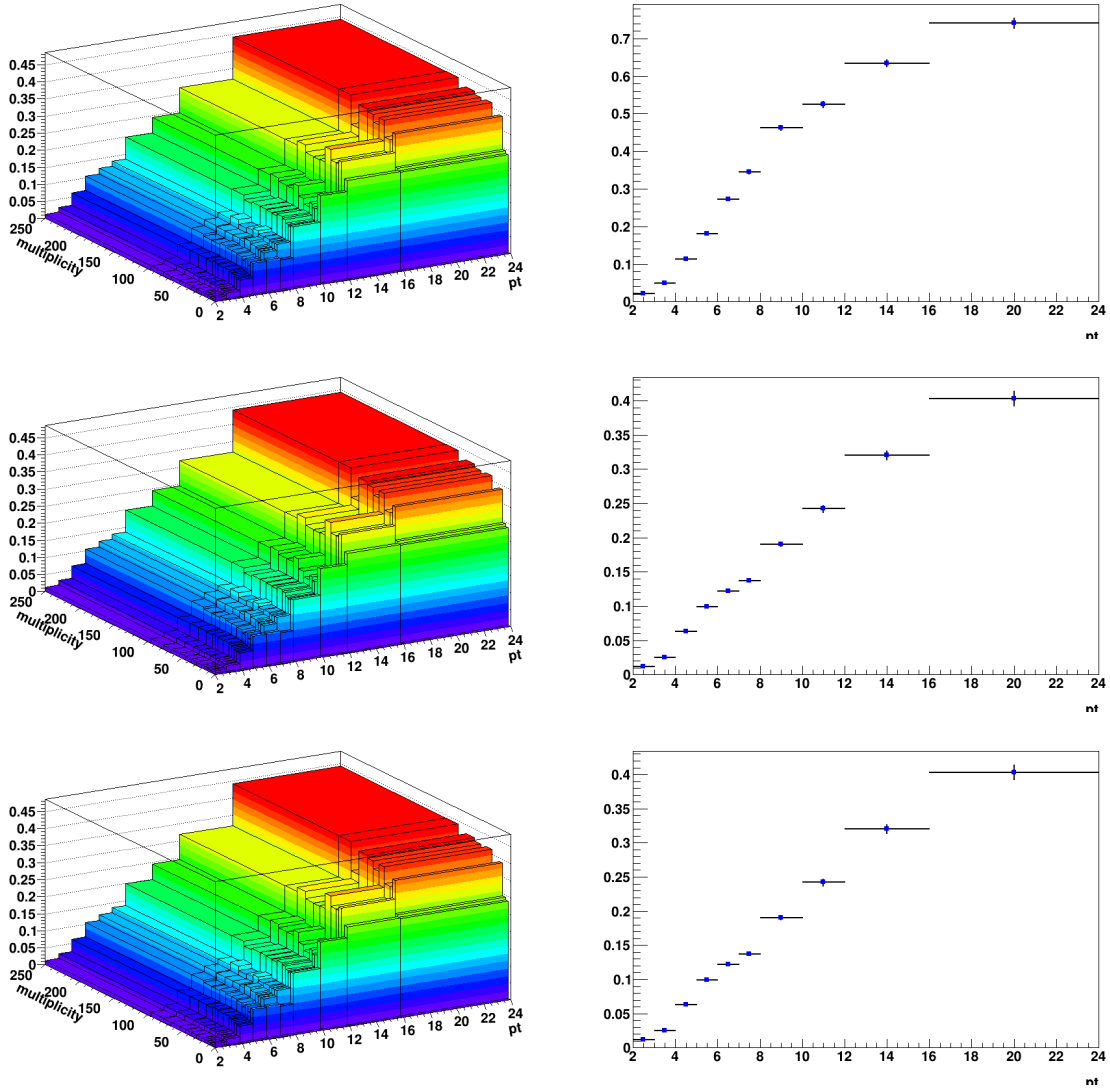


**Figure 78:** Top panel: ( $p_T$ , multiplicity) dependence (left) and  $p_T$  dependence (right) of prompt  $D^0$  meson efficiency in 0-20%. Mid panel: ( $p_T$ , multiplicity) dependence (left) and  $p_T$  dependence (right) of prompt  $D^0$  meson efficiency in 20-60%. Bottom panel: ( $p_T$ , multiplicity) dependence (left) and  $p_T$  dependence (right) of prompt  $D^0$  meson efficiency in 60-100%.

941 strongly dependent on the statistical fluctuations, while using the fit or the moving average smoothen the  
 942 fluctuation, but also the structures with a physical origin. For this reason, a comparison of the outcome  
 943 of the correction after applying either of the approaches (and the old 'flat' correction approach) was  
 944 performed. The results of the check is shown in Fig. 84, for  $3 < p_T^{\text{trig}} < 5 \text{ GeV}/c$  (situation is identical  
 945 in the other D-meson  $p_T$  ranges). The difference of the new approaches w.r.t. the flat one is around  
 946 1% at maximum (under the near-side, for  $p_T(\text{assoc}) > 1 \text{ GeV}/c$ , while the outcome of the correction is  
 947 completely equivalent when using either of the new approaches.

948 The correction was independently evaluated on each centrality class (by applying the event weights to  
 949 the Monte Carlo). No significant deviations of the purity were found among the different centralities. As  
 950 an example, Figs. , , show the average purity contribution (linear fit over the distributions of slide), for  
 951 the various kinematic regions, for each centrality class (one per figure). The same conclusion about the  
 952 compatibility among the various classes holds also for the differential correction, effectively applied on  
 953 data.

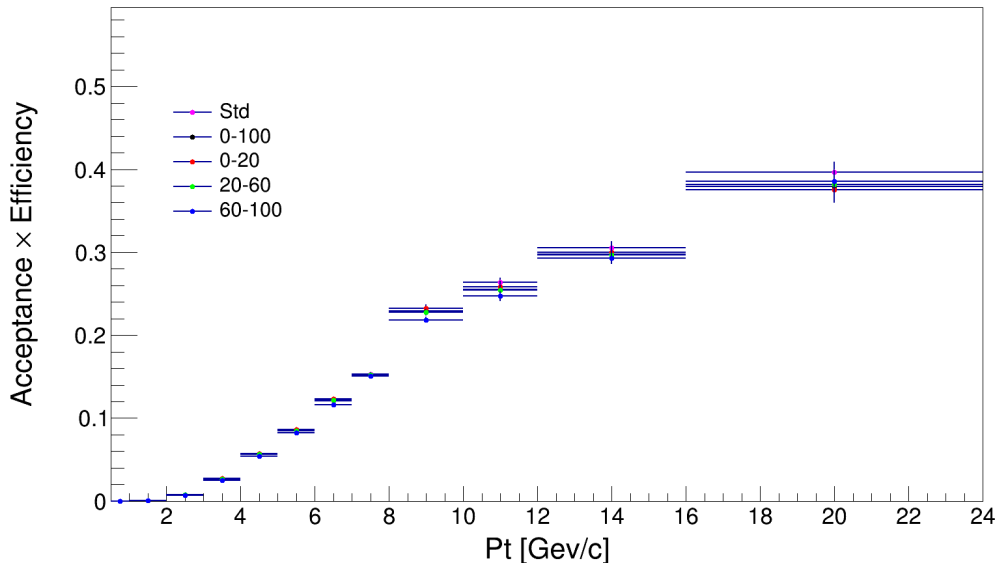


Figure 79:  $D^+$  reco and selection efficiency for the various centrality classes (1D projection).

### 6.2.7 Feed-down correction

The technique for performing the feed-down correction is based on the subtraction of templates of correlation distributions of feed-down  $D$ - and charged particle correlations obtained from Monte Carlo simulations - after their rescaling by means of the fraction of prompt  $D$  meson in the reconstructed  $D$ -meson sample,  $f_{\text{prompt}}$ . The procedure fully coincides to that used for the cent-integrated analysis, described in details in subsection 3.3.5. The only modification consists in a possible dependence of the feed-down correction on the centrality of the event, for the following reasons:

- Variation of  $D$ -meson efficiency vs centrality, due to the lower primary vertex reconstruction efficiency at low multiplicity and, for  $D^0$ , to centrality-dependent topological cut values. This, in turn, impacts on  $f_{\text{prompt}}$  because of its dependence on the  $D$ -meson efficiency.
- Possible variation of  $R_{p\text{Pb}}(B)/R_{p\text{Pb}}(D)$ , on which  $f_{\text{prompt}}$  depends, on the centrality of the event.
- Dependence of the  $B \rightarrow D$ -hadron correlation peaks on the event centrality. This would require modifying the MC templates for  $B \rightarrow D$ -hadron correlations used for each centrality class. This effect was neglected, since no evidences exist, at the moment, on a possible modification of the heavy-flavour quark fragmentation versus the event multiplicity.

To consider the above effects, an independent evaluation of  $f_{\text{prompt}}$  was performed in each centrality class, using the specific trigger efficiency maps and possible ranges of  $R_{p\text{Pb}}(B)/R_{p\text{Pb}}(D)$  (entering in the  $f_{\text{prompt}}$  uncertainty), from 0.9-1.1 in 60-100% to 0.9-1.3 in 0-20%. The resulting  $f_{\text{prompt}}$  values are shown, for the three  $D$  mesons, in Figs. 88, 89, 90.

## 6.3 Systematic uncertainties

In the following, the seven systematic uncertainties on the  $\Delta\phi$  correlation distributions are described first, and then the systematic uncertainties on the fit observables are shown.

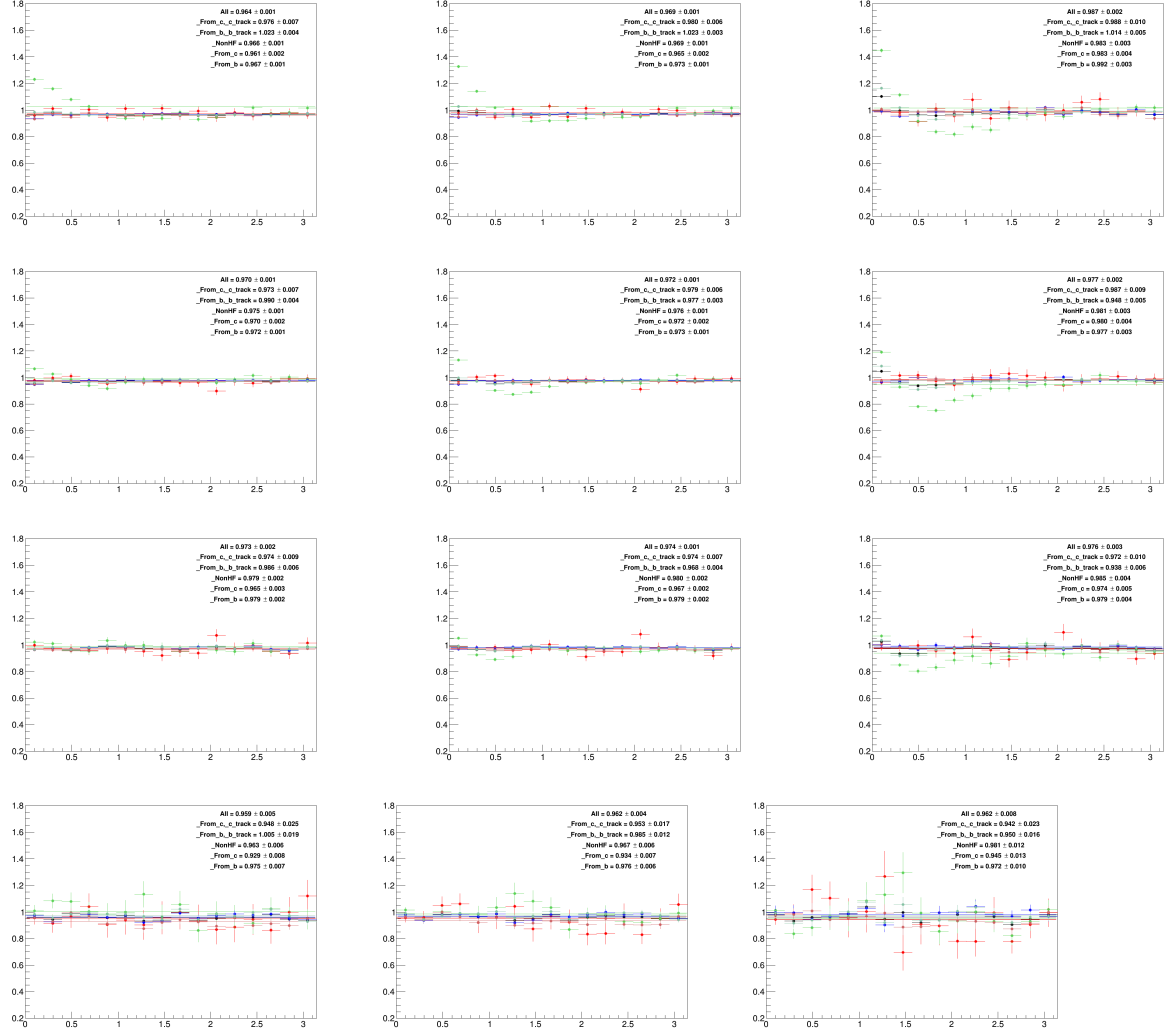


**Figure 80:** Kine/Reco ratio of  $D^0$ -hadrons azimuthal correlation distribution obtained from Monte Carlo in 0-20% centrality class. Black points: All  $D^0$ -all hadrons, normalized by all  $D^0$  triggers; light red points:  $D^0$  from c-hadrons from c, normalized by c- $D^0$  triggers; dark red points:  $D^0$  from c-all hadrons, normalized by c- $D^0$  triggers; light green points:  $D^0$  from b-hadrons from b, normalized by b- $D^0$  triggers; dark green points:  $D^0$  from b-all hadrons, normalized by b- $D^0$  triggers; blue points: All  $D^0$ -hadrons from light quarks, normalized by all  $D^0$  triggers. The panels show the ranges:  $3 < p_T(D) < 5 \text{ GeV}/c$ ,  $0.3 < p_T(\text{assoc}) < 1 \text{ GeV}/c$  (top-left);  $3 < p_T(D) < 5 \text{ GeV}/c$ ,  $p_T(\text{assoc}) > 1 \text{ GeV}/c$  (top-right);  $8 < p_T(D) < 16 \text{ GeV}/c$ ,  $0.3 < p_T(\text{assoc}) < 1 \text{ GeV}/c$  (bottom-left);  $8 < p_T(D) < 16 \text{ GeV}/c$ ,  $p_T(\text{assoc}) > 1 \text{ GeV}/c$  (bottom-right).

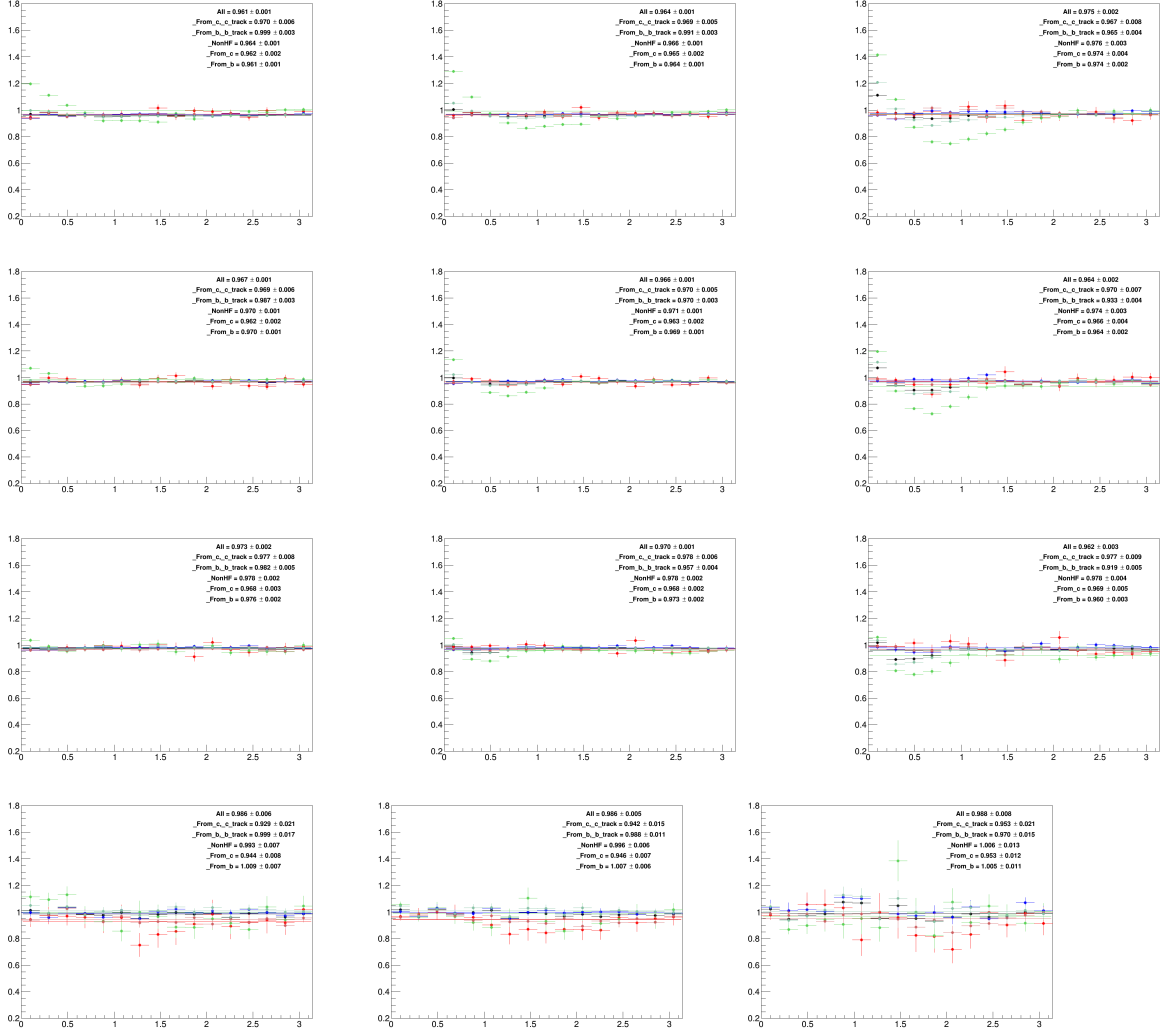


**Figure 81:** Kine/Reco ratio of  $D^0$ -hadrons azimuthal correlation distribution obtained from Monte Carlo in 20-60% centrality class. Black points: All  $D^0$ -all hadrons, normalized by all  $D^0$  triggers; light red points:  $D^0$  from c-hadrons from c, normalized by c- $D^0$  triggers; dark red points:  $D^0$  from c-all hadrons, normalized by c- $D^0$  triggers; light green points:  $D^0$  from b-hadrons from b, normalized by b- $D^0$  triggers; dark green points:  $D^0$  from b-all hadrons, normalized by b- $D^0$  triggers; blue points: All  $D^0$ -hadrons from light quarks, normalized by all  $D^0$  triggers. The panels show the ranges:  $3 < p_T(D) < 5 \text{ GeV}/c$ ,  $0.3 < p_T(\text{assoc}) < 1 \text{ GeV}/c$  (top-left);  $3 < p_T(D) < 5 \text{ GeV}/c$ ,  $p_T(\text{assoc}) > 1 \text{ GeV}/c$  (top-right);  $8 < p_T(D) < 16 \text{ GeV}/c$ ,  $0.3 < p_T(\text{assoc}) < 1 \text{ GeV}/c$  (bottom-left);  $8 < p_T(D) < 16 \text{ GeV}/c$ ,  $p_T(\text{assoc}) > 1 \text{ GeV}/c$  (bottom-right).

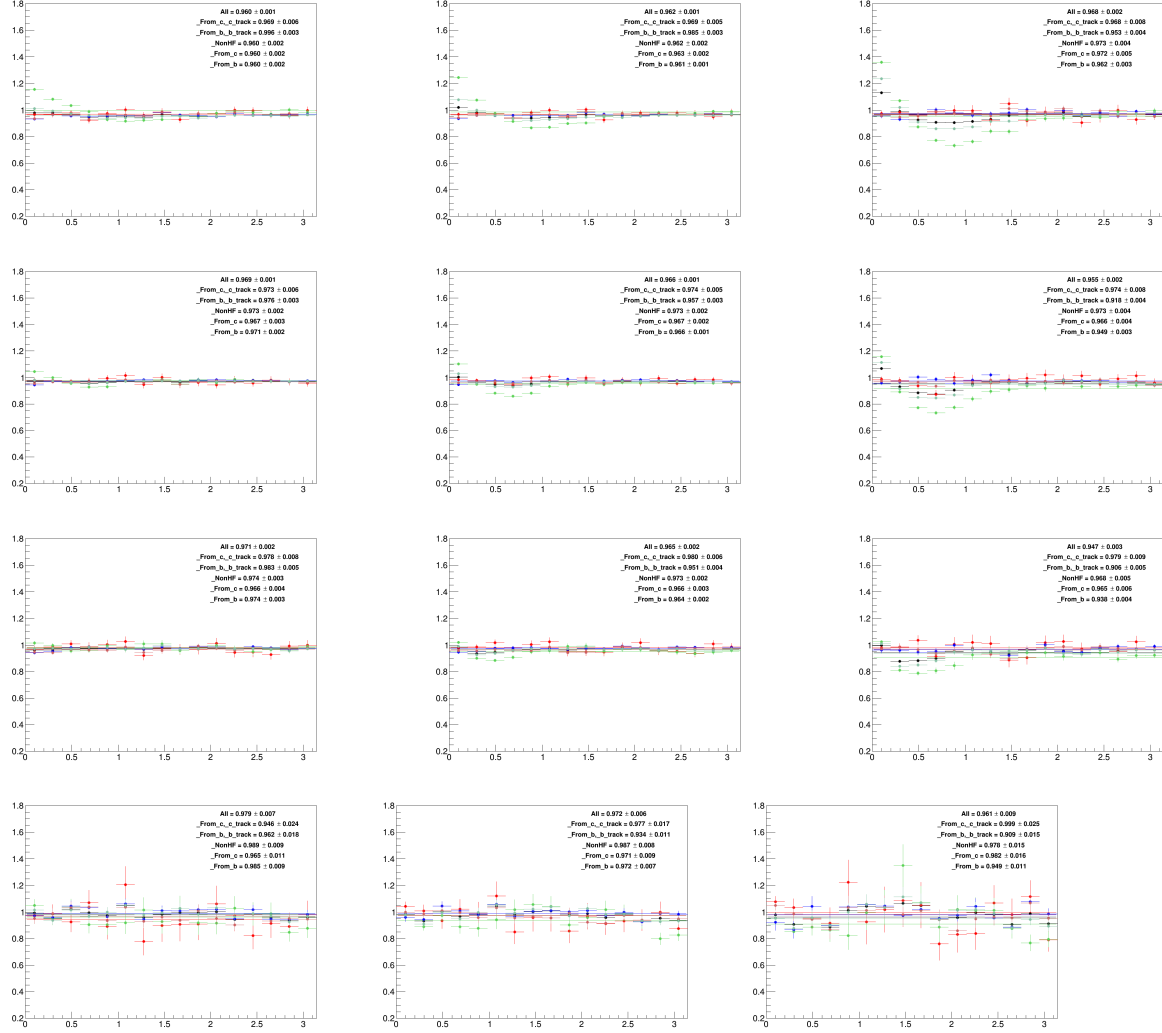


**Figure 82:** Kine/Reco ratio of  $D^0$ -hadrons azimuthal correlation distribution obtained from Monte Carlo in 60-100% centrality class. Black points: All  $D^0$ -all hadrons, normalized by all  $D^0$  triggers; light red points:  $D^0$  from c-hadrons from c, normalized by c- $D^0$  triggers; dark red points:  $D^0$  from c-all hadrons, normalized by c- $D^0$  triggers; light green points:  $D^0$  from b-hadrons from b, normalized by b- $D^0$  triggers; dark green points:  $D^0$  from b-all hadrons, normalized by b- $D^0$  triggers; blue points: All  $D^0$ -hadrons from light quarks, normalized by all  $D^0$  triggers. The panels show the ranges:  $3 < p_T(D) < 5 \text{ GeV}/c$ ,  $0.3 < p_T(\text{assoc}) < 1 \text{ GeV}/c$  (top-left);  $3 < p_T(D) < 5 \text{ GeV}/c$ ,  $p_T(\text{assoc}) > 1 \text{ GeV}/c$  (top-right);  $8 < p_T(D) < 16 \text{ GeV}/c$ ,  $0.3 < p_T(\text{assoc}) < 1 \text{ GeV}/c$  (bottom-left);  $8 < p_T(D) < 16 \text{ GeV}/c$ ,  $p_T(\text{assoc}) > 1 \text{ GeV}/c$  (bottom-right).

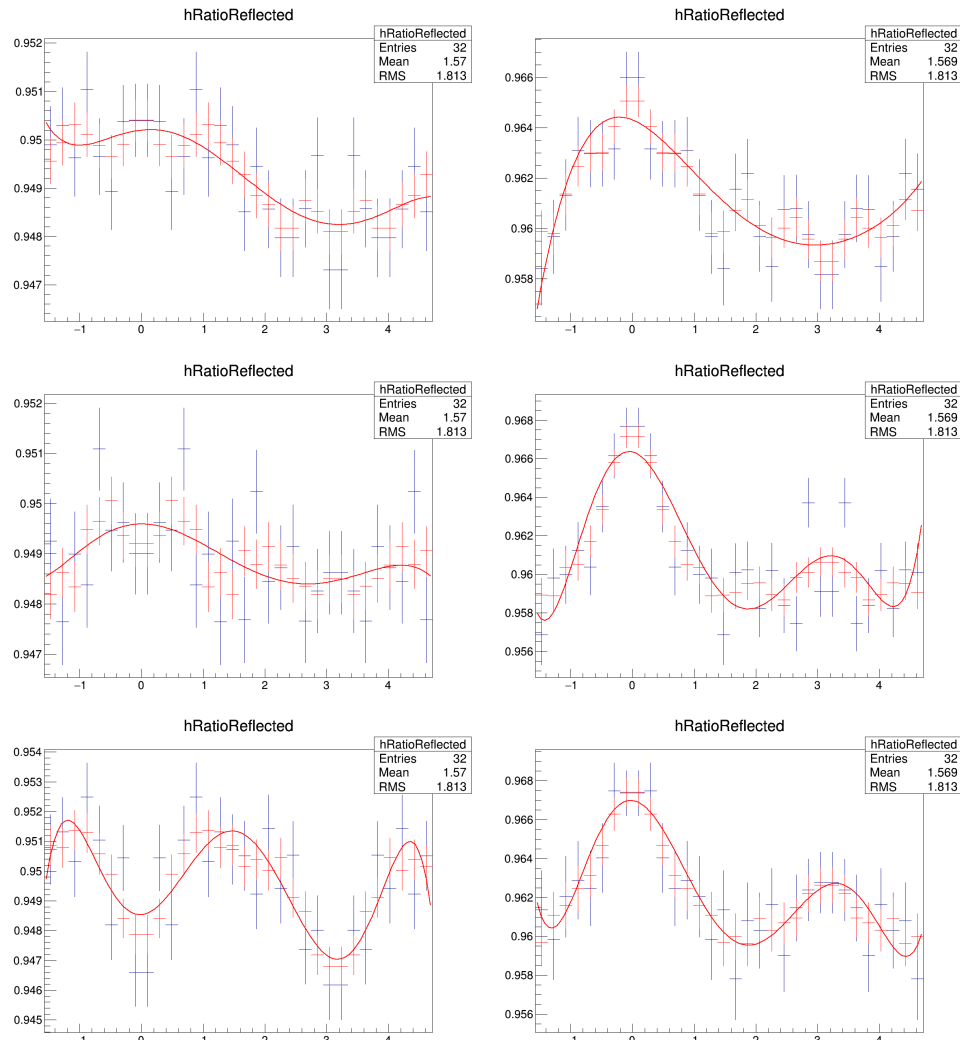


**Figure 83:** Fraction of primary track in the reconstructed associated track sample (blue histogram). The polynomial fit function (red curve) and the 3-point moving average (red histogram) are also superimposed. The  $p_T(D)$  ranges are 3-5, 5-8, 8-16 GeV/c, respectively for each row, and  $0.3 < p_T(\text{assoc}) < 1$ ,  $p_T(\text{assoc}) > 1$  GeV/c inside each row.

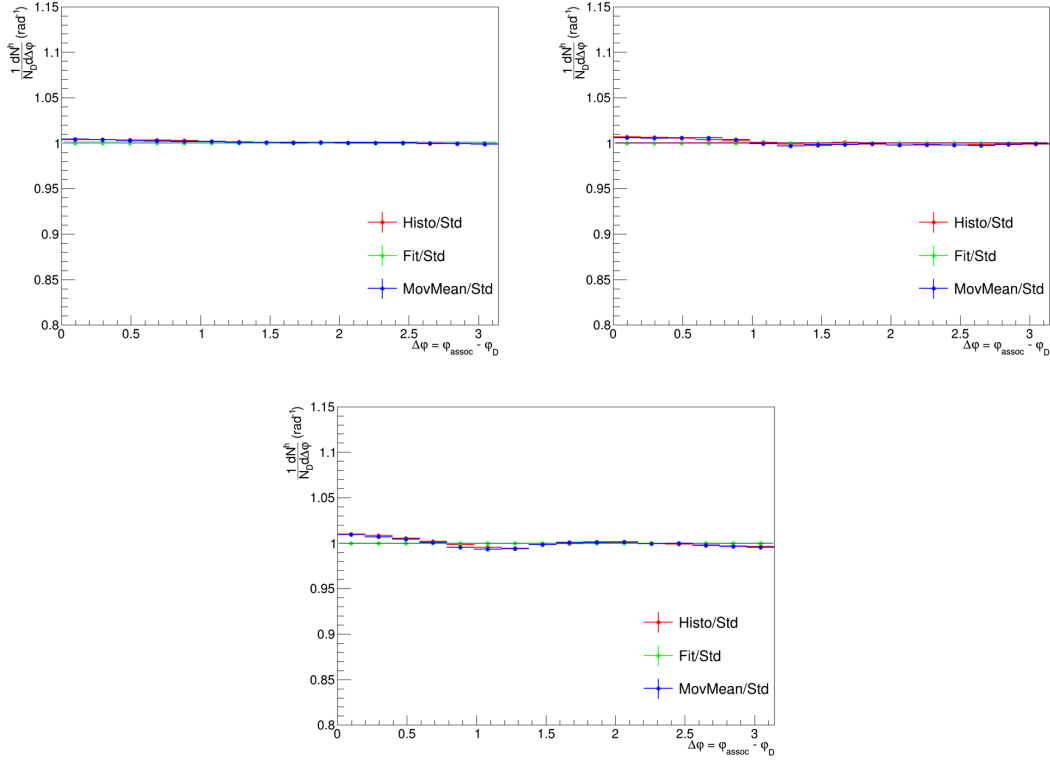


**Figure 84:** Ratio of correlation distribution after purity correction with  $\Delta\phi$  differential correction over those with flat purity correction, for the three associated  $p_T$  ranges in  $p_T(D)$  3-5 GeV/c.

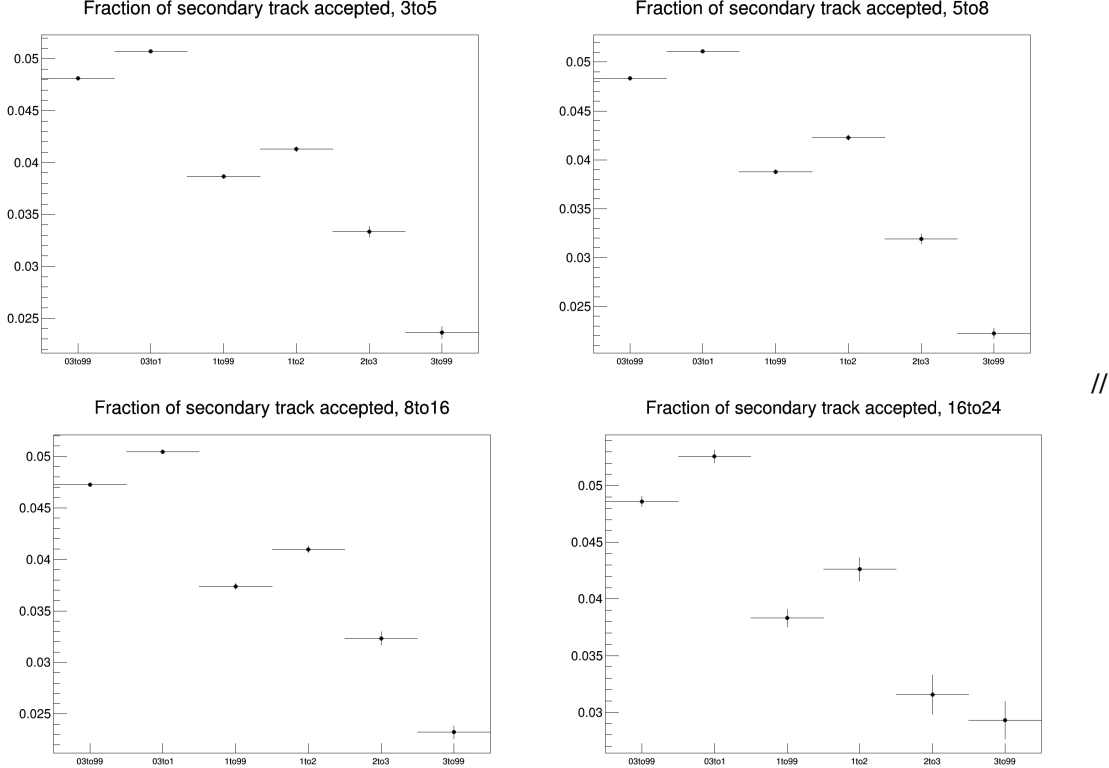


**Figure 85:** Overall value of purity (averaged over  $\Delta\phi$ ) for the various associated track  $p_T$  ranges, in 0-20%.  $D^0$  meson is taken as trigger particle. Each panel represent a  $D$ -meson  $p_T$  bin.

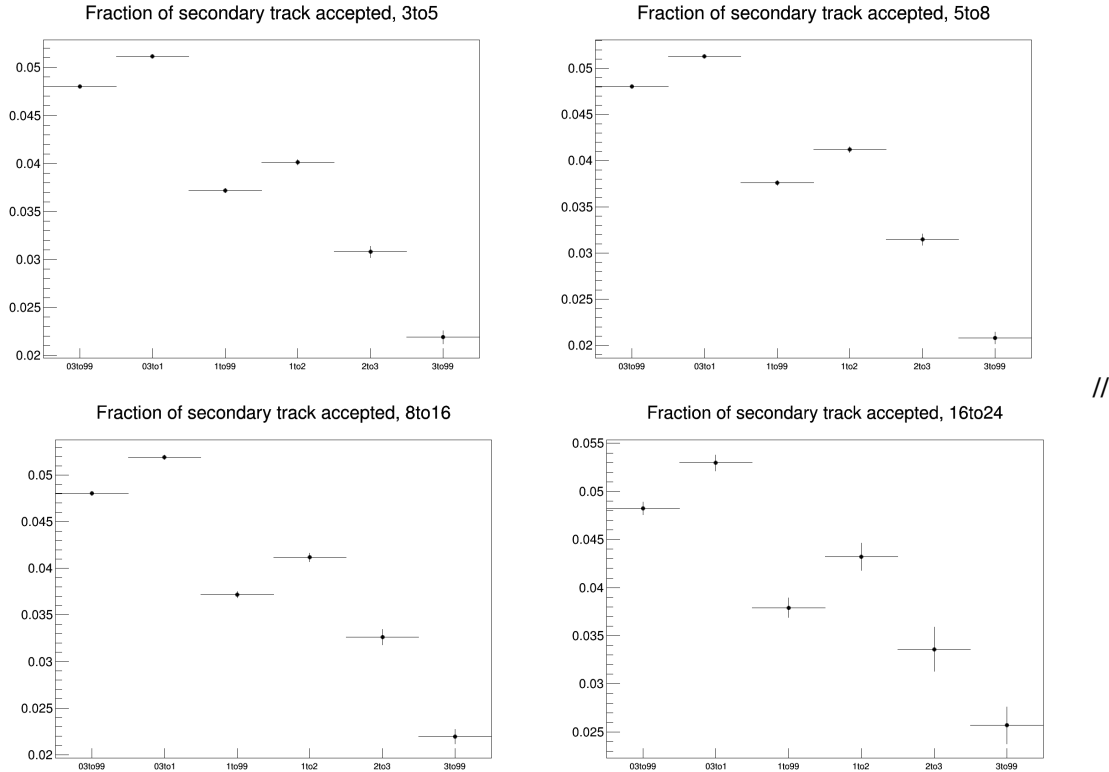


**Figure 86:** Overall value of purity (averaged over  $\Delta\varphi$ ) for the various associated track  $p_T$  ranges, in 20-60%.  $D^0$  meson is taken as trigger particle. Each panel represent a D-meson  $p_T$  bin.

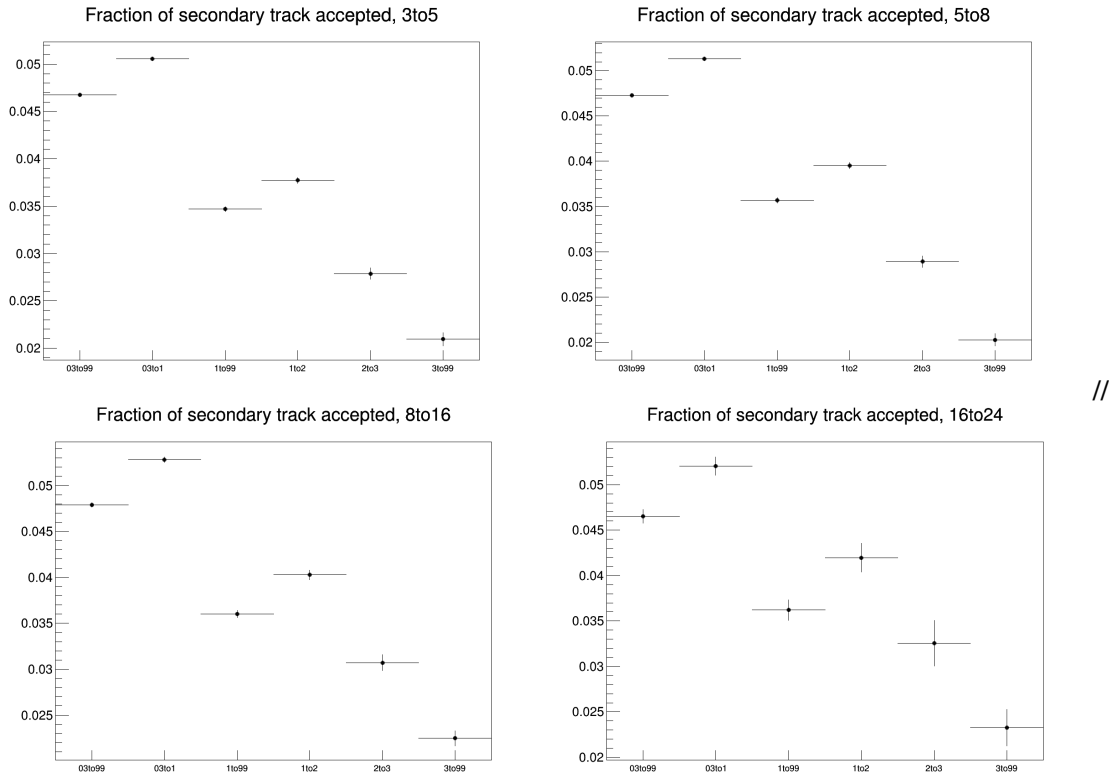


**Figure 87:** Overall value of purity (averaged over  $\Delta\varphi$ ) for the various associated track  $p_T$  ranges, in 60-100%.  $D^0$  meson is taken as trigger particle. Each panel represent a D-meson  $p_T$  bin.

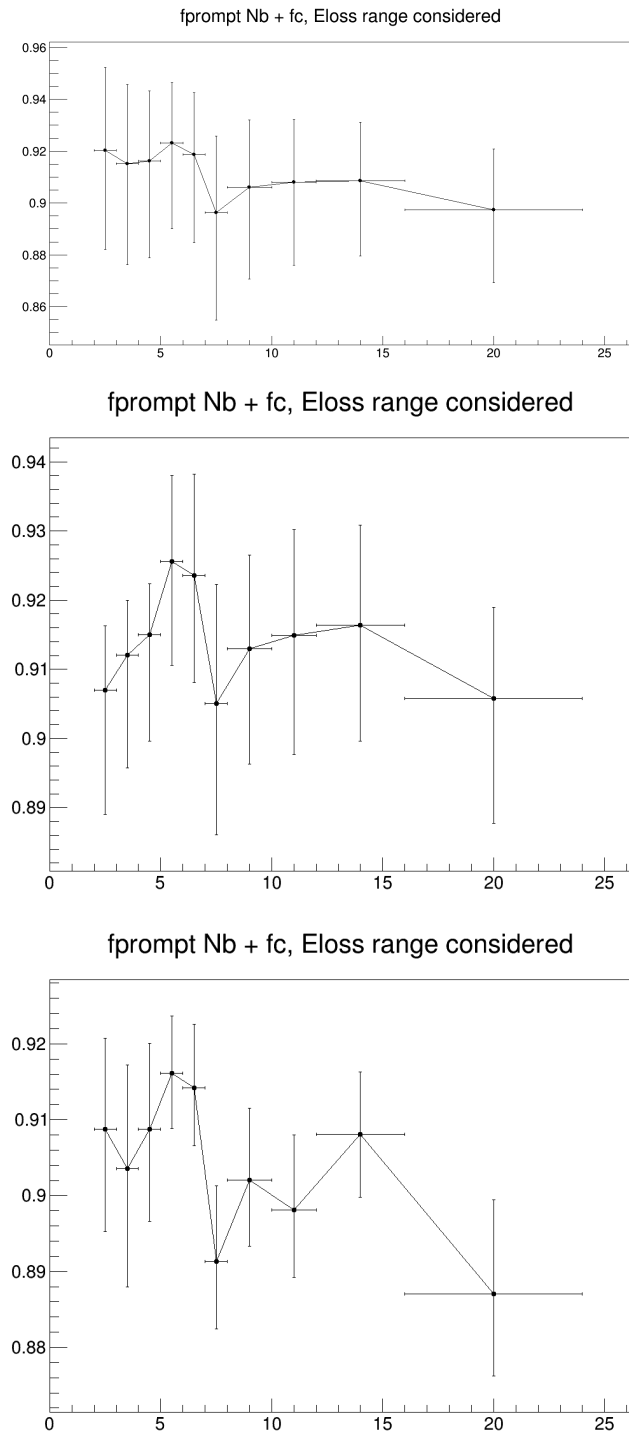


**Figure 88:**  $f_{\text{prompt}}$  as a function of the  $p_T$  for  $D^0$  in 0-20% (top), 20-60% (mid) and 60-100% (bottom) estimated on the basis of FONLL predictions

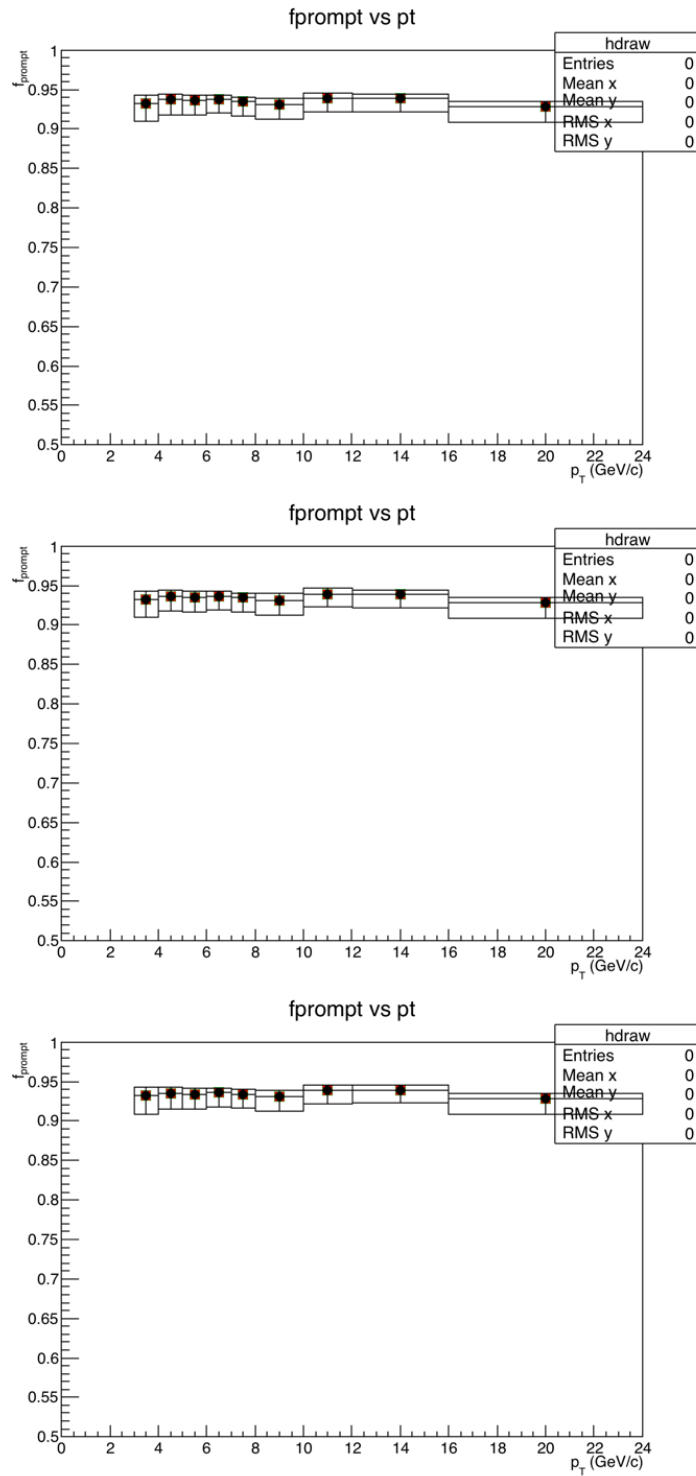


**Figure 89:**  $f_{\text{prompt}}$  as a function of the  $p_T$  for  $D^{*+}$  in 0-20% (top), 20-60% (mid) and 60-100% (bottom) estimated on the basis of FONLL predictions

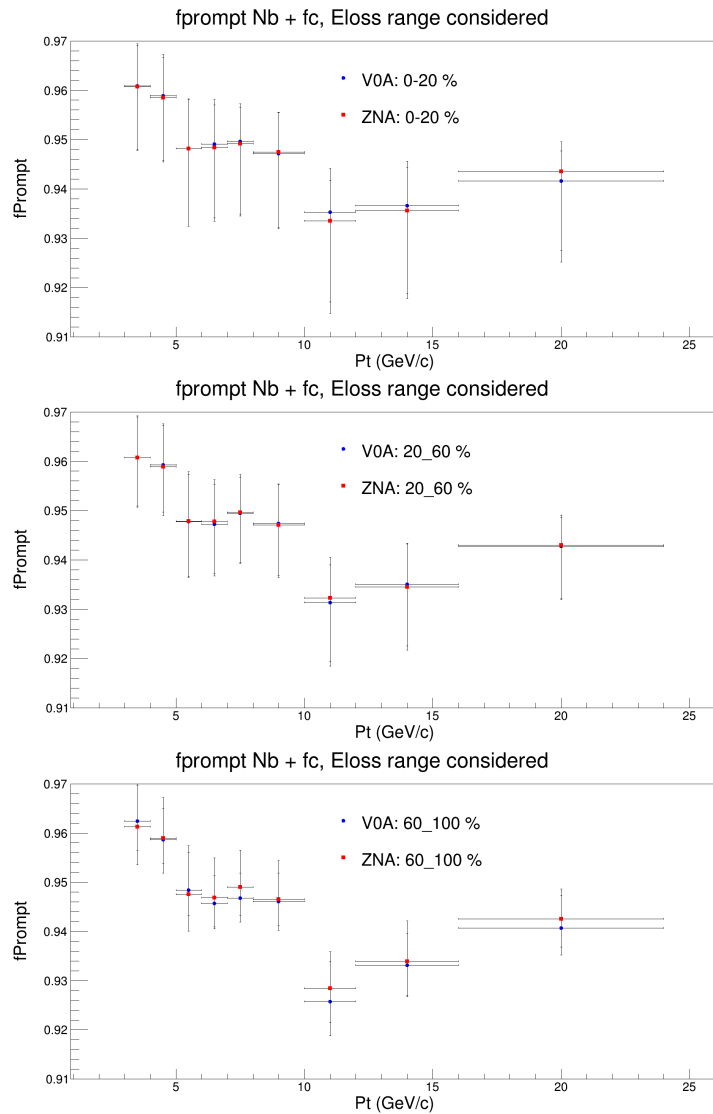


**Figure 90:**  $f_{\text{prompt}}$  as a function of the  $p_T$  for  $D^+$  in 0-20% (top), 20-60% (mid) and 60-100% (bottom) estimated on the basis of FONLL predictions

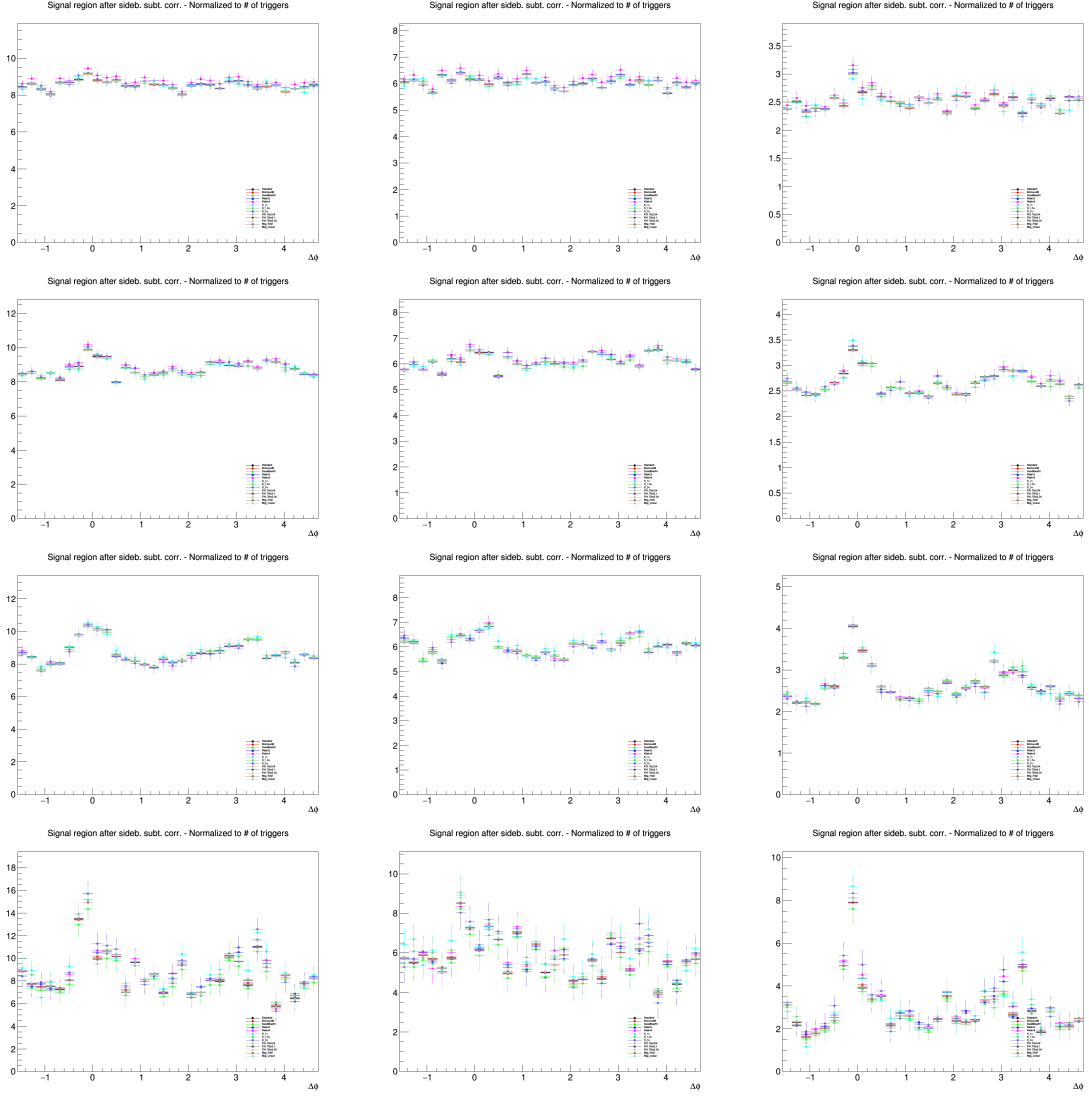


**Figure 91:** Ratios of  $D^0$ - $h$  correlation plots obtained with alternate S and B extraction approaches over those obtained with the standard procedure. For 0-20% centrality. Rows:  $p_T(D^0)$  3-5, 5-8, 8-16, 16-24  $\text{GeV}/c$ . In each row, the panels show the associated track  $p_T$  ranges  $> 0.3$ ,  $0.3-1$ ,  $> 1 \text{ GeV}/c$ , respectively.

### 977 6.3.1 S and B extraction

978 The systematic uncertainty on possible biases in the extraction of the D meson yield and background  
 979 value under the peak was determined separately for the three mesons. It was obtained by performing  
 980 the analysis adopting different fit, and extraction, criteria for the invariant mass spectra with respect  
 981 to the default approach, in the same way as what described in the subsection 4.1. This affects both  
 982 the values of S and B, and possibly the range of signal and sideband regions. After evaluating the  
 983 ratio of the correlation distributions retrieved with the alternate approaches over those with the standard  
 984 approach, the maximum value of the deviations w.r.t. 1 (with a grain of salt, i.e. excluding the ratios  
 985 from approaches where a clear bias in the procedure is identified). This procedure will hold also for the  
 986 evaluation of the other uncertainties affecting the correlation distributions (and won't be repeated in the  
 987 following).

988 In Figs. 91, 92, 93 the above ratios are shown for the  $D^0$  approach, for the three centrality ranges, in each  
 989 kinematic range addressed. The values of the systematic uncertainties assigned for this source are, for  
 990 all centrality ranges, 1% for  $p_T(D) < 16 \text{ GeV}/c$ , and 2% for  $16 < p_T(D) < 24 \text{ GeV}/c$ .

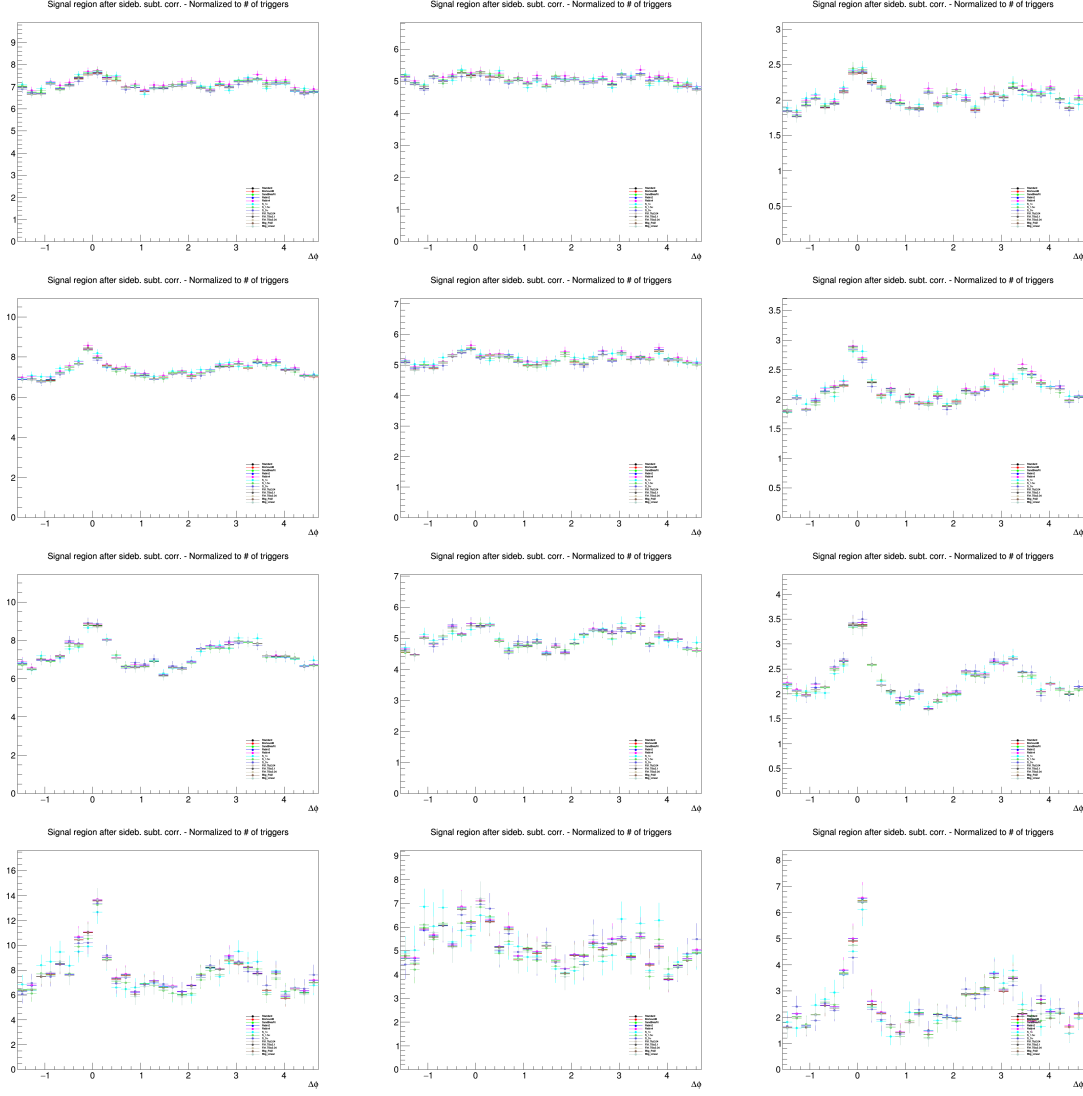


**Figure 92:** Ratios of  $D^0$ - $h$  correlation plots obtained with alternate S and B extraction approaches over those obtained with the standard procedure. For 20-60% centrality. Rows:  $p_T(D^0)$  3-5, 5-8, 8-16, 16-24  $\text{GeV}/c$ . In each row, the panels show the associated track  $p_T$  ranges  $> 0.3$ , 0.3-1,  $> 1 \text{ GeV}/c$ , respectively.

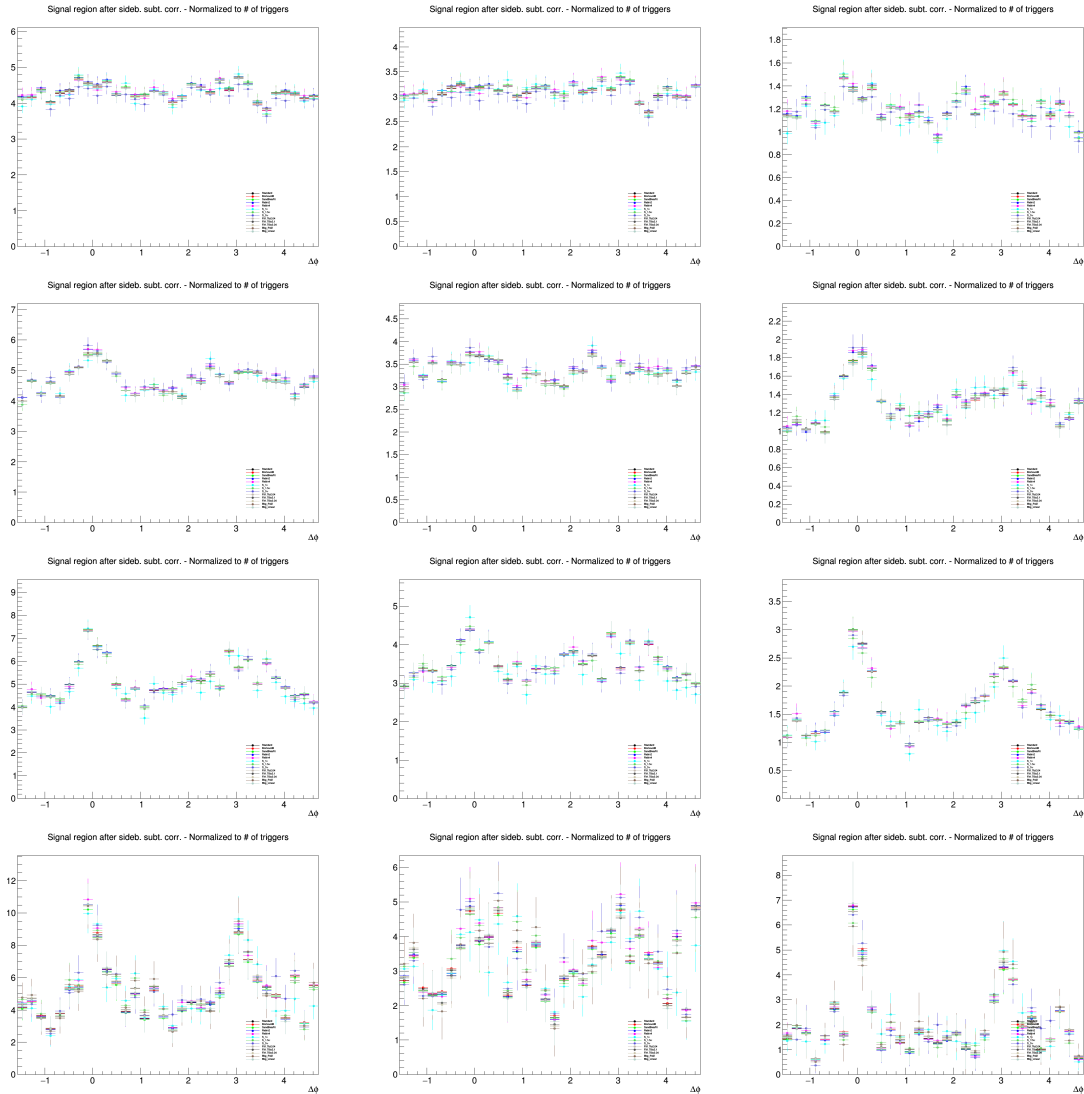


**Figure 93:** Ratios of  $D^0$ -h correlation plots obtained with alternate S and B extraction approaches over those obtained with the standard procedure. For 60-100% centrality. Rows:  $p_T(D^0)$  3-5, 5-8, 8-16, 16-24 GeV/c. In each row, the panels show the associated track  $p_T$  ranges  $> 0.3$ ,  $0.3-1$ ,  $> 1$  GeV/c, respectively.

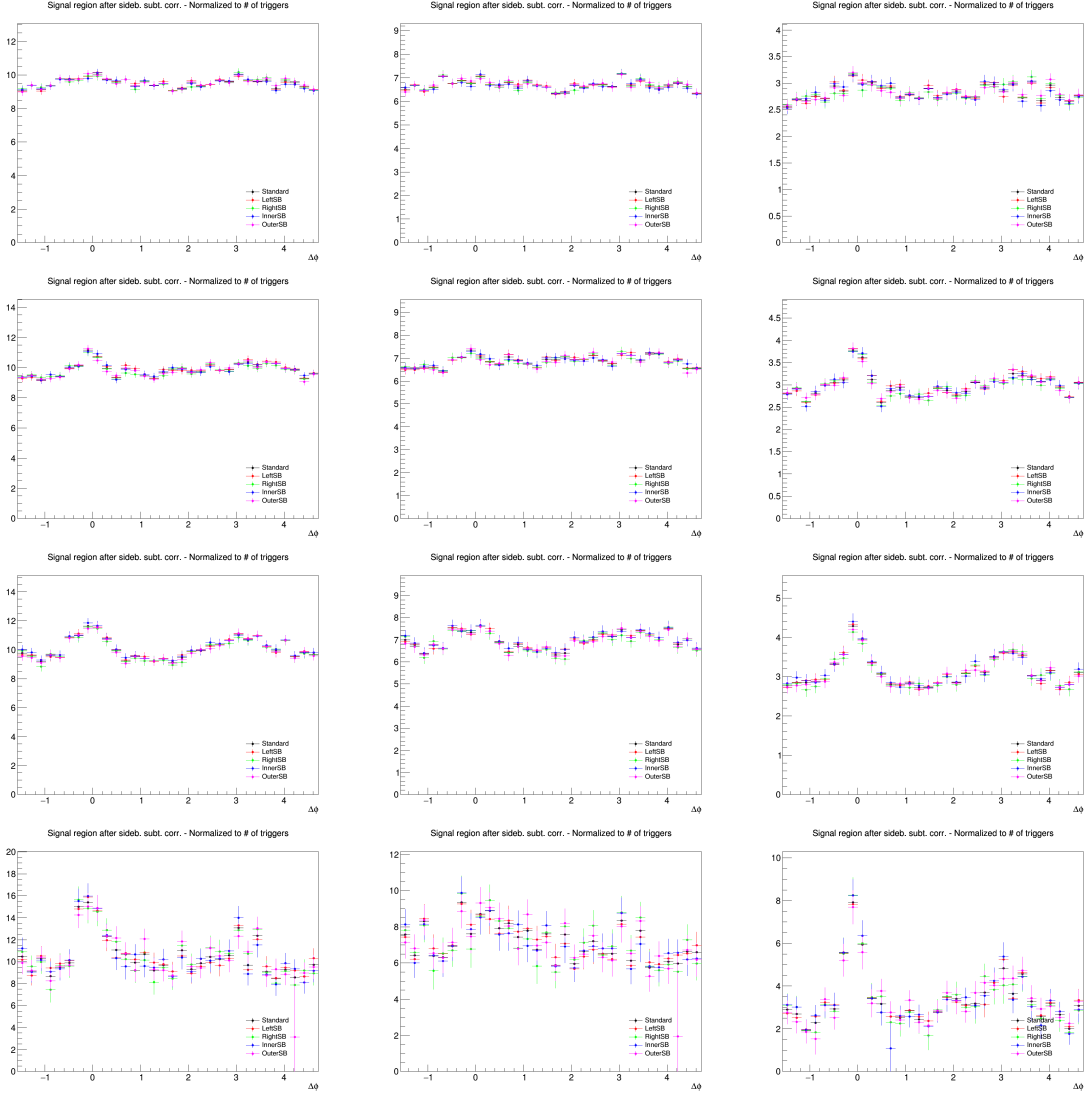


**Figure 94:** Ratios of  $D^0$ - $h$  correlation plots obtained with alternate sideband definition over those obtained with the standard sideband definition. For 0-20% centrality. Rows:  $p_T(D^0)$  3-5, 5-8, 8-16, 16-24  $\text{GeV}/c$ . In each row, the panels show the associated track  $p_T$  ranges  $> 0.3$ ,  $0.3-1$ ,  $> 1 \text{ GeV}/c$ , respectively.

### 991 6.3.2 Background correlation shape

992 A systematic effect can arise from the an incorrect description of the background correlations, for back-  
 993 ground triggers under the signal peak, when correlations considered using sideband candidates are con-  
 994 sidered to mimic this contribution. An uncertainty is addressed by varying the range of the D-meson  
 995 sidebands in the invariant mass spectra (differently for each D-meson specie), similarly to what shown  
 996 in subsection 4.2.

997 The ratio of correlation distributions with alternate/standard sideband definition is shown in Figs. 94,  
 998 95, 96 for the  $D^0$  meson. The uncertainty assigned to this source is 1% for  $p_T(D) < 16 \text{ GeV}/c$ , and 2%  
 999 for  $16 < p_T(D) < 24 \text{ GeV}/c$  for 0-20% and 20-60%. For 60-100%, the uncertainty is 2% for all the  
 1000 kinematic ranges.

### 1001 6.3.3 D-meson cut stability

1002 A systematic effect can also be due to a residual discrepancy between data and Monte Carlo in the dis-  
 1003 tributions of the topological values used for the D-meson selection. To quantify the uncertainty to assign

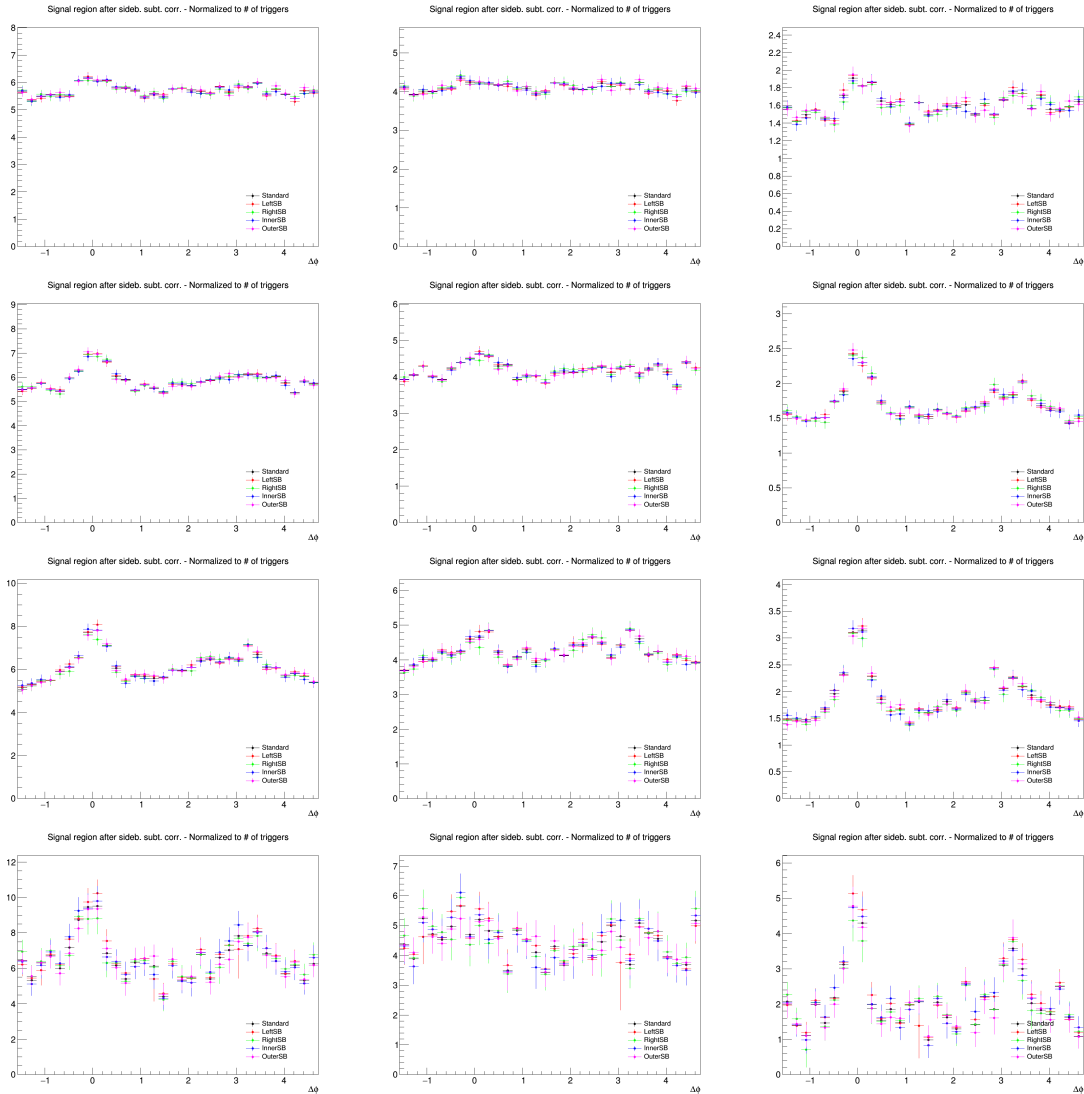


**Figure 95:** Ratios of D<sup>0</sup>-h correlation plots obtained with alternate sideband definition approaches over those obtained with the standard sidebands. For 20-60% centrality. Rows:  $p_T(D^0)$  3-5, 5-8, 8-16, 16-24 GeV/c. In each row, the panels show the associated track  $p_T$  ranges  $> 0.3$ ,  $0.3-1$ ,  $> 1$  GeV/c, respectively.

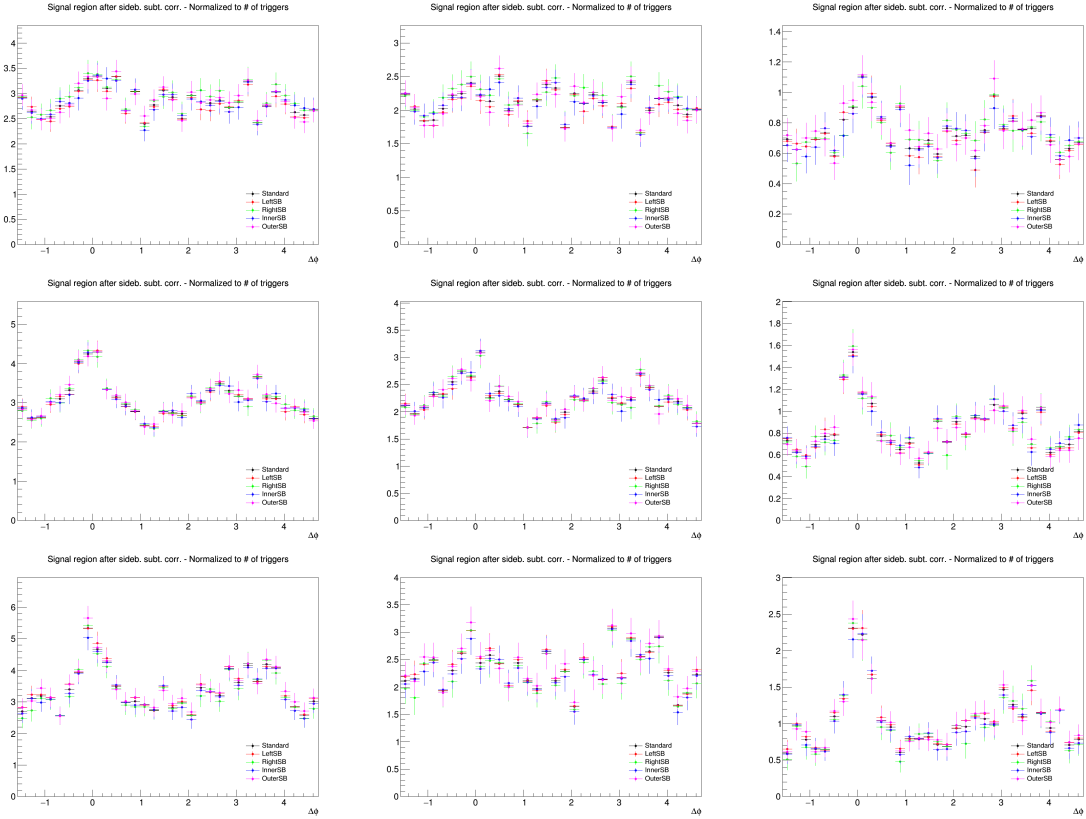


**Figure 96:** Ratios of  $D^0$ - $h$  correlation plots obtained with alternate sideband definition over those obtained with the standard sidebands. For 60-100% centrality. Rows:  $p_T(D^0)$  3-5, 5-8, 8-16, 16-24 GeV/ $c$ . In each row, the panels show the associated track  $p_T$  ranges  $> 0.3$ ,  $0.3-1$ ,  $> 1$  GeV/ $c$ , respectively.

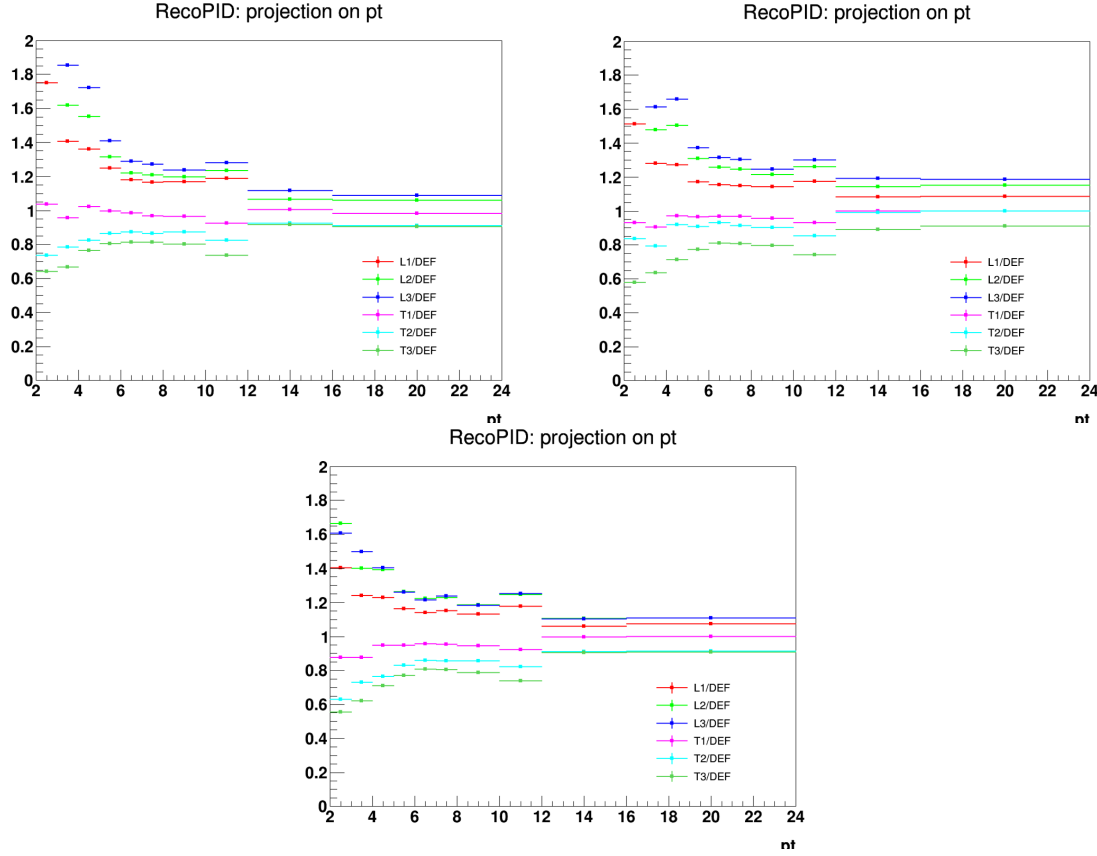


**Figure 97:** Variation of prompt  $D^0$  selection efficiencies with alternate cut sets, for 0-20%, 20-60%, 60-100% centrality class (first to third panel).

for this effect, the analysis is repeated by considering alternate looser or tighter selection, following what done in subsection 4.3, after verifying that the alternate cut sets induce a significant variation on the D-meson efficiency.

Figure 97 shows the ratio of the prompt  $D^0$  selection and reconstruction efficiency for alternate/standard cut sets.

In Figs. 98, 99, 100 the ratio of correlation distributions with alternate/standard cut sets is shown, for the three centrality ranges, in the various  $p_T$  ranges, for the  $D^0$  meson. The assigned uncertainty is a flat 2% for 0-20% and 20-60%, and 2% for  $p_T < 5 \text{ GeV}/c$  and 3% above  $5 \text{ GeV}/c$  for 60-100%.

#### 6.3.4 Tracking efficiency

The systematic uncertainty assigned to cover a possible bias on the associated tracking efficiency is evaluated by varying the associated track selection. With respect to what done in subsection 4.4, additional variations were studied, for all the D-mesons, in particular:

- No request on the minimum number of ITS clusters
- Minimum 3 ITS clusters + kAny request for SPD + filterbit 4 request
- Minimum number of TPC crossed row or 90
- Minimum ratio of TPC crossed rows/findable crossed rows of 0.9
- $p_T$ -dependent cut on minimum number of TPC clusters ( $> 120 - (5/p_T)$ )

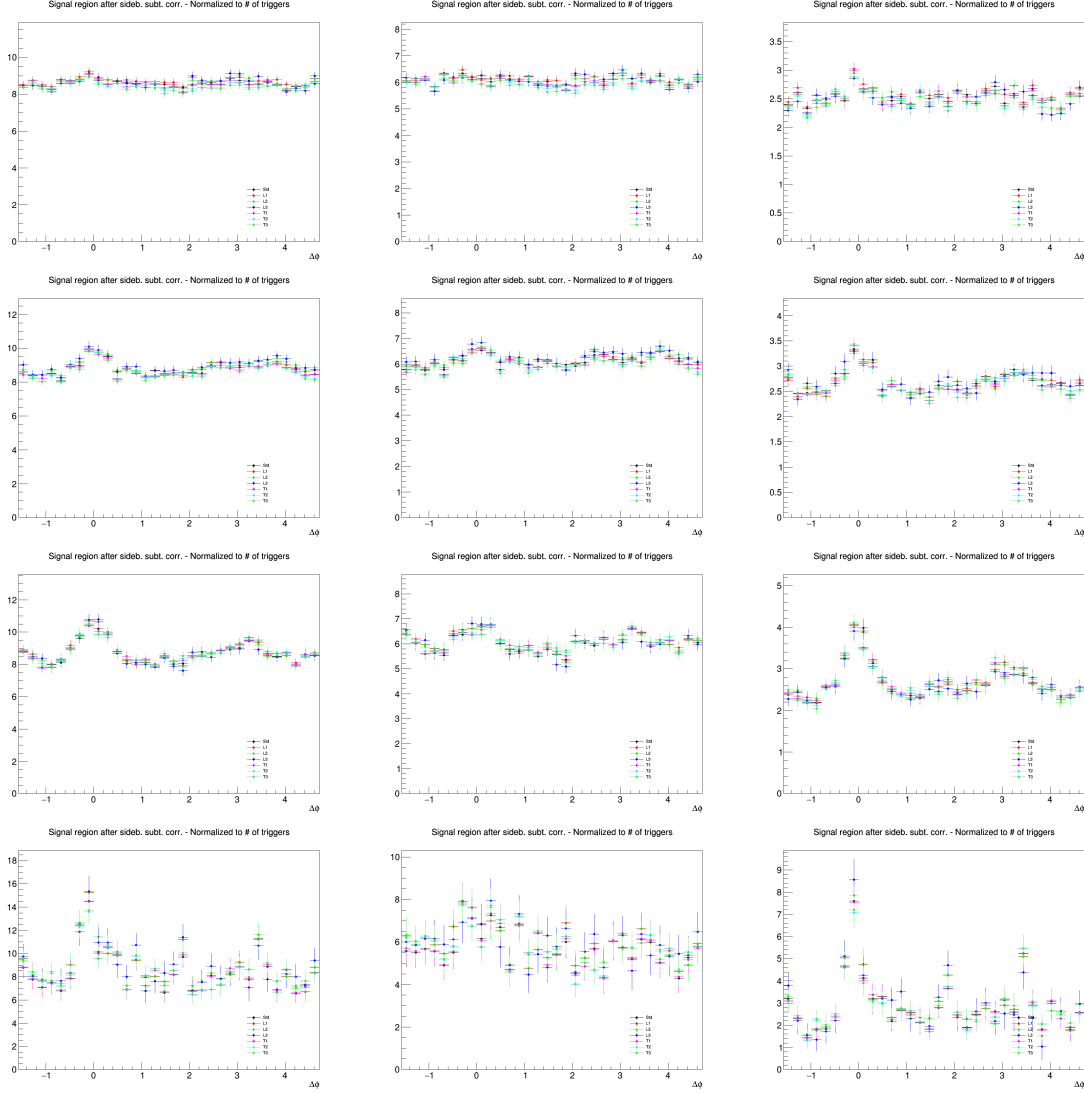


**Figure 98:** Ratios of  $D^0$ -h correlation plots obtained with alternate  $D^0$  selection cuts over those obtained with the standard cuts. For 0-20% centrality. Rows:  $p_T(D^0)$  3-5, 5-8, 8-16, 16-24 GeV/c. In each row, the panels show the associated track  $p_T$  ranges  $> 0.3$ ,  $0.3-1$ ,  $> 1$  GeV/c, respectively.

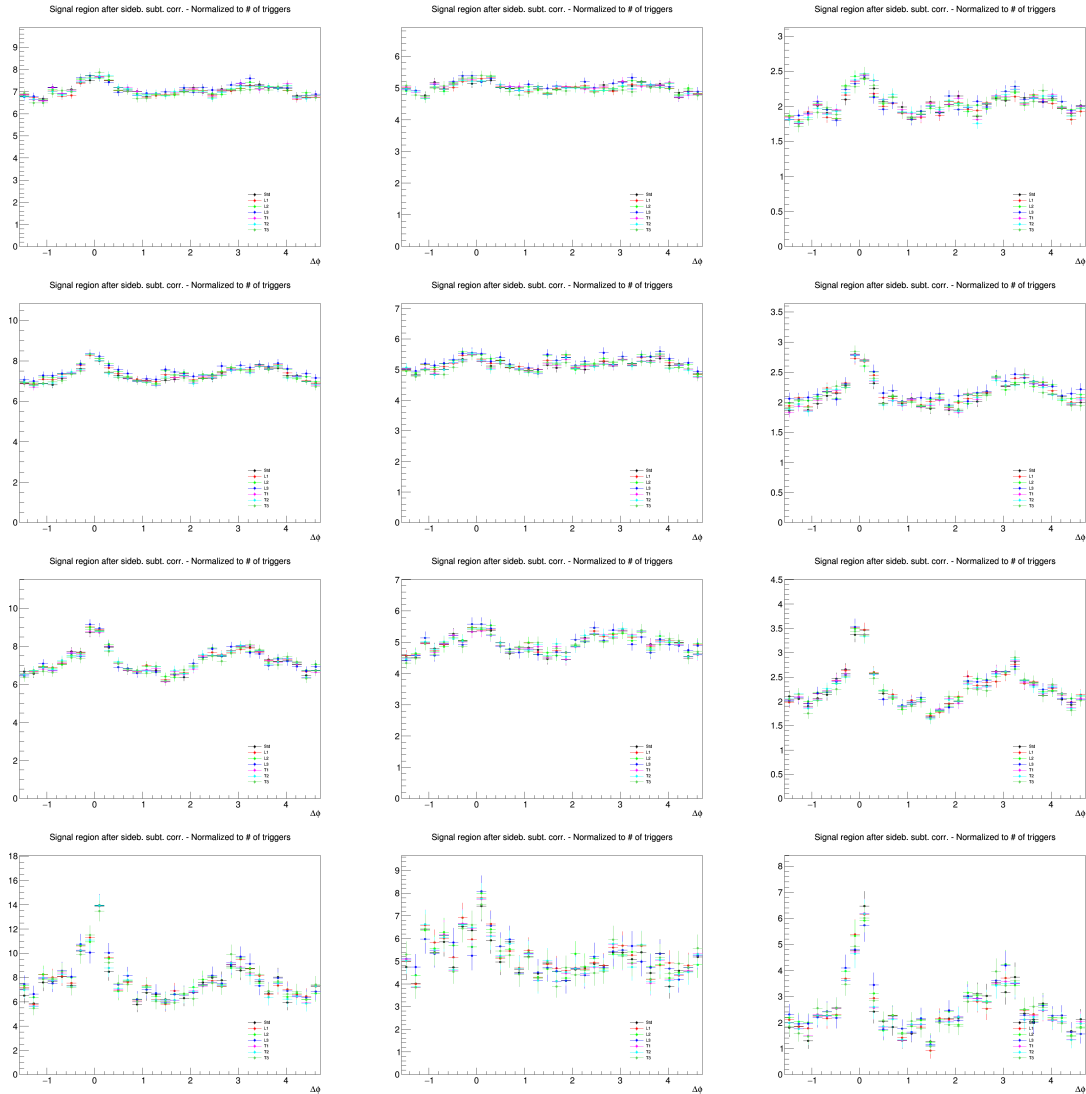


**Figure 99:** Ratios of  $D^0$ - $h$  correlation plots obtained with alternate  $D^0$  selection cuts over those obtained with the standard cuts. For 20-60% centrality. Rows:  $p_T(D^0)$  3-5, 5-8, 8-16, 16-24  $\text{GeV}/c$ . In each row, the panels show the associated track  $p_T$  ranges  $> 0.3$ , 0.3-1,  $> 1 \text{ GeV}/c$ , respectively.

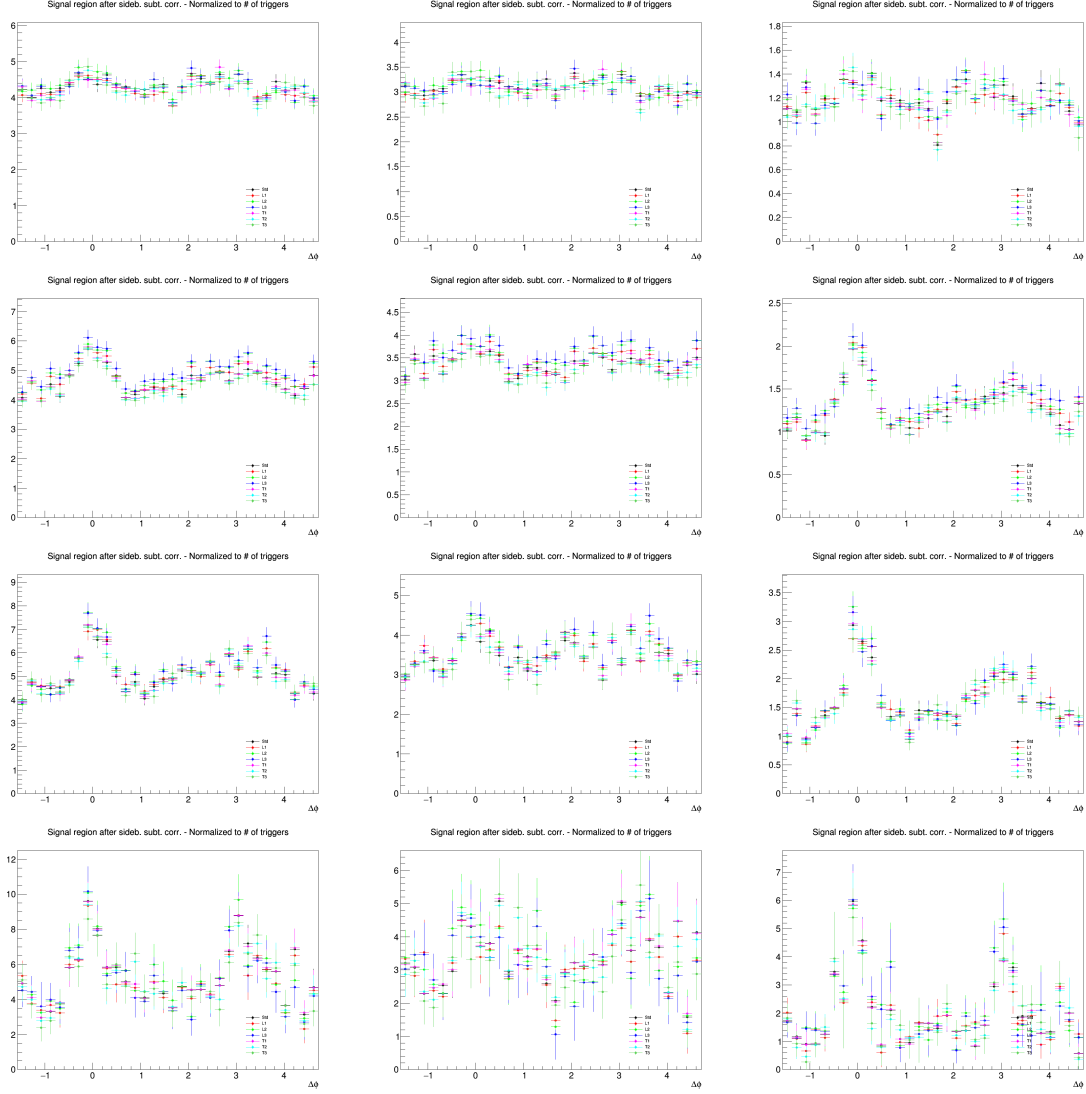


**Figure 100:** Ratios of  $D^0$ -h correlation plots obtained with alternate  $D^0$  selection cuts over those obtained with the standard cuts. Rows:  $p_T(D^0)$  3-5, 5-8, 8-16, 16-24 GeV/c. In each row, the panels show the associated track  $p_T$  ranges  $> 0.3$ , 0.3-1,  $> 1$  GeV/c, respectively.

1021 Figures 101 show the associated track selection and reconstruction efficiencies (and their ratios w.r.t.  
 1022 standard-cut efficiency) for alternate cut sets.

1023 In Figs. 102, 103, 104, the ratio of correlation distributions with alternate/standard track selection is  
 1024 shown, for the three centrality ranges, in the various  $p_T$  ranges, for the  $D^0$  meson as trigger. For this  
 1025 uncertainty, to the values obtained from the above ratio an additional 2%, for a wrong evaluation of the  
 1026 ITS-TPC matching efficiency, is added in quadrature, as prescribed by the DPG group. The assigned  
 1027 uncertainty is a flat 3% for 0-20% and 20-60%, and a flat 3.5% for 60-100%.

### 1028 6.3.5 DCA cut stability

1029 Due to the negligible dependence of the purity on the centrality selection (reflecting no centrality depen-  
 1030 dence on the DCA variable distribution), no centrality-dependent studies were performed, and the same  
 1031 systematic values adopted for 0-100% analysis for this systematic uncertainty (from subsection 4.5) were  
 1032 used.

### 1033 6.3.6 Feed-down subtraction

1034 This uncertainty is automatically evaluated during the feed-down correction stage, exactly as described in  
 1035 subsection 4.6, with no difference at all (i.e. by varying the  $f_{\text{prompt}}$  value and the Monte Carlo generator  
 1036 for building the feed-down correlation template).

### 1037 6.3.7 Correction for bias on B to D decay topologies

1038 As explained in subsection 4.7, the uncertainty on the correction for this bias is directly taken from the  
 1039 results on the dedicated studied, as a symmetric uncertainty of  $(\text{correction})/\sqrt{12}$  (the correction applied  
 1040 is already shown in subsection 9.1 for the centrality-dependent studies).

### 1041 6.3.8 Final table of systematics on correlation distributions

1042 A table summarizing the systematic uncertainties on the  $\Delta\phi$  correlation distribution for the  $D^0$  meson is  
 1043 shown in Fig. REF.

### 1044 6.3.9 Uncertainties on fit observables

1045 The evaluation of the systematic uncertainty on the fit observables is exactly the same as that described  
 1046 in subsection 5.3 for the centrality-integrated analysis (but considering, of course, in each centrality  
 1047 class the corresponding uncertainty values, as described in the previous section). The only modification  
 1048 involves the values chosen for the  $v_2$  hypothesis (also dealt in subsection 5.3), which are differentiated  
 1049 on the bases of the centrality class. The hypotheses on the charged particle  $v_2$  versus centrality were  
 1050 guessed on the bases of the results shown in Fig. 105, taken from the analysis note on charged hadron  $v_2$   
 1051 in p-Pb collisions (2016 sample) in different V0A multiplicity classes. Though the estimator is different  
 1052 from the ZNA we use, the rather flat values of  $v_2$  versus centrality ensures the possibility of using these  
 1053 results as reference.

1054 The hypotheses on D-meson  $v_2$  were guessed starting from ALICE preliminary results of heavy-flavour  
 1055 decay electron  $v_2$  in the same collision system, using the ZNA estimator (left panel of 106. The mea-  
 1056 surement was performed in lower  $p_T(e)$  ranges, but which by chance are fairly similar to the average  
 1057  $p_T$  of out D-meson correlation ranges, if the  $p_T$  of the parent D-hadron is considered for charm-origin  
 1058 heavy-flavour decay electrons - as shown in the right panel of Fig. 106. The drawback of this choice  
 1059 relies in the fact that these  $v_2$  values are obtained after the HM-LM subtraction, while in our analysis  
 1060 we need hypotheses for  $v_2$  in each CC (considering this, we used just flat values in each CC following  
 1061 the charged particle trend), and also in the fact that heavy-flavour electron  $v_2$  includes the contribution

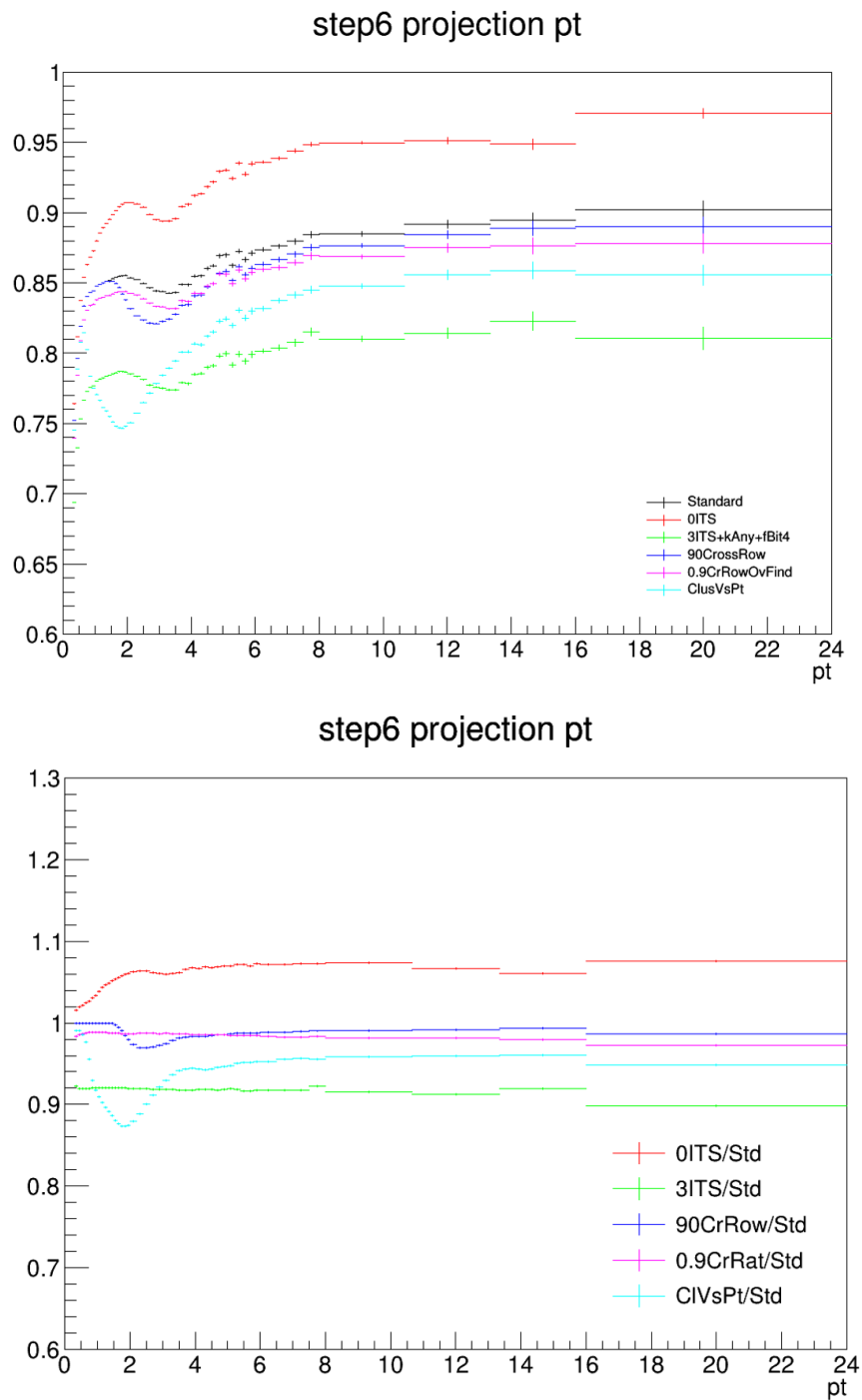


**Figure 101:** Top: associated track selection and reconstruction efficiencies for alternate selections. Bottom: ratios w.r.t. standard-cut efficiency.

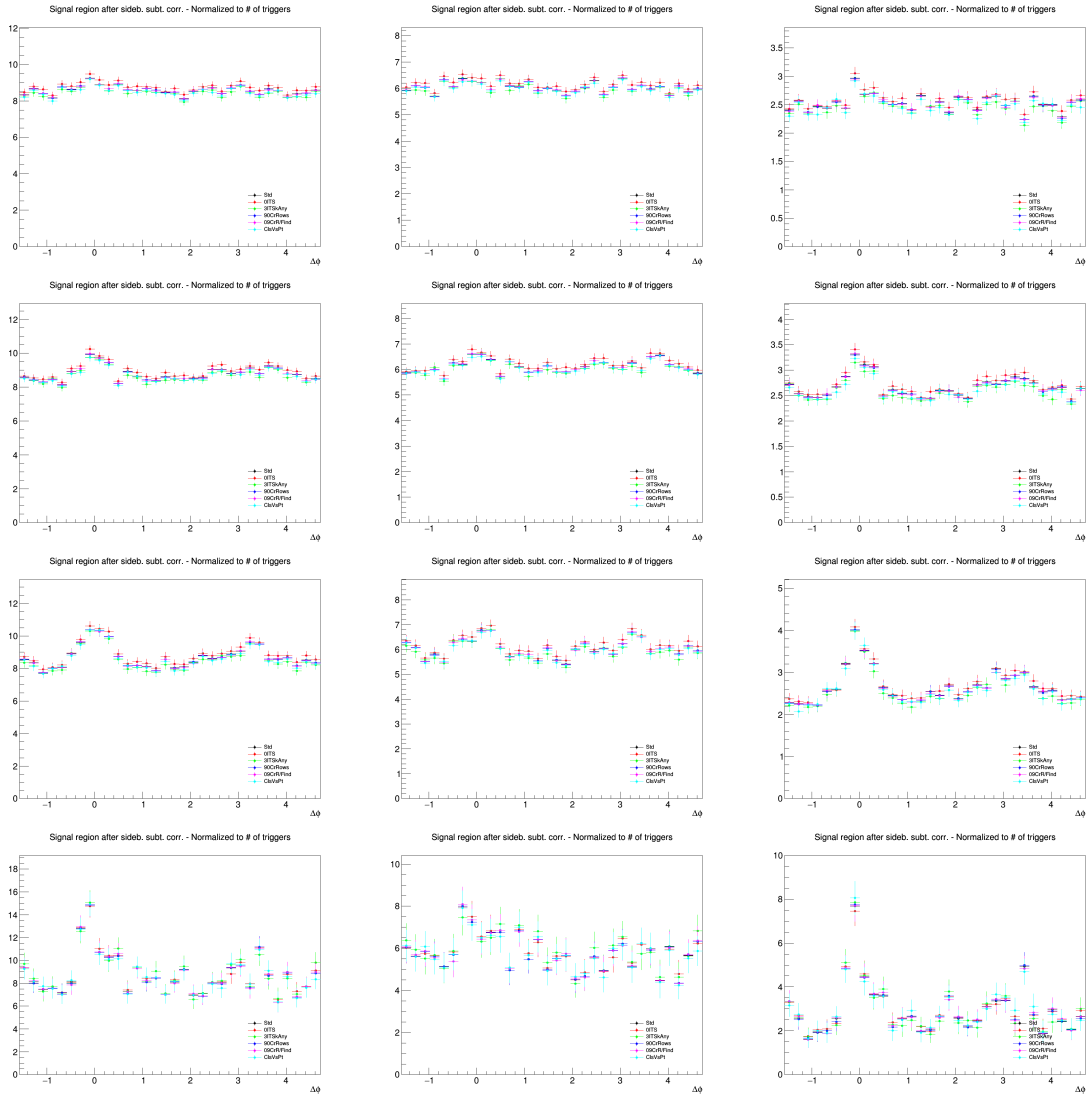


**Figure 102:** Ratios of  $D^0$ - $h$  correlation plots obtained with alternate associated track selection over those obtained with the standard cuts. For 0-20% centrality. Rows:  $p_T(D^0)$  3-5, 5-8, 8-16, 16-24 GeV/ $c$ . In each row, the panels show the associated track  $p_T$  ranges  $> 0.3$ ,  $0.3-1$ ,  $> 1$  GeV/ $c$ , respectively.

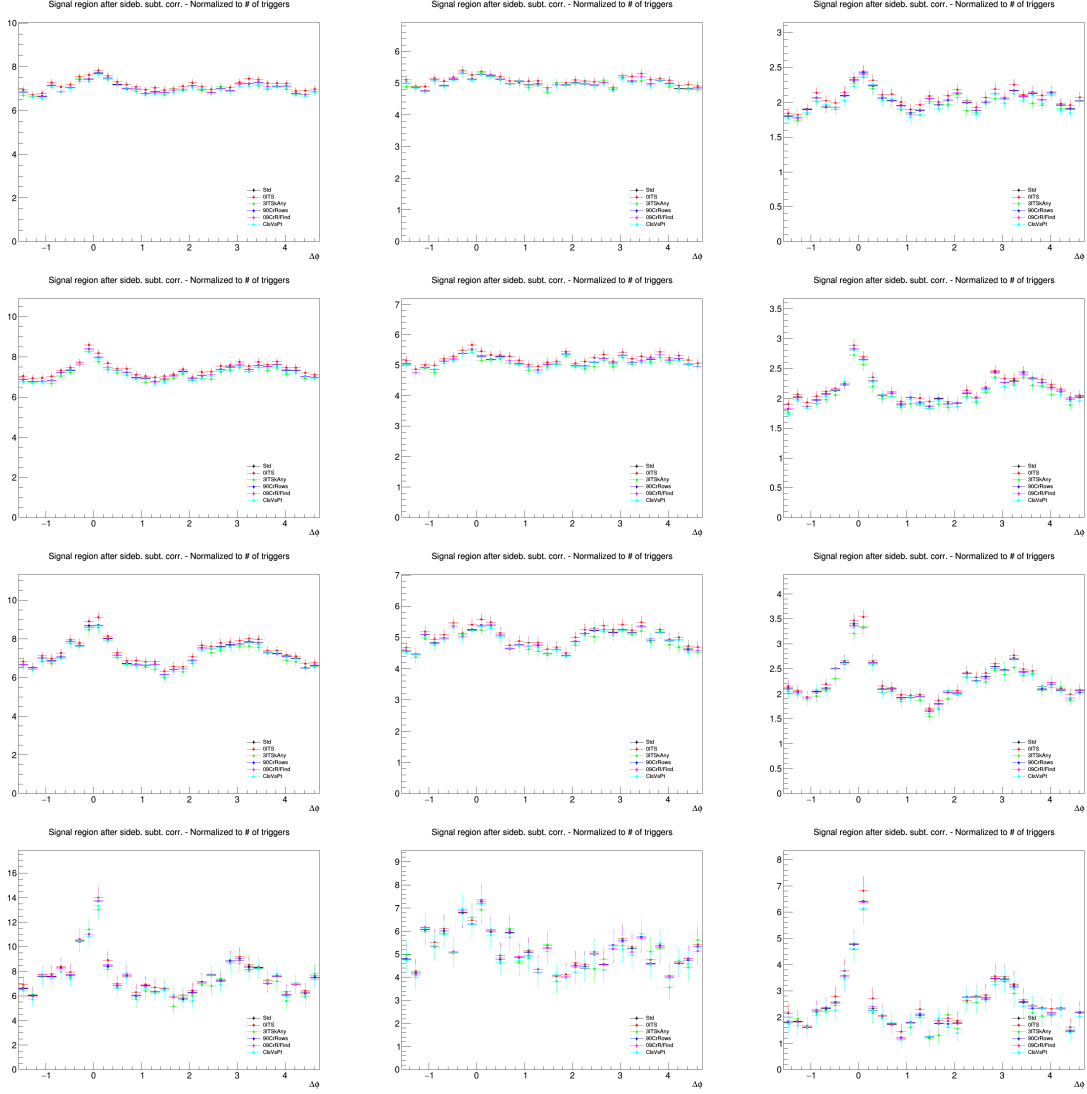


**Figure 103:** Ratios of  $D^0$ - $h$  correlation plots obtained with alternate associated track selection over those obtained with the standard cuts. For 20–60% centrality. Rows:  $p_T(D^0)$  3–5, 5–8, 8–16, 16–24  $\text{GeV}/c$ . In each row, the panels show the associated track  $p_T$  ranges  $> 0.3$ , 0.3–1,  $> 1 \text{ GeV}/c$ , respectively.

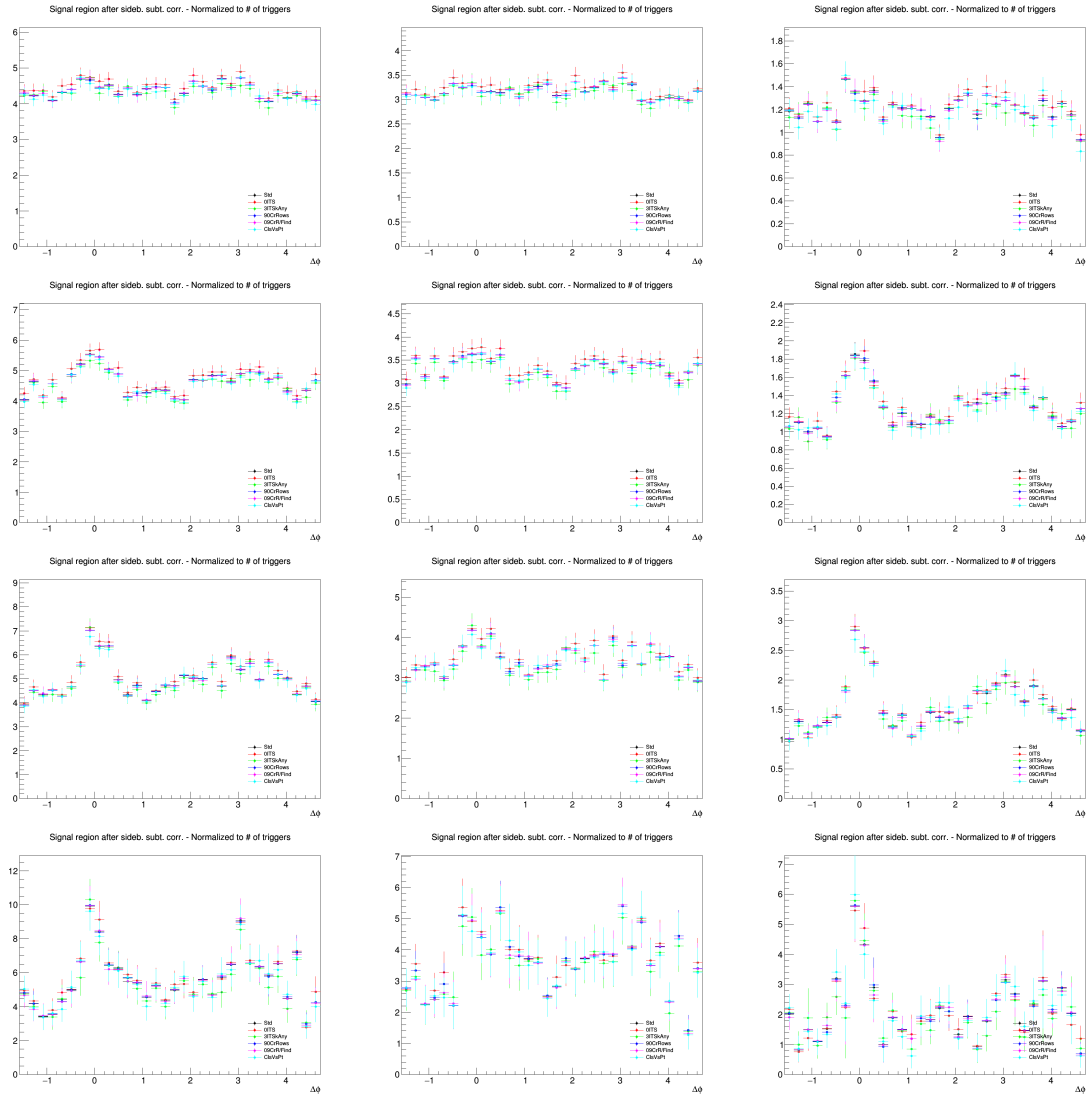


**Figure 104:** Ratios of  $D^0$ - $h$  correlation plots obtained with alternate associated track selection over those obtained with the standard cuts. Rows:  $p_T(D^0)$  3-5, 5-8, 8-16, 16-24  $\text{GeV}/c$ . In each row, the panels show the associated track  $p_T$  ranges  $> 0.3$ , 0.3-1,  $> 1$   $\text{GeV}/c$ , respectively.

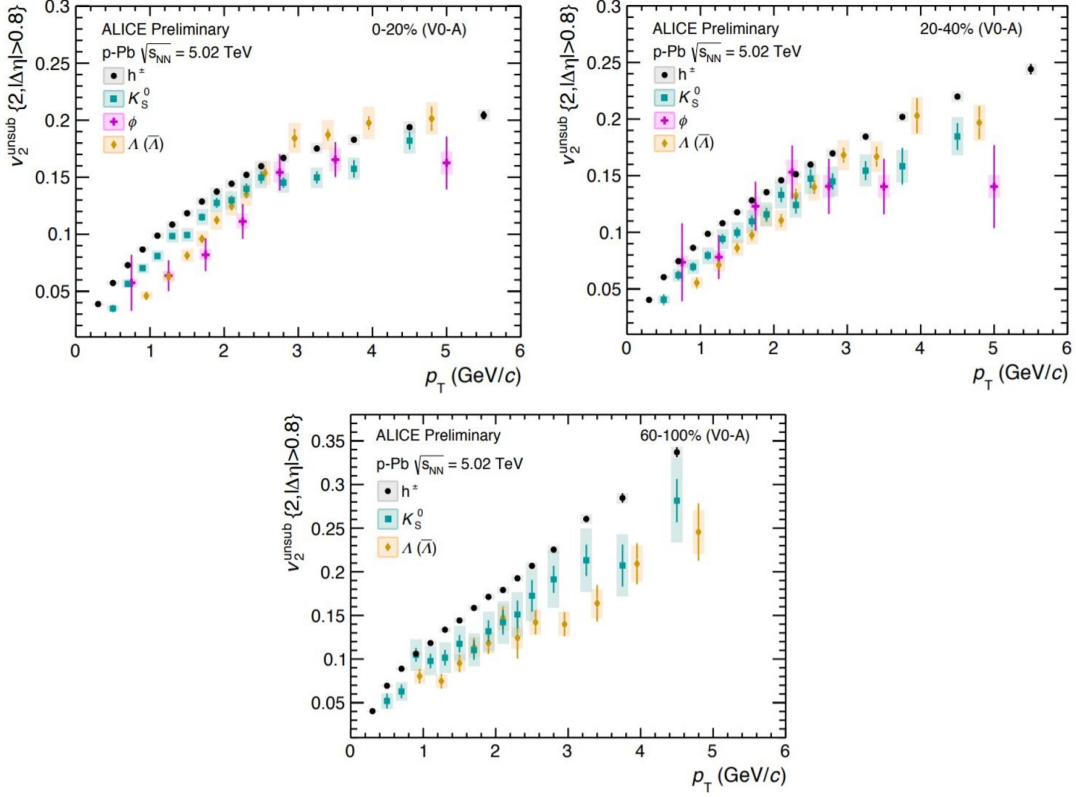


**Figure 105:** Reference plots for estimation of  $v_2(h)$  hypotheses in the three CC.

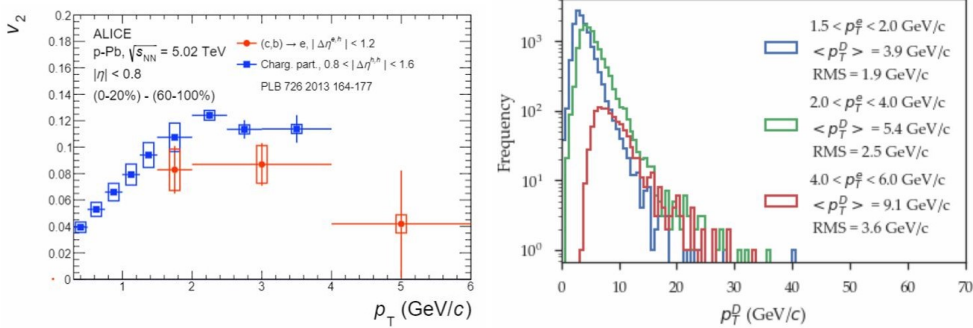


**Figure 106:** Left:  $v_2$  of heavy-flavour decay electrons in p-Pb, after HM-LM subtraction. Right: correspondence of  $p_T(e)$  and  $p_T$  of the parent D-meson (for charm-origin electrons).

from, beauty-hadron decay electrons (though small for  $p_T < 3$  GeV/c), while the B-feed-down is instead subtracted in our D-meson analysis.

In the following, thus, we enlist the  $v_2$  hypotheses we adopted for the evaluation of the systematic on the fit observables due to a possible presence of flow:

- For 0-20%: 0.08, 0.08, 0.04, 0.02 (for  $p_T(D)$  3-5, 5-8, 8-16, 16-24 GeV/c); 0.08, 0.05, 0.11 (for  $p_T(\text{assoc}) > 0.3, 0.3-1, > 1$  GeV/c)
- For 20-60%: 0.08, 0.08, 0.04, 0.02 (for  $p_T(D)$  3-5, 5-8, 8-16, 16-24 GeV/c); 0.08, 0.05, 0.11 (for  $p_T(\text{assoc}) > 0.3, 0.3-1, > 1$  GeV/c)
- For 60-100%: 0.08, 0.08, 0.04, 0.02 (for  $p_T(D)$  3-5, 5-8, 8-16, 16-24 GeV/c); 0.10, 0.06, 0.13 (for  $p_T(\text{assoc}) > 0.3, 0.3-1, > 1$  GeV/c)

**6.4 Results**

The procedure for, after having evaluated all the needed correction, is totally equivalent to that described in Section 5. As a quick reminder, the weighted average of the azimuthal correlation distributions for the three D-meson species are evaluated for each kinematic range under study, and a fit function (composed of a double Gaussian for the near- and away-side peak and a constant baseline) is applied to the average distribution, in order to extract quantitative observables as the NS and AS associated yield and widths. Of course, the procedure is performed independently on each of the three centrality classes, and a comparison of the correlation distributions (after the baseline subtraction) and of the NS and AS peak observables is done. The results of the analysis for each centrality class, and of the comparison, are shown in the following.

**6.4.1 Single-meson azimuthal correlation distributions**

In Figs. , , (0-20%), , , (20-60%) and , , (60-100%), the correlation distributions for  $D^0$ ,  $D^+$  and  $D^{*+}$  mesons are shown, after having applied all the corrections, and after having reduced the range of the  $\Delta\phi$  axis to  $[0, \pi]$ , by reflected the symmetrical points (same procedure as for the cent-integrated analysis).

**6.4.2 Average-D correlation distributions**

The average D-hadron correlation distributions are shown in Fig. 116, 117, 118 for all the kinematic ranges and for each of the centrality classes.

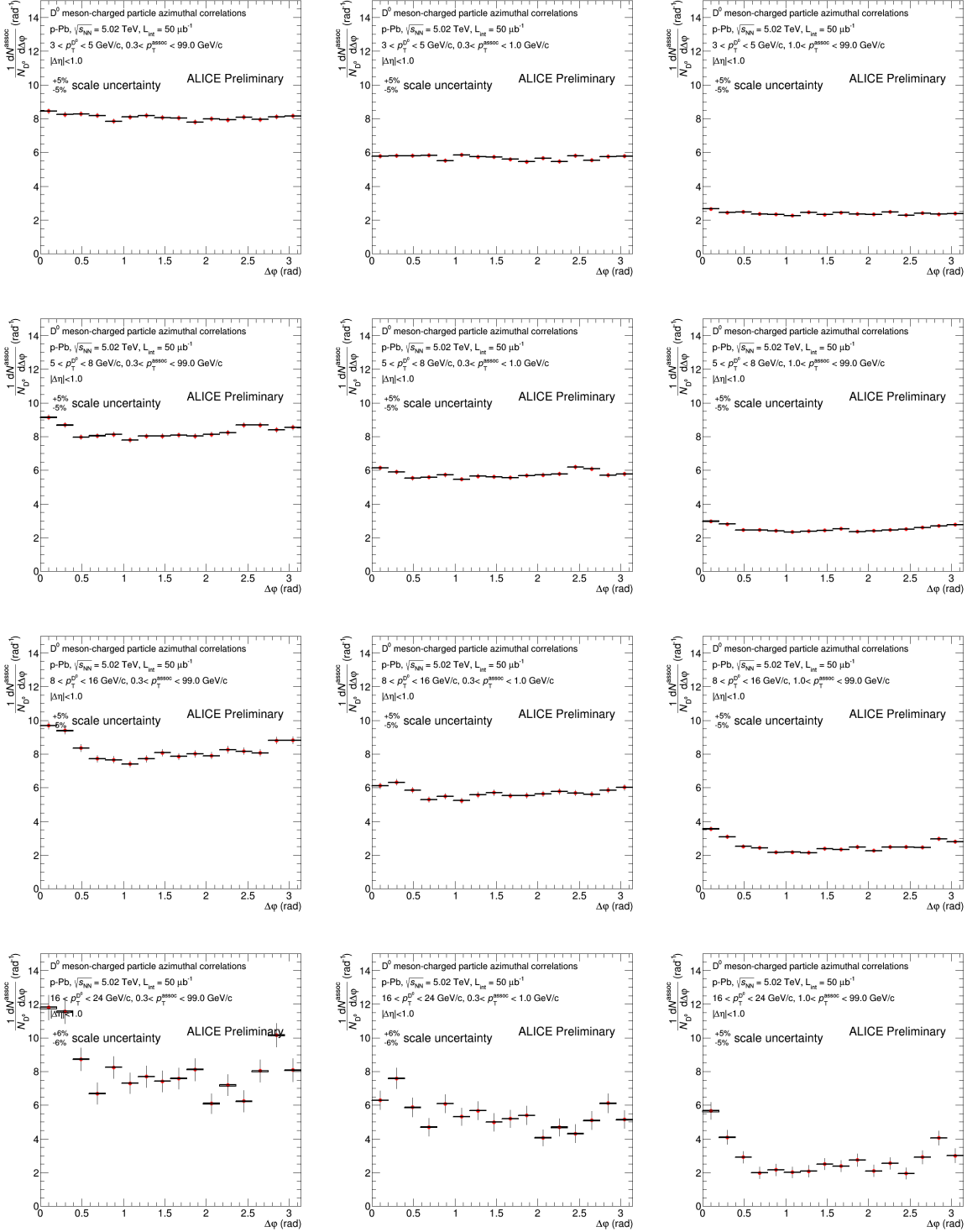


**Figure 107:** Correlation distributions for D<sup>0</sup> meson as trigger particle (0-20%). Each row is a different p<sub>T</sub>(D) range, each column a different p<sub>T</sub>(assoc) range. The systematic uncertainties labelled in the plots are not final. Note: the L=50  $\mu\text{b}^{-1}$  is a typo of the drawing macro (it shall be 300  $\mu\text{b}^{-1}$ ).

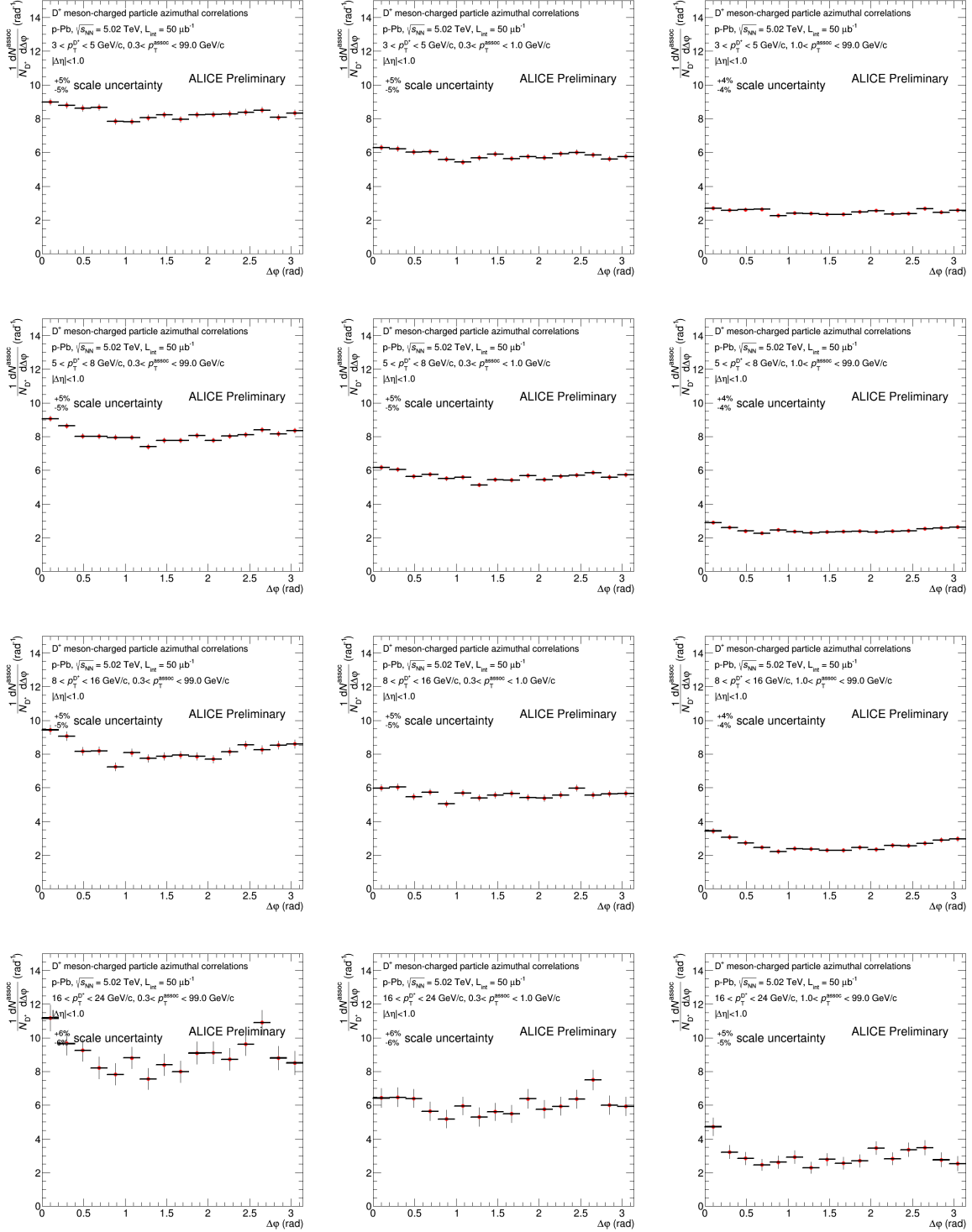


**Figure 108:** Correlation distributions for  $D^+$  meson as trigger particle (0-20%). Each row is a different  $p_T(D)$  range, each column a different  $p_T(\text{assoc})$  range. The systematic uncertainties labelled in the plots are not final. Note: the  $L=50 \mu\text{b}^{-1}$  is a typo of the drawing macro (it shall be  $300 \mu\text{b}^{-1}$ ).

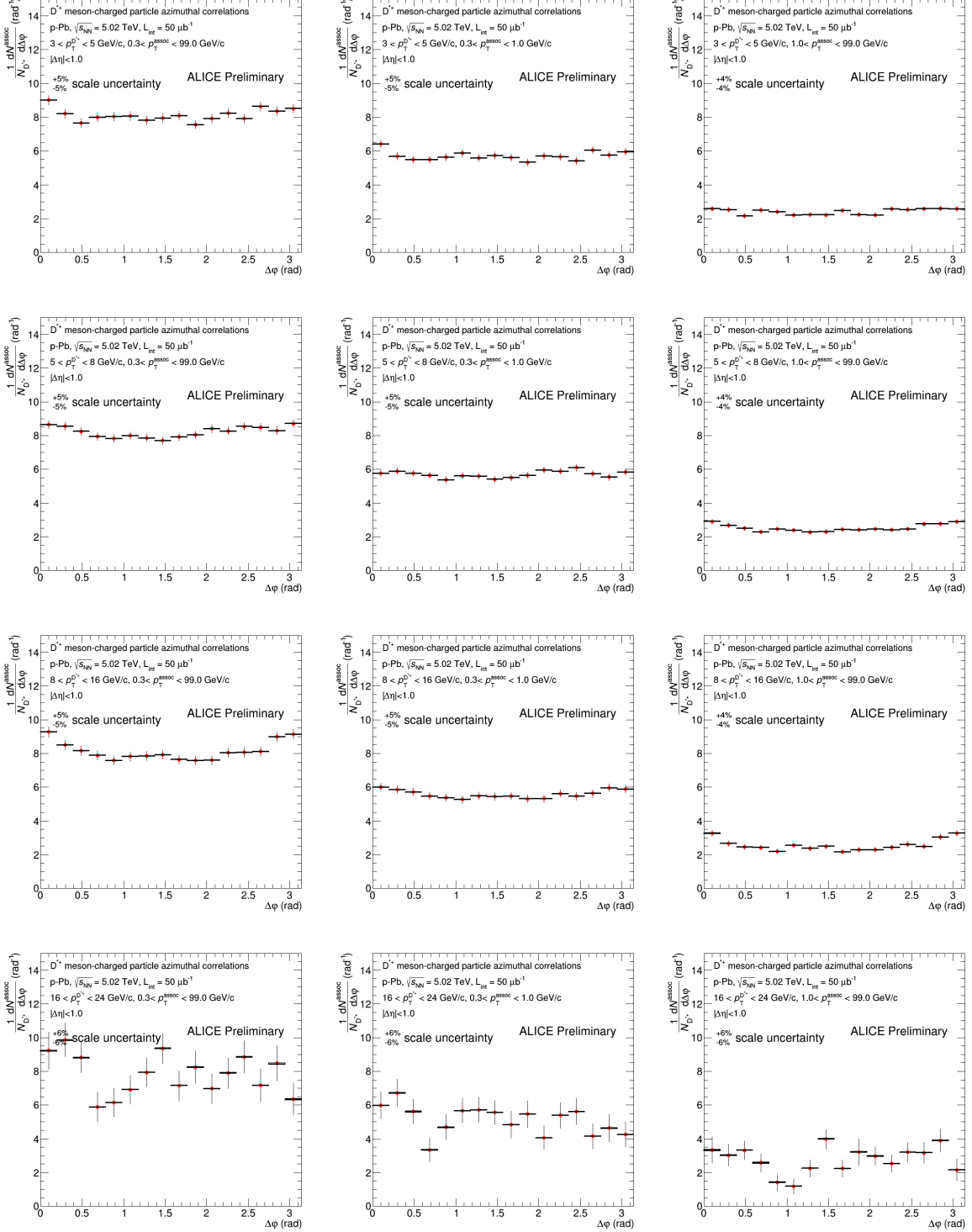


**Figure 109:** Correlation distributions for D<sup>\*+</sup> meson as trigger particle (0-20%). Each row is a different  $p_T(\text{D})$  range, each column a different  $p_T(\text{assoc})$  range. The systematic uncertainties labelled in the plots are not final. Note: the L=50  $\mu\text{b}^{-1}$  is a typo of the drawing macro (it shall be 300  $\mu\text{b}^{-1}$ ).

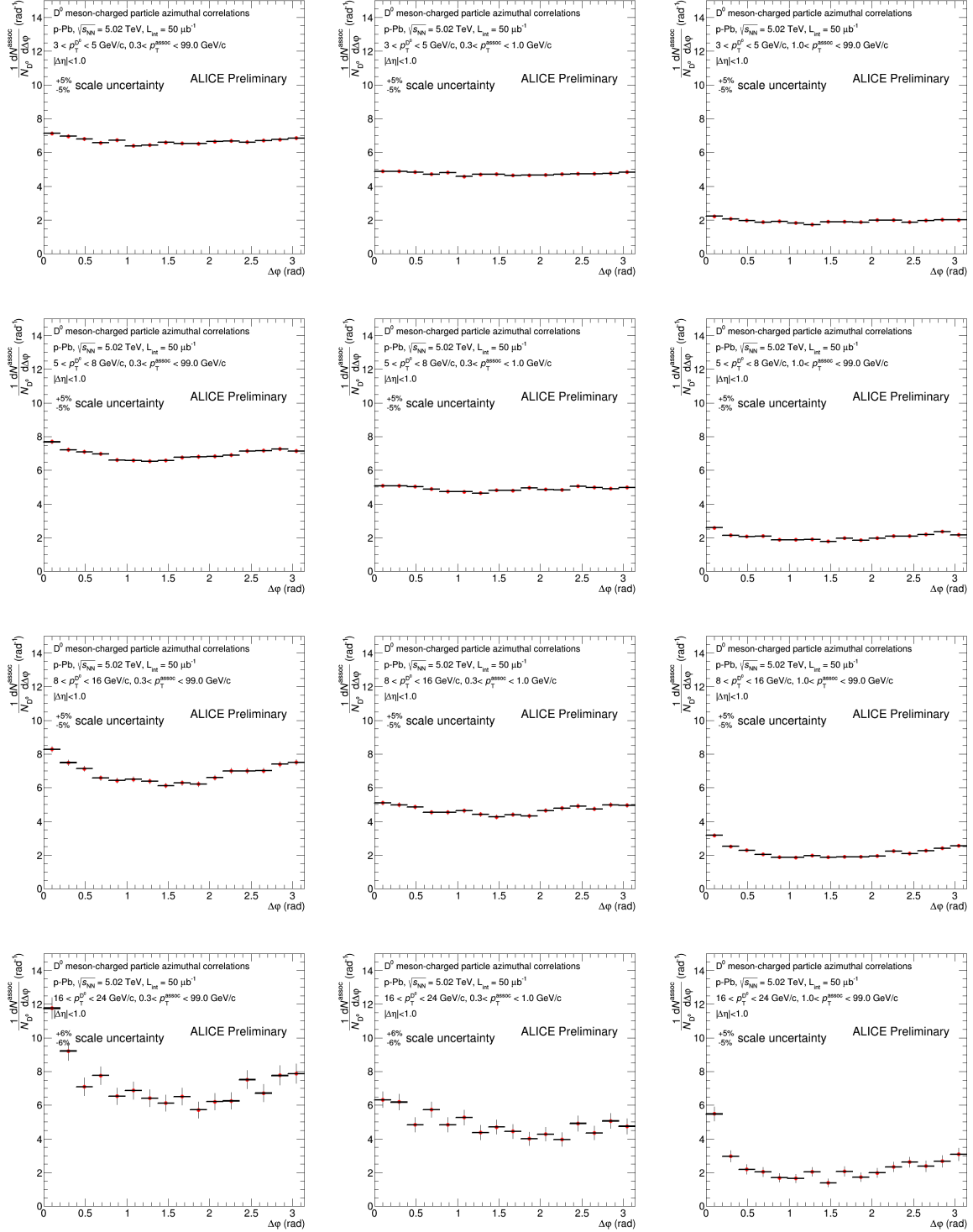


**Figure 110:** Correlation distributions for  $D^0$  meson as trigger particle (20-60%). Each row is a different  $p_T(D)$  range, each column a different  $p_T(\text{assoc})$  range. The systematic uncertainties labelled in the plots are not final. Note: the  $L=50 \mu\text{b}^{-1}$  is a typo of the drawing macro (it shall be  $300 \mu\text{b}^{-1}$ ).

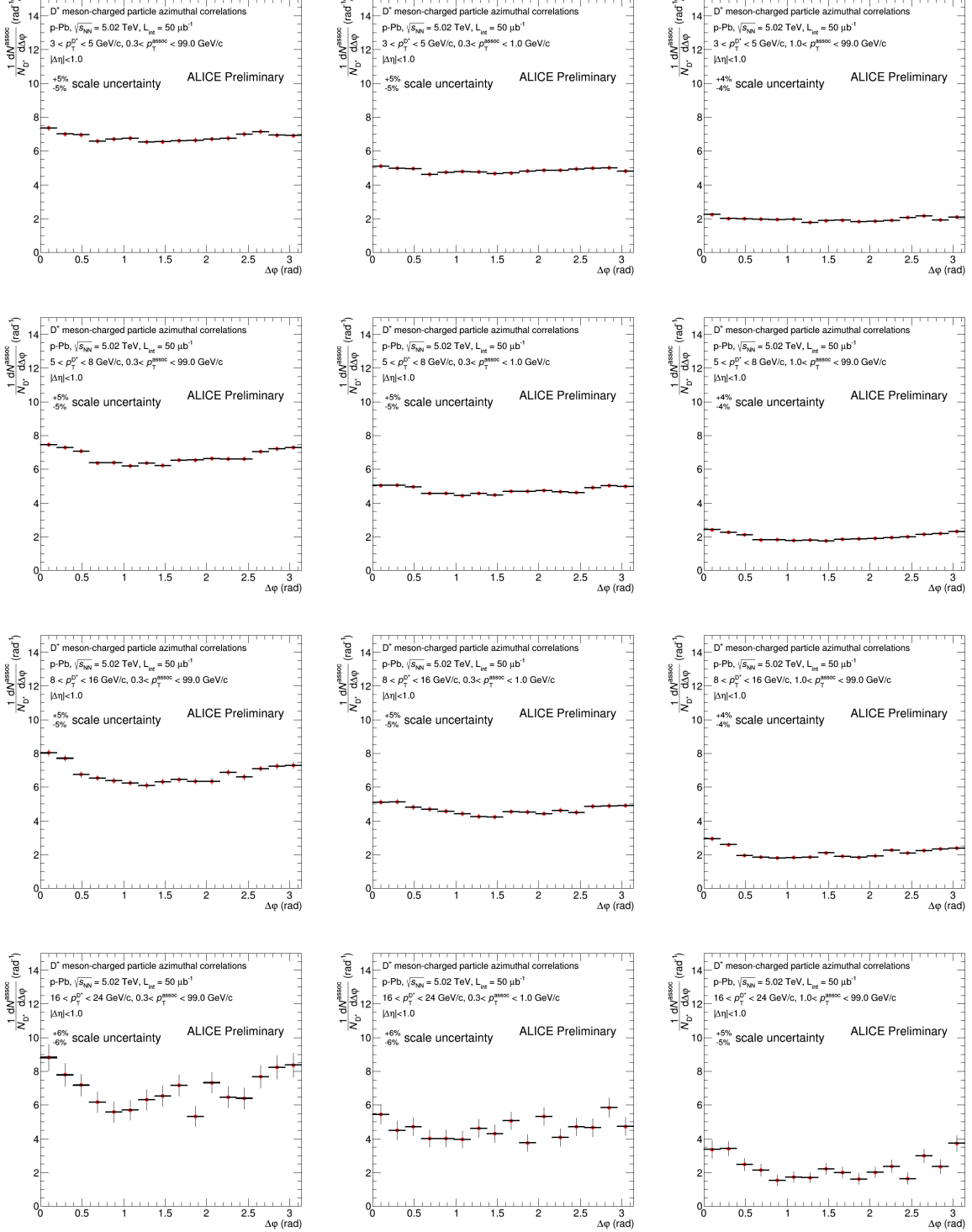


**Figure 111:** Correlation distributions for  $D^+$  meson as trigger particle (20-60%). Each row is a different  $p_T(D)$  range, each column a different  $p_T(\text{assoc})$  range. The systematic uncertainties labelled in the plots are not final. Note: the  $L=50 \mu\text{b}^{-1}$  is a typo of the drawing macro (it shall be  $300 \mu\text{b}^{-1}$ ).

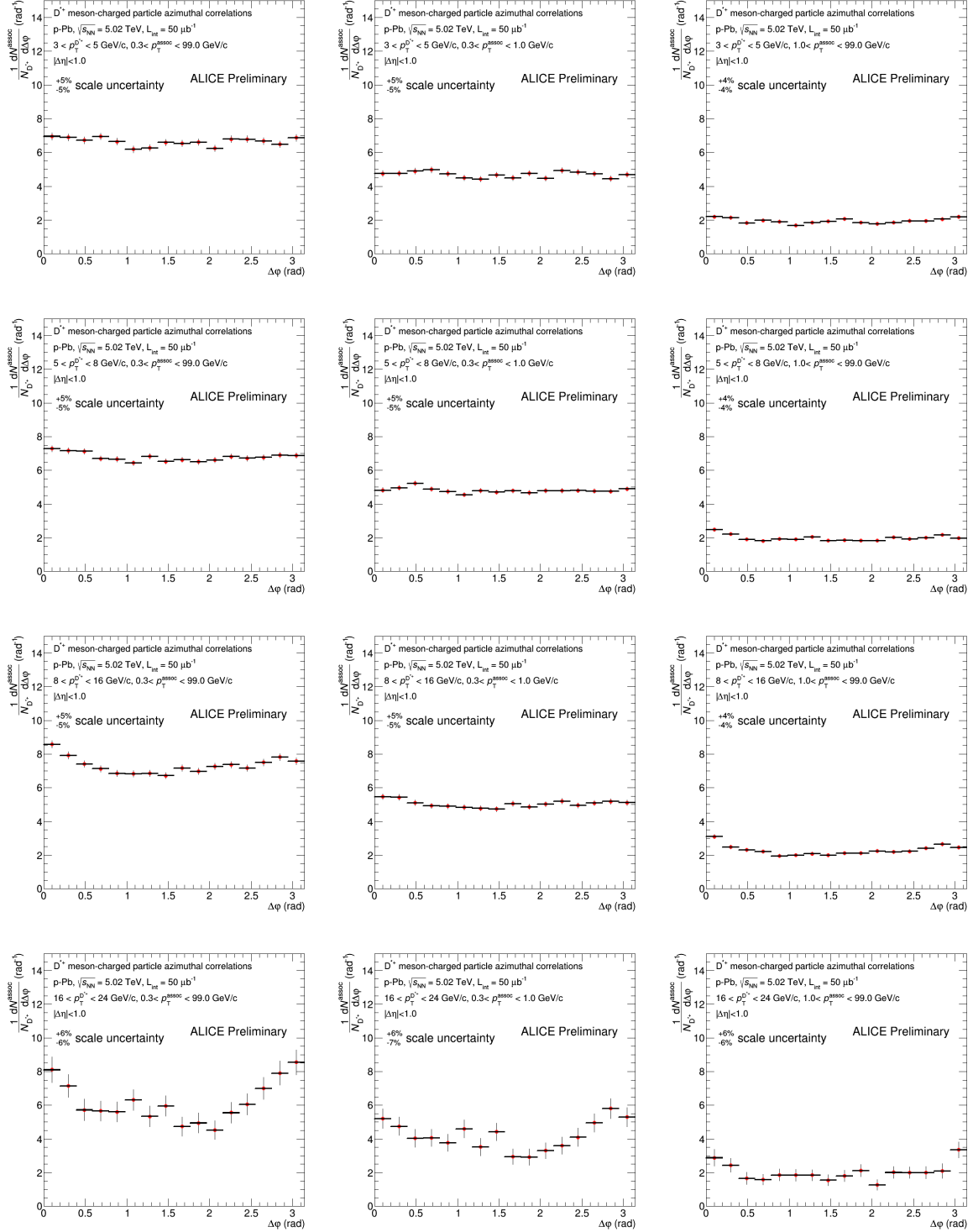


**Figure 112:** Correlation distributions for  $D^{*+}$  meson as trigger particle (20-60%). Each row is a different  $p_T(D)$  range, each column a different  $p_T(\text{assoc})$  range. The systematic uncertainties labelled in the plots are not final. Note: the  $L=50 \mu\text{b}^{-1}$  is a typo of the drawing macro (it shall be  $300 \mu\text{b}^{-1}$ ).

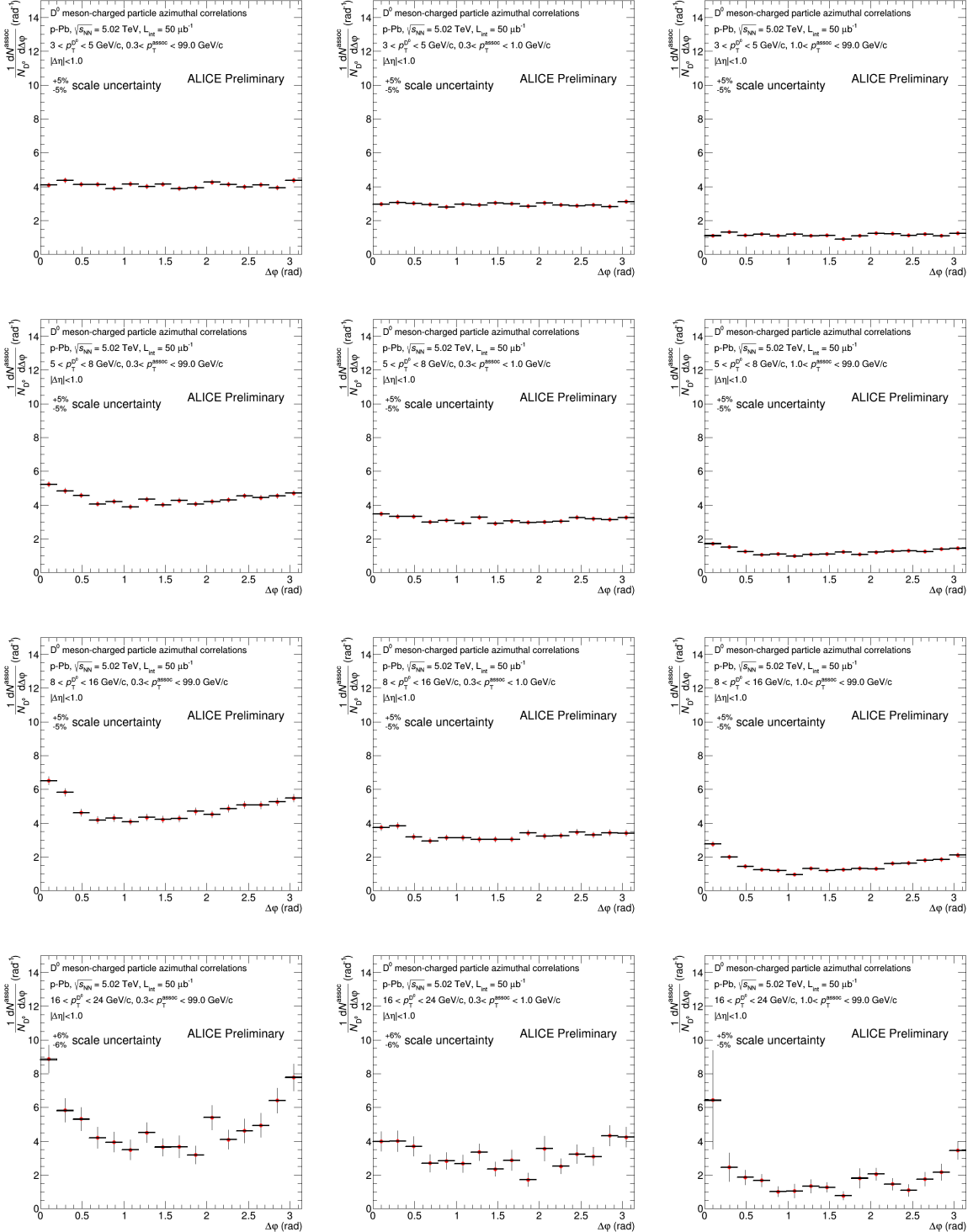


**Figure 113:** Correlation distributions for D<sup>0</sup> meson as trigger particle (60-100%). Each row is a different p<sub>T</sub>(D) range, each column a different p<sub>T</sub>(assoc) range. The systematic uncertainties labelled in the plots are not final. Note: the L=50  $\mu\text{b}^{-1}$  is a typo of the drawing macro (it shall be 300  $\mu\text{b}^{-1}$ ).

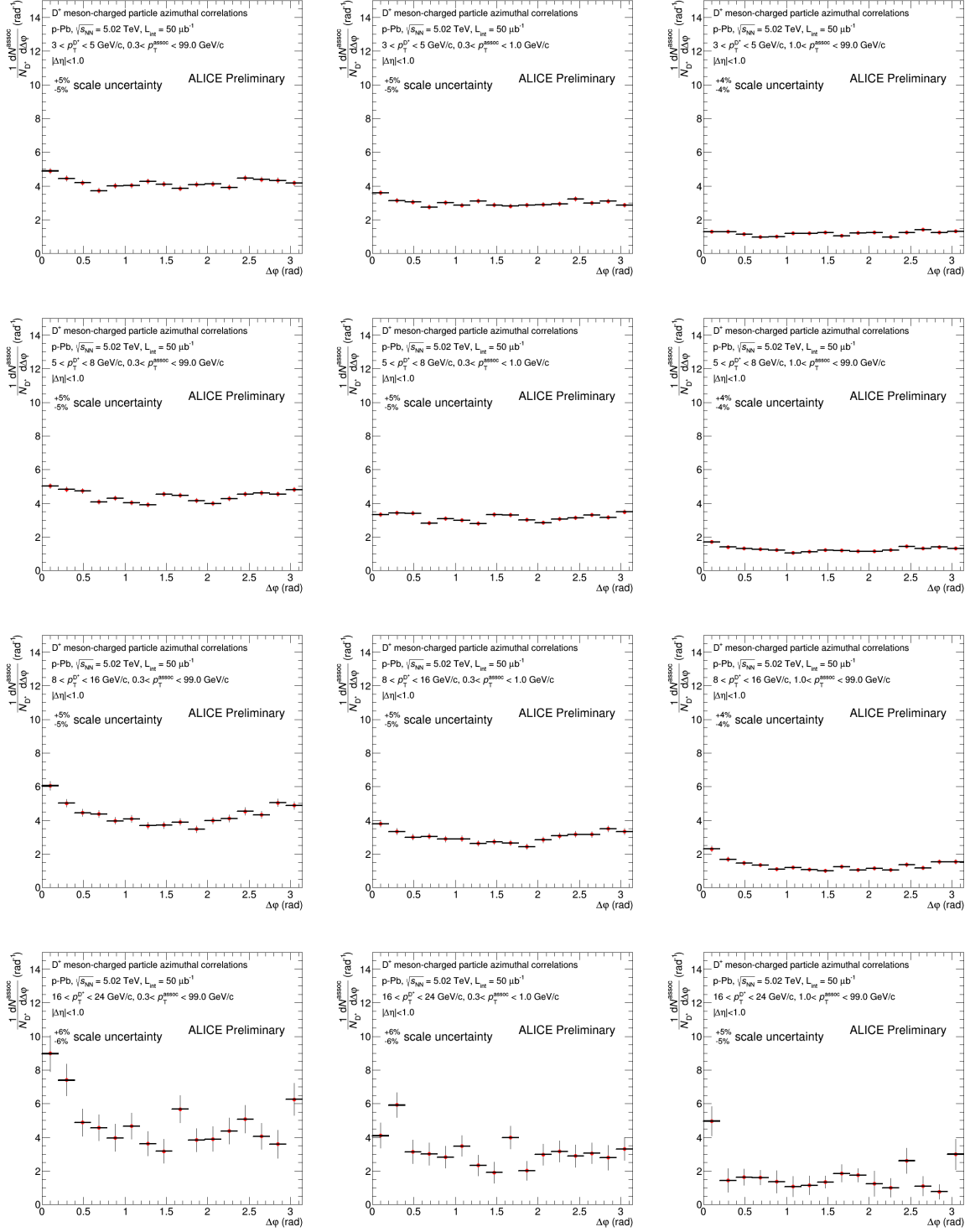


**Figure 14:** Correlation distributions for  $D^+$  meson as trigger particle (60-100%). Each row is a different  $p_T(D)$  range, each column a different  $p_T(\text{assoc})$  range. The systematic uncertainties labelled in the plots are not final. Note: the  $L=50 \mu\text{b}^{-1}$  is a typo of the drawing macro (it shall be  $300 \mu\text{b}^{-1}$ ).

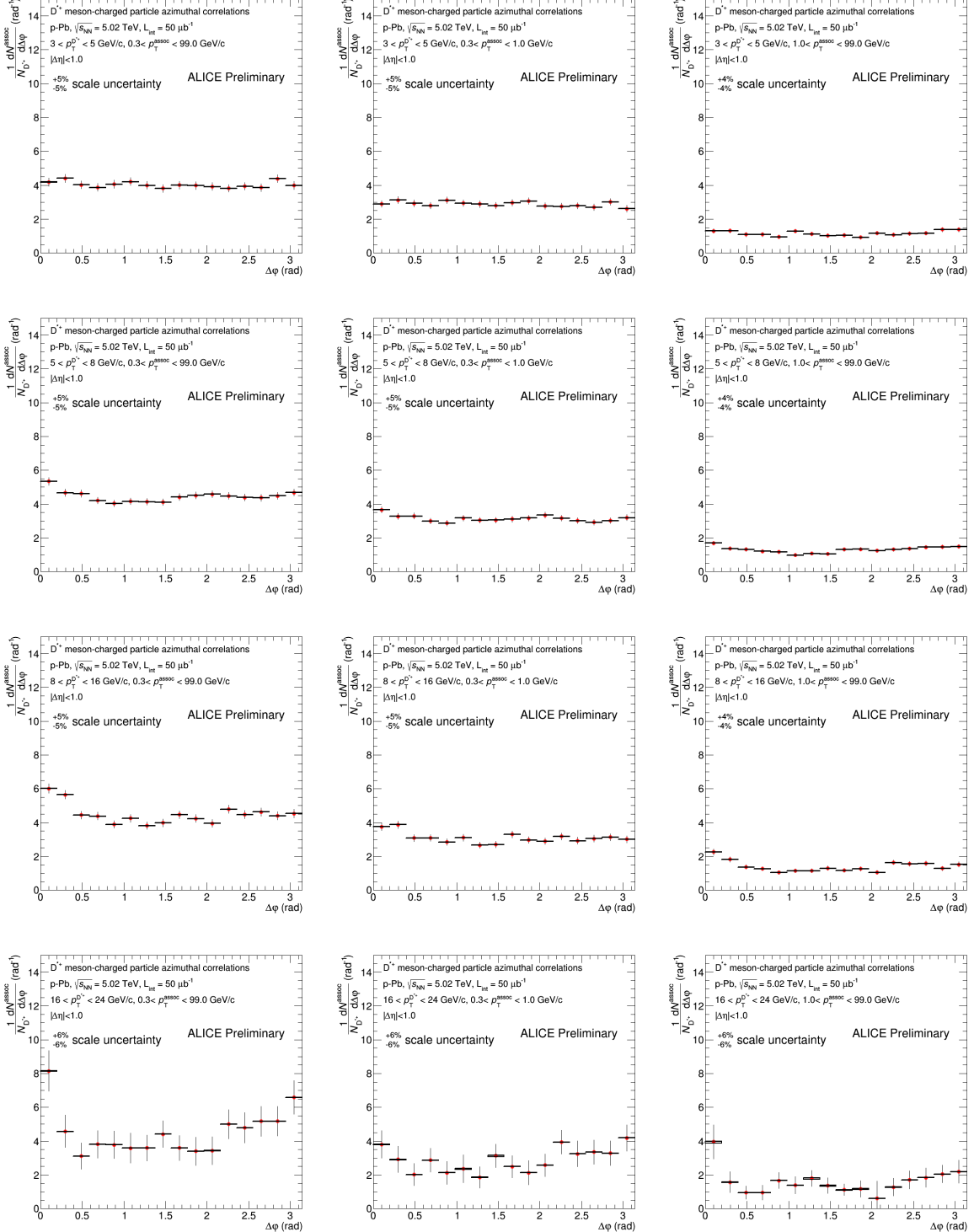


**Figure 115:** Correlation distributions for  $D^{*+}$  meson as trigger particle (60-100%). Each row is a different  $p_T(D)$  range, each column a different  $p_T(\text{assoc})$  range. The systematic uncertainties labelled in the plots are not final. Note: the  $L=50 \mu\text{b}^{-1}$  is a typo of the drawing macro (it shall be  $300 \mu\text{b}^{-1}$ ).

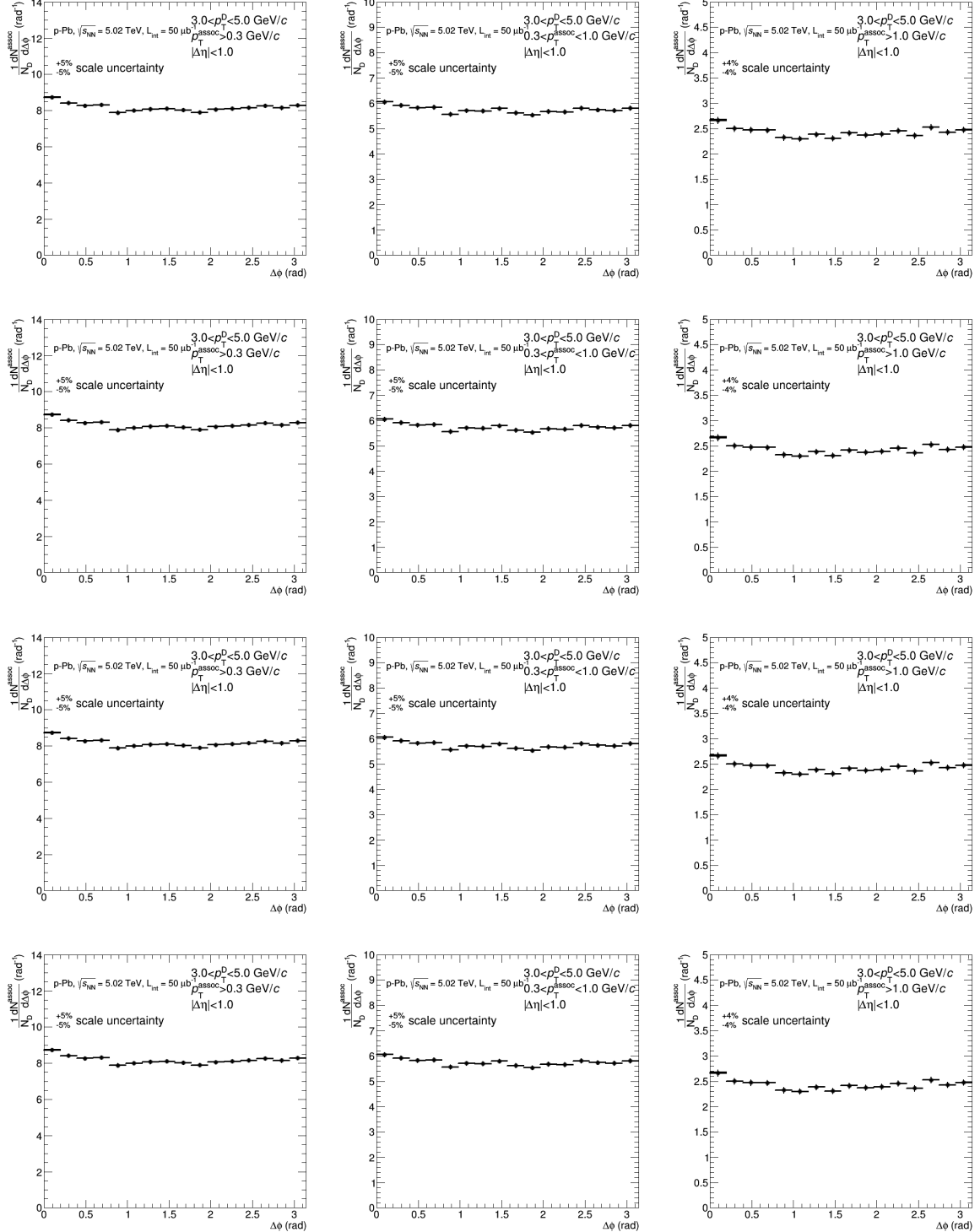


**Figure 116:** Average D-hadron correlation distributions in 0-20% centrality class. Each row is a different  $p_T(D)$  range, each column a different  $p_T(\text{assoc})$  range. The systematic uncertainties labelled in the plots are not final. Note: the  $L=50 \mu\text{b}^{-1}$  is a typo of the drawing macro (it shall be  $300 \mu\text{b}^{-1}$ ).

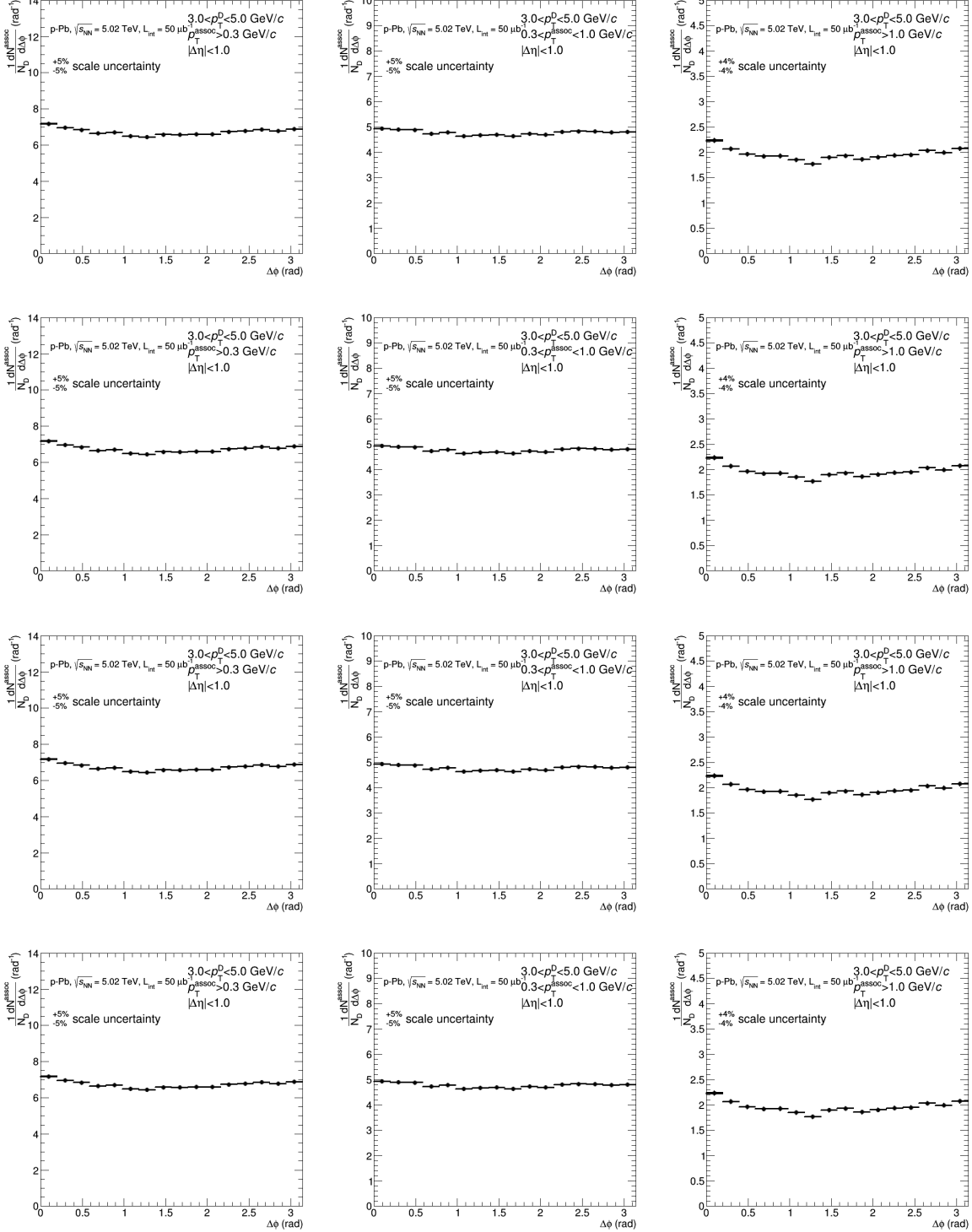


**Figure 117:** Average D-hadron correlation distributions in 20-60% centrality class. Each row is a different  $p_T(\text{D})$  range, each column a different  $p_T(\text{assoc})$  range. The systematic uncertainties labelled in the plots are not final. Note: the  $L=50 \mu\text{b}^{-1}$  is a typo of the drawing macro (it shall be  $300 \mu\text{b}^{-1}$ ).

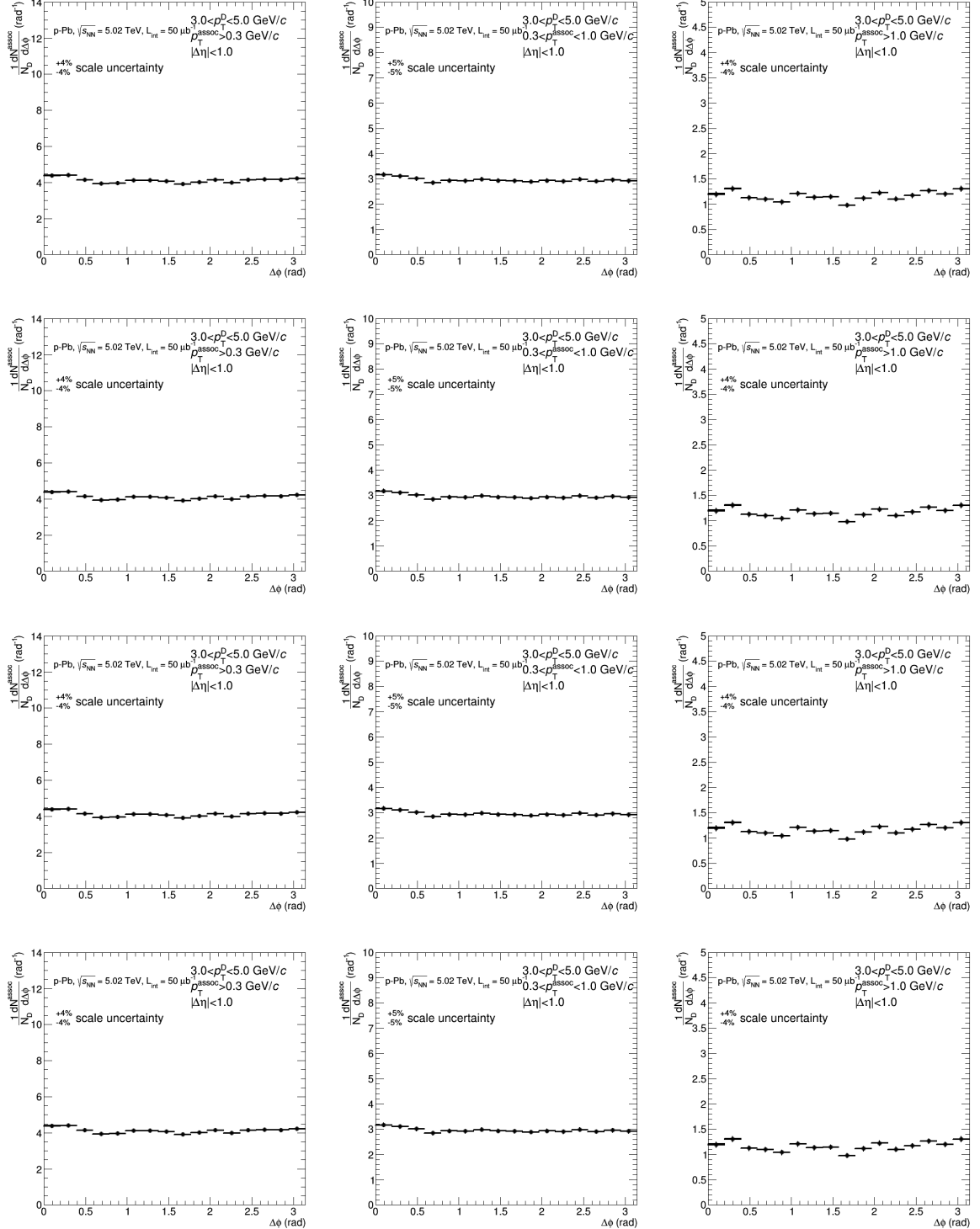


**Figure 118:** Average D-hadron correlation distributions in 60-100% centrality class. Each row is a different  $p_T(\text{D})$  range, each column a different  $p_T(\text{assoc})$  range. The systematic uncertainties labelled in the plots are not final. Note: the  $L=50 \mu\text{b}^{-1}$  is a typo of the drawing macro (it shall be  $300 \mu\text{b}^{-1}$ ).

**1089 6.4.3 Observables from fit to correlation distributions**

1090 The outcome of the fits to the above correlation distributions are shown in Fig. 119, 120, 121, for the  
1091 three centrality ranges.

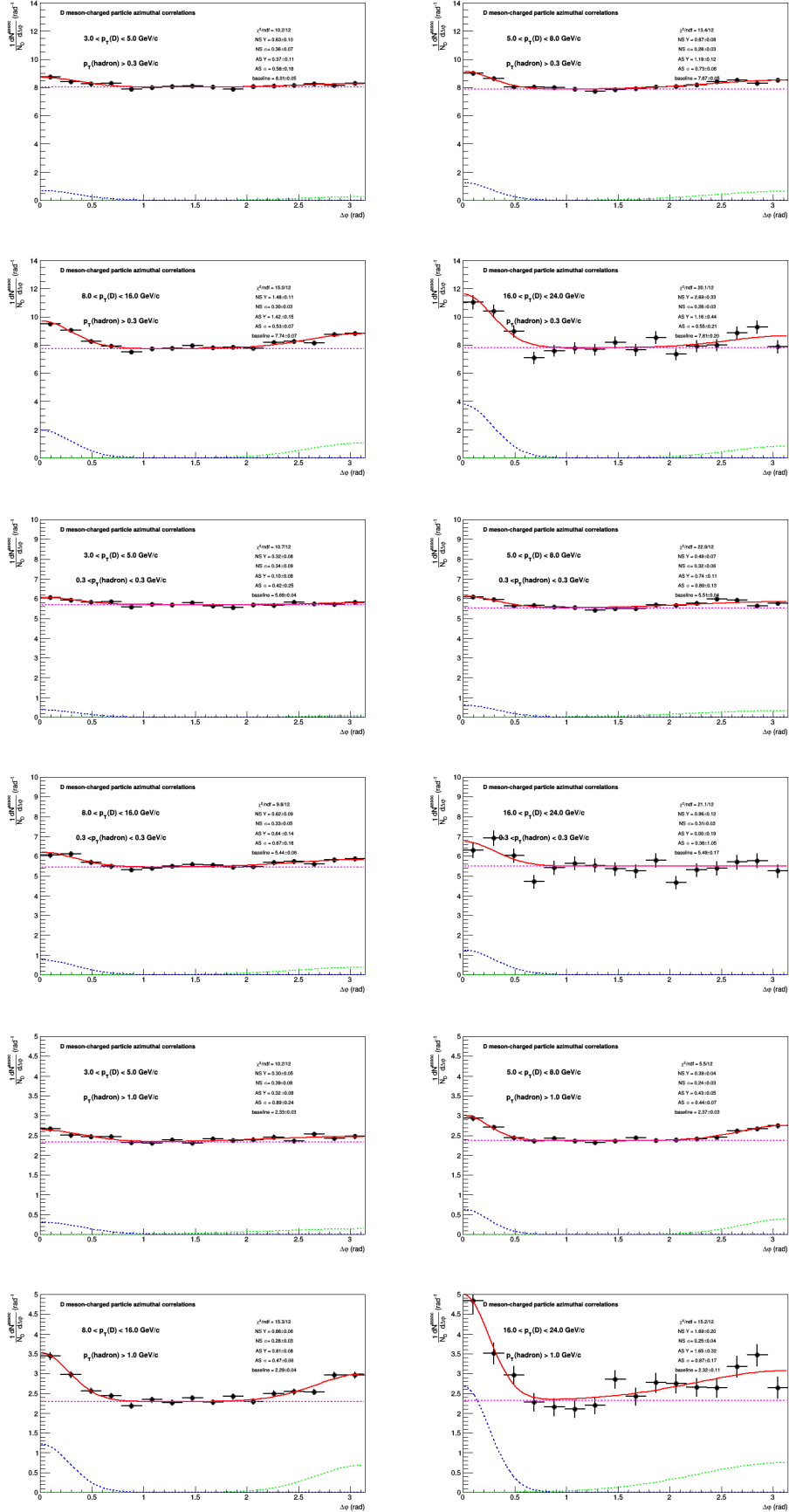


**Figure 119:** Outcome of fit to correlation distributions in 0-20% centrality class. Each sub-figure shows the 4  $p_T(D)$  ranges of a given  $p_T(\text{assoc})$  range.

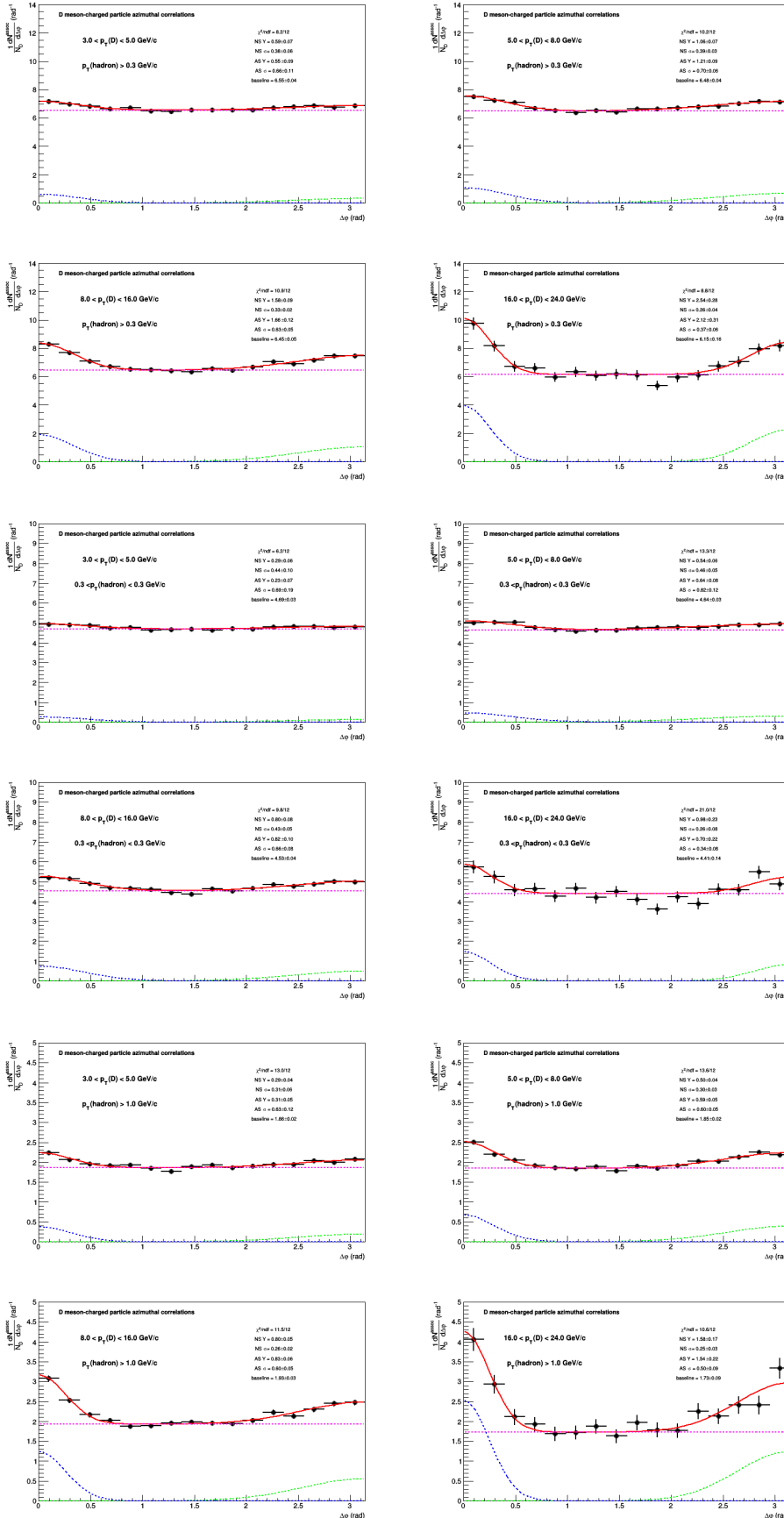


**Figure 120:** Outcome of fit to correlation distributions in 20-60% centrality class. Each sub-figure shows the 4  $p_T(D)$  ranges of a given  $p_T(\text{assoc})$  range.

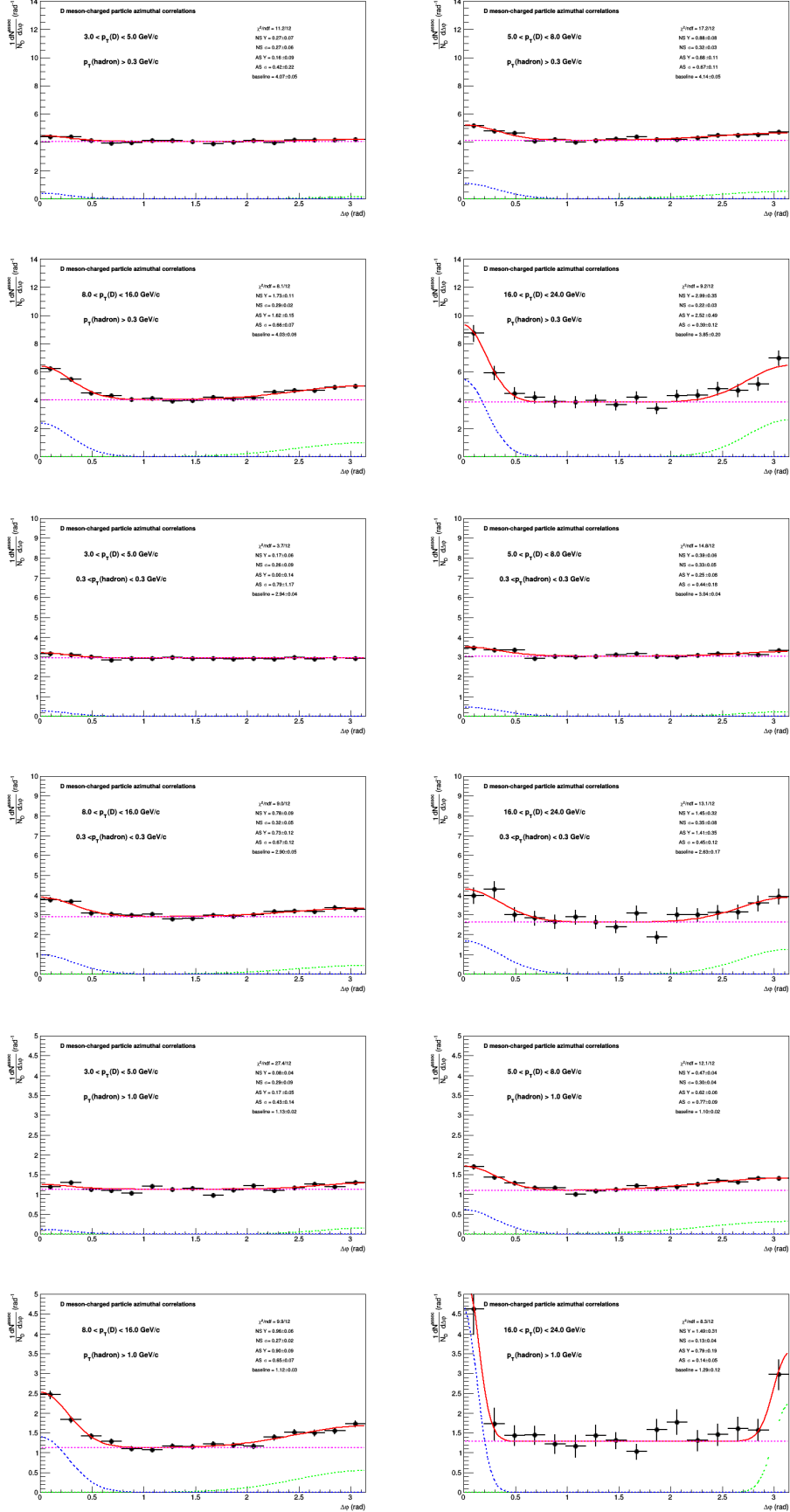


**Figure 121:** Outcome of fit to correlation distributions in 60-100% centrality class. Each sub-figure shows the 4  $p_T(\text{assoc})$  ranges of a given  $p_T(D)$  range.

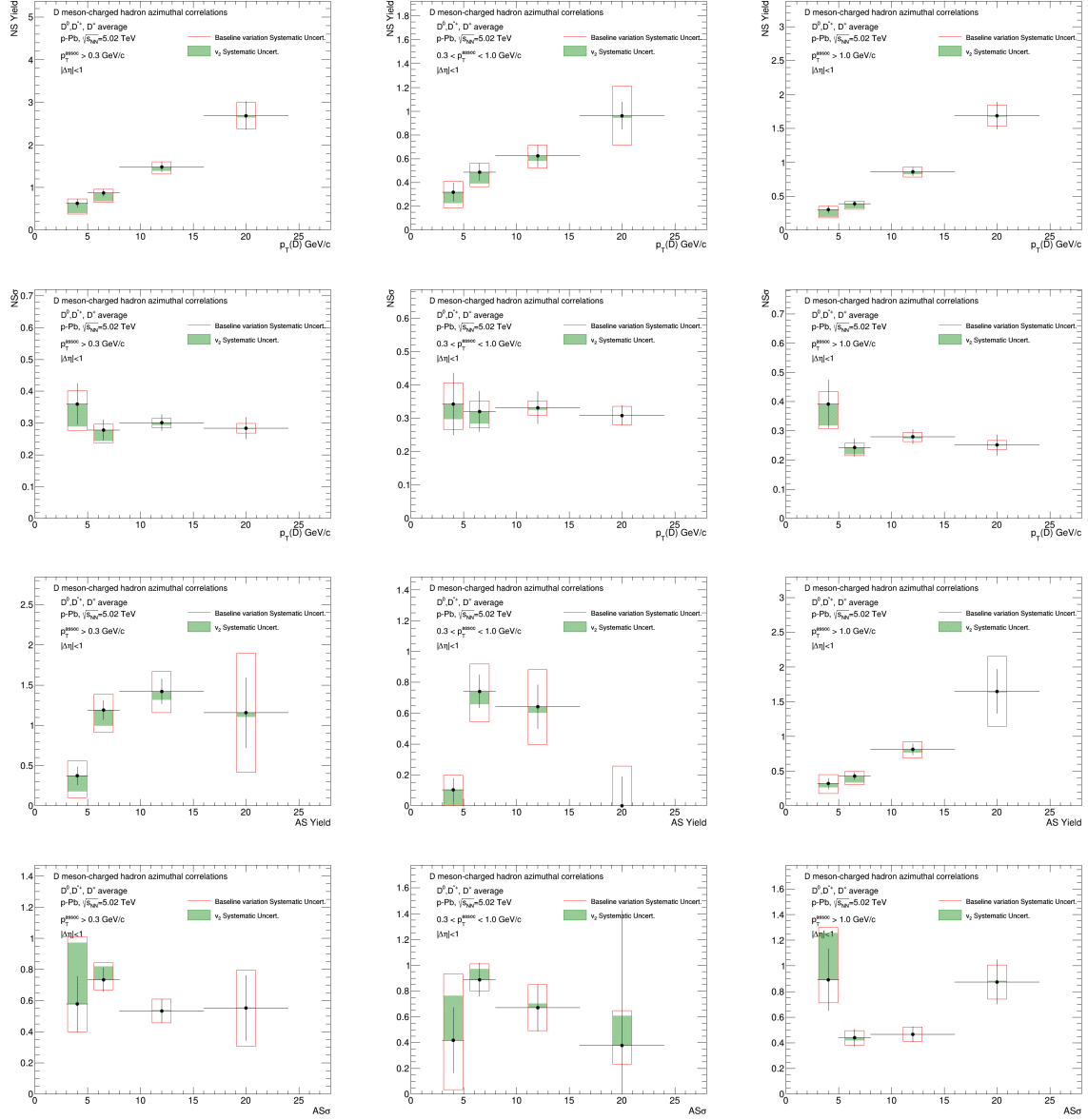


**Figure 122:** Near-side yield (rows 1-3) and width (4-6) and away-side yield (7-9) and width (10-12), for 0-20%. Each row represents a  $p_T(\text{assoc})$  range, and each panel shows the  $p_T(D)$  trend of the observable for a given  $p_T(\text{assoc})$  range.

1092 In Fig. 122, 123, 124 the quantitative observables (i.e. near-side and away-side yields and widths)  
1093 extracted from the fit are presented.

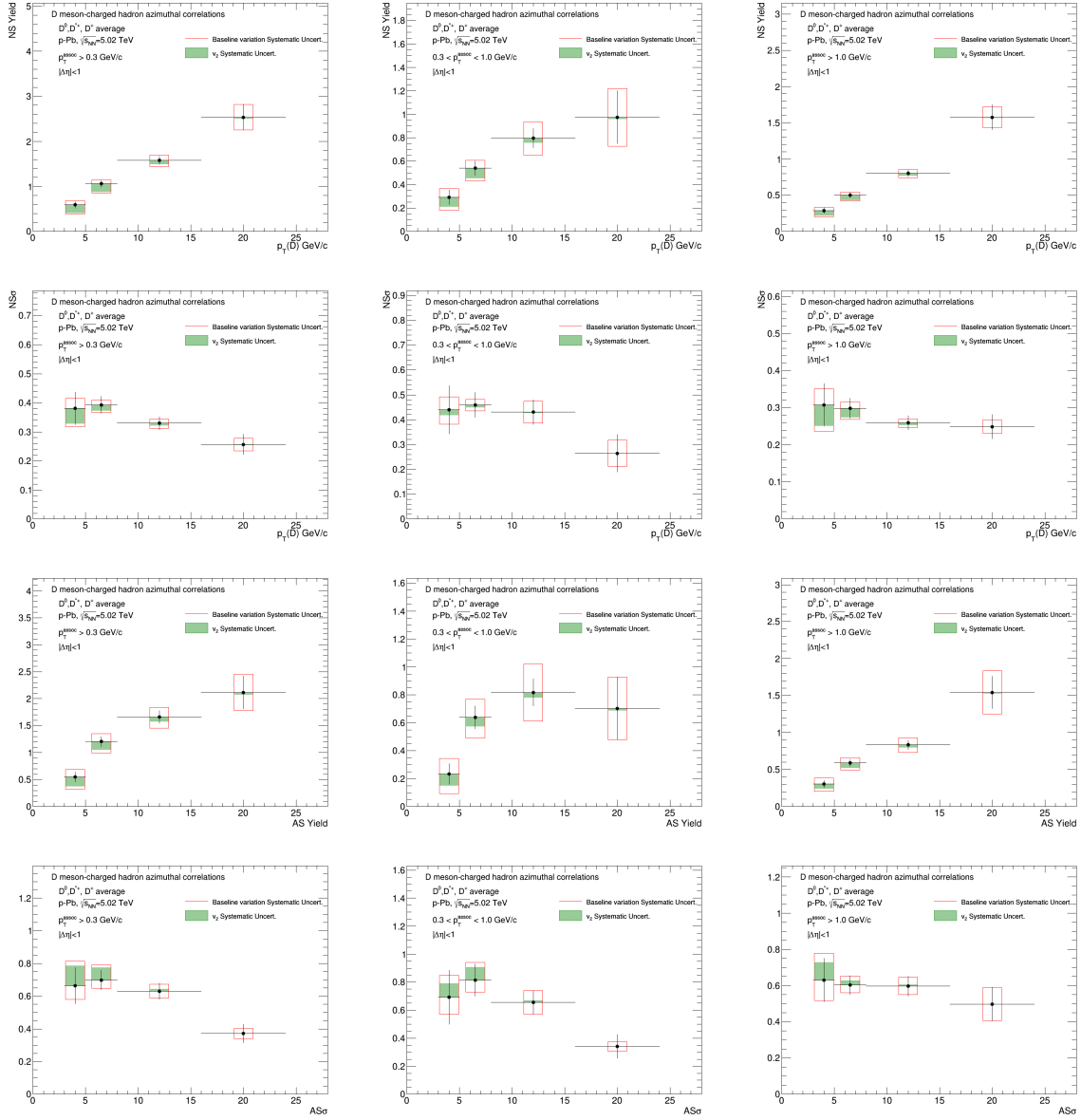


**Figure 123:** Near-side yield (rows 1-3) and width (4-6) and away-side yield (7-9) and width (10-12), for 20-60%. Each row represents a  $p_T(\text{assoc})$  range, and each panel shows the  $p_T(D)$  trend of the observable for a given  $p_T(\text{assoc})$  range.

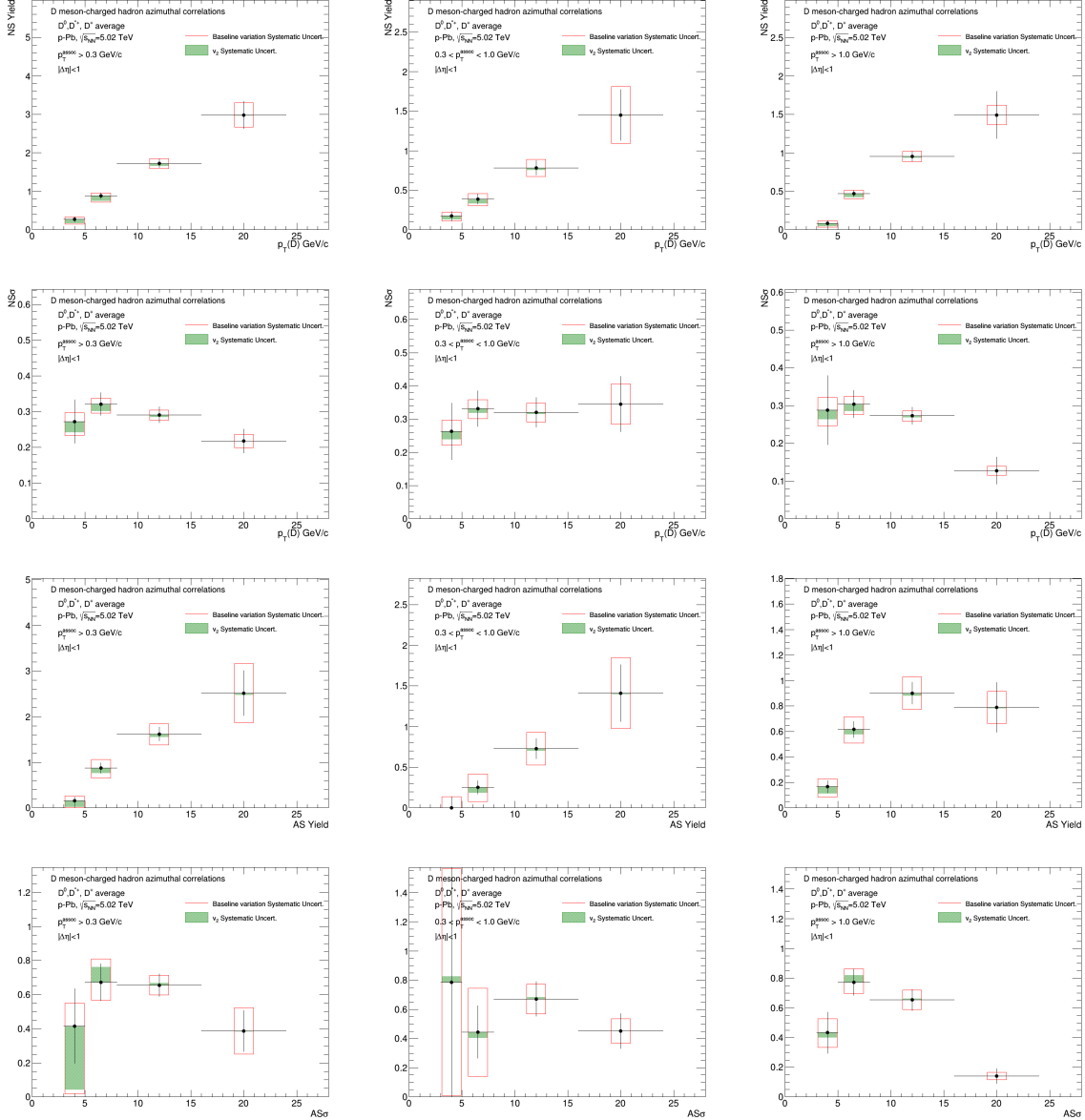


**Figure 124:** Near-side yield (rows 1-3) and width (4-6) and away-side yield (7-9) and width (10-12), for 60-100%. Each row represents a  $p_{\text{T}}(\text{assoc})$  range, and each panel shows the  $p_{\text{T}}(\text{D})$  trend of the observable for a given  $p_{\text{T}}(\text{assoc})$  range.

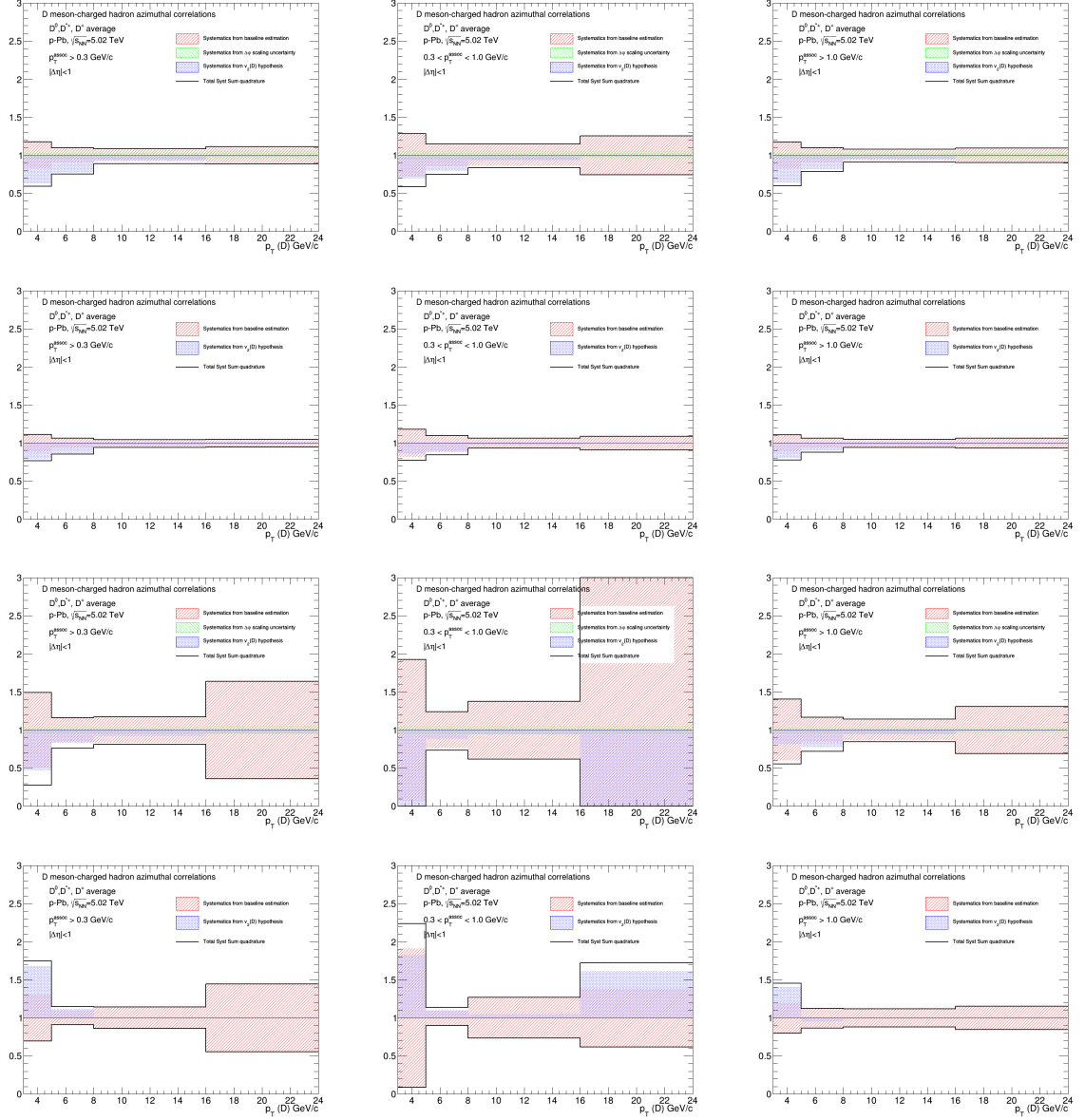


**Figure 125:** Near-side yield (rows 1-3) and width (4-6) and away-side yield (7-9) and width (10-12), for 0-20%. Each row represents a  $p_{\text{T}}(\text{assoc})$  range, and each panel shows the  $p_{\text{T}}(\text{D})$  trend of the observable for a given  $p_{\text{T}}(\text{assoc})$  range.

1094 The systematic uncertainties on the fit observables, including those related to the variation of the trans-  
 1095 verse region for the baseline evaluation, the possible presence of a  $v_2$  modulation, and the  $\Delta\phi$  scaling  
 1096 uncertainty (for the yields only), are shown in Fig. 125, 126, 127.

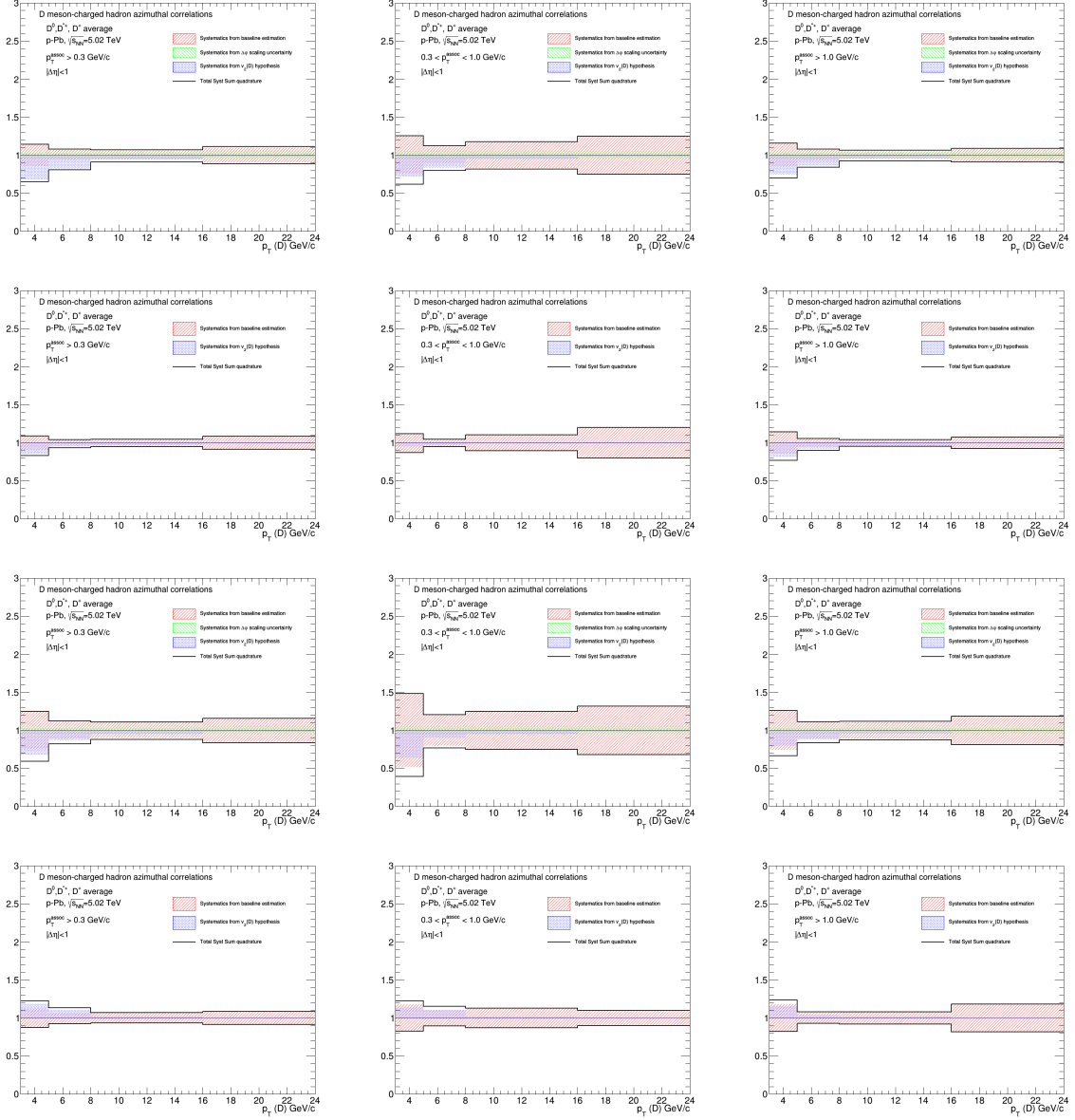


**Figure 126:** Near-side yield (rows 1-3) and width (4-6) and away-side yield (7-9) and width (10-12), for 20-60%. Each row represents a  $p_T(\text{assoc})$  range, and each panel shows the  $p_T(D)$  trend of the observable for a given  $p_T(\text{assoc})$  range.

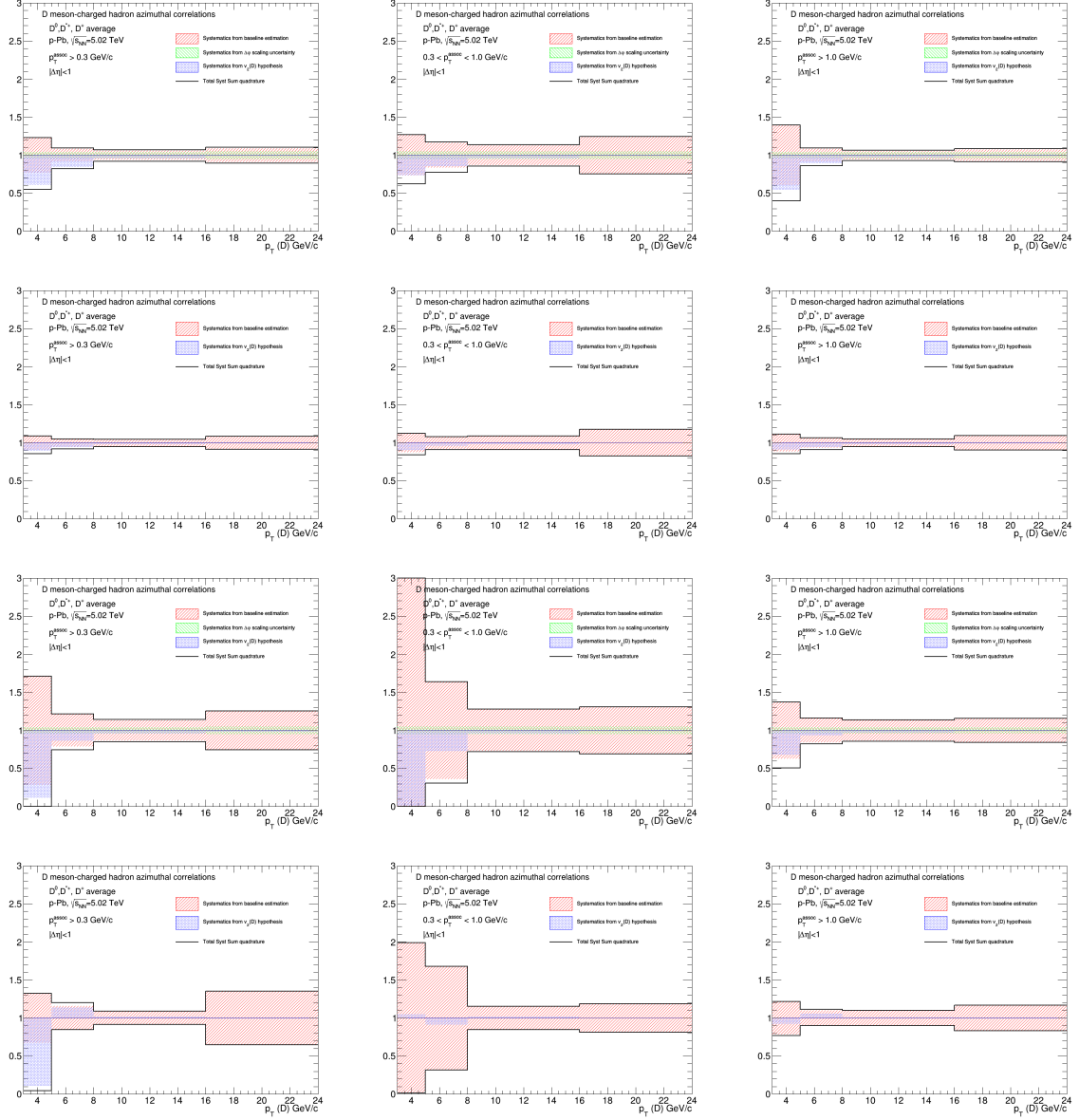


**Figure 127:** Near-side yield (rows 1-3) and width (4-6) and away-side yield (7-9) and width (10-12), for 60-100%. Each row represents a  $p_T(\text{assoc})$  range, and each panel shows the  $p_T(\text{D})$  trend of the observable for a given  $p_T(\text{assoc})$  range.

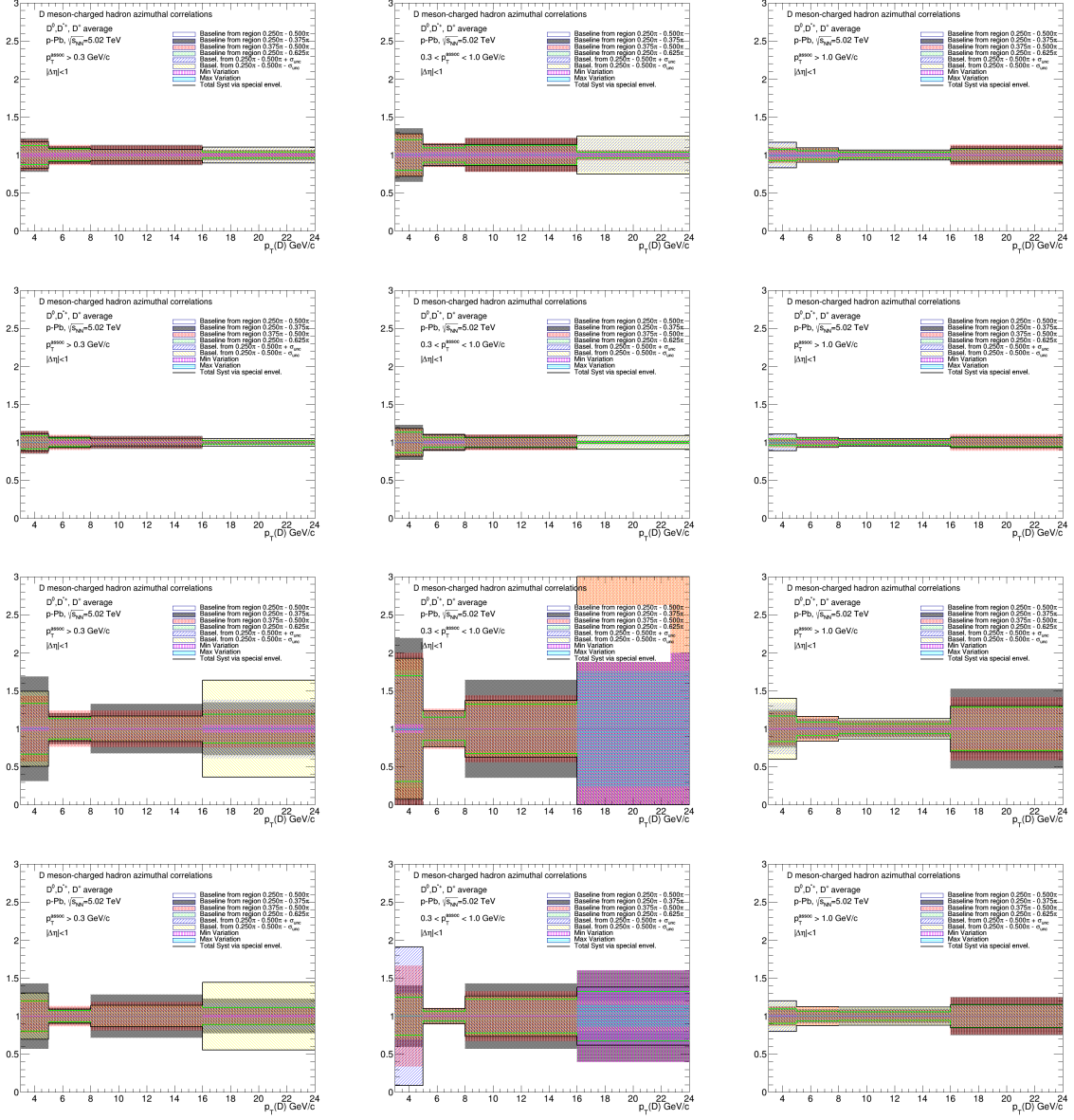


**Figure 128:** Near-side yield (rows 1-3) and width (4-6) and away-side yield (7-9) and width (10-12), for 0-20%. Each row represents a  $p_T(\text{assoc})$  range, and each panel shows the  $p_T(\text{D})$  trend of the observable for a given  $p_T(\text{assoc})$  range.

In particular, the breakdown of the uncertainties coming from the alternate fits done with different transverse region definition (as well as from the alternate fits by moving the baseline value from its default value) are shown in Fig. 128, 129, 130.

#### 6.4.4 Plots proposed for preliminaries

In the following, the two figures for which an approval as preliminary is requested are presented.

The first is a comparison of the correlation distributions, after the baseline subtraction, among the three centrality classes (showing also the 0-100% results, i.e. the previously approved preliminary results). Each panel represents a different kinematic range. In all the three centrality classes, the correlation distributions show very similar shapes of the correlation peaks, and a consistent  $p_T$  evolution. Most probably, the last column will be cropped, due to the too large statistical uncertainty on the 16-24 GeV/c

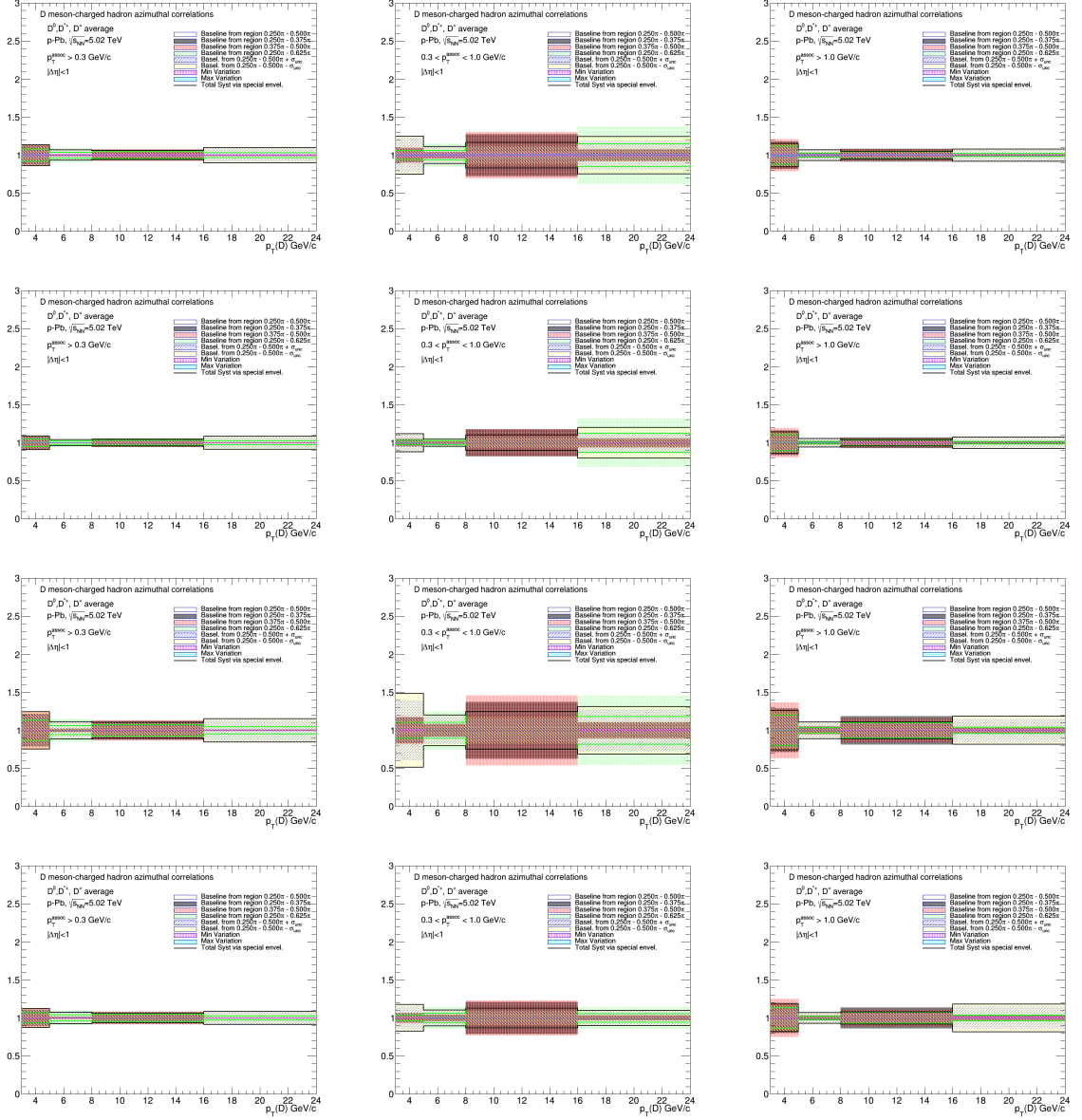


**Figure 129:** Near-side yield (rows 1-3) and width (4-6) and away-side yield (7-9) and width (10-12), for 20-60%. Each row represents a  $p_T(\text{assoc})$  range, and each panel shows the  $p_T(D)$  trend of the observable for a given  $p_T(\text{assoc})$  range.

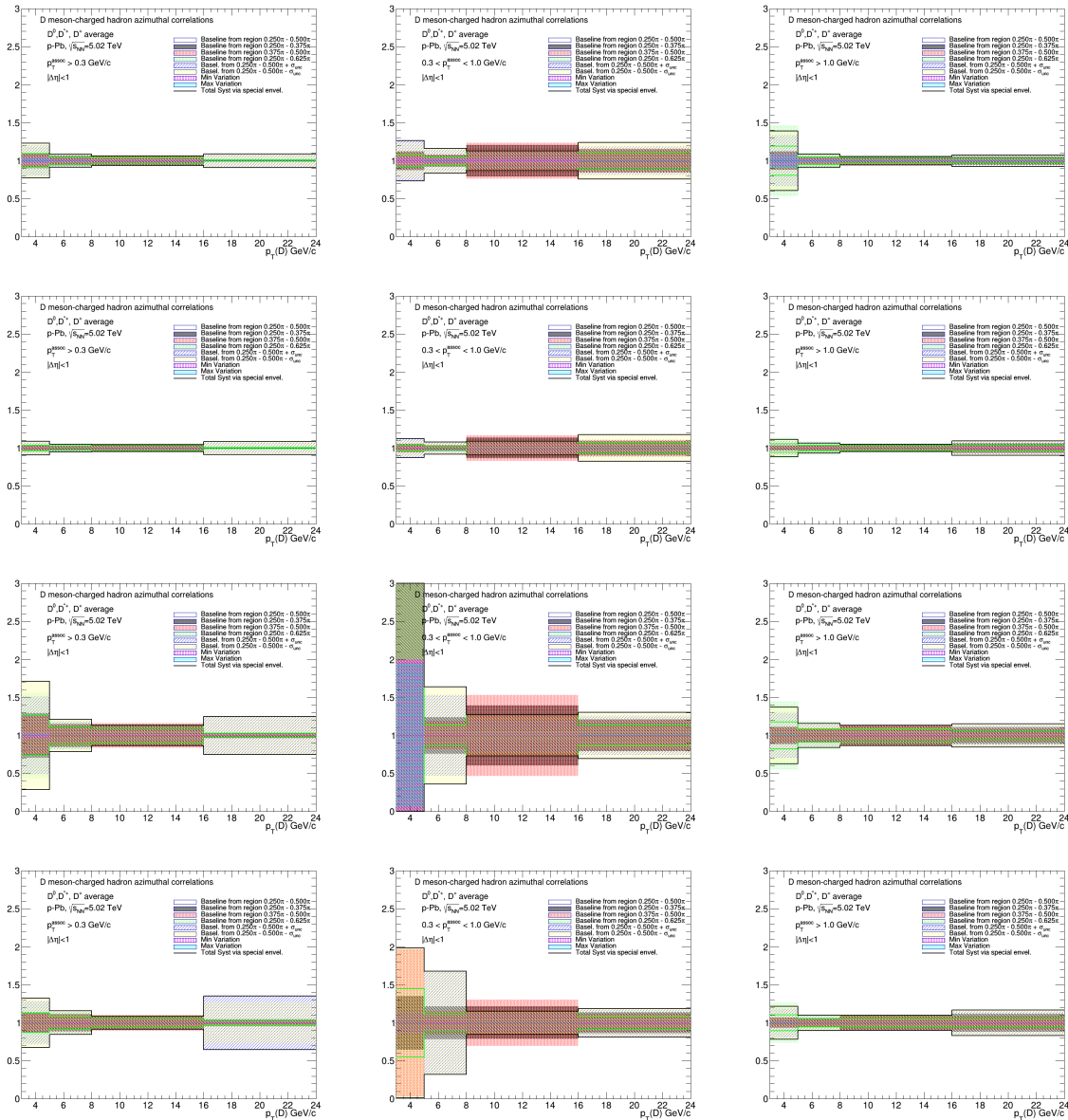


**Figure 130:** Near-side yield (rows 1-3) and width (4-6) and away-side yield (7-9) and width (10-12), for 60-100%. Each row represents a  $p_T(\text{assoc})$  range, and each panel shows the  $p_T(D)$  trend of the observable for a given  $p_T(\text{assoc})$  range.

<sup>1107</sup> correlation distributions.

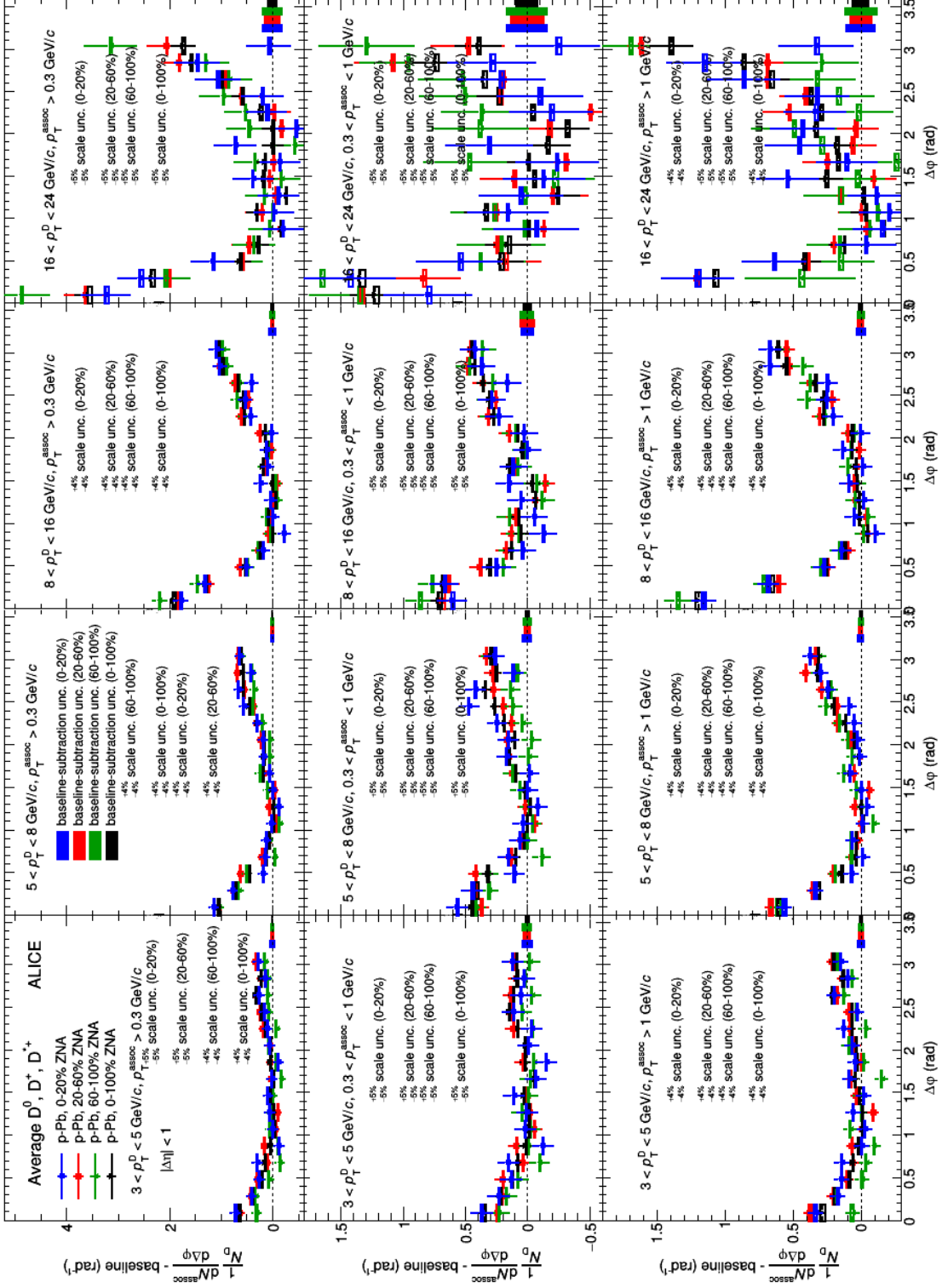


**Figure 131:** Comparison of baseline-subtracted correlation distributions in the different centrality classes. Each color is a different centrality class, as described in the legend. The error bars represent the statistical uncertainty, the empty boxes represent the overall systematic uncertainties, the shaded boxes represent the  $v_2$  related uncertainties.

1108 The second is a comparison of the near-side fit observables (yields and width) among the three cen-  
1109 trality classes, also here showing the 0-100% results as well, i.e. the previously approved preliminary  
1110 results. Within the current uncertainties, no clear modifications of the near-side peak properties appear  
1111 for the different centrality classes (nor w.r.t. the 0-100% results). The same increasing trend with  $p_T(D)$   
1112 is observed, due to the increased energy of the originally parton which results in more production of  
1113 fragmentation tracks, as a similar slight decrease of the peak sigma when going to higher  $p_T(D)$  is also  
1114 observed, due to the stronger collimation of the fragmentation tracks of the charm quark. The small  
1115 value of the yield in the 3-5 GeV/c range in 60-100% (especially for the higher  $p_T(\text{assoc})$  range) is most  
1116 probably not a physical feature, but comes from an unlucky positioning of the points at  $\Delta\varphi \approx 0$  of the  
1117 azimuthal correlation (mainly due to fluctuations), especially for the first point, as it can be seen from  
1118 the previous figure (green points).

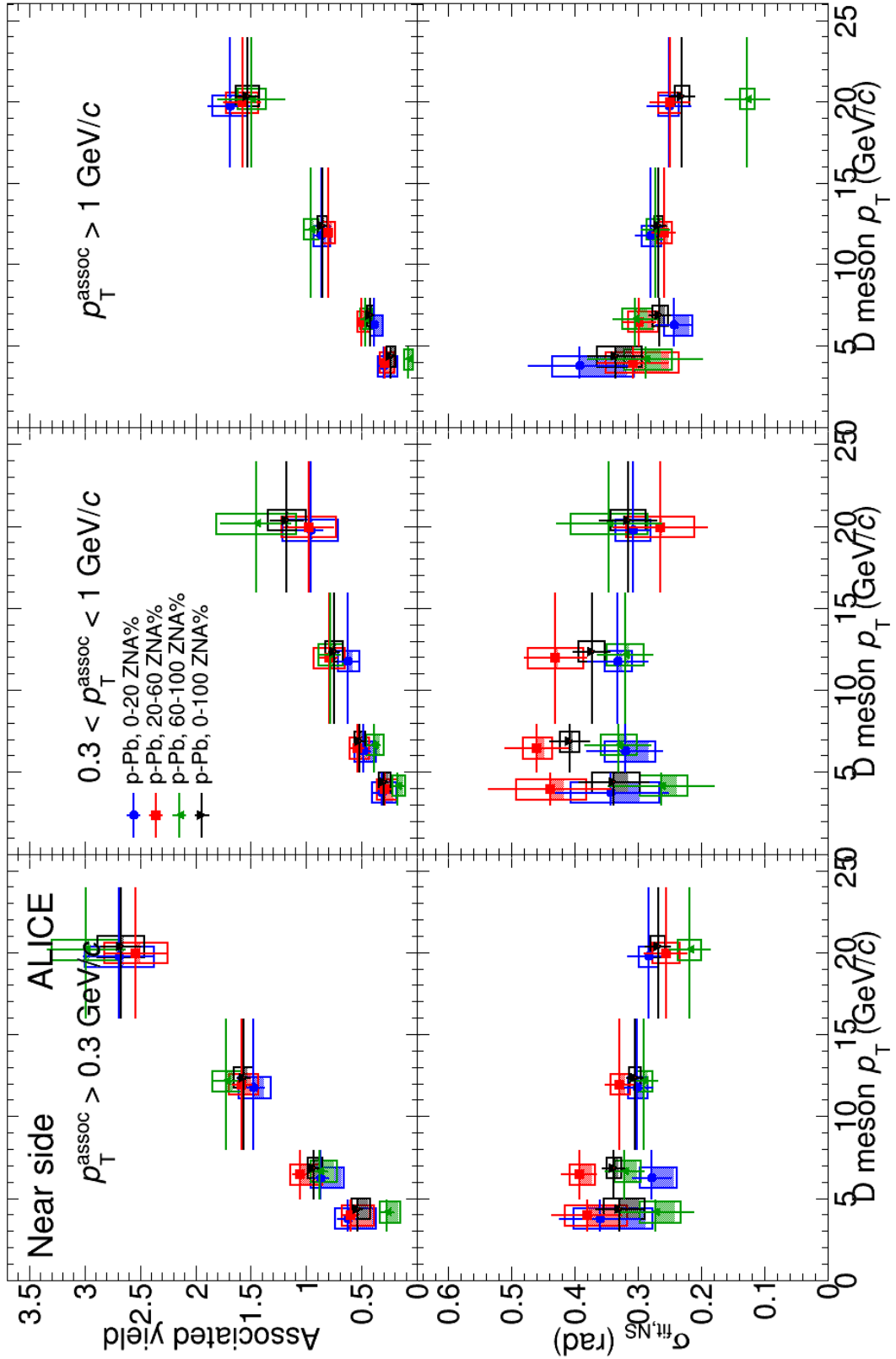


**Figure 132:** Comparison of near-side observables in the different centrality classes. Each color is a different centrality class, as described in the legend. The error bars represent the statistical uncertainty, the empty boxes represent the overall systematic uncertainties, the shaded boxes represent the  $v_2$  related uncertainties.

1119 For completeness, the comparison of the away-side fit observables are also shown. Anyway, due to the  
1120 too large uncertainties, especially those related to the fitting procedure, we will most probably not request  
1121 an approval for this figure. Indeed, some of the fits even fail in reproducing the away-side peak, while  
1122 this doesn't happen for the near-side peak region. On top of the uncertainties, an increase of the yields  
1123 with  $p_T(D)$ , though probably slightly milder than for the near-side, can be observed, as well as a very  
1124 similar slightly decreasing trend for the away-side width - though the values are approximately twofold  
1125 w.r.t. the near-side width.

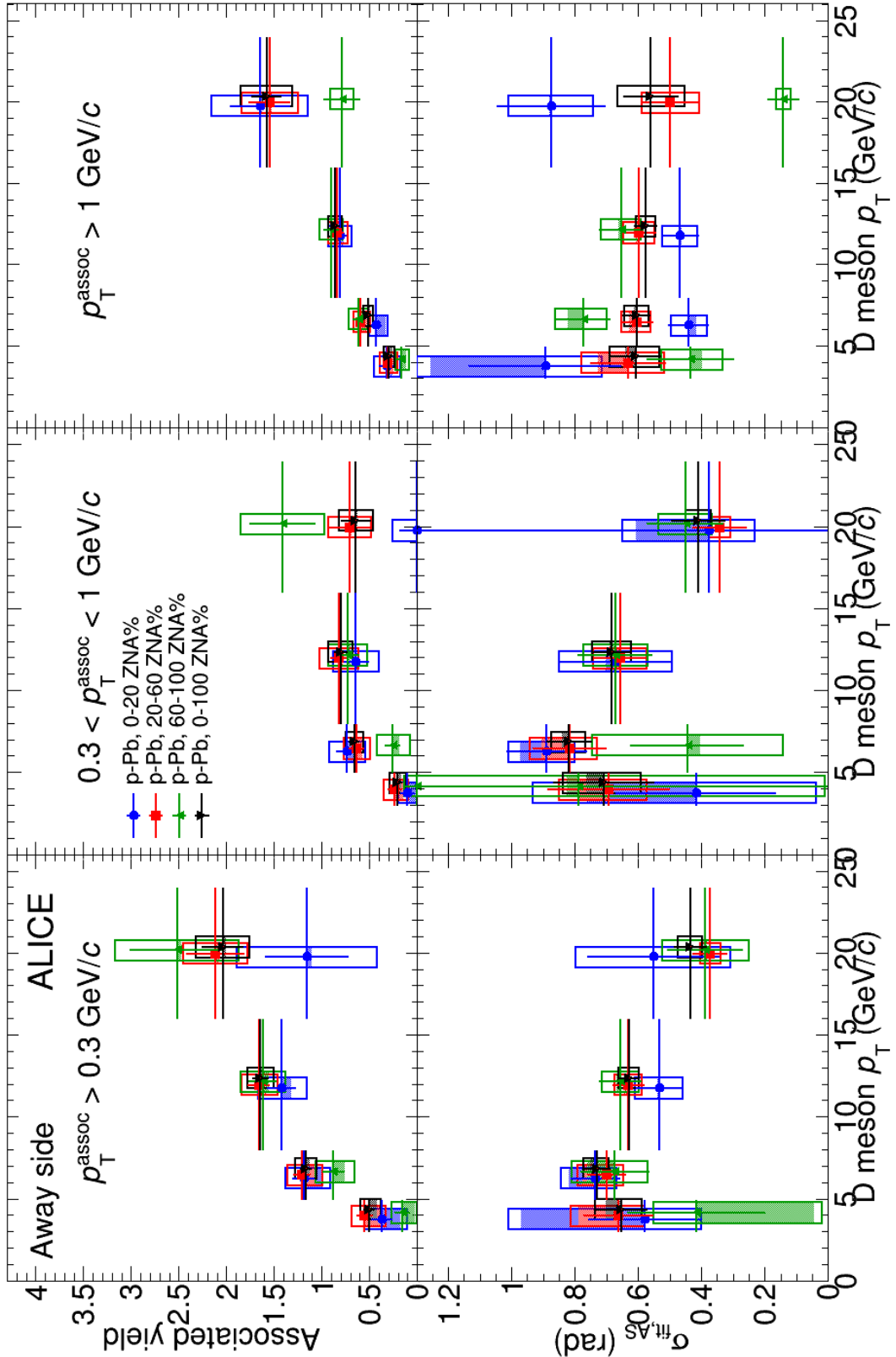


Figure 133: Comparison of away-side observables in the different centrality classes. Each color is a different centrality class, as described in the legend. The error bars represent the statistical uncertainty, the empty boxes represent the overall systematic uncertainties, the shaded boxes represent the  $v_2$  related uncertainties.

1126 **7 Bibliography**

1127 **References**

- 1128 [1] B. Abelev et al. [ALICE Collaboration], JHEP **01** (2012) 128  
1129 [2] B. Abelev et al. [ALICE Collaboration], Eur. Phys. J. C (2017) 77:245  
1130 [3] B. Abelev et al. [ALICE Collaboration], Phys.Lett. B719 (2013) 29-41  
1131 [4] B. Abelev et al. [ALICE Collaboration], Phys.Lett. B726 (2013) 164-177  
1132 [5] ALICE Collaboration, arXiv:1609.06643 [nucl-ex]  
1133 [6] <https://aliceinfo.cern.ch/Notes/node/300>  
1134 [7] <https://aliceinfo.cern.ch/Notes/node/238>  
1135 [8] <https://aliceinfo.cern.ch/Notes/node/201>